University of Alberta

HEALTH MONITORING OF BURIED PIPELINE BUCKLING BY USING
DISTRIBUTED STRAIN SENSORY SYSTEMS

by

Zou-Long Chou

A thesis submitted to the Faculty of Graduate Studies and Research in partial
fulfillment of the requirements for the degree of

Doctor of Philosophy

in

Structural Engineering

Department of Civil & Environmental Engineering

Examining Committee

Dr. J.J. Roger Cheng, Civil and Environmental Engineering

Dr. Vivek S. Bindiganavile, Civil and Environmental Engineering

Dr. Samer Adeeb, Civil and Environmental Engineering

Dr. Xiaodong Wang, Mechanical Engineering

Dr. Hanping Hong, Civil and Environmental Engineering,
University of Western Ontario

ABSTRACT

As the demand for oil and gas resources increases pipeline construction pushes further into the Arctic and sub-Arctic regions. Consequently, these buried pipelines suffer much harsh environmental and complex loading conditions. Moreover, to increase the transporting efficiency, larger size pipes and higher operation pressure are used more frequently. Therefore, these conditions increase the risk of pipeline failure, especially local buckling (wrinkling) failure. To prevent the buried pipes from buckling failure, an automatic warning system for continuously monitoring pipeline buckling is needed. A method to achieve this purpose was studied and presented here.

The research program is divided into three phases. In the first phase, a literature review has concluded that it is feasible to detect pipe wrinkling by monitoring the signatures of distributed strains and curvatures along a buried pipe and by using the distributed strain sensory systems in a structural health monitoring (SHM) system. Subsequently, the test results and the field strain distribution data were used to verify the viability of using distributed strain sensors for early detecting wrinkles in buried pipes.

In the second phase, finite element (FE) models were developed and calibrated by the results of full-scale pipe buckling tests and then used to obtain the patterns (or signatures) of the strain distributions along pipes under combined loading. Based on the results of the parametric study, a SHM system is proposed. The system

integrated the distributed strain sensing system (such as Brillouin scattering fiber-optic sensory system), numerical models (FE models), and damage detection models (artificial neural network (ANN)) into a reliable, real-time monitoring system. Thereby, a methodology of health monitoring of the buried pipe buckling was carried out.

The last phase of the research focuses on the development of the damage detection models (DDM) in the SHM system. The effects of different parameters on the strain distribution patterns were studied by using a total of 74 FE models. The framework of the damage detection models was achieved mainly by four trained ANN protocols. The proposed damage detection model provides an accuracy of 90% in evaluating the health of the buried pipes during buckling and can reliably detect the onset of pipe wrinkling before the maximum strains accumulated on the monitored pipe reach 65% of the critical strain.

ACKNOWLEDGEMENTS

TABLE OF CONTENTS

APPENDICES

LIST OF TABLES

LIST OF FIGURES

LIST OF SYMBOLS AND ABBREVIATIONS

Latin Symbols

A%   Expected accuracy for an artificial neural network

C_ε Strain coefficient in transformation of Brillouin frequency

C_T Temperature coefficient in transformation of Brillouin frequency

d (t)   Desired output in the calculation of the delta rule

dy   Distance between the original and current positions for the shift of a

              neutral axis

d_p Desired output for the pattern p in MLP

d_m Mean of the desired outputs for all patterns in MLP

d_{pj} Desired output for the pattern p on the layer j in MLP

D   Nominal diameter of a pipe cross-section

L_0 Initial length between points over a corresponding demec (gauge) span

L_1 Current (deformed) length between points over a corresponding demec

              span

Ep Error function of the output for the pattern p on the layer j in MLP

f_j Threshold function of the weighted sum for the layer j in MLP

f_k Threshold function of the weighted sum for the layer k in MLP

f_{th} Threshold function of the weighted sum for a single layer network

L/r   ratio of nominal pipe length to nominal radius of the pipe cross section

n   Degree of arc used in the trigonometric functions

N_h Number of the hidden neurons in an artificial neural network

N_i Number of the input neurons in an artificial neural network

N_o Number of the output neurons in an artificial neural network

N_t Number of patterns in the training sets in an artificial neural network

$O_A(t)$ Responses of a civil system or a structure in either time series or a specific time

$O_m(t)$ Output of the learning model of a diagnostic system in SHM system, which is used to compare with $O_A(t)$ for evaluating conditions of the structure

R^2 The coefficient of multiple determination ($1 - \dfrac{\sum\limits_{p}(d_p - y_p)^2}{\sum\limits_{p}(d_p - d_m)^2}$)

t_{pj} Net input for the pattern p on the layer j in MLP

t_{pk} Net input for the pattern p on the layer k in MLP

T_o Temperature corresponding to the reference Brillouin frequency v_{BO}

T Temperature corresponding to a Brillouin frequency v_B

u_0 Displacement on the X-direction of the middle plane

v_e Displacement on the Y-axis for the end point over a corresponding demec span

v_i Displacement on the Y-axis for the start point over a corresponding demec span

w Out-of-plane displacement on the Z-direction of the middle plane

w_e Displacement on the Z-axis for the end point over a corresponding demec span

w_i Displacement on the Z-axis for the start point over a corresponding demec span

$w(t)$ Weigh applied in the connectivity between at a specific time

w_{ik} Weight applied in the connectivity from the layer i to the layer k in MLP

w_{kj} Weight applied in the connectivity from the layer k to the layer j in MLP

$|w|$ Number of weights in an artificial neural network

$x_i(t)$ Input on the node i for a single layer network

X_n Normalized strain

x_m, y_m Mean strains of distributed strains x and y, respectively

x, y a pair of distributed strains compared in the correlation function

(xp, yp) Coordinates corresponding to the best matching position of the two images with the cross-correlation technique

y_p Actual output for the pattern p in MLP

y_{pi} Actual output for the pattern p on the layer i in MLP

y_{pj} Actual output for the pattern p on the layer j in MLP

y_{pk} Actual output for the pattern p on the layer k in MLP

$y(t)$ Actual output in the calculation of the delta rule

Y_e Y-coordinate of the end point over a corresponding demec span

Y_i Y-coordinate of the start point over a corresponding demec span

Z_e Z-coordinate of the end point over a corresponding demec span

Z_i Z-coordinate of the start point over a corresponding demec span

Greek Symbols

δ_{pj} Output error for the pattern p on the output layer j in MLP

δ_{pk} Output error for the pattern p on the hidden layer k in MLP

Δ Output error in the calculation of the delta rule

ΔA Azimuth (rotation) change over the two selected measurements along a pipeline.

ΔP Pitch (rotation) change over the two selected measurements on the plane perpendicular to the azimuthal plane.

ΔS Spacing (distance) between the two selected measurements along the pipeline

ε_c Longitudinal strain on the compression side

ε_{cr} Critical longitudinal strain

ε_h Longitudinal strain on the horizontal direction

ε_n Longitudinal strains in the different circumferential positions in a pipe

ε_o Strain corresponding to the reference Brillouin frequency ν_{B0}

ε_t Longitudinal strains on the tension side

ε_v Longitudinal strain on the vertical direction

ε_{x0} Middle-surface longitudinal strain on the X-direction during large deflection

η Gain term, or called learning rate, $0 \leq \eta \leq 1$

Π Pi. A mathematical constant, approximately equal to 3.14159

κ Curvature over a specific gauge span

κ_h	Curvature in the plane orthogonal the vertical bending plane
κ_o	Global curvature
κ_v	Curvature in the vertical bending plane
ν_B	Brillouin frequency;
ν_{BO}	Reference Brillouin frequency;
σ	Standard deviation of the distributed strains
σ^2	Variance of the distributed strains
θ_b, θ_t	Rotation measured by a bottom and a top rotation meters respectively

Abbreviations

ADALINEs Adaptive linear neurons

AI   Artificial Intelligent

ANN   Artificial Neural Network

CI   Confidence interval in statistical analysis

CSA   Canadian Standard Association

cm   Units of centimeters

DAQ   Data acquisition system

FEA   Finite Element Analysis

FOS   Fibre-optic sensor

Geopig Pipe Geometry pigs, the in-line inspection equipment

GW   Girth weld

kN   Units of kilonewtons

LVDT   Linear variable different transducer

MLP   Multiple layer perceptrons

MPa   Units of megapascals (N/mm^2)

MSE   Mean square errors in the ANN output file

MTS   Material test system

m   Units of meters

mm   Units of milimeters

N   Units of newtons

NP   Non-pressure

NPS   Nominal pipe size, North American set of standard size for pipes

OD   Outside diameter of a pipe cross section

PM   Peak moment of a pipe during buckling

PL   Peak load of a pipe during buckling

RVDT   Rotational variable different transducer

SHM   Structural health monitoring

SMYS   Specified minimum yield strength

Tanh   Hyperbolic tangent function

UTS   Universal test system

WT   Wall thickness of a pipe

1. INTRODUCTION

1.1 The Energy Pipelines in Alberta

Alberta energy industry plays a very important role not only in Canadian economy but also in North American energy supplies. Over 80% of oil and natural gas production in Canada is produced in Alberta, and over 100,000 km long of large transmission pipelines operated in Canada over 85% are in Alberta (Cheng 2004). However, as the demand for these resources increases pipeline construction pushes further into the Arctic and sub-Arctic regions of the Canadian North. Consequently, these buried pipelines suffer much harsh environmental conditions, such as freeze and thaw, differential settlement, soil movement, and permafrost. Therefore, they sustain extremely complex loading conditions. In addition, higher strength materials, larger size pipes and higher operation pressure are becoming more frequently used in these pipes. These severe and unknown conditions increase the risk of pipeline failure, especially local buckling failure (wrinkling), as shown in Figure 1.1. The local buckling failure and sequential pipe fracture not only cause enormous cost loss but also lead to high risk in safety and environmental impact.

1.2 Structural Health Monitoring (SHM)

Structural Health Monitoring (SHM) is a relatively new term in civil engineering applications, and its definition has not yet to be standardized. Herein, SHM is defined both by its objectives and by the physical system (ISIS 200l). The objectives of SHM are to monitor the in-situ behaviour of a structure accurately and efficiently, to assess its performance under various service loads, to detect damage or deterioration, and to determine the health or condition of the structure. The physical diagnostic tool of SHM is a comprehensive integration of the following systems: a sensory system, a data acquisition system, a data processing system, a communication system, a damage detection and modeling system. The potential benefits of a SHM system include continuously real-time monitoring

and reporting, reducing down time, and improving safety and reliability, while reducing maintenance costs.

1.3 Health Monitoring for Buried Pipelines

Through larger number of full-scale tests in pipe buckling conducted at the University of Alberta in the last 15 years, a significant progress has been made in understanding the behaviour of pipe buckling under various combined loading conditions in laboratory settings. However, there is still a large void in field monitoring data for line pipes under complex environmental loading. In addition to the shortage of field information, because of the nature of complex surroundings and loadings, the critical buckling criteria developed for pipes (Mohareb et al. 1995, Dorey 2001) are difficult to apply in evaluation of the field conditions of buried pipelines. A reliable method for real-time monitoring and predicting the health of buried pipelines is needed to provide early detection of any damage that might occur in the pipes.

1.3.1 Difficulties for Monitoring Buried Pipelines

Not only are the critical buckling criteria difficult to apply in evaluating the field conditions of buried pipelines, but current technologies also are not easy to apply in monitoring the health of buried pipeline buckling due to interference of applications of these technologies by surroundings of the pipeline. Some extrinsic technologies, such as vibration and image processing techniques, are difficult to extract behavioural signatures of a buried pipeline from the measured data which can be flooded with serious noise; while some instruments, such as strain gauges and acoustic emission, cannot survive in severe underground environment. Therefore, for the thousands of kilometer of buried pipelines in the remote Canadian North, it is very difficult to detect their damage

1.3.2 Need of SHM for Buried Pipelines

In the past, to prevent the buried pipelines from buckling failure, engineers need to inspect the pipeline in the field periodically, and then to decide the schedule to release accumulated strains on the pipelines through excavation as shown in Figure 1.2. The whole inspection procedure is based on engineers' judgment; and the excavation process is quite expensive. Furthermore, this procedure has no active warning system for possible failures between inspections. Therefore, to overcome these problems, structural health monitoring (SHM) system has become a promising and effective technology. Among variety of SHM instrumentations, such as pipe deflection indicators, ultrasonic systems, and strain gauges, fiber-optic sensors (FOSs) have gradually gained acceptance in monitoring line pipes (Reed et al. 2004). However, the FOSs are still difficult to be used in monitoring of buried pipelines. The reason is that even though fiber-optic sensor technology has been progressing in the past decade, most of the FOSs, such as Fabry-Pero and Bragg Grating FOSs, are similar to conventional strain gauges in providing only localized information and cannot be used to monitor pipeline responses distributed over a long distance. Nevertheless, the distributed sensory systems, such as Geopig and recently developed Brillouin scattering fiber-optic sensing (BSFOS) system have become the excellent candidates for monitoring the buried pipelines because of its special ability of measuring distributed curvatures and strains respectively along the pipelines. The proposed SHM system in this research program is to integrate the distributed strain sensory system, numerical models (finite element models), and damage detection models (artificial neural network (ANN)) into a reliable, real-time, on-demand monitoring system for the local buckling of buried pipelines. The success of the program will allow engineers to reliably diagnose the pipe behaviour without interrupt the normal operation of buried pipelines.

3

1.4 Objectives of the Research Program

This research program is designed in three phases. In the first phase, the potential of using distributed strain sensors in predicting the inception of wrinkles in a pipe is studied and validated through experimental programs. In the second phase, finite element models are developed and calibrated by the results of full-scale pipe buckling tests. The models are then used to conduct the patterns (or signatures) of the strain distributions of pipe buckling of a pipe under combined loading, and to find the relationship of strains at different locations axially and circumferentially. In the last phase, a prediction algorithm for pipe wrinkling using distributed strain patterns is developed. The Artificial Neural Network (ANN) is trained to identify the condition of pipe deterioration so the initiation of pipe wrinkle can be detected. The ultimate goal of the program is to provide pipeline operators with a continuously real-time, active warning system for detection of buried pipeline wrinkling by using distributed strain sensors.

1.5 Layout of the Thesis

A literature review of the behaviour of buried pipelines, as well as the monitoring technologies for line pipes are presented in Chapter 2.

Distributed strain patterns along the pipe segments, including previous experimental and field pipes under combined loading, are discussed in Chapter 3.

The most recent techniques of monitoring distributed strains are explained in Chapter 4. These techniques are applied to monitor the experimental pipes in this research program. The results of these experiments are used to verify the feasibility of using distributed strain sensors in predicting the wrinkling of buried pipes and presented in Chapter 4.

In Chapter 5, through a comprehensive analytical program, the behavioural signatures of the pipe buckling revealed on strain distribution patterns are

confirmed. Accordingly, the methodology of health monitoring of the buried pipe buckling is proposed.

In Chapter 6, based on the proposed health monitoring methodology, a parametric study is processed for developing a reliable damage detection system for buried pipe wrinkling.

The damage detection model is explained in Chapter 7, and a warning system with artificial neural networks (ANNs) employed by the damage detection model is proposed here. The warning system is applied in monitoring buried pipes for buckling using distributed strain sensors. A framework of the warning system is also presented here.

Chapter 8 provides conclusions and recommendations of this research program.
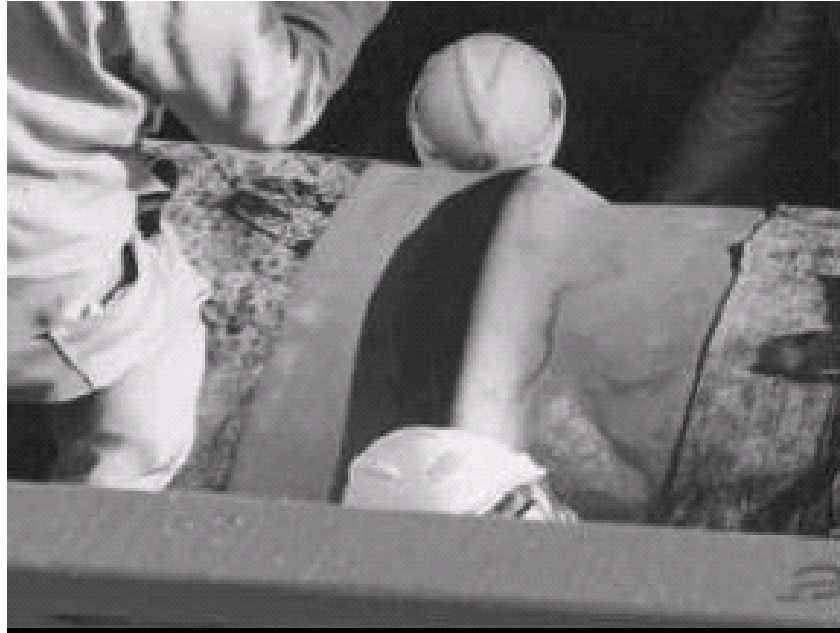
Figure 1.1 Local Buckling (Wrinkle) of a Pipeline

Figure 1.2 Excavation of a Pipeline

2. LITERATURE REVIEW

2.1 Previous Investigation on Buried Pipelines

2.1.1 Behaviour of Buried Pipelines

Behaviour of line-pipes was reviewed comprehensively by Stephens and Kulak (1982) with respect to the theoretical development and design formula of the line-pipe buckling. The report reviewed researches conducted from 1920's to 1970's. In the report, the behaviour of pipe buckling with different slenderness conditions was explained; the contributions of different pipe parameters, such as the length to radius (L/D) ratio, the diameter to wall thickness (D/t) ratio, and material properties, to the strength of pipe buckling were investigated; and the ultimate strength formula of pipe buckling were examined and recommended. However, most researches concerned mainly on the strength of the pipe buckling before 1970's. The deformation (or strain) criteria of the pipe buckling did not attract significant attention until a series of analytical and experimental works were done at the University of Alberta. Murray (1997) summarized the benchmark researches on the strain criteria and identified some important characteristics of the behaviour of buried pipes. He concluded that the overall characteristics of the pipeline-soil system can be seen as a beam element with a series of non-linear spring supports, while its local behaviour can be modeled as cylindrical shell behaviour. Moreover, Murray postulated that the limit states of a buried pipe arising from geotechnical movement should be the deformation not the strength. Well-known pioneer tests of industrial line-pipes were done by Bounkamp and Stephen (1973) and were reviewed in Murray's paper. After examination of the test program, Mohareb et al. (1993) conducted a series of full-size pipe experiments at the University of Alberta. These experiments considered different pipe geometries, pipe materials, loading conditions, operation pressure and temperature, and girth weld condition. All experimental results confirmed the behavioural characteristics of the buried pipes. The principal characteristics of

local buckling (wrinkling) behaviour for the buried pipelines can be summarized as follows:

- A single wrinkle is eventually developed over only a small length of the line-pipe, equal or less than a diameter of the pipe, even if a periodic waveform initially occurs over the pipe.

- As the wrinkle grows in the post-buckling stage, its capacity to carry load decreases and the pipe softens

- While the strains in the vicinity of the wrinkle continue to increase, the strains in the regions outside of the wrinkle decrease because of strain localization.

At the same time, Datta (1999) reviewed papers published from 1980s' to 1990s' concerning the seismic response of buried pipes. He postulated that the basic concept governing the response of the buried pipeline is that the pipeline is constrained by soil, and hence the pipeline has to conform to the earthquake deformation resulted from ground motion. These deformations are mainly curvature and shearing. The large deformations leading to pipe buckling are particularly imposed on the pipe segment crossing a fault. He found that the behaviour of a buried pipe remains a quasi-static response when earthquake generates dynamic ground motion. Accordingly, the behavioural characteristics of the buried pipeline under seismic loading should be similar to that stated by Murray (1997).

In addition, Song (2007) and He (2007) investigated the effect of the operation and construction load on the pipe behaviour. Cyclic and impact loads are frequently imposed on the buried pipes during excavation procedure. Therefore, the cyclic load is applied in Song's experimental pipe specimens, and effect of the impact load on buried line-pipe is examined in He's field tests. The results showed that, under operation of the excavation, deformation imposed on a line-pipe due to the impact load is not large enough to trigger the buckling of the

8

buried pipe, and the cyclic load due to repeated stress relieved procedures has negligible effects on the behavioural characteristics of a line-pipe.

2.1.2 Failure of Buried Pipelines

As mentioned previously, buried pipelines have been extended to higher risk terrains, and consequently more complex behaviour of buried pipelines are induced. The behavioural characteristics of the buried pipelines have been reviewed above, and the possible failures of the buried pipelines are investigated in the followings. Geologically unstable terrain and permafrost in the Arctic are the most concerned by researchers and engineers due to their extremely uncertain conditions. For geotectonic hazard area, O'Rourke and Liu (1999) and O'Rourke and Ayala (1993) addressed seismic hazards for buried pipeline in their works. They noticed that permanent ground deformation of earthquake is not a main factor to damage the buried pipelines, but the seismic wave propagation that can cause the buried pipeline damage in the area of relatively abrupt changes in subsurface conditions. Such damage is usually resulted from extra axial extension at joints of the line-pipes and consequently leads to leak or crush in these joints. In addition, soil liquefaction due to strong shaking of earthquake on sand layer will make buried pipelines lose their constraint, and then flotation of the pipelines induces large deformation on the buried segments (Ling et al. 2003, Shinozuka et al. 1995). Slope instability is other issue of geotechnical movement. It not only causes pipe wrinkling (Yoosef-Ghodsi et al. 2000), but also leads to pipe tearing failure (Das et al. 2002).

In addition to geotechnical movement, the buried pipelines frequently suffer freeze-and-thaw settlement and frost heave in the Arctic and sub-Arctic regions as a pipe route crosses permafrost and unfrozen ground. In Palmer and Williams' investigation (2003), upheaval usually causes the consequence of pipe instability because soil burden decreases during pipe deflection resulted from frost heave; on the other hand, sag bend of the buried pipe segment can become stable due to increase of resistance during pipe deformation. In addition, ice keel movement to

damage offshore pipelines is another issue for the pipelines buried near the Arctic area. Nobagar et al. (2007) pointed out that because of ice keel movement, the huge ice block applies enormous force on the sea bed above the buried pipeline and subsequently induces large deformation on the pipe segment. The large deformation is resulted from the combined loadings such as axial load, shear force, bending moment, and surrounding pressure.

The structural failure of the buried pipelines can come from the above factors, as well as other occasional conditions such as construction, rock fall, and collision. These occasional loads usually induce an impact load on the buried pipe segment. Picher et al. (2006) studied the effect of impact load on a gravel-buried pipe due to rock fall. Czyz et al. (2003) investigated the offshore pipeline dent damage because of impact of collision between a ship anchor and a buried line-pipe.

In summary, the buried pipelines can experience the structural failures as follows: over bend, local buckling (wrinkle), tearing, dent, and shear failure, and consequently lead to pipe malfunction, crack or leak. However, the local buckle failure (wrinkle) of buried pipes is the focus in this research program.

2.2 Structural Health Monitoring (SHM)

2.2.1 Development of Structural Health Monitoring

Although the use of instruments to assess the integrity of structure could go far back in 19th century when engineers had used various measuring instruments in bridge field tests (ISIS 2001), Structural Health Monitoring (SHM) is a relatively new concept in civil engineering and the concept of SHM was first systematically proposed by Pau (1981). In Pau's book (1981), the relation of damage extent and performance condition is systematically defined, the criteria of condition evaluation were proposed based on the reliability analysis, and monitoring techniques along with statistical and probability theories are applied in many mechanical systems, such as vibration and acoustic systems. Following Pau's idea, the interrelationship between the civil-system performance, monitoring, and

diagnosis is illustrated in Figure 2.1. The figure shows the philosophy used in SHM that is generally accepted by current researchers and engineers. The integrated SHM system should include a monitoring system and a diagnostic system (see Figure 2.1). The characteristics of each of failure modes envisaged should be built as learning data for a diagnostic system. SHM is expected to remotely monitor the responses $O_A(t)$ of a civil system or a structure in either time series or a specific time, or both. Upon structural failure or deterioration is detected by the learning model output, $O_m(t)$, of the diagnostic system, it must be possible to take one of the following actions very quickly: alarm or warning, appropriate repairs arranged in maintenance action if the structure is accessible, and reconfiguration if the structure cannot be accessed. However, the Pau's research focuses on mechanical components, not on civil engineering infrastructure. Housner et al. (1997) reviewed the most recent history of SHM applied in civil engineering area. This review paper covered the SHM papers published in 1980 to 1997. Different monitoring techniques, analytical algorithms, and some applications were interpreted. ISIS Canada (ISIS 2001) proposed that the main components for a SHM system in the civil engineering infrastructure should contain acquisition of data, communication of data, intelligent processing of data, storage of processed data, and diagnostics and retrieval of data. Furthermore, it profiled the SHM systems for practical applications. Los Alamos National Laboratory (LANL 2003) published a report of reviewing SHM papers from 1996 to 2001. They found that many advanced monitoring technologies had been further progressing, and gradually been applied in engineering practices. These advanced technologies include semiconductor systems, fibre-optic systems (FOS), micro-electro-mechanical systems (MEMS), etc. Some monitoring sensing systems applied in the pipeline industry will be covered in the later section. In addition to the explanation of the advanced monitoring technologies, the methods relevant to discrimination of features for damage detection were also reviewed (LANL 2003). These methods include statistical discrimination, such as Fisher's discriminant, Bayesian expression, and outlier analysis, neural network, and fuzzy logic. It was found that, for a SHM

project, using only one method to extract features from the monitored structure and to identify structural health generally is not practical. The usual action is to employ one to weigh parameters of the monitored structure, and to apply the other to locate and quantify damage. It can be illustrated in the following two examples:

Worden et al. (2000) detected damage in composite plates using Lamb waves by using outlier analysis, neural networks, and estimation of the probability density function (PDF), sequentially. Through the outlier analysis and an iterative procedure in the neural networks, the novelty index corresponding to a new pattern is defined as the Euclidean distance between the target output (or input) and the output from the trained network. Then, the probability density function (PDF) of the features over the normal condition set is evaluated. Once a new feature is obtained, the new feature is classified as either damaged or undamaged by comparing the new feature against the PDF of the normal condition. Accordingly, the damage can be identified.

In the other case, Chae and Abraham (2001) described the development of an automated data interpretation system for sanitary sewer pipelines. The system obtained optical data from the Sewer Scanner and Evaluation Technology (SSET); then multiple neural networks were used for feature pattern recognition; and finally using of fuzzy logic systems refined the diagnosis of the anomaly of the pipeline. In this project, even though the neural networks can recognize the type and level of the defects in the pipeline, the outputs from the neural network system still have certain errors. Fuzzy set theory and fuzzy implication techniques were used to automatically identify, classify, and rate pipe defects by minimizing the errors from the neural network system.

2.2.2 Health Monitoring for Buried Pipelines

2.2.2.1 Current Technologies

The most recent technologies for SHM can be classified into two main groups: smart materials and in-situ monitoring techniques. The former is to embed monitoring sensors into a pipe material, such as embedding fibre-optic sensors (FOSs) in carbon fibre reinforced polymer (CFRP) pipe (Bastianini et al. 2003), when it is being manufactured; while the latter is to install a monitoring system along pipelines either before, during, or after construction (Inaudi and Clisic 2006). In this section, the latter one is mainly concerned. The following in-situ monitoring technologies are usually used for on-line/in-line pipe inspection.

Strain gauges:
Use of strain gauges is still the most common technique for monitoring structural strains because of low cost, simple installation, and well proven. The foil and weldable strain gauges are the two main types used in monitored structures. The weldable strain gauges can be used in long-term monitoring since the gauges are boned on a structure with spot welds, but not adhesive which has the potential to creep and low resistance to harsh environment. Although the weldable strain gauges are mechanical robust, but they still surfer the following deficiencies: interference of electromagnet, high noise in long-distance transmission, and need of conduct electricity.

Ultrasonic sensors:
Ultrasonic measurement techniques are used on pipelines to measure the wall thickness and to assist in predicting the existing life of a pipeline. The fundamental concept is the use of the pulse-echo method to detect flaws in a line-pipe. Recent techniques allow a ring of ultrasonic sensors to be permanently mounted on the pipeline so that these sensors can be routinely interrogated by phone lines.

Pressure systems:

Pressure evaluation systems like the Supervisory Control and Data Acquisition (SCADA) system are widely used to monitor pressure fluctuation in pipelines and alarm warning for pipe leak. Some of the shortcomings include inability to accurately pinpoint the leak as well as susceptibility to operator error. Leak detection through pressure testing is also done by pressurizing a closed-circuit pipeline system to see if the pressure is maintained, and a serious drawback of this approach is that the pressurization sometimes weakens existing deficiencies or actually causes the pipe to rupture.

Acoustic emission:

Acoustic techniques can be the most cost-effective method and are usually used with stethoscopes, ground microphones, and acoustic correlators (Covas et al. 2005). Noise Correlators are a common trade name for these type devices, and by monitoring acoustic wave patterns or sound patterns the failure mode of the monitored pipe can be detected by the noise once the crack occurs in the pipe.

Vibration systems

Vibration systems are similar to acoustic systems, but they are attempting to measure the high-frequency signals associated with a leak. They differ from the microphone systems in their sensor. Most solutions involve accelerometers or micro phonic solutions. Vibration systems are also used to detect the change of pipe properties, such as geometry and wall thickness by monitoring the frequency change during pipe deformation.

Semiconductor relevant sensing systems:

Semiconductor relevant systems have been widely used in monitoring pipe parameters, such as strain, temperature, pressure, vibration frequency, etc. Piezoresistors, piezoelectric systems, and micro-electro-mechanical systems (MEMS) are gradually used in pipeline monitoring (Housner et al. 1997). The electric properties, such as voltage, of these sensing systems are directly

proportional to the applied force, pressure, or strain; the output signal is then related to this mechanical force as if it had passed through the equivalent circuit. Most of these systems are made of silicon or ceramics in current commercial products. The piezoresistor, a semiconductor strain gauge, can measure strain in excellent accuracy, e.g. a nanometer, but it is very expensive and temperature-sensitive. The piezoelectric system is a device that can monitor pressure, acceleration, strain or force by measuring an electrical signal in pipe response. It can perform both sensing and actuation functions in a monitoring system. This kind of system usually has the characteristics of both the acoustic system and vibration system. A key feature of the piezoelectric sensors is that these sensors are easily integrated in plurality along a pipeline system due to their conformability, and have ability to continuously monitor and locate anomaly. Another advantage is that the piezoelectric wafer can also act as a data transmission system (Pretorius et al. 2005). The new generation of semiconductor sensors has been developed in last decade. A micro-electro-mechanical system (MEMS) is a representative of them. The MEMS is the integration of mechanical elements, sensors, actuators, and electronics on a common silicon substrate through micro fabrication technology. It contains the advantages the same as those of piezoresistor and the piezoelectric system, at the same time reduces the size of a sensor and increases the stability in both data transmission and environmental sensitivity. The MEMS technology has to be able to measure temperature, acceleration, frequency, strain, and/or pressure for the civil engineering infrastructure.

Magnetic Flux Leakage (MFL) tools:

MFL has capability to assess the general pipe wall condition both inside and outside of the pipe section; but it is usually difficult for these tools to detect narrow-long defects along the pipe segment because MFL tools use an axially oriented magnetic field. The fundamental concept of MFL measurement (Sutherland and Paz 2000) are based on: magnets produce magnetic fields that exert a force of attraction on ferromagnetic materials; lines of flux can represent

the strength and direction of the magnetic field; magnetic flux tends to travel through steel rather than air or gas since it is a ferromagnetic material. Magnetic flux leakage measurement is built on a relationship of magnetic saturation and flux leakage in the monitored area by placing sensors adjacent to the pipe wall within the magnetic circuit. Accurate determination and interpretation of the size of the defects relies upon a magnetic field that is not only strong but uniform and consistent.

Guided wave pipe inspection system:

Typical operation of guided wave pipe inspection tool usually uses ultrasonic Lamb waves to measure reduction of pipe wall thickness due to localized corrosion at pipe supports. Lamb waves have the main advantage that being guided by the structure itself. Lamb waves will permit inspection of plates or shells more quickly than bulk waves (Legendre 2000). The technique typically uses two transducers in a pitch-catch mode to sent and receive a selected Lamb wave. The wave travels along the pipe wall in the circumferential direction. The time-of-flight between two transducers is influenced because of the reduction of pipe wall. In addition, fibre-optic sensors (FOS) can be seen as another guided wave inspection system. An optical fibre is cylindrical dielectric waveguide made from silica glass or a polymer material. The waveguide is a structure that guides waves such as electromagnetic waves, light, or sound waves, and there are different types of waveguide for each type of wave. Optical waveguide is one of them, and the most common optical waveguide in measurement is optical fiber.

Fibre-Optic Sensors (FOS):

Fibre-optic sensor technology is being seen as a good candidate for a range of sensing tasks, including strain measurement and environmental parameter monitoring. The major attractive features of optical fibre sensors are their abilities to (1) function without the need for direct electrical power, (2) transmit relatively weak signals over long distances without deterioration and with low noise, (3) distributed measurements and multiplexing capability along the length of the

optical fibre in data channel, (4) avoidance of electromagnetic interference, and (5) very large band width of fibre sensing systems. In addition to the above benefits from the optical fibre technology, another reason why the fibre-optic sensors become more popular in the recent years is the decrease of cost. Before, single mode optical fibre costs US$20/m in 1979, but now costs less than US$0.1/m with vastly improved optical and mechanical properties. Many types of FOSs have been developed in last two decades (Udd 1991). Three types of FOSs, fibre grating sensors, long gauge sensors, and Brillouin distributed sensors, are explained in the followings because of their own unique capabilities and applications (Housner et al. 1997, ISIS 2001, Lee 2003, Mufti et al. 2003, Zou et al. 2004, Ravet et al. 2004 and 2006, Inaudi and Clisic 2006, Tennyson et al. 2007).

Fibre-optic grating sensors:

Fibre-optic grating seneors have been widely used to support the measurement of strains and temperatures. Current techniques allow the fibre-optic grating sensors to measure multi-parameters simultaneously, by appropriate installation (Udd 2007). The Fibre Bragg Grating (FBG) sensor is very commonly used in the current civil engineering infrastructure. The FBG measures parameters, such as strains and temperatures, based on shift of the wavelength of the reflected light in grating portion of the optical fibre. The FBG sensors possess the following unique characteristics:

- Sensed information is encoded directly into optical wavelength, which is an absolute parameter. Therefore, the output does not depend on the light intensity levels, losses in the connecting fibres and couplers, or recalibration or re-initialization of the system.

- FBG sensors can also handle wavelength division multiplexing by the fabrication of each grating at a slightly different frequency within the broadband source spectrum on a single fibre.

The above characteristics make FBG possible to process distributed sensing by installing multi-grating portions along the sensing fibre.

Long gauge sensors:

Long-distance measuring sensors (ISIS 2001) can broadly be classified into two systems: one is long gauge length system; the other is distributed sensing system. The former is discussed in this paragraph. Long gauge length system uses a conventional telecom optical fibre of arbitrary length bonded to a structure. It measures relative displacement between two points, usually at the both ends of the sensing fibre, on the monitored component by means of two mirrors formed on a fibre-optic lead. The distance between the two mirrors along the fibre-optic cable defines the gauge length. The long gauge length system can be configured to read sensors from as small as 5 cm to as long as 100 m, and is such flexible optical fibre that it can be used in many different configurations. This system is well suited to monitor permanent long-term static deformation either from thermal or mechanical loading.

Distributed fibre –optic sensing systems:

Distributed fibre-optic sensing systems (ISIS 2001) are the other long-distance measuring sensors, and among the distributed sensing techniques, Brillouin scattering fibre-optic is a speedily developed one. Brillouin scattering fibre-optic sensors also use standard telecom optical fibre and can be used to measure strains and/or temperature due to thermal or mechanical loading. This method has the crucial advantage that it is a "distributed" sensor that can take readings at various positions along the optical fibre over very long distances, e.g. 20 km order. The detail discussion will be presented in Section 4.1.

Intelligent pigs:

They are usually fitted with sensors to measure parameters of interest, and with on-board electronics to capture the data. The following three types of pigs are usually used in the pipeline industry (Reed et al. 2004): Metal Loss pigs, Leakage pigs, and Pipe Geometry pigs (Geopig). The system of these pigs is a vehicle or a small robot carrying sensors, lasers, camera, ultrasonic equipment, or other

facilities depending on different purposes. Metal Loss pig mainly employs the MFL technology, and Leakage pig uses ultrasonic or laser system to pinpoint the location of leak from the pipe. Pipe Geometry pigs, such as caliper pig and inertial navigation pig, have successfully be applied to measure pipe deflection, curvatures, and strains in the distributed locations along the pipeline for several years. The Geopig will be interpreted in details in the next chapter.

2.2.2.2 Assessment of Monitoring Technologies

The monitoring technologies frequently used in on-line/in-line pipe inspection have been explained above. A general assessment for these technologies is shown in Table 2.1. In the table, the evaluated parameters contain monitoring parameters and applicability. The monitoring parameters include wall thickness, pipe deflection, strains and curvatures on the pipe, pipe leakage, pipe crack, and joint integrity. The applicability considers the ability of the technology in distributed sensing and continuously monitoring with normal operation of pipeline. Herein, the term "continuously" is in contrast to the term "periodically". The capacity of the continuous monitor can reduce the risk of pipeline failure during the interval between periodic inspections.

In addition, some technologies, shown in Table 2.1, can have various types of inspection tools, and hence the cost and measurement accuracy are usually influenced depending on different requirements of an inspection plan. For instance, for intelligent pigs used in pipeline monitoring, clients can employ caliper pig for survey of pipe-wall deformation, or they need Geopig with GPS for locating pipeline anomalies (such as bucking) and pipeline mapping. These two cases are quite different in cost. For another example, as distributed FOS is asked to only profile a trend of strain distribution, engineers may allow the strain error of the system up to $100\mu\varepsilon$; while the more expensive system can provide strain accuracy less than $10\mu\varepsilon$.

As mentioned, the limit states of buried pipes should be focused more on the deformation than on the strength. The deformation parameters include strains, curvatures, and deflections, and therefore the current technologies applied in monitoring the health of buried pipeline buckling should have an ability of measuring pipe strains, curvatures, or deflection. Moreover, some instruments such as strain gauges and acoustic emission cannot survive in severe underground environment, and some technologies such as MEMS and point FOS provide only localized information and cannot be used to monitor pipeline responses distributed over a long distance. On the other hand, the distributed FOS and intelligent pigs should be better candidates for monitoring the buried pipelines because of their special ability of measuring distributed curvatures and strains respectively along the pipelines.

2.3 Summary

Through the above literature review, it can be seen that the behaviour of the buried pipeline is quite complex due to the nature of soil-structure interaction. Even if the design criteria for steel pipes have been further improved and refined by considering more complete parameters and validating with a large amount of experimental data (Moherab et al. 1993, Dorey et al. 2001), a main variable of geological and soil conditions is difficult to be evaluated. Soil stiffness (modulus) is one of the most important soil properties and is the main contributor to the soil-pipe system performance. Different soil stiffness induces different driving force along line-pipe surface, and forms different constrains surrounding the pipeline (Moser, 2001). By contrast, the characteristics of the buried pipeline during wrinkling are well researched and defined. That is, it is possible to detect pipe wrinkling through behavioural signatures revealed on the buried pipe itself. The signatures should be deformation-relevant parameters such as strains and curvatures rather than strength-relevant parameters such as forces and stresses.

To monitor the deformation parameters of pipelines, some technologies have been highlighted for this purpose from the above review of the monitoring

20

technologies. Among them, the FOS and intelligent pigs appear to be the better candidates because of high measurement accuracy and negligible electromagnetic interference. Furthermore, considering the ability of the technologies to distributed sensing, the intelligent pig such as Geopig and distributed FOS system such as recently developed Brillouin scattering fiber-optic sensing (BSFOS) system are selected for monitoring the buried pipelines, and will be further discussed in the sequent chapters.

Table 2.1 Assessment of Monitoring Technologies							
Parameters:	Monitoring Techniques						
	Strain Gauges	Ultrasonic Sensors	Acoustic Emission	MEMS	MFL Tools	Point FOS	Distributed FOS	Intelligent Pigs
Wall Thickness	N.A.	Good	N.A.	N.A.	Good	N.A.	N.A.	A.
Pipe Strains or Curvatures	Good	N.A.	N.A.	Good	N.A.	Good	Good	Good
Pipe Deflection	A.	N.A.	A.	A.	N.A.	A.	A.	Good
Crack Growth	N.A.	Good	Good	A.	Good	A.	A.	A.
Pipe Leakage	N.A.	A.	N.A.	A.	A.	N.A.	N.A.	N.A.
Joint Integrity	N.A.	N.A.	N.A.	N.A.	Good	N.A.	A.	Good
Distributed Sensing	N.A.	N.A.	A.	N.A.	A.	N.A.	Good	Good
Continuous Monitoring	A.	A.	A.	A.	N.A.	Good	Good	N.A.
N.A.: Not Applicable A.: Applicable							
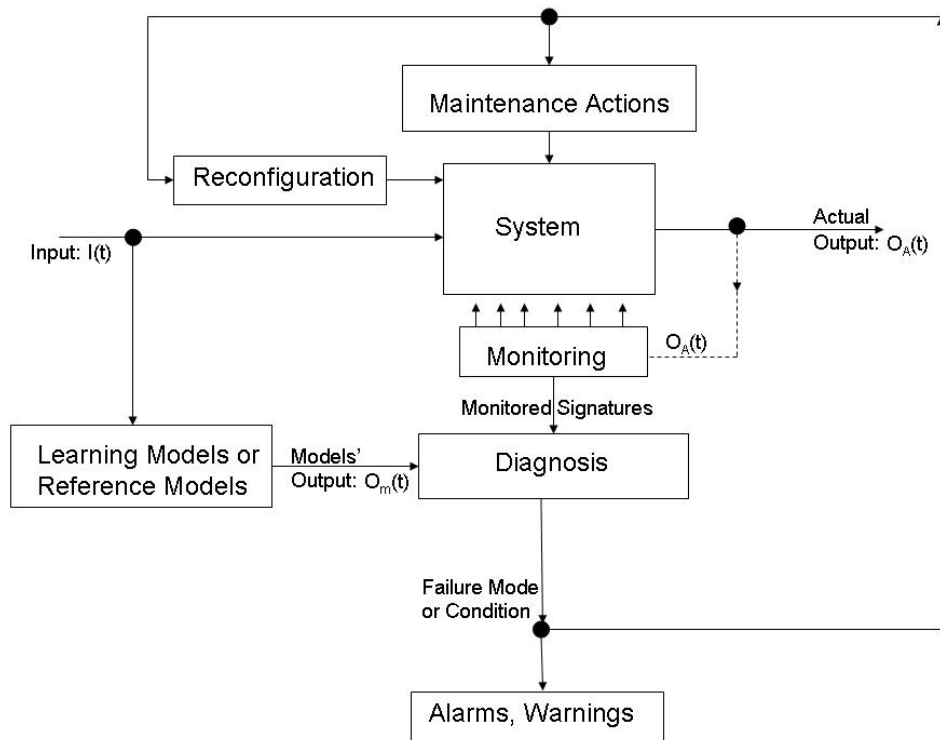
Figure 2.1 Diagnosis, Monitoring, and Performance of the SHM System

3. DISTRIBUTED STRAINS (CURVATURES) ALONG BUCKLED LINE-PIPES

As mentioned in Sections 2.2 and 2.3, distributed sensing tools, such as a Geopig and distributed fibre-optic sensory system, are better choices for in-line/on-line inspection of the bucking of buried pipeline. They are usually used to determine the anomalies of pipelines by detecting the development of distributed strains or distributed curvatures along the pipeline. Therefore, the distributed strains and curvatures in different pipe conditions during buckling need to be reviewed.

3.1 Distributed Strains of Buried Pipelines during Buckling

The distributed measurement for pipeline inspection, especially for buried pipelines, usually is processed by using various pigs. One of them, called Geopig, is shown in Figure 3.1. The Geopig was first developed twenty years ago, and has been widely applied in pipeline inspections in the last ten years. Many components are included in the current commercial pigs, but the basic components of the Geopig are gyros, accelerometers, odometer wheels, and sensors. Gyros are used to measure the differences in the attitudes along a pipe segment and the positions of the measurements around the pipe in the segment; accelerometers and odometer wheels are used to measure the distances between the measurements along the pipe. The functions of these components overlap to verify the correctness of the measured results. With these components, the distributed curvatures along a line-pipe can be measured. An example of curvature distribution is shown in Figure 3.2(a), and the typical data for pipe inspection using a Geopig is shown in Figure 3.2(b). The distributed curvatures can be converted into distributed strains (Czyz and Adams 1994). The distributed strain data can be used to diagnose the health of pipelines. These distributed strains must be collected and studied to develop a reliable warning system that monitors distributed strain patterns to detect pipeline wrinkling.

3.1.1 Distributed Strains Collected from Geopig

The distributed strains presented in Figures 3.3 to 3.8 were collected mainly from Geopig measurments (Czyz and Wainselboin 2003, Lukasiewicz et al. 2006). A total of six strain distribution patterns were found for different pipe diameters, from 8 in to 36 in (203.0 mm to 914.4 mm), and different surrounding conditions that triggered pipe wrinkling. Because the localized strain distributions are probably similar for a dented pipe and for a wrinkle pipe, one of the above patterns was collected from pipe dent damage (Figure 3.3) to verify that the developed decision-making system can distinguish between these two damage events. The distributed strains in Figures 3.4 to 3.8 show that during pipe wrinkling, the strain was localized and concentrated over a much large range, e.g., 3 meters. This finding disagrees with the findings in previous studies. In Mohareb's investigation (1995), the wrinkling range usually covered half a diameter of a pipe for an outward (bulge) type wrinkle and a diameter of a pipe for an inward (diamond) type wrinkle. Accordingly, the wrinkling range in the selected data should be less than 1 meter. The disagreement between the results from using pig measurements and the behaviour of the pipes comes from the pig's operating limitations. To clarify this argument, the operation of pigs will first be explained.

The pigs can handle a pipeline ranging in diameter from NPS 8 to NPS 52 (or outside diameter (OD) from 8 in to 52 in). The tools, in general, can deal with three times diameter bends and temperatures up to 70°C, and some of them have been designed to run 1.5 times-diameter bends (Czyz and Wainselboin 2003).The typical line speeds for the pigs are 2 m/sec to 3 m/sec, and the pigs can function well at up to 5 m/sec. The higher velocity will cause spacing of measurements too far apart to be useful in structural interpretation. With a pig traveling at 2 m/sec, a complete set of data samples is provided every 40 mm. While the previous data are collected in equal interval, the weld-detected information is recorded only at a girth weld.

The fundamental formula to compute the vertical and horizontal curvatures (κ_v and κ_h) in the pigs is shown in Equation 3.1:

$$\kappa_v = -\frac{\Delta P}{\Delta S} \; ; \; \kappa_h = -\frac{\Delta A}{\Delta S} \cos P \qquad\qquad (3.1)$$

As the pig travels along a pipeline which follows different topographical altitudes and orientations on the required route, the attitude of the pig usually needs to be changed during the in-line inspection procedure. Accordingly, the curvature measured by the pig is usually a spatial curvature computed from the different attitudes of the pig over a distance S. ΔP and ΔA are changes of the tangent vector along the centerline of the pipe in vertical and horizontal directions, respectively, in a certain interval ΔS. The distance ΔS used in actual computations is several times longer than the distance between two consecutive samples recorded by the inertial system. The distance ΔS is usually three times the pipe diameter, mainly due to the need to reduce noise (perturbation) in the curvature. The perturbation is caused by the pig's vibration.

As strain-base design has been recommended in pipe design standards, e.g. CAN/CSA Z662-03, the pigs present not only the curvature data, but also the longitudinal strains along a monitored pipe. Kirchhoff's hypothesis, a plane remains a plane during pipe deforming is considered, and, thus, the strains can be computed according to Equation 3.2. In Equation 3.2, D represents a pipe diameter and dy is a distance between the original and current positions of the neutral axis as it shifts during pipe wrinkling. The vertical and horizontal strains (ε_v and ε_h) are obtained by replacing the curvature κ with κ_v and κ_h, respectively, in Equation 3.2. The strain resultant ε_{max} can be calculated by using Equation 3.3.

$$\varepsilon = (\frac{-D}{2} + dy) * \kappa \qquad\qquad (3.2)$$

$$\varepsilon_{max} = \sqrt{\varepsilon_v^2 + \varepsilon_h^2} \qquad\qquad (3.3)$$

3.1.2 Distributed Strains for the Buried Pipes

The strain distribution patterns resulting from pipe buckling were collected and are presented in Figures 3.4 to 3.8, along with one from dent damage (Figure 3.3). The pipe buckle was triggered by different factors, such as slope instability, soil bed settlement, and high operating temperature.

NPS36 Pipe (Figure 3.3)

The pipe suffered from dent damage. A distributed strain pattern was collected from the caliper measurements of a pig for the pipe with D/t ratio of 139. The pipe dent was up to 21 mm deep, and caused around 1.6% strain localization. A very dramatic fluctuation was concentrated in a relatively narrow wrinkle range.

NPS12 Pipe (Figure 3.4)

The gas line was investigated after several years of the pipe's operation. This pipe was under bend over 40 m. Strain as high as 1.5% was concentrated in a 0.7 m long field joint, as shown in Figure 3.4.

NPS24 Pipe (Figure 3.5)

Figure 3.5 presents the results of the strain distribution in the free spanning segment of an offshore gas line. Due to soil settlement in the 500 m long free span, additional external force introduced a high strain into the location near a pipeline support.

NPS8 Pipe (Figure 3.6)

The pipe was buckled as the operating temperature rises, and this pipe was buried in insufficient backfill and constrain in a swamp area. Pipe upheaval caused over bend in the buried pipe. The strain distribution pattern is shown in Figure 3.6. The localized deformation was intercepted in the girth weld location, nearby the 80 m point in the X-axis.

Due to landslide, the pipeline suffered a 25 mm outward wrinkle. This wrinkle was just beside the girth weld location. As the pipe was under 4º sag bend over a 5 m long segment, a 10 mm wrinkle was formed circumferentially around the pipe. As shown in Figure 3.7, the girth weld location is close to the 30 m point along the X-axis.

Another case is that a pipeline was buried in a mountainous region. The slope instability induced large axial load to the line-pipe and resulted in the pipe buckle in a 1.7 m horizontal movement over a 500 m segment of pipeline. The strain distribution is shown in Figure 3.8.

3.2 Distributed Strains (Curvatures) of Experimental Line-Pipes during Buckling

A large amount of experimental data for line-pipe has been generated by University of Alberta researchers in the last two decades, and these researchers have made important contributions to the study of pipeline behaviour and of the critical strains in the line-pipes. However, very little data have been analyzed or even collected for distributed strains.

In the past, strain measurements were often difficult to collect exactly at a critical location, e.g., wrinkling location. Even if the strain gauge is placed right on the critical location, reliable measurements in large deformations of pipe during post-buckling are difficult to obtain. Alternatively, a demec gauge becomes a more reliable tool for strain measurements in the line pipes as strain gauges are not placed on exact buckled locations, cannot cover the range of measurement, or both. Compared with strain gauges, a main disadvantage of demec gauges is that they provide an average of strains in a certain gauge length (say 200 mm gauge length), and, therefore, the measured strain is probably smaller than the actual strain at a specific location. These issues all complicate the collection and analysis of distributed strains and curvatures. Mohareb (1995) discussed the

importance of the longitudinal strains along a line-pipe, and demonstrated the longitudinal strain distributions of the experimental pipes used in his research project. The line-pipes used in Mohareb's research were D/t = 51 to 64 plain pipes, and Yoosef-Ghodsi et al. (1994) studied the distributed strains of the girth weld pipes in the same series. These researchers were the first U of A researchers to study the relationship between pipe buckling behaviour and development of longitudinal strain distributions, and to demonstrate the presence of more distributed strain and curvature curves than had been found previously.

Later, researchers from U of A gradually collected more and more distributed strain data during their projects. In this section, some of the distributed strains and curvatures obtained by previous researchers are analyzed and then presented. In these experiments, the strain distribution was obtained mainly from strain gauge readings, but as a strain gauge evidently cannot provide correct results, distributed strains were obtained from demec readings.

The qualitative observations of the development of the distributed strains and curvatures during the initiation of pipe wrinkling are described in the following sections.

3.2.1 Distributed Strains (Curvatures) for the Pipes with Typical Pipe Conditions

In this section, the strain and curvature distributions are collected from the previous experiments conducted by Mohareb (1995) and Yoosef-Ghodsi (1994). The D/t ratios of the pipes used in the experiments are around 50 and 65, and their strength contains 359 MPa and 386 MPa. The properties and loading condition of the pipes are shown in Table 3.1. The girth weld location of the girth-welded pipes is at the centre of the pipes.

While tension-side and compression-side strains were collected in girth-welded pipes: DGA12W, UGA12W, and HGA20W pipes, only compression-side strains were obtained in plain pipes: DGA12 and UGA12 pipes.

29

<u>DGA12 and DGA12W:</u>

Compression strains: as Figures 3.9 and 3.10 reveal, pipe wrinkling could be detected as a strain started to localize and then concentrate at wrinkle location as the applied loading neared the attainment of the limit point. The wrinkle location of the girth-welded pipe was near the location of transverse girth weld. Even though the wrinkle location of the pipes cannot be determined until the limit point, an anomaly in the distributed strains was found to have occurred during the earlier loading stage, i.e. 84% of the peak load (PL) for DGA12W. Here, non-uniform stain distribution was apparently observed.

Tension strains: due to the nature of pipe buckling, at the onset of wrinkling, the magnitude of the strains on the tension side is much smaller than that of those on the compression side, and tensile strain localization has not yet occurred. However, during the pipe wrinkling, the secondary moment effect at the wrinkle location becomes meaningful, and the neutral axis shifts in order that the plane can remain a plane in the wrinkle location. As a result, the tension-side strains increases speedily in this area. Figure 3.11 shows that the tensile strain developed very fast in the range, from the centre to 200 mm below the centre of the line-pipe when the loading stages reached from 97% to 100% of the peak loading. This area was around the wrinkle location. In addition, non-uniform strains occurred clearly when the loading stage reached 84% of the PL.

Distributed curvatures: in previous experimental programs at the U of A, the curvature was computed by using Equation 3.4:

$$\frac{|\varepsilon_t| + |\varepsilon_c|}{D} \tag{3.4}$$

As the development of tension strain (ε_t) and compression strain (ε_c) are not consistent in magnitude during pipe wrinkling and the location of the maximum strain magnitude is not the same on the tension side and on the compression side, the distributed curvature usually has an odd shape in wrinkle location and its

adjacent area. As Figure 3.12 shows, after the loading stage reach 89% of the PL, an irregular curve occurred in the region, from 200 mm above the centre to 400 mm below the centre of the pipe. Non-uniform curvature occurred apparently when the loading stage reached 84% of the PL stage.

UGA12 and UGA12W:

Compression strains: strain anomaly (apparently non-uniform strains) could define a wrinkle location before 98% of the PL for the plain pipe, UGA12, and at around 86% of the PL for the girth-welded pipe, UGA12W, as shown in Figures 3.13 and 3.14, respectively.

Tension strains and curvatures: strains anomaly occurred after 86% of the PL (see Figures 3.15), and the tension strains revealed a wrinkle location in the loading stages approaching the limit point. The distributed curvatures changed from having relatively consistent amplitude to having dominant amplitude occurring at 86% of the PL, as shown in Figure 3.16.

HGA20W:

Compression strains: a wrinkle was located by monitoring the distributed strains near 95% of the PL, but strain anomaly was found in as early as 85% of the PL. Non-uniform strains became evident after 75% of the PL (see Figure 3.17).

Tension strains and curvatures: an anomaly occurred in the tension strains during the loading stages near 95% of the PL. An anomaly occurred in the curvature distribution at 85% of the PL. Moreover, the strains and curvatures started to become apparently non-uniform during these loading stages and shown in Figures 3.18 and 3.19, respectively.

3.2.2 Distributed Strains (Curvatures) for Cold Bend Pipes

Cold bends are required frequently throughout the extent of all energy pipelines in order to make the pipes follow the geometry of the trench formed from the topography of the terrain and to change the orientation of the horizontal

31

projection of the line due to the required route. Figure 3.20 presents a photo of a typical cold-bended pipe. The bend segment of the cold bend line-pipe was formed by repeating the removal of the elastic ring along the specific region and applying end rotation in the line-pipe. An analytical investigation (Naoki et al. 2003) showed that removing the elastic rings and bending in different sequences had little effect on the pipe's elastic response, but the procedure could significantly affect the pipe's post-buckling behaviour. The amount of plastic deformation developed in a specific ring also affected the behaviour at the peak. This finding is reasonable since the behaviour of a pipe at the peak usually depends on the formation of a wrinkle, which is a localized phenomenon. Because of the special nature of cold bend pipe during manufacturing process, residual strain and initial imperfection already significantly exist in the line-pipes before they are buried underground. As a result, the cold bend pipe has a unique behaviour during pipe wrinkling, as well as the blurred behavioural signature of the strain distribution pattern for the pipe buckling. The signature during the onset of wrinkle is probably too indistinct to locate the pipe wrinkle, but should be able to provide a warning of pipe wrinkling. Some distributed strain and curvature curves were extracted from experiments on cold bend pipes (Sen 2006), and studied here. Figures 3.21 to 3.29 show the strain distributions and the curvature distributions of the cold bend pipes. The TCPL1 and TCPL3 are pressurized pipes, while the TCPL2 is a non-pressurized pipe. The properties and condition of the pipes are summarized in Table 3.1.

TCPL1:

Compression strains: as Figure 3.21 reveals, the earliest strain concentration occurred in the location about 800 mm on the left side of the pipe at 84% of the PL; then as loading increased to 95% of the PL, a dominated concentrated strain shifted onto the wrinkle location at around 500 mm on the right side of the pipe; finally the localized deformation developed there. In addition, due to the manufacturing process for cold bend pipes, non-uniform stains developed at a

32

much earlier loading stage, i.e., 33% of the PL, but at this loading stage, these strains do not imply any behavioural signature of the pipe wrinkle.

Tension strains and curvatures: strain anomaly occurred near the attainment of limit point in the tension strains (see Figure 3.22), and for the distributed curvatures, anomaly can be found at 95% of the PL (see Figure 3.23). A meaningful non-uniform strain and curvature distribution shapes occurred after the loading stage reached 90% of the PL. Because of significantly secondary moment effect at the centre of the pipe, the critical strain on the tension side did not occur at the wrinkle location, but at the centre of the pipe. In addition, different locations of the critical strains on the tension and compression sides resulted in very irregular curvature distributions developed along the pipe after the pipe wrinkling was initiated.

TCPL2

Compression strains: as Figure 3.24 shows, in the beginning, the strain concentration occurred in the location about 1000 mm on the left side of the pipe centre; concentrated strains occurred at another location about 250 mm on the right side of the pipe centre from 83% of the PL. Afterwards, the strain speedily increased at this location rather than at the other locations, and a diamond-shaped wrinkle was defined at this location as the loading increased. The strain distribution pattern was apparently changed at 90% of the PL, but the wrinkle location could not be determined until 95% of the PL stage.

Tension strains and curvatures: the tension strains do not show a pipe anomaly before the attainment of the peak moment (see Figure 3.25), but for the distributed curvatures, an anomaly occurred at 95% of the PL (see Figure 3.26). Even though the tension-side strain distributions are relatively consistent for the non-pressurized pipe compared to those for the pressurized pipe, TCPL1, a local maximum strain still occurred around the centre of the pipe after the inception of the pipe wrinkling.

TCPL3

Compression strains: Figure 3.27 shows that TCPL3 had a behavioural signature similar to that of the TCPL1. The initiated strain concentration occurred at a location further away from pipe centre, i.e., at 1000 mm on the left side of the pipe centre when the loading stage had reached between 70% and 85% of the PL, but when the pipe wrinkle was initiated, a dominated concentrated strain occurred in the adjacent area of the pipe centre after 85% of the PL had been reached. Consequently, the wrinkling progressed at this location

Tension strains and curvatures: more progressive change in the tension strain distribution occurred from 95% of the PL to the peak moment, as shown in Figure 3.28. An evident anomaly in the distributed curvature occurred at 95% of the PL, as shown in Figure 3.29.

The above findings show that the significant moment gradient of the cold bend pipe is a main factor in influencing the strain distribution patterns. The maximum secondary moment occurred around the centre of the pipes, so that the pipe wrinkle was triggered by the significant moment gradient rather than by the initial imperfection. The moment gradient also caused extra tensile strains at the centre of the pipes. The effect of moment gradient was more evident on the tension-side strains than the compression-side strains because of the smaller magnitude of the tensile strains in the whole loading history of the pipe buckling.

3.2.3 Distributed Strains (Curvatures) for Pipes under Cyclic Loadings

As the soil slides along a pipe, it imposes axial, transverse and vertical loads on the pipe. These external forces translate into axial compression and bending moment in the pipes. As time passes, the accumulated strains from the external forces cause pipeline buckling and then wrinkling. Some pipeline operators use stress-relief procedures, in which the overburden soil is removed to allow the pipes to rebound, to relieve the accumulated strains. After the stress-relief procedures, the pipes are reburied. For each stress-relief procedure the pipes go

through a load cycle. Song (2007) studied the cyclic-loading effect on line-pipes. Some of Song's data for the distributed strains are collected and analyzed in this paragraph. Due to cyclic load applied on the specimens, the strain and curvature distributions analyzed here correspond to the first loading cycle of the repeated cycles, which used three repeated cycles for each specific loading stage. The schematic of the cyclic loading is shown in Figure 3.30. The following notations are used: AM represents the monotonic axial compressive load applied in the pipe, AC represents the cyclic axial compressive load applied in the pipe, and BC represents the cyclic bending load applied in the pipe. The properties and conditions of the pipes are summarized in Table 3.1. The analyzed distributed strains are shown in Figures 3.31 to 3.38.

D30P80AM-1

Compression strains: non-uniform strain clearly occurred at 90% of the PL, and wrinkling can be located at 96% of the PL. Even if two modes appeared along the line-pipe during pipe buckling, only one dominated and finally resulted in the permanent wrinkle at this location (see Figure 3.31).

D30P80AC-2

Compression strains: during this loading stage, at 89% of the PL, no behavioural anomaly in the line-pie occurred from strain distribution. Moreover, the distributed strains remained uniform during this loading stage. Wrinkling and abnormal strains occurred near 97% of the PL (see Figure 3.32).

D30P80BC-8

Compression strains: Non-uniform strains became apparent at between 66% and 88% of the PL, and wrinkled location can be determined at 88% of the PL, as shown in Figure 3.33.

Tension strains and curvatures: for the tension strains, pipe wrinkling or a change in the strain distribution pattern did not occur during the recorded loading stages

35

(see Figure 3.34). An anomaly in the curvature occurred at 66% of the PL and the wrinkle can be located at 88% of the PL (see Figure 3.35).

The above findings show that both the strain and curvature distribution patterns are different in the axially compressive loads and bending loads. Under the axially compressive load, when deformation localized and the strains concentrated in the wrinkle location, the strains on the outside of the wrinkle area remained relatively consistent. However, the strain and curvature distribution patterns were similar for the cyclic loading and monotonic loading applied to these specimens.

3.2.4 Distributed Strains for High Strength Pipes

As the exploration for oil and gas in Alberta is extended to the Arctic and sub-Arctic regions in the Canadian North, more and more buried pipelines are being constructed across the seismic area and in the geologically unstable region. In order to reduce construction cost in these remote areas, larger sizes of pipes, higher operation pressure, and higher steel strength have become essential. As a result, high strength steel material with the specified minimum yield strength (SMYS) larger than 550 MPa started to be used in pipeline projects in Canada. (Ishikawa, et al. 2006)

High strength steel traditionally acquires higher strength and toughness by using higher cooling rate during the steel's on-line accelerated cooling process (Super-OLAC). However, the process, at the same time, results a high yielding ratio, i.e. steel yielding strength divided by tensile strength, and low ultimate strain, i.e. the strain corresponding to the ultimate tensile stress (see X80 in Figure 3.36). To increase ductility of the high strength steel, in addition to adjusting the alloy elements, a heat treatment on-line process (HOP) along with Super-OLAC was used in a new generation steel plate. For this new generation steel, both higher strength and higher deformability were acquired, but the trade-off is much lower proportional limit stress occurring in the steel plate (see X80h in Figure 3.36).

36

Hereinafter, the "h" designation indicates the new generation high-strength steel material. A typical X100h material properties from a steel pipe are presented in Table 3.2, which shows that the material is not an exactly isotropic. A much higher yielding strength in the transverse direction than in the longitudinal direction, due to the pipe making process, is normally found for the material properties of a high strength pipe.

High-strength pipe buckling tests were conducted in the laboratory of C-FER Technology in Edmonton, Alberta to understand the behavioural characteristics of the high strength steel pipes. Some of the experimental data (see Table 3.3) are collected to study the behavioural characteristics of the distributed strain (curvature) patterns in this section. A laser profile system (see Figure 3.37) was employed to measure deformation profiles of the experimental pipes and also expected to carry out strain distributions along the pipes on the compression side.

By using the laser profile system, a 2-D pipe deformation profile can be obtained (see Figure 3.38). Theoretically, the longitudinal strains along the pipeline can be derived by the s 3.38 and 3.39. Unfortunately, the longitudinal strains could not be carried out, as the laser profile system had no enough accuracy to conduct a correct strain distribution. Consequently, the strain distributions, presented in this section, were obtained from strain gauges.

The strain distributions from the experimental results for the high strength steel pipes are described by using the following three specimens, Pipe#9, Pipe#13, and Pipe#16, because of the relatively denser measurements installed on these pipes. The strain distribution for Pipe#9 was obtained by installing 70 strain gauges along the line-pipe on the compression side. For Pipe#13 and Pipe#16, only three strain gauges were installed on the compression side. Therefore, only the strain distributions on the tension side were reported here.

Pipe#9

Compression strains: the compression strains started to form a non-uniform distribution at 70% of the peak moment (PM), and a more apparent anomaly occurred at 81% of the PM (see Figure 3.40). Wrinkle location can be detected near 93% of the PM.

Pipe#13

Tension strains: Figure 3.41 shows that the tension strains progressed far in some specific locations as the applied moment approached the peak moment. The tension strains developed from relatively uniform distribution into non-uniform distribution at 80% of the PM.

Pipe#16

Tension strains: as Figure 3.42 reveals, the tension strain distributions were similar before the 95% of the PM. Tension strains developed from relatively uniform distribution into non-uniform distribution at 80% of the PM.

3.3 Summary

This chapter explained how the strain and curvature distributions were collected from field pipelines as well as experimental line-pipes. These broad data have shown that the behavioural signatures of the buckled pipes could be revealed during the development of the strain (curvature) distributions, which changed from a relatively consistent distribution to a multiple-waves distribution with an increase of the applied loading or the pipe deformation. As the applied loading approached the attainment of the limit point, localized strains occurred on the strain distribution and concentrate at wrinkle location. Thereby, the pipe wrinkle could be located. However, the distributed curvatures are derived from the distributed strains on the compression side, the tension side, or the both sides, unless the curvatures acquired from Geopig measurements, and, thus, the distributed curvatures are probably not as sensitive as the distributed strains on the compression side to locate a pipe wrinkle in the inception of the pipe

wrinkling. For the curvatures derived from the strains on both the compression side and the tension side, because the development of tension strain and compression strain are not consistent in magnitude during pipe wrinkling and the location of the maximum strain magnitude is not the same on the tension side and on the compression side, the distributed curvature usually has an abnormal distribution. This anomaly occurred on the curvature distribution is a sign to provide a warning of pipe damage, but probably not to distinguish the pipe wrinkle from the other damage event.

In addition, the collected strain distributions (a total of 21 sets of strain distributions) provide referenced data for determining the monitoring thresholds of strain distribution patterns on buried pipelines under combined loadings in Chapter 6; the strain distributions are also used to validate a developed damage detection system for monitoring pipe buckling in Chapter 7.

Table 3.1 Specimen Properties and Loading Conditions in the Previous U of A
Experiments

Specimen No	Grade (MPa)	Diameter (mm)	D/t	Internal Pressure (%SMYS)	Pipe Conditions	Loading Patterns
UGA12	X52 (359)	324	51	0		Monotonic bending with thermal effect
DGA12	X52 (359)	324	51	72		Monotonic bending with thermal effect
UGA12W	X52 (359)	324	51	0	Girth weld	Monotonic bending with thermal effect
DGA12W	X52 (359)	324	51	0	Girth weld	Monotonic bending with thermal effect
HGA20W	X56 (386)	508	64	40	Girth weld	Monotonic bending with thermal effect
D30P80AM-1	X70 (483)	762	88	80		Monotonic axial load
D30P80AC-2	X70 (483)	762	88	80		Cyclic axial load
D30P80BC-8	X70 (483)	762	90	80		Cyclic bending
D30P20BC-9	X70 (483)	762	88	20		Cyclic bending
TCPL1	X65 (448)	762	93	40	Cold bend	Monotonic bending
TCPL2	X65 (448)	762	93	0	Cold bend	Monotonic bending
TCPL3	X65 (448)	762	93	80	Cold bend	Monotonic bending

Table 3.2 Sample Material Properties for a High Strength Steel Pipe

X100h	OD (mm)	WT (mm)	Yield Stress (MPa)	Tensile Stress (MPa)	Elongation (%)	Yielding Ratio (%)
Transverse	914.4	13.2	779	851	22	92
Longitudinal			642	816	23	79

Table 3.3 Specimen Properties and Loading Conditions in the High Strength Pipe Buckling Experiments

Specimen	Grade (MPa)	Diameter (mm)	D/t	Length (mm)	Internal pressure (%SMYS)	Girth Weld	Loading Patterns
Pipe#9	X80h (550)	762	57	2667	77	No	Monotonic bending
Pipe#13	X100h (690)	762	55	2667	0	No	Monotonic bending
Pipe#16	X100h (690)	762	55	2654	77	No	Monotonic bending

caliper and sensors

gyros

odometer wheels
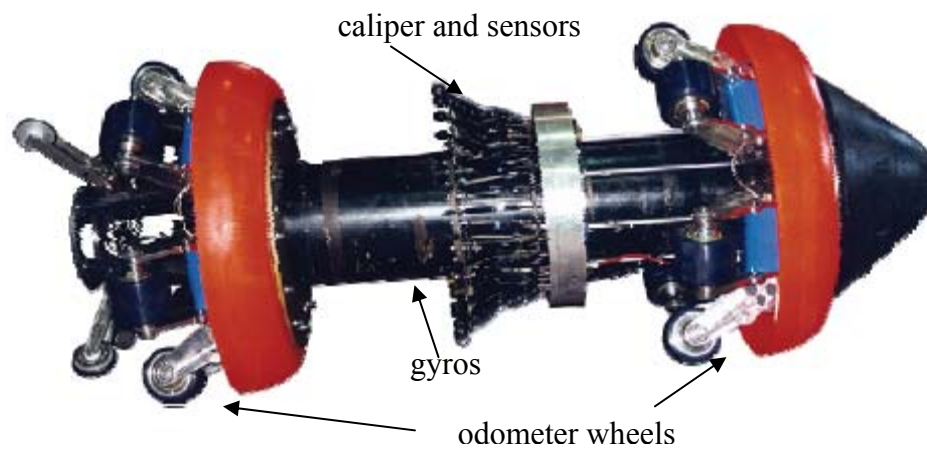
Figure 3.1 Geopig Configuration
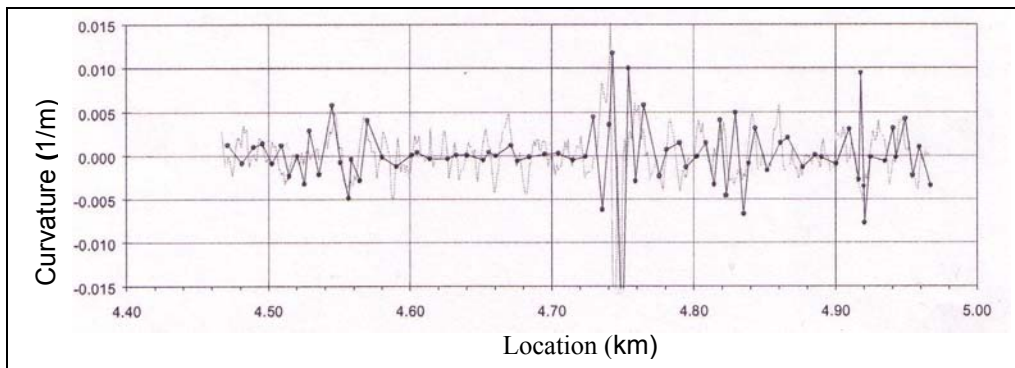
(a) a Curvature Distribution
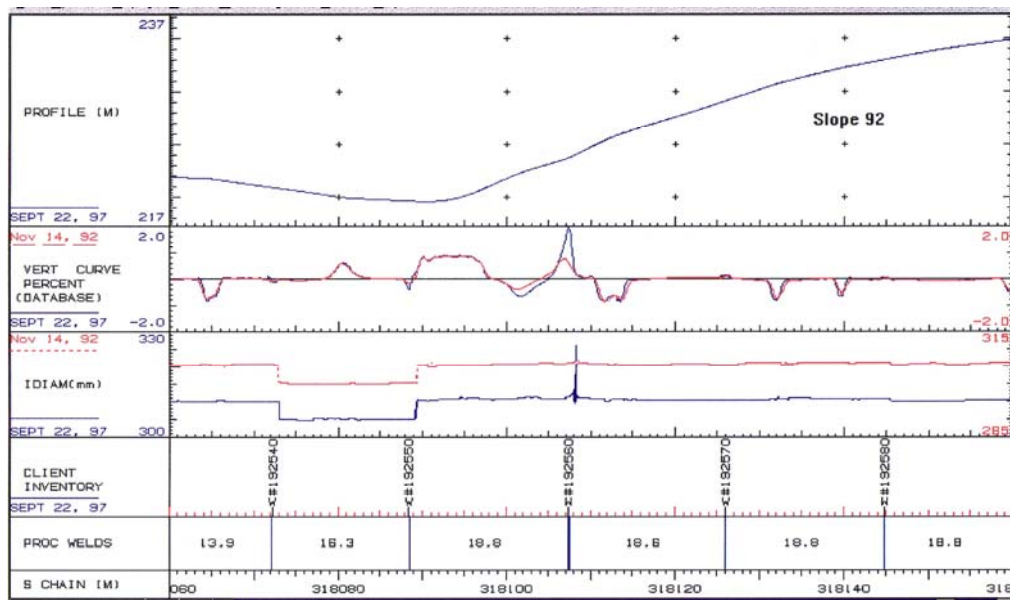
(b) Typical Inspection Results

Figure 3.2 Examples for Geopig Data
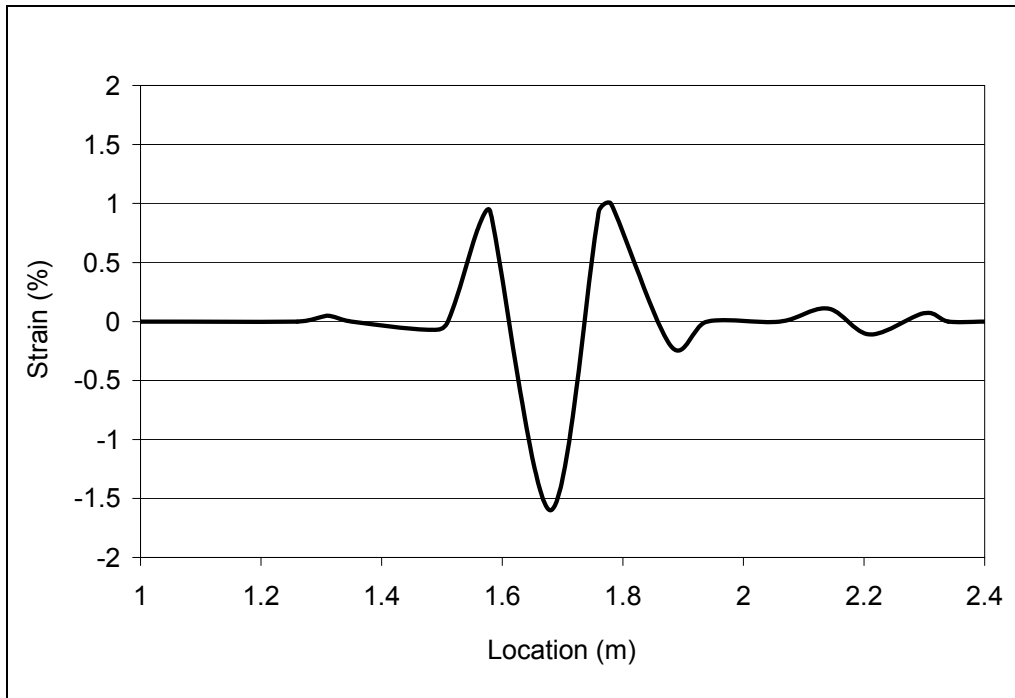
Figure 3.3 Strain Distribution for NPS36 Pipe Dent
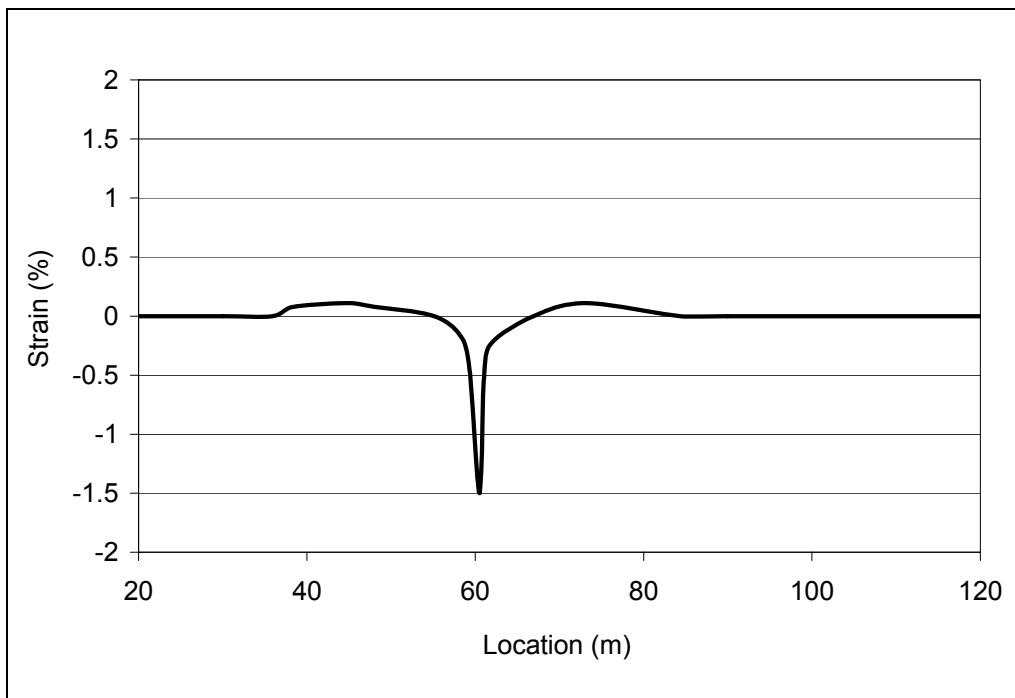
Figure 3.4 Strain Distribution for NPS12 Pipe Wrinkle beside a Pipe Joint
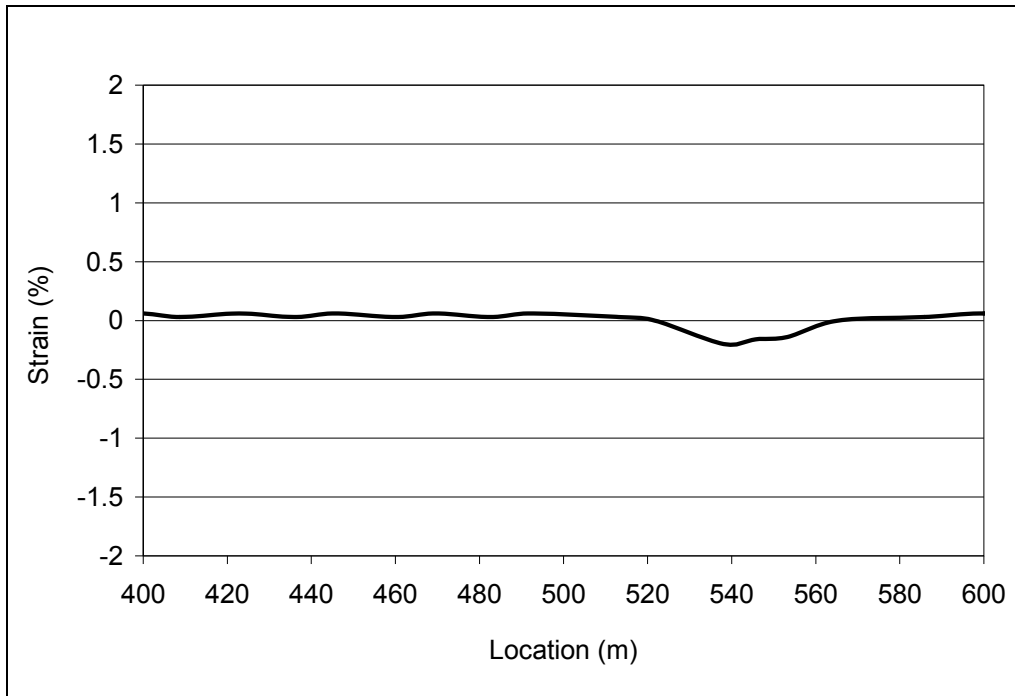
Figure 3.5 Strain Distribution for NPS24 Pipe Buckling during a Pipe Settlement
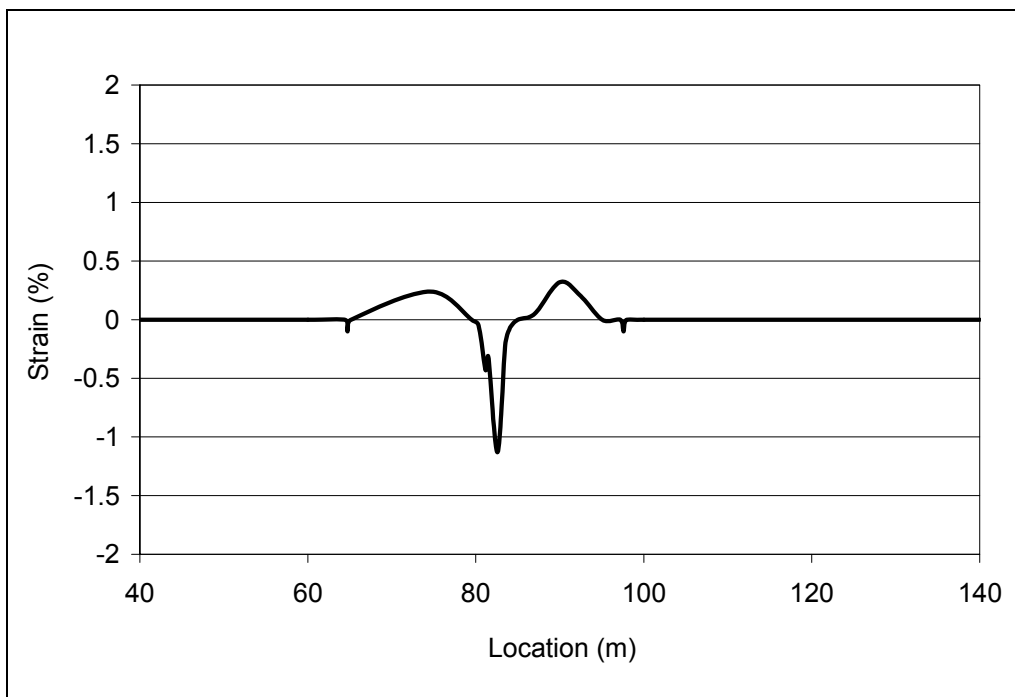
Figure 3.6 Strain Distribution for NPS8 Pipe Wrinkle during Pipe Upheaval
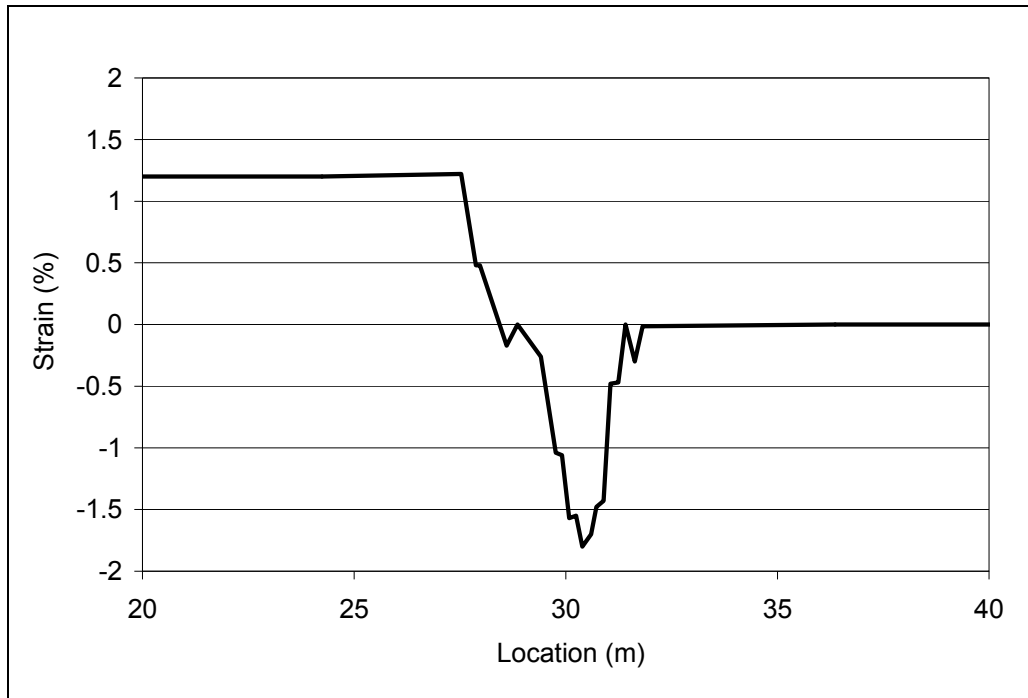
Figure 3.7 Strain Distribution for NPS30 Pipe Wrinkle during Pipe Sag-bend
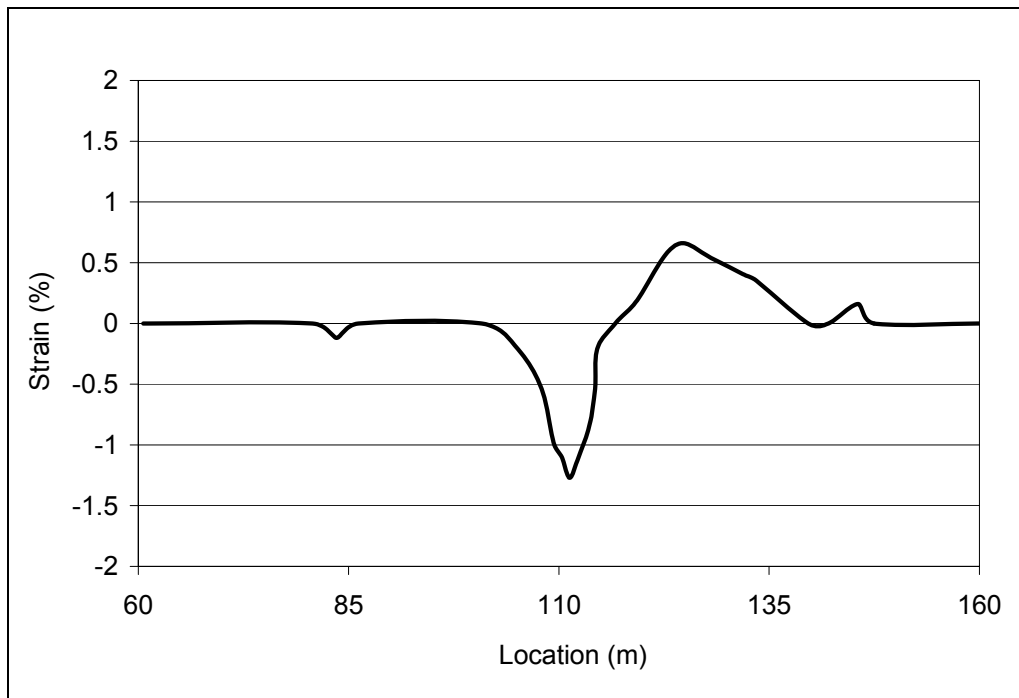
Figure 3.8 Strain Distribution for NPS30 Pipe Wrinkle during Geological
Movement

46
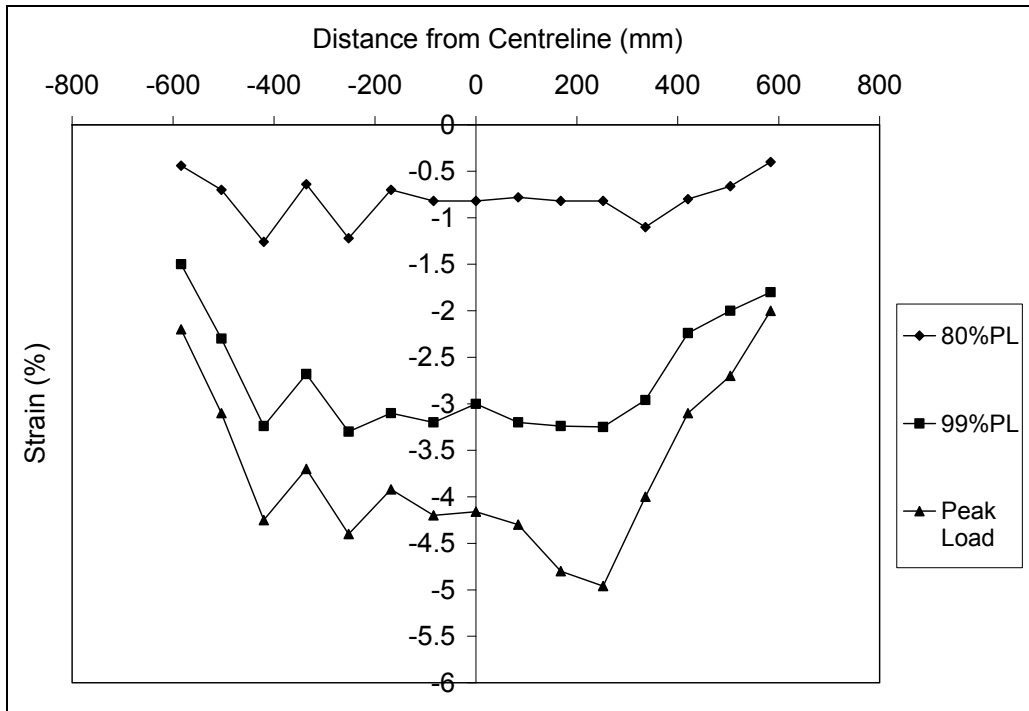
Figure 3.9 Compressive Strain Distributions for Specimen DGA12
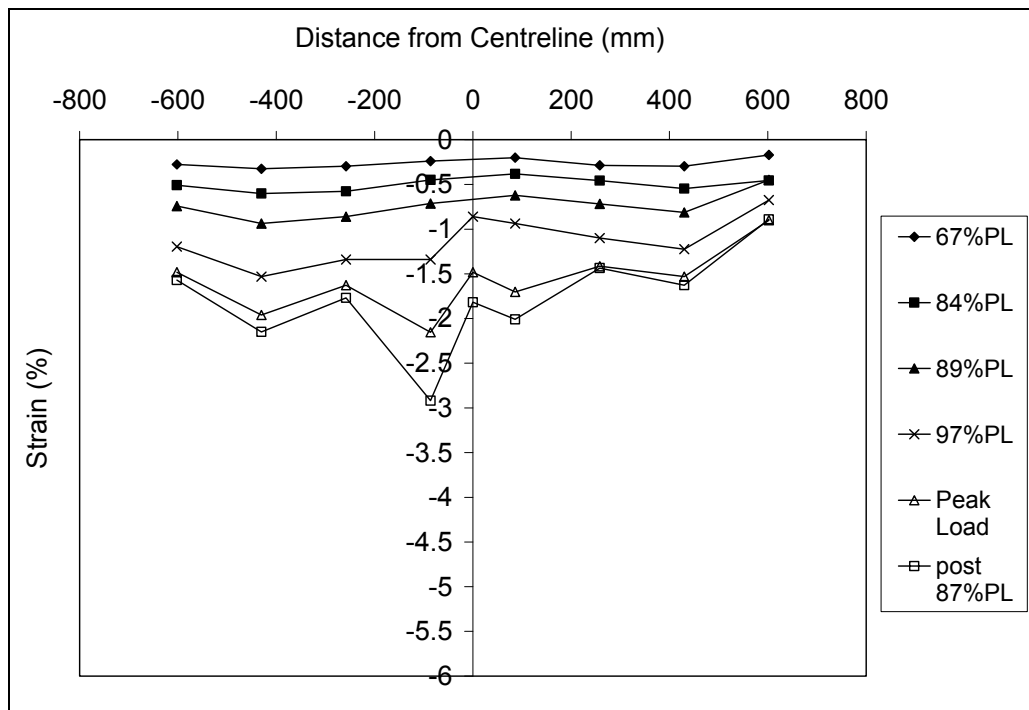
Figure 3.10 Compressive Strain Distributions for Specimen DGA12W

47
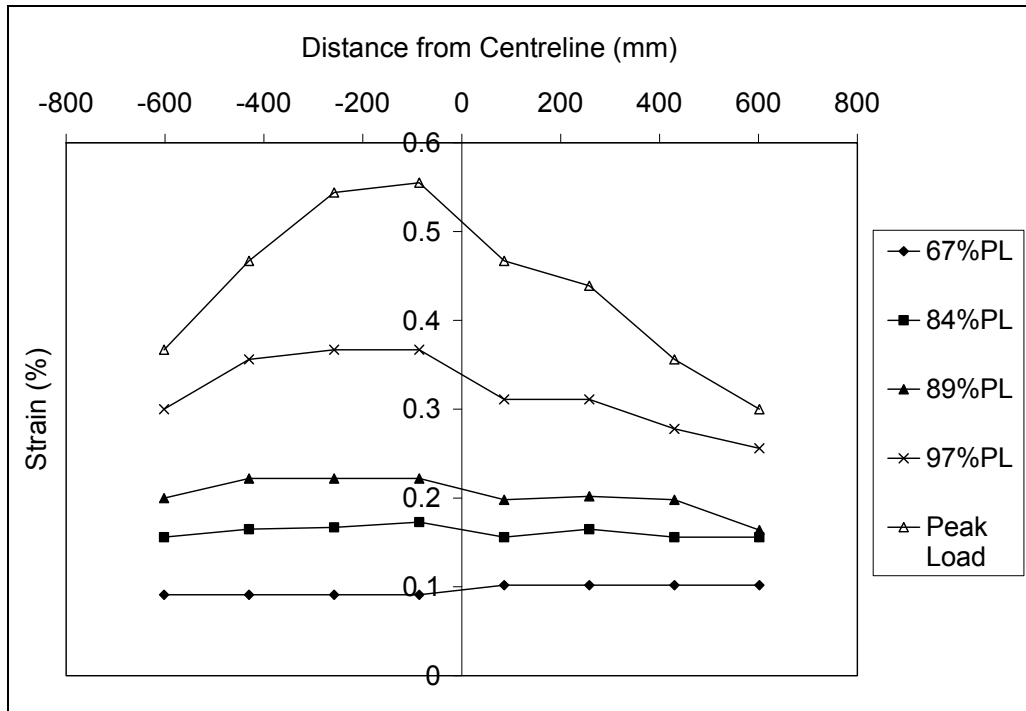
Figure 3.11 Tensile Strain Distribution for Specimen DGA12W
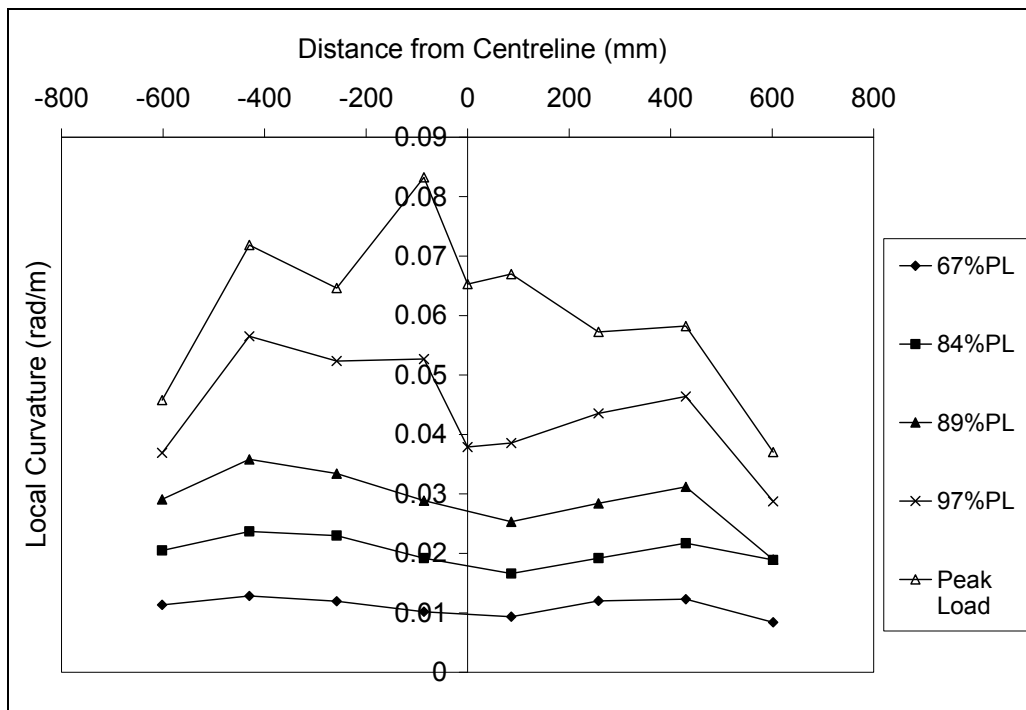
Figure 3.12 Curvature Distribution for Specimen DGA12W

48
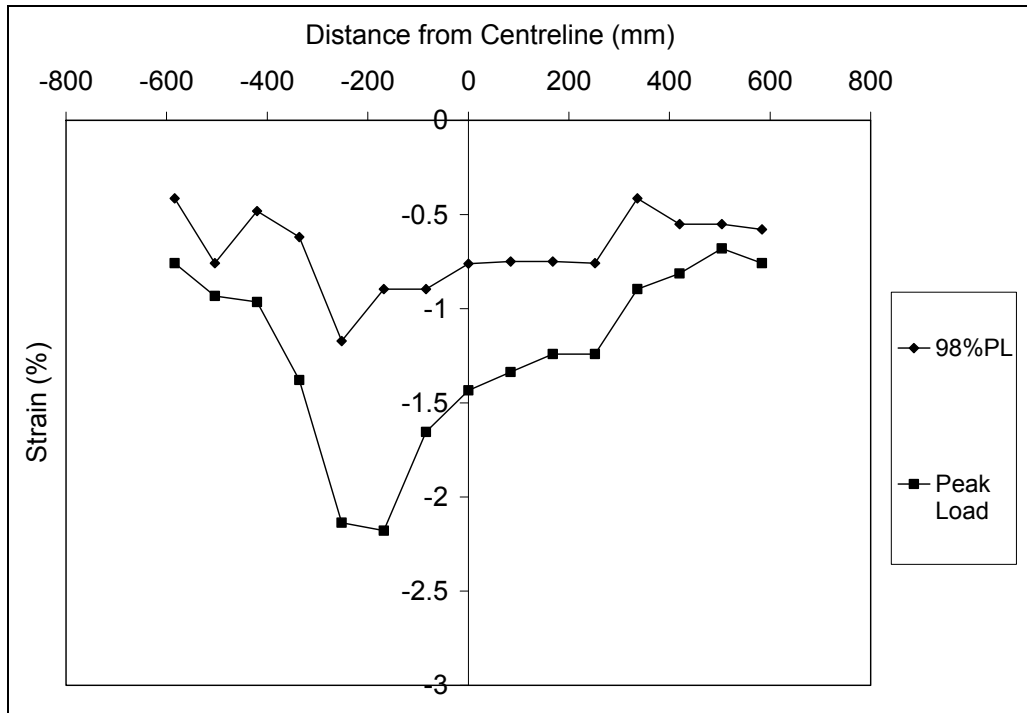
Figure 3.13 Demec Compressive Strain Distribution for Specimen UGA12
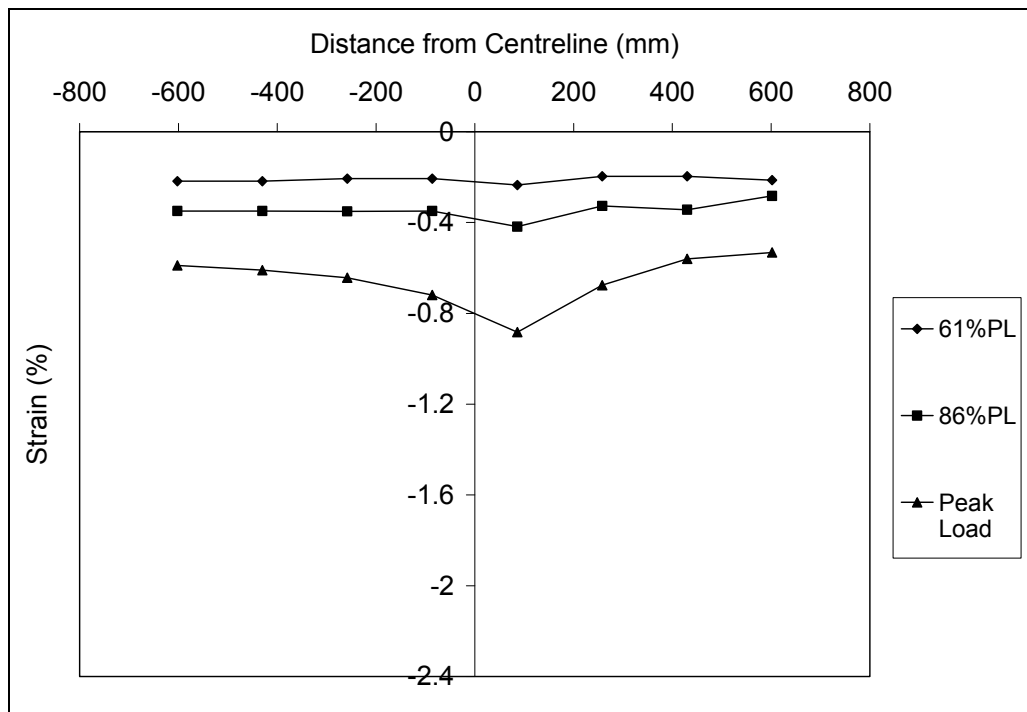
Figure 3.14 Compressive Strain Distribution for Specimen UGA12W
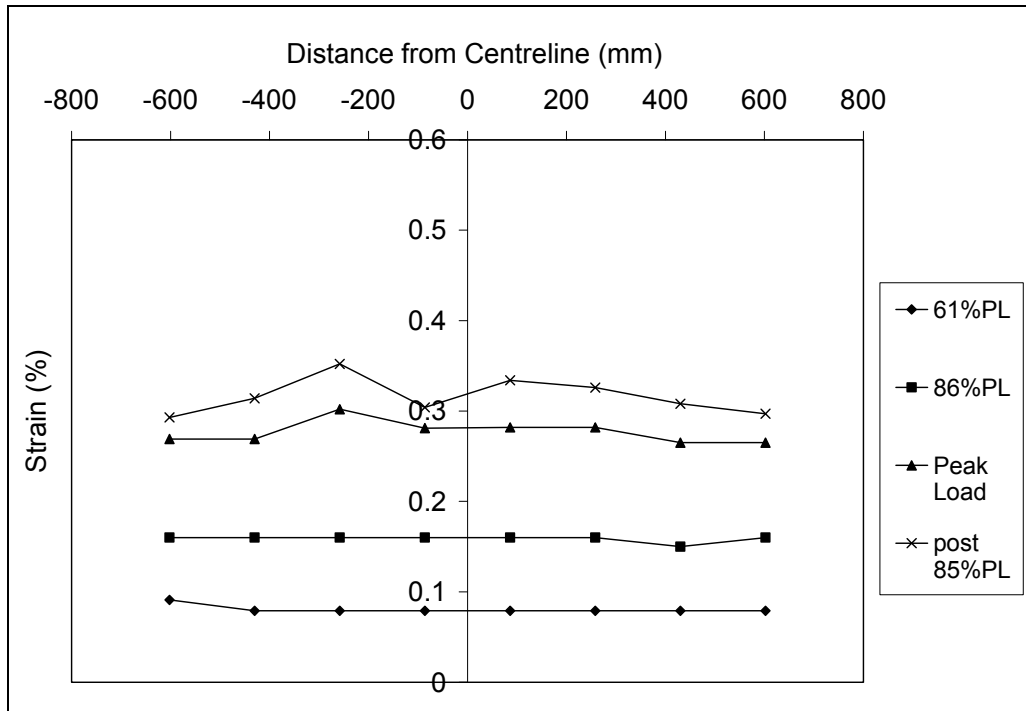
Figure 3.15 Tensile Strain Distribution for Specimen UGA12W
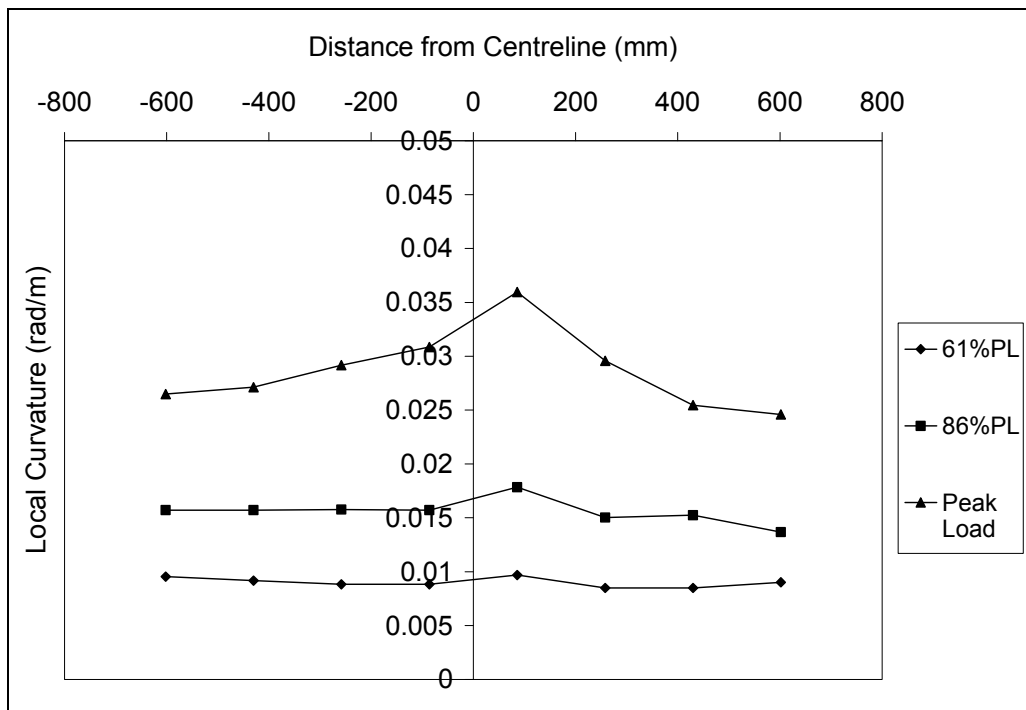
Figure 3.16 Curvature Distribution for Specimen UGA12W

50
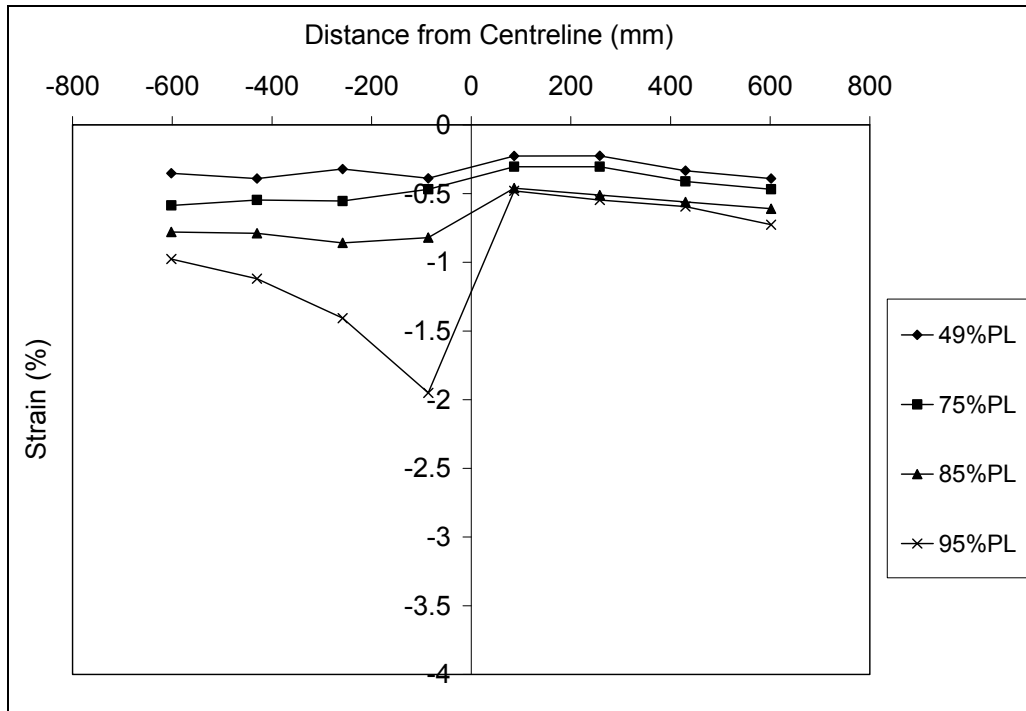
Figure 3.17 Compressive Strain Distribution for Specimen HGA20W
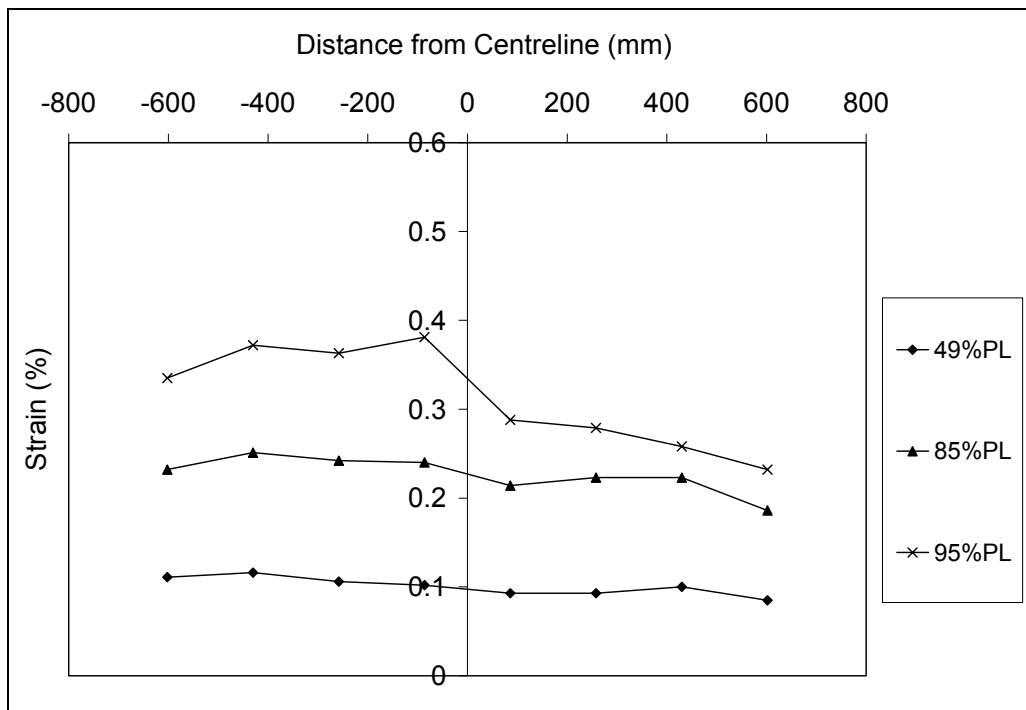
Figure 3.18 Tensile Strain Distribution for Specimen HGA12W

51
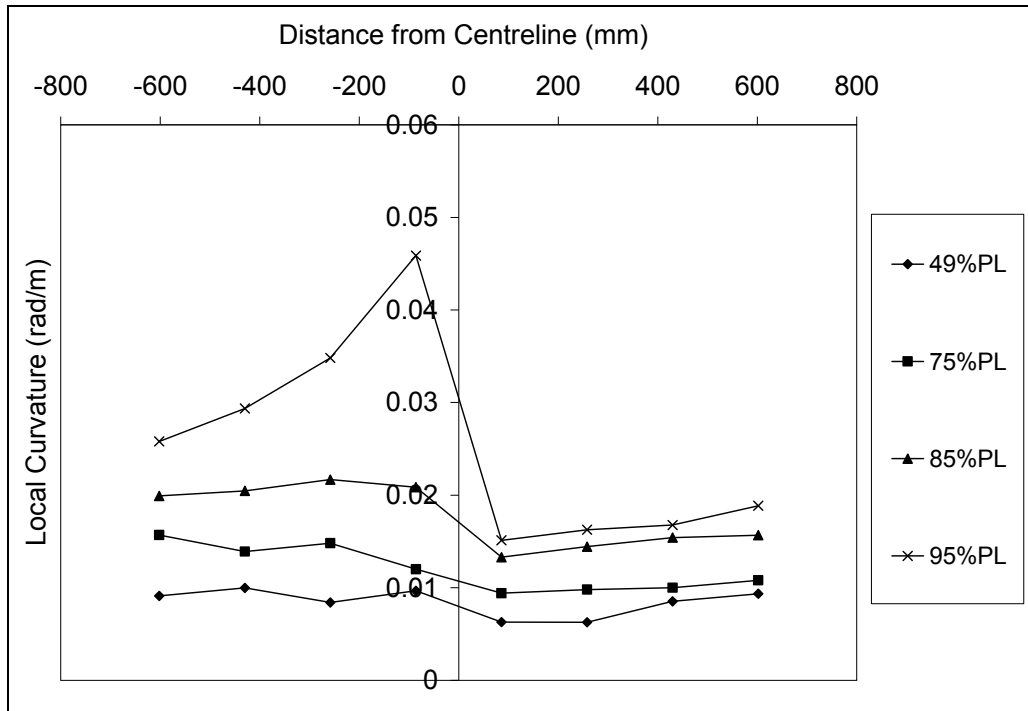
Figure 3.19 Curvature Distribution for Specimen HGA12W

Figure 3.20 Typical Cold Bend Pipe Experiment
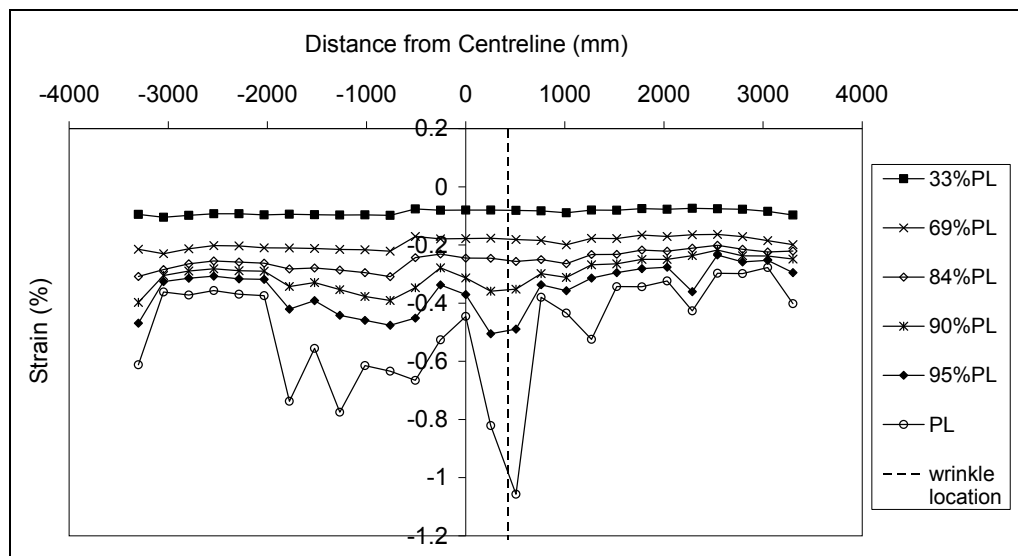
Figure 3.21 Compressive Strain Distribution for Specimen TCPL1
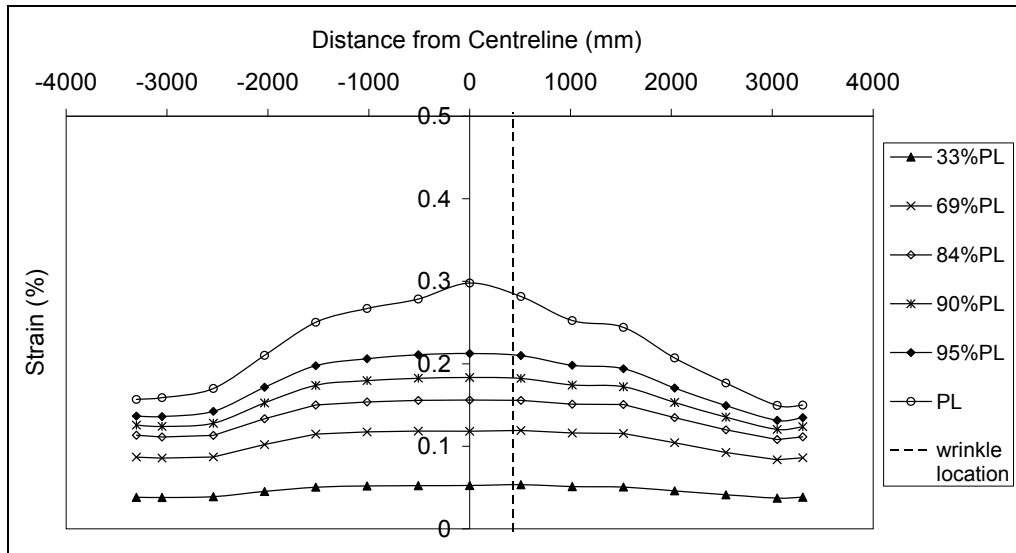
Figure 3.22 Tensile Strain Distribution for Specimen TCPL1
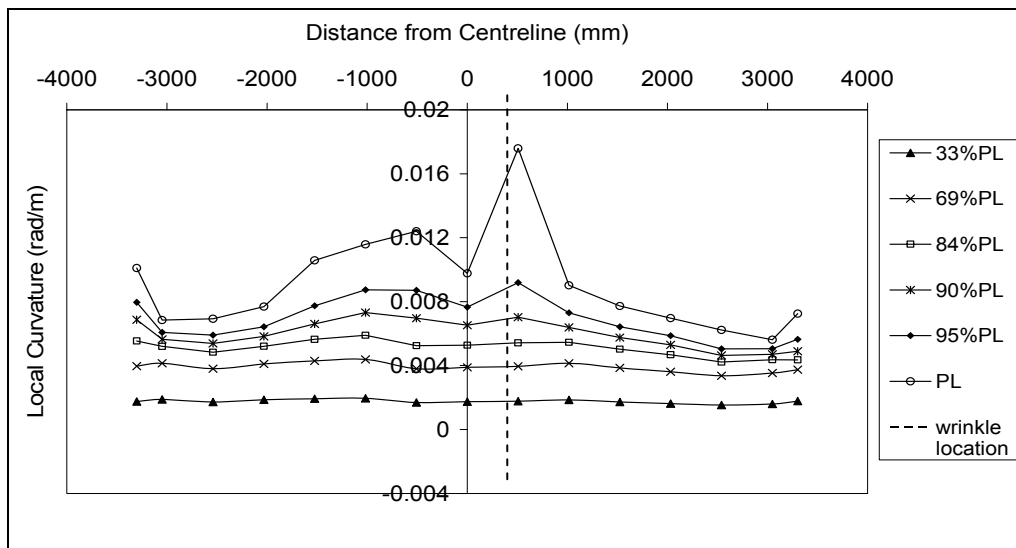
Figure 3.23 Curvature Distribution for Specimen TCPL1
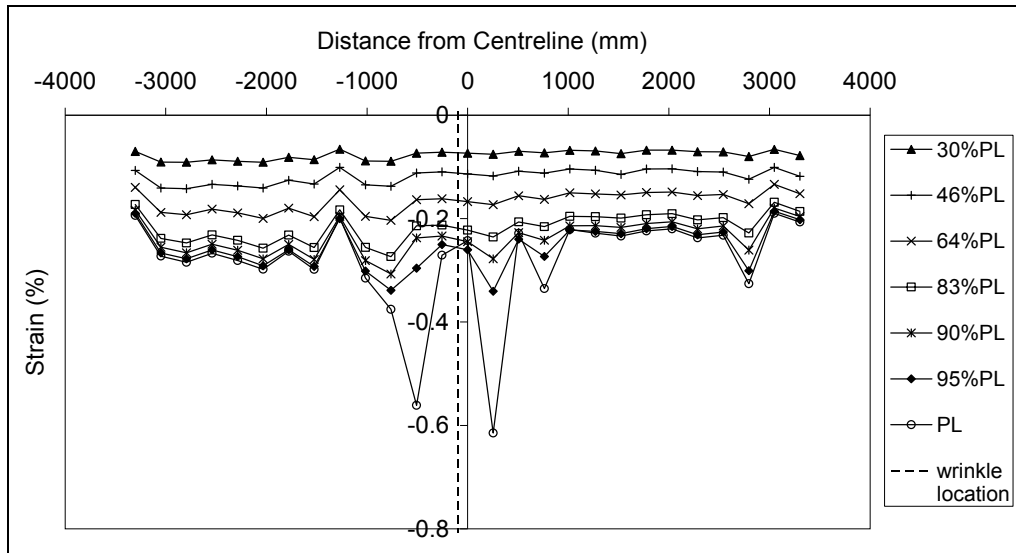
Figure 3.24 Compressive Strain Distribution for Specimen TCPL2
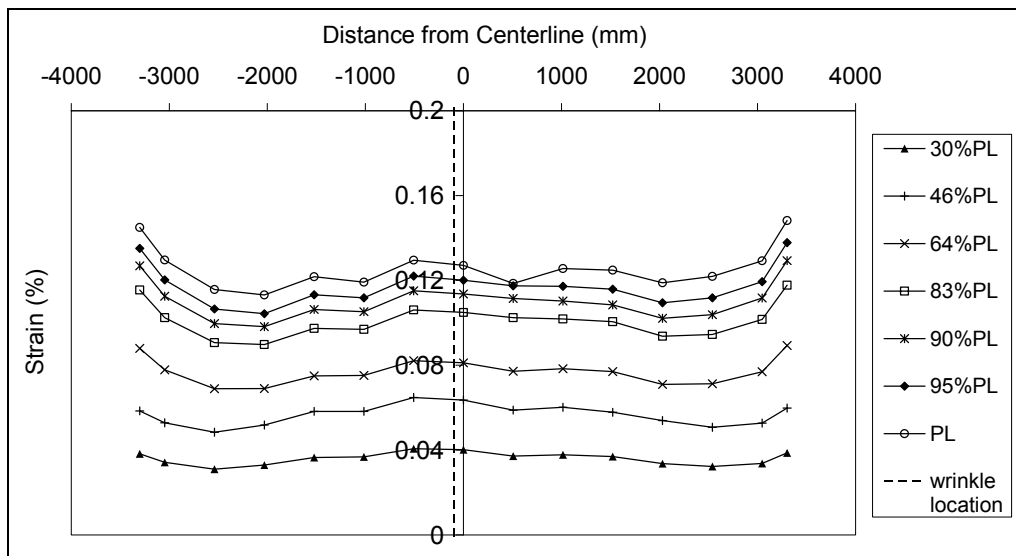
Figure 3.25 Tensile Strain Distribution for Specimen TCPL2
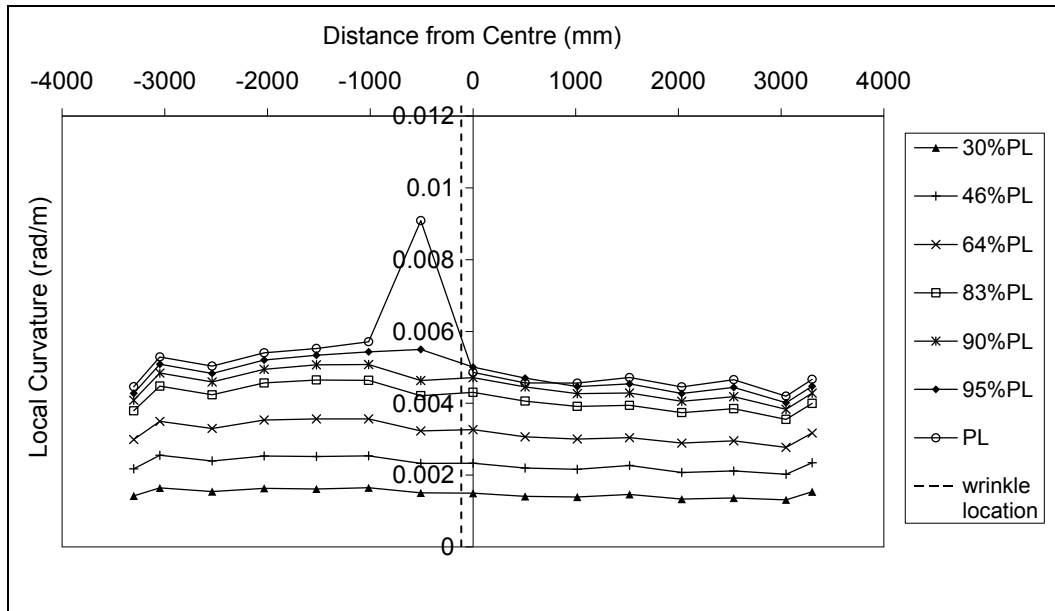
Figure 3.26 Curvature Distribution for Specimen TCPL2
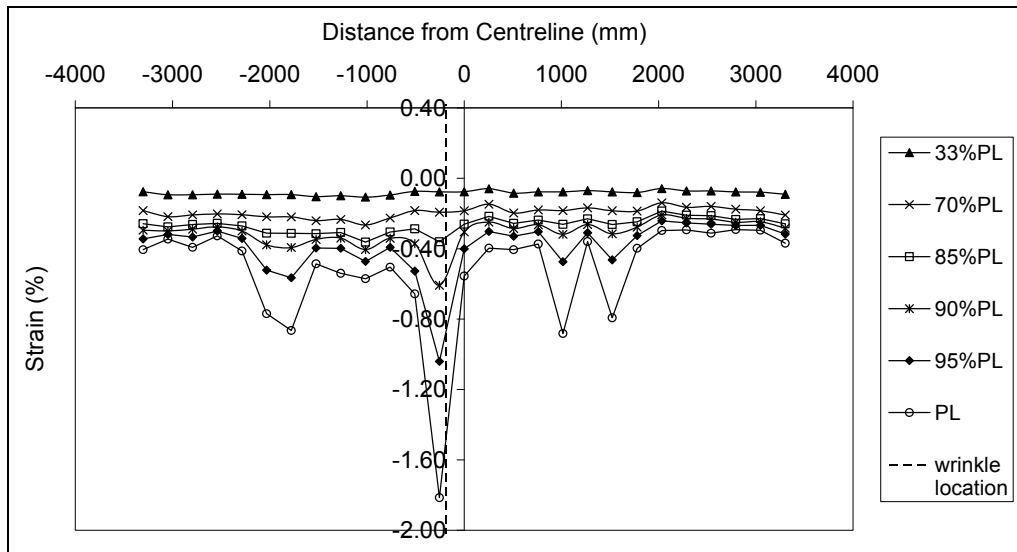
Figure 3.27 Compressive Strain Distribution for Specimen TCPL3
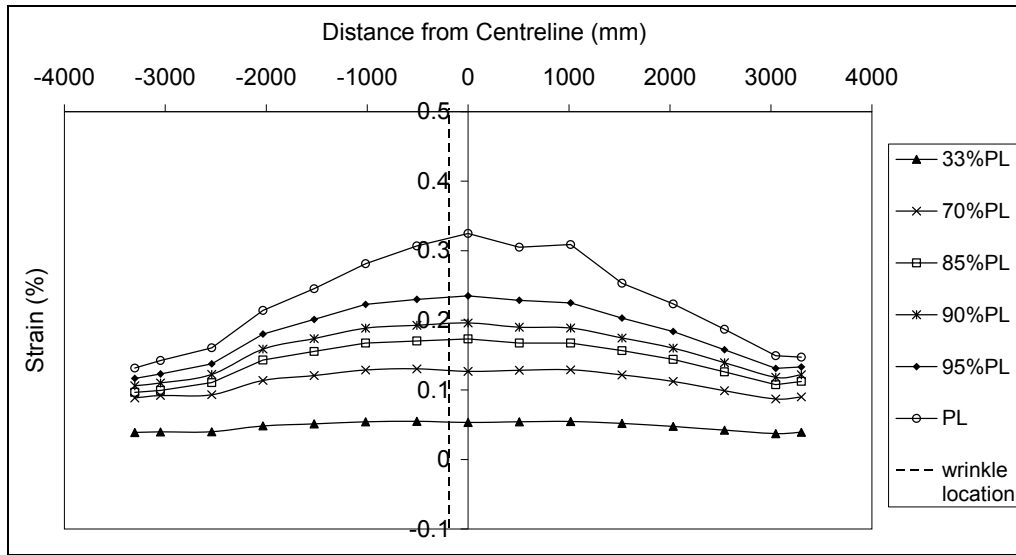
Figure 3.28 Tensile Strain Distribution for Specimen TCPL3
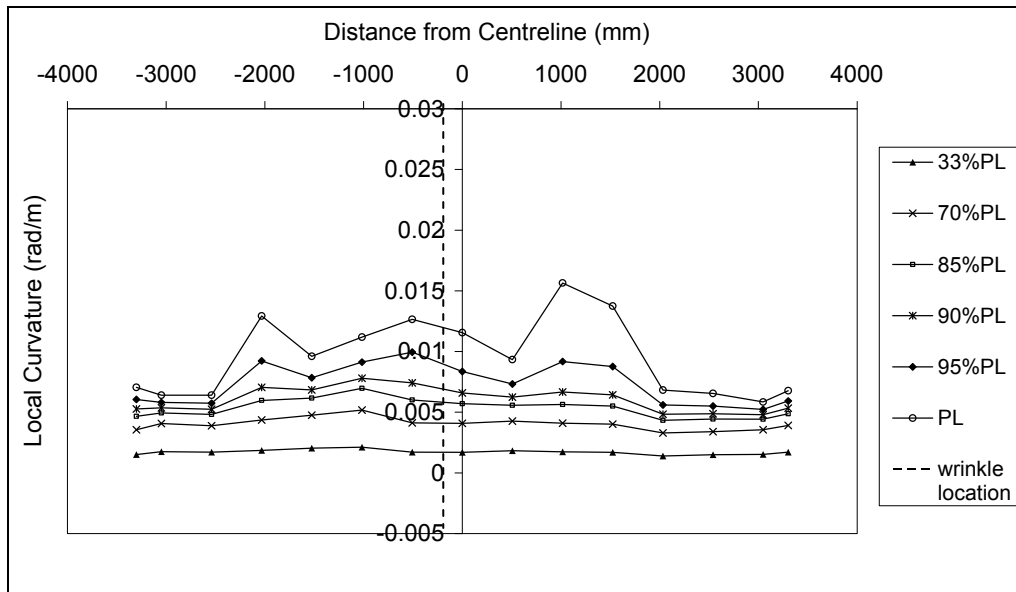
Figure 3.29 Curvature Distribution for Specimen TCPL3
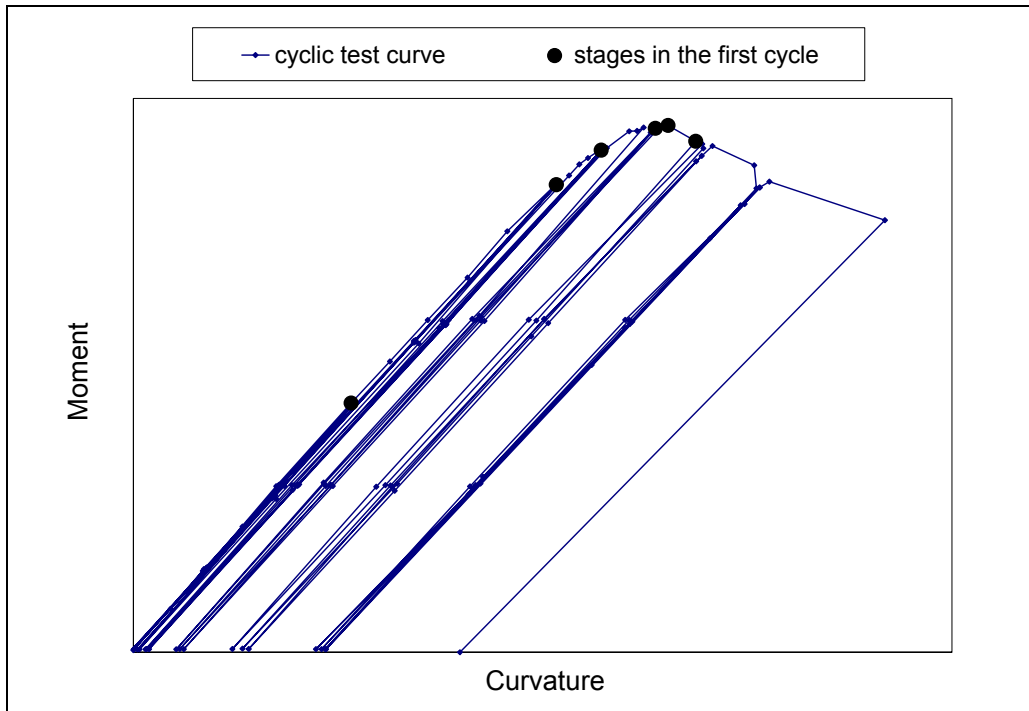
Figure 3.30 Schematic of the Cyclic Loading
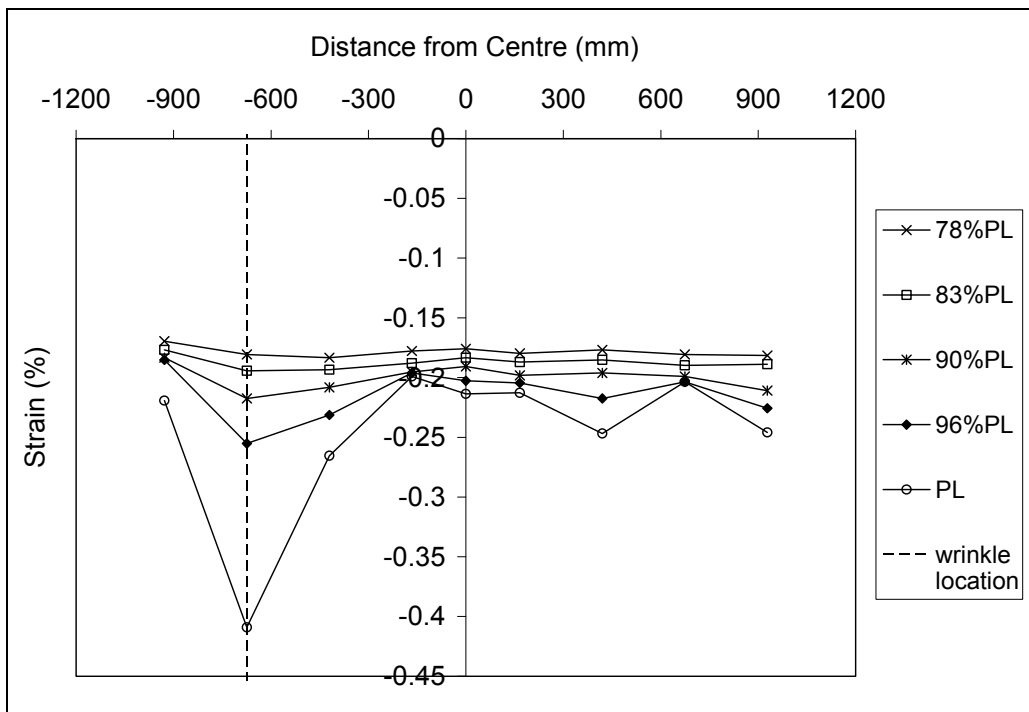
Figure 3.31 Compressive Strain Distribution for Specimen D30P80AM-1

58
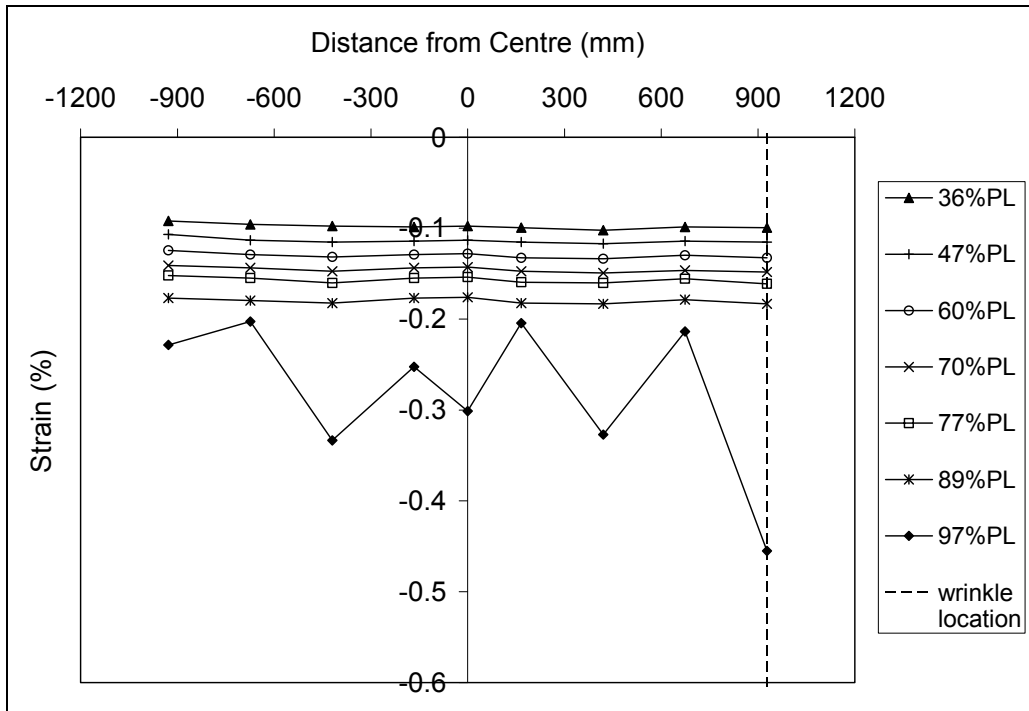
Figure 3.32 Compressive Strain Distribution for Specimen D30P80AC-2
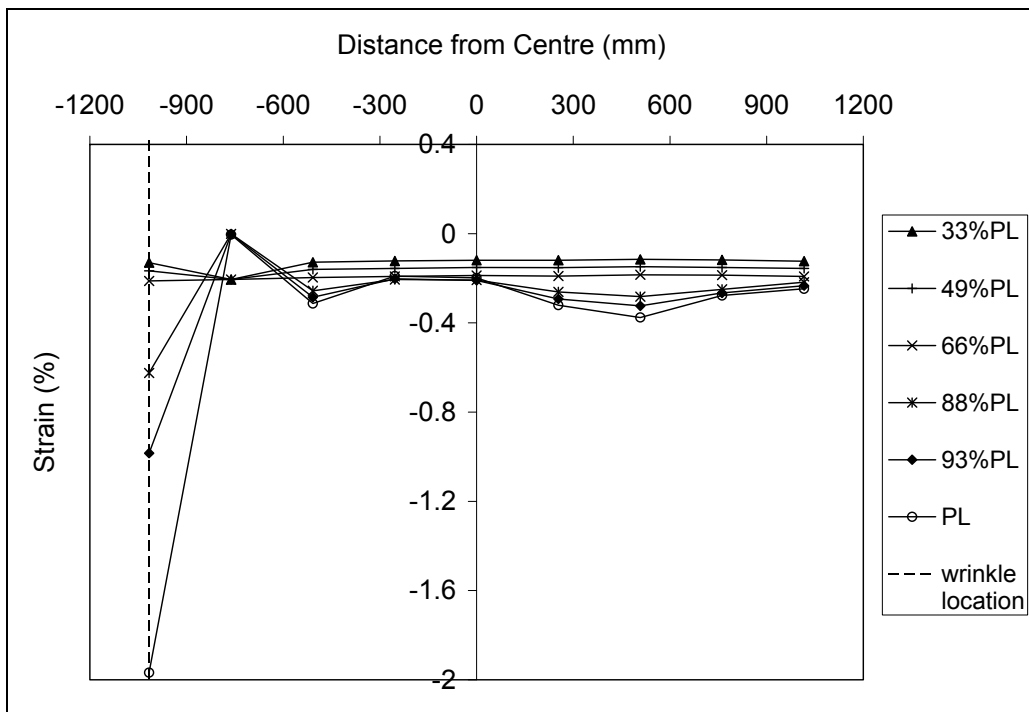
Figure 3.33 Compressive Strain Distribution for Specimen D30P80BC-8

59
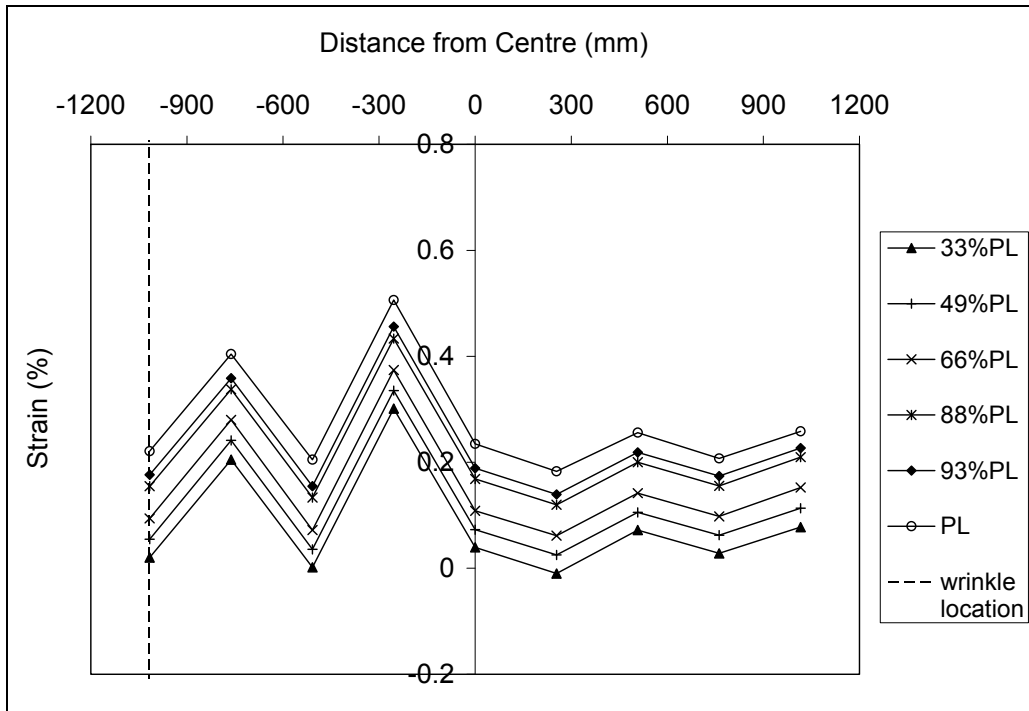
Figure 3.34 Tensile Strain Distribution for Specimen D30P80BC-8
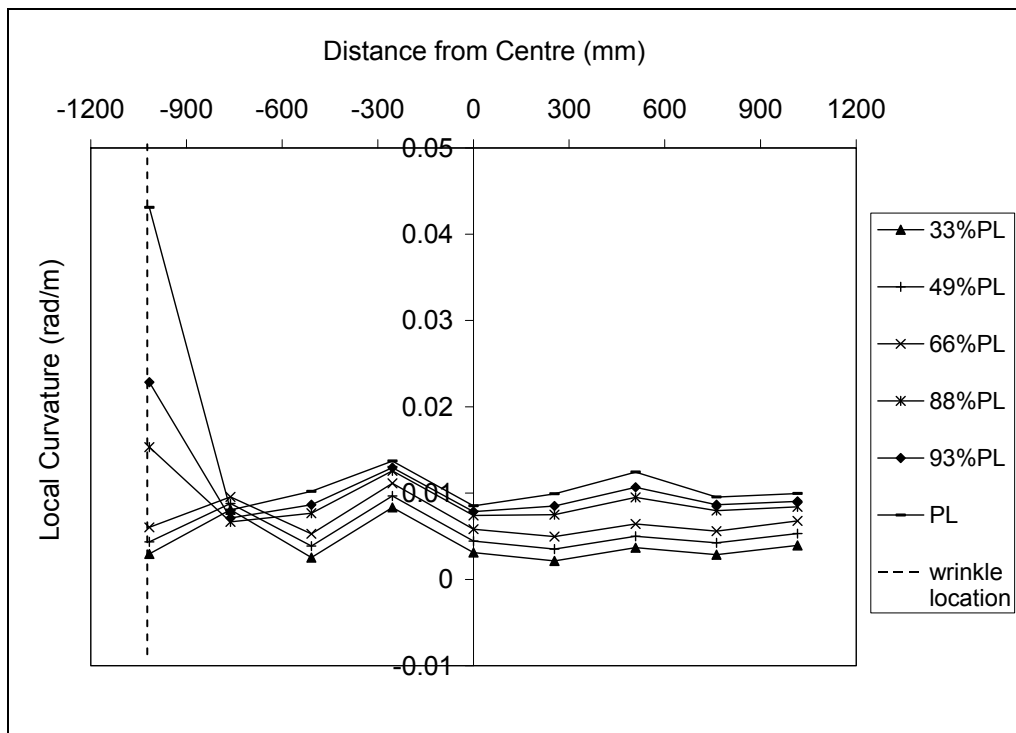
Figure 3.35 Curvature Distribution for Specimen D30P80BC-8

60
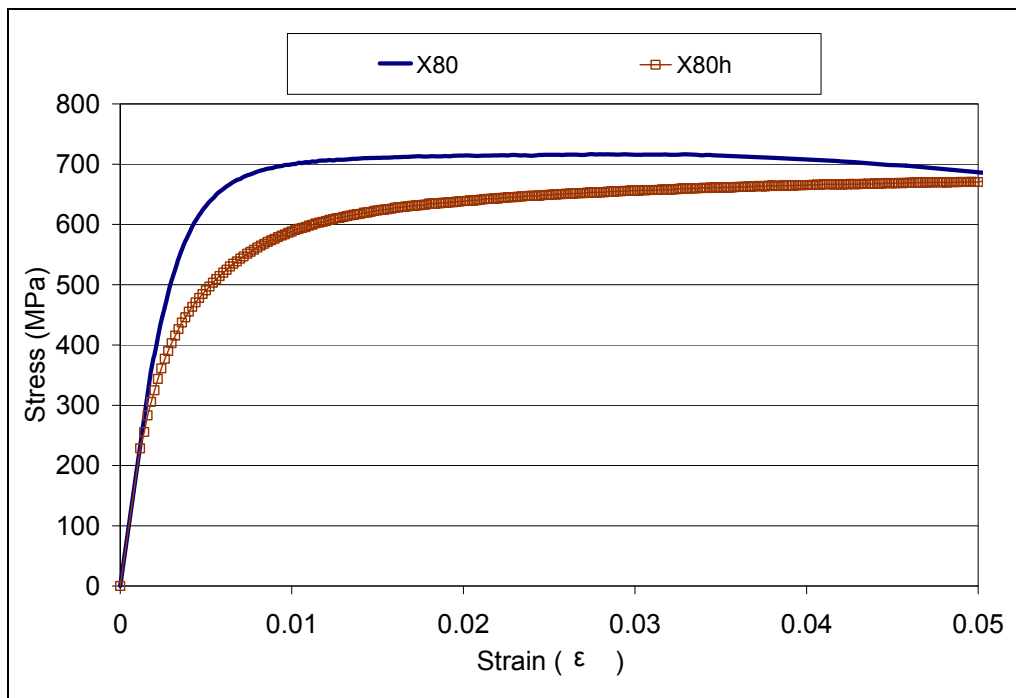
Figure 3.36 Longitudinal Engineering Stress-Strain Curve for Steel Material
X80 and X80h
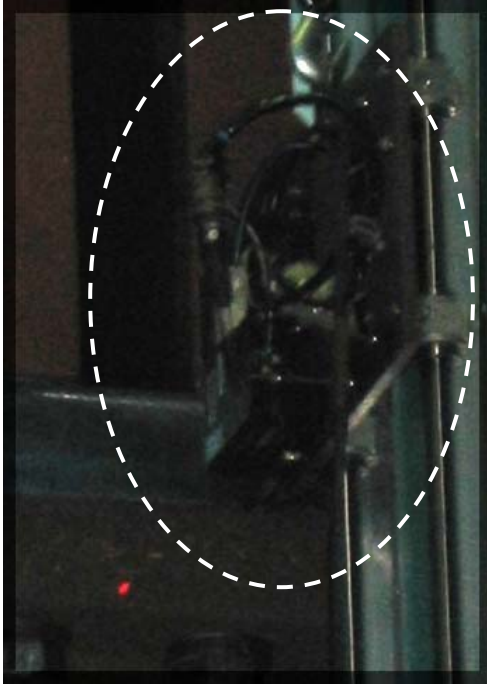
Figure 3.37 a Laser Profile System
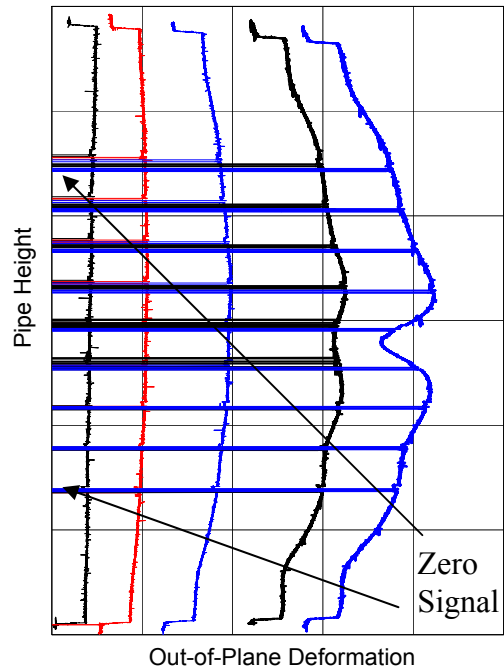
Figure 3.38 Typical Pipe Deformation Profile

Figure 3.39 Measuring Marks on a Line-pipe for the Laser Profile System
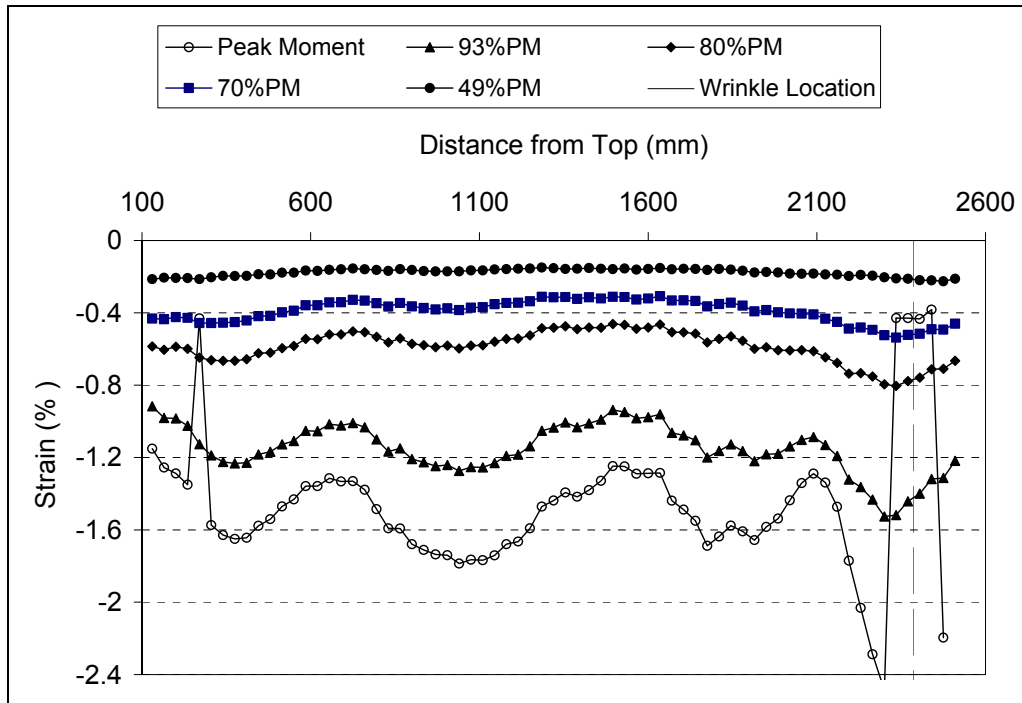
Figure 3.40 Strain Distribution For Specimen Pipe#9
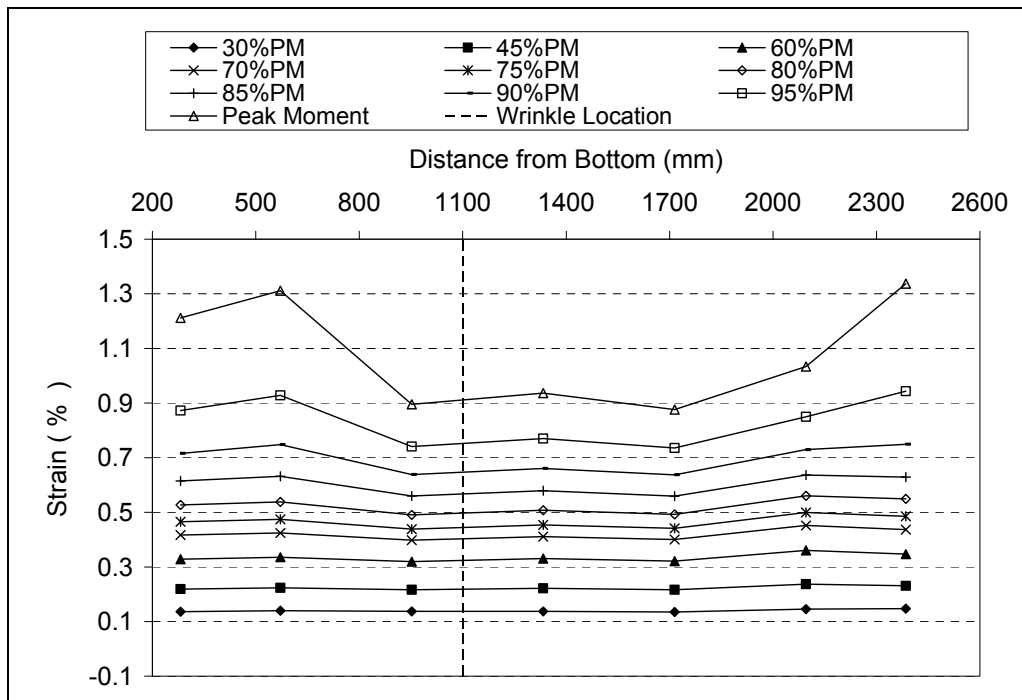
Figure 3.41 Strain Distribution For Specimen Pipe#13
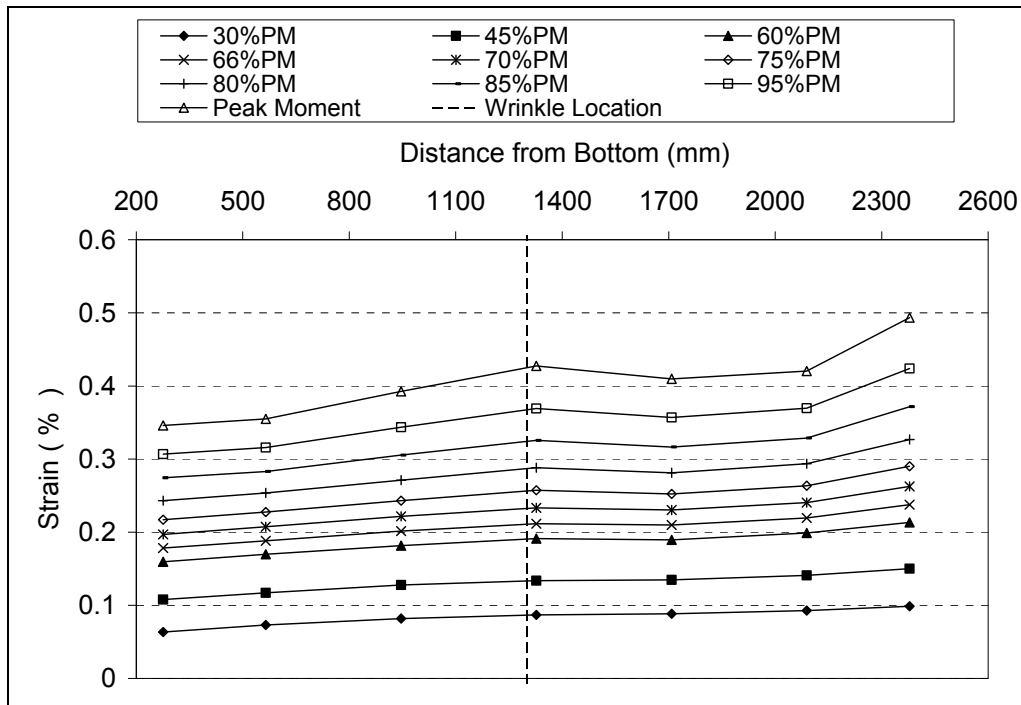
Figure 3.42 Strain Distribution for Specimen Pipe#16

4. THE FEASIBILITY STUDY OF USING DISTRIBUTED STRAIN SENSORS IN PREDICTING THE WRINKLING OF BURIED PIPES

Although behavioural signatures of the pipe wrinkling were observed on the distributed strains under different pipe conditions, further experiments were done to validate that strain distribution can be a reliable signature in detecting the initiation of pipe wrinkling and that using distributed strain sensory systems, such as BSFOS system, in the field is feasible. Three experimental programs conducted in this research project were pipe buckling tests using the BSFOS system and a digital camera system, respectively, and excavation tests of buried line-pipe using the BSFOS system.

4.1 Pipe Buckling Experiment Using the BSFOS System

Previous chapters revealed that an active warning system is needed for monitoring possible failures between pipelines' inspections and that the behavioural signatures of pipe wrinkling can be found in the development of distributed strains. These facts form the motivations of studying the potential of the recently developed Brillouin scattering fiber-optic sensing (BSFOS) system to be used in detecting pipe wrinkling. Theoretically, the BSFOS system allows engineers to remotely and continuously monitor distributed strains along the buried pipelines. However, there is no comprehensive study to verify the applicability of the BSFOS system in predicting pipe wrinkle. Therefore, a pipe-buckling test for studying the potential of BSFOS system was developed. The test was sponsored by TransCanada Pipelines Ltd. (TCPL) and conducted in the laboratory of C-FER Technology.

4.1.1 Specimen Fabrication

The pipe specimen, Pipe#14, was one of the specimens used in the high-strength pipe buckling experiments at C-FER Technology, and the experimental program had been mentioned in Secton 3.2.4. The specimen has 762 mm outside diameter (D) and D/t ratio of 55. The specimen's dimensions, material properties, and test

conditions are summarized in Table 4.1. The specimen fabrication, including the groove welds between end plates and the pipe, was undertaken by TCPL.

4.1.2 Test Set-up

Pipe#14 was tested by using the 15000 kN MTS Universal Testing System (UTS) in C-FER technology, as shown in Figure 4.1. Bending moments were applied to the specimen through two steel moment arms, which were attached to the specimen end plates using high-strength bolts and connected to the UTS and the strong floor, respectively, through hinges. A pair of hydraulic rams (see Figure 4.1) connected the moment arms with hinges in order to apply bending forces to each end of the specimen. The test set-up was similar to that used in the pipeline experimental programs at the U of A (Dorey 2001).

4.1.3 Instrumentation

The comprehensive instrumentation used in the program included the BSFOS system, the laser profiling system, conventional strain gauges, linear variable displacement transducers (LVDTs), rotation meters (RVDTs), and cable transducers. The layout of instrumentation is presented in Figure 4.2. The BSFOS system used in Pipe#14 test was developed in cooperation with the Dr. Bao's research group in the Department of Physics, University of Ottawa. A total of 20 meters of optical fibre of the BSFOS system was installed longitudinally at 10 positions around the pipe circumference, and was spaced at 45° intervals circumferentially, as shown in Figures 4.3 and 4.4. The resolution of the BSFOS system used in this test was under 100 micro-strains for a gauge length of 50 mm. Conventional strain gauges were also used (see Figure 4.3) to validate the strain data acquired from the BSFOS system.

Since the BSFOS system is a relatively new technology used in civil engineering applications, and, hence, the system is briefly discussed in the following.

66

The Brillouin scattering fibre-optic sensing (BSFOS) system is based on the Brillouin loss technology (Bao et al. 1993) whereby two counter-propagating laser beams, a pulse (stokes wave) and a constant wave (cw), exchange energy through an induced acoustic field. When light travels through a transparent media, most of the light travels straight forward while a small fraction is back scattered. The Brillouin scattering is simulated in backward direction. Scattering occurs due to inhomogeneities of the refractive index or acoustic waves known as phonons. In the BSFOS system, an electro-optic modulator, shown in Figure 4.5, creates an optical pulse, and then the pulse propagates through the fibre and interacts with the cw pump. The pump power variation, the so-called Brillouin loss, is measured by a photodiode at the pulse input. A Brillouin loss spectrum centered at the Brillouin frequency ν_B is obtained by measuring the depleted cw pump and by scanning the beat frequency of two lasers, as shown in Figure 4.6.

The Brillouin frequency ν_B has a linear dependence with the temperature (T) and strain (ε) (Horiguchi et al. 1989, Kurashina et al. 1990). The distributed strains can be obtained through the frequency measured along the fibre-optic sensors attached onto a pipeline (Zou et al. 2004). The strain and temperature can be calculated from the following formula:

$$\nu_B = C_\varepsilon (\varepsilon - \varepsilon_o) + \nu_{BO} \tag{4.1}$$

$$\nu_B = C_T (T - T_o) + \nu_{BO} \tag{4.2}$$

where C_ε and C_T are the strain coefficient and the temperature coefficient, respectively, in transformation of Brillouin frequency; ν_{BO} is a reference Brillouin frequency, which needs to be measured before measuring strain ε or temperature T; ε_o and T_o are an initial strain and an initial temperature, respectively, corresponding to ν_{BO} and can be set as zero. The strains obtained from Equation (4.1) are engineering strains.

The accuracy of the measurements of the BSFOS system depends on the spatial resolution of the sensing region. For the most recent developed BSFOS system,

the strain accuracy can be as low as 2 micro-strains with the spatial resolution up to 10 cm; the measurement range can be more than 30 km; and the strain range is more than 1%.

Data processing of the BSFOS system includes the following steps:

(1) Pre-processing: the length of the optical fibers, including the leading fiber, the glued sensing fiber, and the designed loosing fiber must be exactly measured before data collection. By monitoring the specific signals occurring in the loosing fibers, the system's operator can confirm the condition of data processing. Since the processing speed of laser beams is constant and the processing distance is known, the processing time of the laser beams, in relation to the location where data are acquired, can be obtained by calculation; and then the timing information is stored in the control computer of the data acquisition system. In this project, SMF28 optical fibers were used in this system. A typical value for the Brillouin frequency of the SMF28 was 12800 MHz at 1319 nm and 10850 MHz at 1550 nm. Therefore, the data acquisition system should perform trial scans in order to obtain the preliminary range of the frequencies detected during monitoring to reduce the time for data collection.

(2) Data processing: The data collected from a BSFOS system are the Brillouin-loss power spectra, not the strain, so the data processing is different from that in the conventional acquisition system. In addition, the signals are handled in the frequency domain in order to increase the efficiency of data processing, but they can also be simultaneously observed in the time domain (see Figure 4.6).

(3) After an experiment was completed, the measured data from the BSFOS were stored with the frequency and corresponding time in a file. These data in the frequency domain were analyzed and synthesized, and the actual central frequencies in relation to the distributed, measured locations were obtained. The distributed strains along the optical fiber were computed based on Equations (4.1) and (4.2).

4.1.4 Test Procedure

 The test procedure is similar to that of the pressurized pipe buckling experiments conducted at the U of A (Dorey 2001) and is described as follows:

(1) After trial runs to ensure that test set-up was correct and instrumentation was functioning normally, pre-processing was performed on the BSFOS system.

(2) A hydraulic pump was used to apply internal pressure up to a designed level, i.e. 18.4 MPa or 77% of SMYS in hoop stress, and an additional axial force was applied by the UTS system to counteract to the internal pressure load on the specimen end caps. The initial strains were then taken by the BSFOS system by performing data processing. Because strain errors were set to be smaller than 100 $\mu\varepsilon$ for this experiment, a scanning range for searching the central frequency was set around 100 MHz, e.g. from 1220 MHz to 1320 MHz. If the range is too narrow, the accuracy of the measurements may not be good enough; while the range is too broad, the processing time could be too long. The processing time required for each load stage was around 15 to 20 minutes in this experiment.

(3) The UTS and the pair of hydraulic rams increased bending moment incrementally on the specimen until an abnormal signal was detected from the BSFOS system at about 90% of the peak moment. The BSFOS system had measured distributed strains in four specific loading stages: two were within the proportional limit range; two were in the inelastic range. At each loading stage, loads applied on the specimen (including internal pressure) had to be held steady in order that the BSFOS system searched the central frequency at every measured location.

(4) After confirming that the optical fiber was broken on the compression side at the loading stage of 90% of the peak moment, the BSFOS system stopped to measure strains, and the loading continued under stroke control until the target load was reached during the post-buckling stage, i.e. at about 50% of the peak moment. The measured data from the BSFOS were analyzed in frequency domain and converted to strain data.

4.1.5 Investigation of Distributed Strains

Although a total of four sets of distributed strains were measured by using the BSFOS system, only the strains measured during the inelastic loading stages are shown in Figures 4.7 to 4.10. In addition, the strain gauge readings in three locations, the middle, upper one-third, and lower one-third of the pipe specimen are shown in Figures 4.11 and 4.12. The wrinkle location marked on these figures was determined by observing the location of strain localization on the compressive strain distributions.

Compression strains: The distributed strains measured with the BSFOSs revealed the pipe wrinkling at a much earlier loading stage, i.e. at 75% of the peak moment (PM), as shown in Figure 4.7, and at 86% of the PM., the wrinkle location was sufficiently defined (see Figure 4.8). For the comparison of strains at the three locations, 572 mm, 1334 mm, and 2096 mm away from the bottom of the pipe, the average ratio between the strains from the BSFOS system and the strain gauges at 75% of the peak moment (see Figures 4.7 and 4.11, respectively) was 0.90, and the ratio was 0.91 when loading approached 86% of the peak moment (see Figures 4.8 and 4.11, respectively). The results revealed that the compressive strains obtained from the BSFOS system and the strain gauges were in a good agreement.

Tension strains: Because the scales used in Figures 4.9 and 4.10 were much larger than that used in Figure 4.12, very wide fluctuation of strains occurred in Figures 4.9 and 4.10 for the BSFOS system's measurements. However, the tension-side strain distributions from the BSFOS measurements and the strain gauge readings have a similar trend (see Figures 4.9, 4.10, and 4.12). The results from both systems show that more non-uniform strains occurred from the loading stage of 86% of the PM (see Figures 4.10 and 4.12), and strain gauge readings showed no clear sign of the wrinkle location on the tension-side strain distributions before attainment of the peak moment (see Figure 4.12). For the comparison of strains in the wrinkle area, the average ratio between the strains from the BSFOS system

70

and from the strain gauges at 75% of the peak moment (see Figures 4.9 and 4.12, respectively) was 1.06, and the ratio was 0.95 when loading approached 86% of the peak moment (see Figures 4.10 and 4.12, respectively).

4.1.6 Potential of Brillouin Scattering Fibre-Optic Sensing (BSFOS) System

As mentioned, pipe wrinkling can be detected by monitoring either distributed strains or deformation profile along a pipe. The advantage of detecting the pipe wrinkling by using the distributed strain sensors is discussed here. Figures 4.7 and 4.13 clearly demonstrate the advantage of the BSFOS system. Even with the laser profiling system, the occurrence of wrinkling could not be positively identified until the loads were very close to the peak moment, which corresponds to 1.32% compression strain shown in Figure 4.13. On the other hand, the distributed strains measured with BSFOSs revealed the same wrinkle area in a much earlier loading stage, i.e., at 75% of the peak moment (see Figure 4.7), which corresponds to 0.41% compression strain. No apparent sign indicated the wrinkle location in the deformation profile obtained from the laser profiling system at this early loading stage.

4.2 Pipe Buckling Experiment Using Digital Camera System

Another similar pipe buckling test was conducted in the I.F. Morrison Structural Laboratory at the U of A. The test is designed to further verify the potential of strain distributions to be used as a reliable signature in detecting the pipe wrinkling, to study the feasibility of the digital camera system in lieu of demec gauges and strain gauges, and to verify that test results from the digital camera system are comparable to the demec readings obtained from the previous pipe buckling experiments at the U of A. The confirmation from the test will allow the use of previous experimental strain distributions, majority of them are obtained from the demec gauges, in developing the damage detection model.

4.2.1 Specimen Fabrication and Measurements

The pipe specimen, UofA#2, was provided by TCPL. The specimen has 762 mm outside diameter (D), D/t ratio of 59, and pipe length of 2588 mm. The specimen's dimensions, material properties, and test conditions were summarized in Table 4.1. The specimen fabrication was undertaken by TCPL, including the end plate welding.

In addition, a measuring imperfection device, shown in Figure 4.14, was used to measure the initial imperfections for UofA#2 prior to the pipe test, as shown in Figure 4.15. This figure shows that initial imperfections were larger at the center and both ends of the pipe. For the pipe buckling test, the initial imperfection on the compression side, i.e., at the 0º position, is of major concern. As shown in Figure 4.15, the largest inward imperfection at the 0º position occurred at about 750 mm below the pipe center with a magnitude of 0.2 mm.

4.2.2 Test Set-up

UofA#2 was tested by using the MTS 6000 kN Universal Test System at the U of A, as shown in Figure 4.16. The test set-up is similar to the ones used in previous experimental programs (such as Dorey 2001).

The moment arms were attached to the specimen end plates with high-strength bolts; they were attached to the MTS and the strong floor with roller systems (see Figure 4.16). In order to accommodate the end rotations up to 3.5º from this experiment, an angled shim plate and an offset were used in the curved roller bearing system, as shown in Figure 4.17.

4.2.3 Instrumentation

The present safety regulation in the laboratory does not allow persons to access pipes during test, so that some of the previous techniques for measuring strains, such as demec gauges, can no longer be used. As mention in the previous section,

the demec gauges is a promising tool for measuring strains along a line-pipe when a strain gauge cannot be put on exactly the wrinkle location or the strain gauge falls out during the large deformation stage. However, to measure the relative displacement between a pair of demec points, manual readings are needed at some specific loading stages during the experiment. To replace the demec gauges in strain measurement, a digital camera system was employed in this experiment. In addition to the digital camera system, conventional strain gauges, linear variable displacement transducers (LVDTs), rotation meters (RVDTs), and cable transducers were also used. The layout of instrumentation is presented in Figure 4.18.

Since this was the first time that the digital camera system was used in pipe buckling test at the U of A, the camera system and its operation are discussed here.

A pair of digital cameras is used to measure the displacement and longitudinal strains on the compression face along a line-pipe during the test. As a pipe deforms under combined loadings, the deformations contain in-plane and out-of-plane deformations. Therefore, two cameras are needed to capture this 3-D deformation of a line-pipe. The deformation data are analyzed through image processing with the commercial software Vic-3D. The fundamental concept of the image processing employed in this software is the use of the cross-correlation technique (National Instruments 2003, Sadek et al. 2003). The peak score of a correlation function $C(x, y)$ can be obtained by calculating the sum of dot product of the two functions, $g(i, j)$ and $f(x+i, y+j)$, for each possible amount of sliding x and y as shown in Equation (4.3):

$$C(x,y) = \frac{1}{KL} \sum_{i=0}^{K-1} \sum_{j=0}^{L-1} g(i,j) \cdot f(x+i, y+j)$$ (4.3)

where

$$x = 0, 1, ..., K-1; y = 0, 1, ..., L-1$$

When the two functions match, the value of *C(x, y)* is maximized. Accordingly, the cross-correlation technique searches the peak score of a correlation function and then locates the best matching position between two images. For example, many photos were taken during the pipe experiment, and the one taken in the initial loading condition is usually selected as the reference image. Subsequently, the other images were compared with this reference image. In each comparison, the software finds the peak score throughout the correlation function at a location, called the peak location, corresponding to the coordinates (x_p, y_p), and this position is the best matching position. That is, when the best matching between the selected image and referenced image occurs, the selected image has to shift such that its origin is placed on the location (x_p, y_p). In accordance with the peak location, the magnitude and direction of the displacement of the moving body could be measured. In general, for measuring the movement of two large images, they are usually divided into subimages or interrogation windows. The cross-correlation is calculated for each pair of the corresponding interrogation windows. The peak scores at the various interrogation windows represent the complete picture of the movements of the different parts of the image.

In addition to the explanation for the image processing technique, the operating of the camera system are discussed as follows: before a pipe is painted, the rust, dust, and oil on the surface of a pipe must be eliminated by using sand paper or rags without small fluff. This monitored area must be kept clean in order to prevent false sparkles from appearing. The area monitored by the camera system is expected to have a white background with covering black sparkles. This arrangement can improve the contrast in an image.

In current version of the camera system, each sparkle needs to cover at least 3 pixels to ensure the accuracy of test results. A template of the sparkle pattern (see the photo on the right side of Figure 4.19) was made by drilling hundreds of 5 mm diameter holes on a sailcloth-like material for the pipe buckling experiment and the template is expected to be used in future pipe experiments. The minimum angle between the axial tangent vector on the deformed surface of a test specimen and the camera system's local horizon has to be larger than 20°; otherwise, the camera system cannot catch the image of the rotational deformation of the test specimen.

After the cameras have been set up, they are calibrated automatically by the system's software. The software analyzes the images taken from a template board shown in Figure 4.20 and estimates the standard deviation of the analytical results. As the standard deviation reaches the allowable range, i.e., less than 0.05, the calibration results are accepted and the calibration is complete. The template board is expected to be small to reduce errors in the image analysis, but the board needs to cover as much of the monitored area of the specimen as possible. Therefore, for a large-size specimen like a line-pipe, the selected template board has to cover the monitored area and to fit in the digital cameras' range. In this experiment, since both camera could not take a complete image of the template board at the same time, as shown in Figure 4.20, each camera was calibrated separately. Consequently, the template board was put on different locations for the respective calibrations. In this procedure, the relative position between the template board used for the first camera and for the second camera is unknown. In order to solve this problem, the camera system needs to take a sample picture of the specimen after the two respective calibrations and analyzes the sample image. The camera system's calibration is not completed until the sample image is analyzed successfully. In addition, during a test, the camera, lighting systems, and the monitored specimen have to be fixed, because any movement or serious vibration will change the conditions used during the calibration of the camera system, so that significant errors may occur in the test results. The camera system

takes photos at a specific loading stage, and the loading does not need to be stopped during the system's operation.

For the digital camera system, the accuracy of measurement and the gauge length cannot be calculated straightforwardly. They are affected by spatial resolution, and the resolution can vary for different test specimens because an image covers different dimension of the specimen. In the camera system, the maximum error is 0.01 pixels over 100 pixels. The equivalent gauge length depends on the interval size of the signal processing. However, in this project, the maximum strain error was around 100 $\mu\varepsilon$ and the gauge length was 5 mm for each measurement. Even though the camera system analyzed data in every 0.1 mm interval, the distributed strains with the camera system were extracted in 20 mm spacing in this experiment so that noise and misleading strain distribution could be eliminated.

In UofA#2 test, the image taken by the digital camera system covered a range from the compression side to the position about 55º on the right side of the pipe, as shown in Figure 4.19. Demec points were put on the pipe as references (see Figure 4.18) for calculating camera demec-strains. The camera demec-strains were acquired by using the same algorithm applied in the calculation of the demec gauge readings. The formula of computing the camera demec-strains are presented in Appendix A. Conventional strain gauges were used to validate the data acquired from the digital camera system. In addition, two sets of LVDTs with a 300 mm gauge length were attached to the middle and lower one-third of the pipe on the compression side respectively, as shown in Figure 4.16, to examine the accuracy of the measurements from the camera system.

 4.2.4 Test Procedure

The test procedure was similar to that of the pressurized pipe buckling experiments conducted at the U of A (Dorey 2001), except the digital camera system was used for distributed strain measurements. Thus, only the test procedure relevant to the operation of the camera system is explained here. To

verify that the new system can measure strains successfully during the experiment, a test of a hollow structural section (HSS) column under an eccentric compressive load was processed in advance. The test description and data analysis for the HSS column test are presented in Appendix A.

After validation of the camera system in the HSS column test, the pipe buckling test was conducted in two stages. The first stage was to verify that the camera system can accurately measure strains during the pipe buckling test; the second stage was to conduct a complete pipe buckling test. These two stages are discussed as follows:

(1) The first stage: As mentioned, for a large-size specimen like a line-pipe, the pair of cameras cannot take a complete image of the template board at the same time, so each camera needs to be calibrated separately. This calibrating procedure was different from that in the HSS column test. Moreover, the camera system's capacity for measuring strains on a large-size and long narrow area needed to be further validated. Accordingly, a trial run of the pipe buckling test was performed in this stage. To provide significant strain readings for the camera system and to avoid any permanent deformation in the pipe specimen, the proving test was loaded within 36% of the target load (5737 kN-m), which was the pipe's peak moment obtained from the FEA. The corresponding strain to the proving load was about 0.2%. The test procedure is described below:

After the camera system was calibrated, the pneumatic pump applied the internal pressure up to the designed level inducing 20% of the SMYS in hoop stress, and an additional axial force was applied by the MTS system to counteract to the internal pressure load on the specimen's end caps. A jack load of a pair of hydraulic rams was set as zero reading. The camera took an initial image. By increasing the jack load and adjusting the corresponding MTS load, the MTS and the pair of hydraulic rams applied bending moment incrementally on the specimen under load control. When the proving test

77

completed, the camera system had taken images at 6 loading stages. The strain results in the first two stages were examined during the test, and the rest of images were analyzed after the test. After all data were studied and showed that the test results obtained from the camera system were reliable, the test procedure was moved forward to the second stage.

(2) The second stage: Since the camera, lighting equipment, and pipe specimen were remained at the same locations for these two stages, the camera system was not calibrated again in the second stage. Because the bending moment was unloaded to zero after the proving test had completed, the camera system need to take an initial image at the beginning of the test in this stage. The subsequent loading phase of the specimen has the similar procedure used in the first stage. The only differences are that loading would be applied up to the target load, and a smaller loading increment, 50 KN, was applied in the jack load when the pipe behaviour went to the non-linear range. However, the test was stopped just after 75% of the target load because of the weld failure between the end plate and the bottom of the pipe.

Even though the loading could not reach the limit point in this experiment, the objectives of this experiment were achieved by studying the strains occurred on the inelastic deformation stages. In the following sections, the PM represents the target load determined from the FEA.

4.2.5 Investigation of Distributed Strains

Compression strains: The distributed strains measured by the camera system revealed that strain localization occurred on the bottom of the pipe at a much earlier loading stage, i.e., at 38% of the PM (see Figure 4.21). Once the loading reached 75% of the PM, the pipe failed at the weld connection between the bottom of the pipe and the end plate. The strains close to the bottom of the pipe experienced serious fluctuation and the pipe shifted at that instant (see the dash line in Figure 4.21). In Figures 4.21 and 4.22, the discrete points represent the

78

strain gauge readings and the continuous lines connect the test results are from the camera system. The camera demec-strain is shown in Figure 4.22. These figures reveal that the compressive strain distributions from the strain gauges and from the camera system were in a good agreement. The average ratios between the strains from the camera system and the strain gauges at 67% and 75% of the peak moment were 1.00 and 1.01, respectively. Observing strain gauge readings in Figure 4.22 shows that strain development changed from being relatively uniform distribution into wave-shaped distribution after 62% of the PM had been reached. After that, the strain was localized on the locations near both ends of the pipe, and the localized strain grew slightly faster on the bottom than on the top of the pipe. An imperfection measurement of this pipe revealed that an inward imperfection appeared around 750 mm below the center of the pipe (see Figure 4.15), and, consequently, a wrinkle is possibly triggered at this location. Even if the wrinkle could not be defined at such an early loading stage, i.e., at about 70% of the PM (see Figure 4.21), the maximum compressive strain was obtained at the same location from the strain gauge and the camera system and an anomaly could be revealed on the distributed strains, as shown in Figures 4.21 and 4.22.

Tension strains: The tension strains were resulted from the strain gauge measurement. Figure 4.23 reveals that more apparently non-uniform strain distribution started during the loading stage of 71% of the PM, and a similar pattern retained during the successive stage.

4.2.6 Validation of the Digital Camera System

The results from HSS column test (see Appendix A) showed that the strains from the digital camera system agreed with the strains from both the strain gauge readings and the demec readings. As strains were larger than 0.4%, the average of the ratio of the camera strains to the strain gauge readings was 1.04 with a standard deviation of 0.004; the average of the ratio of the camera strain to the demec readings was 0.98 with a very low standard deviation of 0.001. Moreover, the results from the UofA#2 pipe buckling test (see Figure 4.21) revealed that as

strains approached 0.2%, the average of the ratio of the camera strains to the strain gauge readings was 0.99 with a standard deviation of 0.035. When loading reached 75% of the PM, the average of the ratio of the camera strains to the strain gauge readings was 1.01 with a standard deviation of 0.025; while the strains shown in Figure 4.22 revealed that the average of the ratio of the camera demec-strains to the strain gauge readings was also 1.01 but the standard deviation was slightly higher around 0.029.

The above comparison of the strain distributions as well as the strain magnitude concludes that the digital camera system can be used, instead of the demec gauge, in large-size pipe buckling tests. In addition, the strain results from the demec readings obtained in the previous pipe buckling experiments at the U of A are comparable to the strains measured by the digital camera system.

4.3 Field Buried Line-pipe Experiment

Although the distributed fibre-optic sensors have been used in field pipelines for a few years (Inaudi and Clisic 2006), and some research using the distributed fiber-optic sensing system in line-pipes have been carried out in laboratories, very limited data have been published for monitoring field pipelines with the distributed fibre-optic system. An opportunity aroused from an excavation research project (He 2007) allows us to study the feasibility of applying the distributed fibre-optic sensing system in a buried pipeline. The project was sponsored by TCPL to conduct a field experiment on the excavation effects on a buried line-pipe. A field monitoring program using BSFOSs in a buried line-pipe was included in this experiment. The research group from the University of Ottawa was responsible for installing and operating the BSFOS system in the field and converting the frequency signals to strain data.

4.3.1 Specimen Fabrication

The buried steel pipe is 27,573 mm in length, 914.4 mm in diameter, and 13.7 mm in thickness; the specific minimum yielding stress (SMYS) of the steel is 483

MPa. Since the line-pipe had been previously used for an air testing, it had to be modified for the excavation experiment. A blind flange at its center had to be removed and the pipe was re-welded.

4.3.2 Test Set-up

After modification, the line-pipe was moved into a workshop for the installation of strain gauges and optical fiber cables. The optical fiber cables of the BSFOS system were separated into 3 routes: a main route was mounted at five sections around the line-pipe circumferentially and at two longitudinal locations, i.e. at the top and bottom along this line pipe; the other sub-route focused on either the five circumferential sections or the longitudinal locations along the line-pipe, respectively. The main route of the BSFOSs on the pipe is shown in Figure 4.24. Multi-routes of the BSFOS system were used to avoid outage of the system during excavation processing due to an accidental break of the optical fibre. The set-up of BSFOS system is described as follows.

After the measuring locations were marked, the surface of these locations had to be sanded in order to eliminate rust and paint on the surface, as shown in Figure 4.25. Next, the optical fibers were temporarily taped onto the monitored locations. Then, the sensing fibers were glued onto the pipe, while the loosing fibres were only taped onto the pipe. About one hundred meters of BSFOS fibre were installed on the line-pipe, as shown in Figure 4.26. Once the glue in the fibres had cured, the leading fibres were connected to the ends of the fibres already installed on the pipe by using the fusion procedure, and then the cable connectors were connected to the leading fibres. After the installation of the optical fibres was completed, a pair of probe meters input a laser throughout the route of the optical fibres to ensure that the fibres did not accidentally break during their installment.

 Optical fibre is a water-resistant and chemical-resistant material, but can be easily broken by either a sharp cut or sharp bend. In excavation operations, besides using an excavator, the operators need to use shovels to take out the soil

on the surface of the line-pipe. This procedure is commonly used to prevent pipe damage from the excavation. To prevent the fibre from breaking during the excavation, the optical fibre needs to be sufficiently protected. Therefore, in this experimental program, the fibres were covered by three layers of protection. The first layer used a foam tape, as shown in Figure 4.27(a). This material is very flexible and sticks well to steel material, but doesn't restrain the fibre stretching or contracting. The second layer used silicon material to cover the gauges and optical fibers in a large area on the line-pipe, as shown in Figure 4.27(b). The last layer was a coating of polyethylene (PE) to prevent pipe corrosion and rusting.

After the installation of the instruments, the pipe was buried, and the leading fibers of the BSFOS system was brought above ground by winding around a metal tube, which was pre-welded near the end of the pipe. In this procedure, it is important to prevent the fibers from sharp bend, i.e. near or small than 90º angle. The sharp bend can easily generate serious noise for the data acquisition in the BSFOS system.

4.3.3 Instrumentation

In addition to the BSFOS system, conventional strain gauges were installed on the locations near the main route of the optical fibers, so that the results measured from both the strain gauges and BSFOS system can be compared. Although both high-speed and low-speed data acquisition systems were used to respectively collect dynamic and static strain readings during the excavation, but only static strain readings were used to compare with the strains from the BSFOS system. These static strain data were recorded in one data per second.

The previous discussion in section 4.1 shows that the BSFOS system can measure distributed strains in every 50 mm along a line-pipe, but, to avoid time-consuming data-acquisition processes, the BSFOS system collected the distributed strains at only some specific locations where the measured strains could be compared to the strains from the strain gauges. Therefore, the system can complete a data-

acquisition cycle within 20 minutes, while the whole excavation procedure took 30 to 40 minutes long to complete.

4.3.4 Test Procedure

Five excavation test programs, three in summer and the other two in winter, were conducted in the project (He 2007). The optical fibres installed on the field pipe were examined during all test programs, but the BSFOS system was used only during a pressurized-pipe test of the summer programs. The BSFOS system measures strains in the following stages:

Stage1: the excavator began to excavate;
Stage2: the excavation almost completed;
Stage3: the excavator began to backfill the soil;

During these stages, the excavator's route is shown in Figure 4.28, and the excavation started approximately 2 m before section 1 and ended at about 2 m after section 6, so that the total excavation length was about 13 m. The excavator used in the present project could excavate a length of about 2.6 m at each position with a ditch depth of about 2 m. The test procedure is as follows:

(1) During excavation, an excavator operated at five distinct positions, i.e., at section 2, the middle of sections 2 and 4, section 4, the middle of sections 4 and 7, and section 7.

(2) At each position, the excavator sat on either the left side or right side of the pipeline as shown in Figure 4.28. The left side or right side is determined as the excavator stands at section 1, or the start section, and, face towards section 7 or the end section.

(3) After the excavation had completed the excavator backfilled the pipe trench and prepared for next test. The BSFOS system completed the third-stage data acquisition after the pipe was buried.

In addition, during the excavation test, a digital video recorder was used to record the position of the excavator in relation to the time during each excavation test. Using the recorded time, the test results from the BSFOS system were compared with the strain gauge readings. As the laser light speed of the BSFOS system was constant, and the monitored route and locations were known, the time when the strain was measured at a specific location could be obtained. An example of a strain-time history graphs was created in the excavation project (He 2007) and is shown in Figure 4.29.

4.3.5 Investigation of Distributed Strains

The comparison of the strains from the strain gages and from the BSFOS system is shown in Figures 4.30, 4.31, and 4.32. In Figure 4.32, the 0º position represents the top of the line pipe; the 90º position represents the right side of the line pipe. Because of the absence of initial measurements by the BSFOS system, the strain readings from the two instruments cannot be compared in absolute magnitude. Instead, the relative strains between the first and second stages were compared between the BSFOS system measurements and the strain gauge readings. Because of the small strain results, the different data-acquisition sampling rate, and the measuring error of the BSFOS system in the 50 με to 100 με range, an exact comparison of the magnitude is difficult, but the results from the strain gauges and the BSFOS system are in the same order. There is agreement between the relative longitudinal strains on the top of the line-pipe obtained from the BSFOS system and the strain gauge readings in the trend of strain development (see Figure 4.30). For the relative longitudinal strains on the bottom of the line-pipe, the test results obtained from the BSFOS system and the strain gauge readings are not totally in agreement, but most of the strains is in the same magnitude order (see Figure 4.31). The comparison of longitudinal strains (see Figures 4.30 and 4.31) yielded better agreement than that of hoop strains (see Figure 4.32). In addition, the measuring errors of the BSFOS system result from inherent fluctuations in the readings of the BSFOS system, and the uncertainty due to the

measuring error can be reduced in predicting strains during pipe wrinkling as these strains are usually larger than 1000 $\mu\varepsilon$.

The field experiment has proven that the BSFOSs were able to survive underground, throughout the severe winter weather and during the excavation process.

4.4 Summary

The potential of using distributed stains to detect pipe wrinkling was further validated by the above two experiment programs, Pipe#14 and UofA#2. The Pipe#14 experiment using the BSFOS system revealed that the anomaly of pipe wrinkling can be identified at an earlier loading stage by monitoring the distributed strains than by measuring deformation profiles. The UofA#2 experiment showed that strain localization occurring in the strain distributions could effectively predict the location of the pipe wrinkling before 75% of the PM.

In addition, the field excavation experiments showed that the distributed strain sensory system, BSFOS system, can be used in a buried pipe to monitor the pipe's conditions under severe winter weather and during the excavation process.

As the reliable behavioural signature (development of distributed strains) of the buried pipe buckling is verified and the application of the distributed strain sensory system in the buried pipe is feasible, the developed health monitoring system will employ a distributed strain sensory system to monitor the strain distribution patterns along the buried pipelines in order to predict the pipe wrinkling. The strain distribution patterns and the developed health monitoring algorithm are discussed in the next chapter.

Table 4.1 Specimen Properties and Loading Conditions in the Pipe Buckling
Experiments

Specimen	Grade (MPa)	Diameter (mm)	D/t	Length (mm)	Internal pressure (%SMYS)	Girth Weld	Loading patterns
Pipe#14	X100h (690)	762	55	2667	77	No	Monotonic bend
UofA#2	X100h (690)	762	59	2588	20	No	Monotonic bend
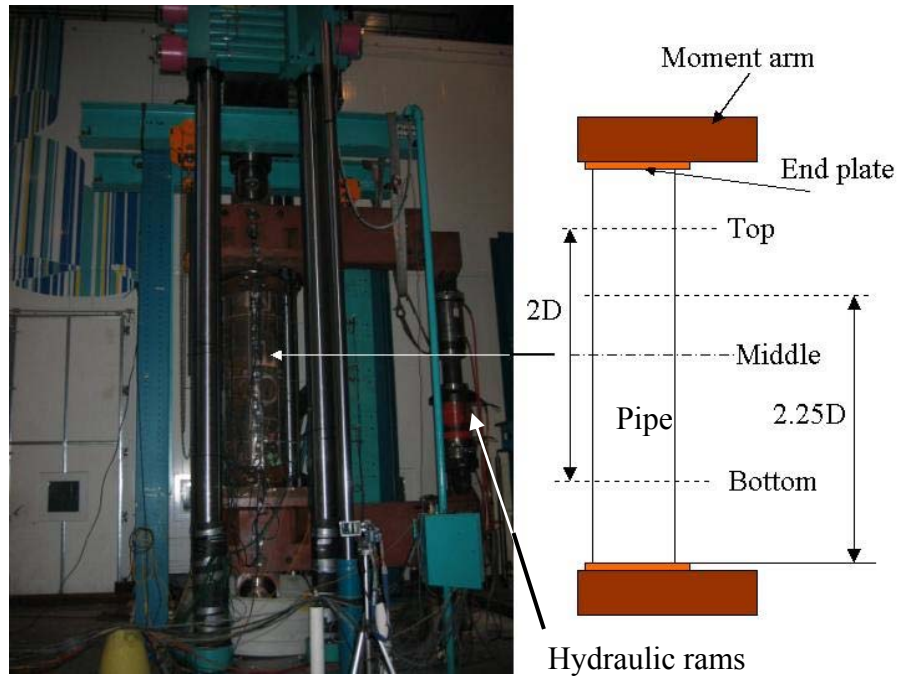
Figure 4.1 Test Set-up for Pipe#14 Experiment
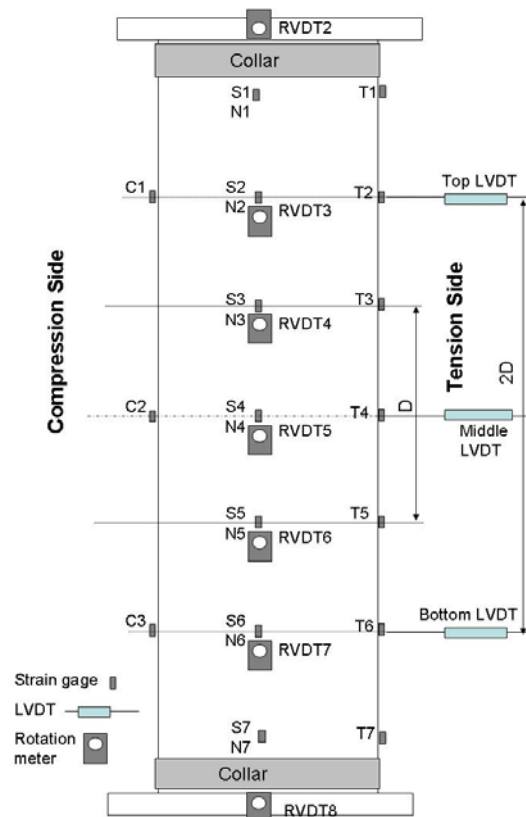
Figure 4.2 Instrument Layout for Pipe#14 Experiment

87
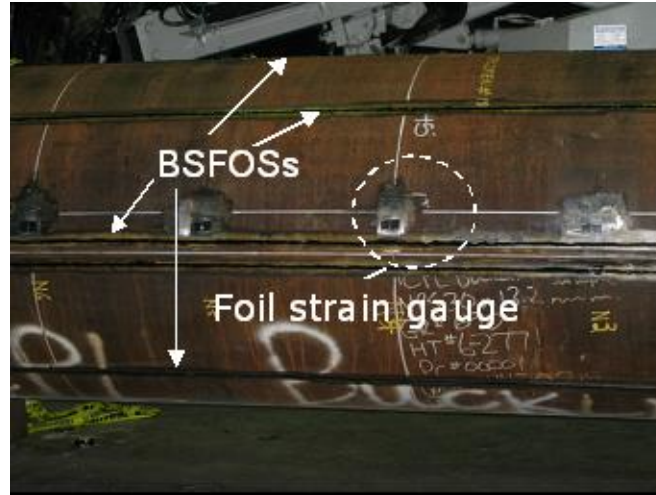
Figure 4.3 BSFOSs and Strain Gauges Used in Pipe#14
Experiment
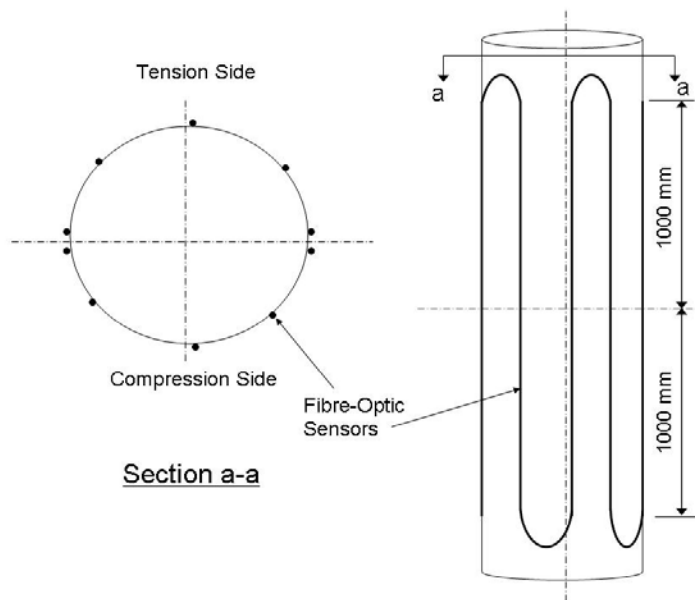
Figure 4.4 BSFOSs layout for Pipe#14 Experiment
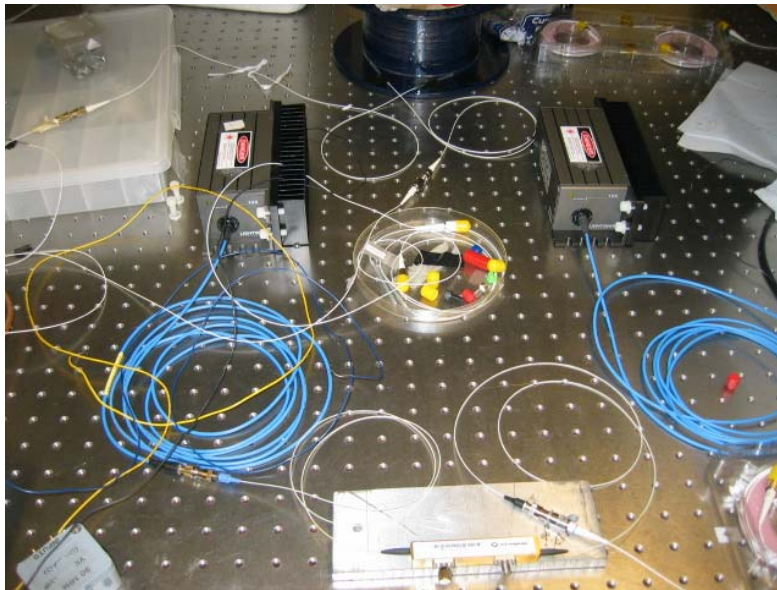
Figure 4.5 Electro-Optic Modulator Used in BSFOS System
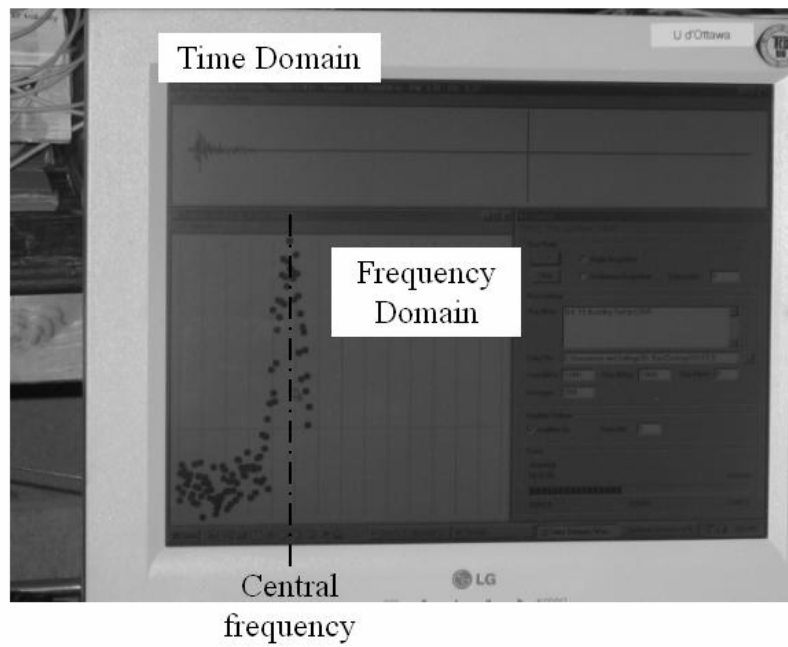
Figure 4.6 Data Acquisition in BSFOS System
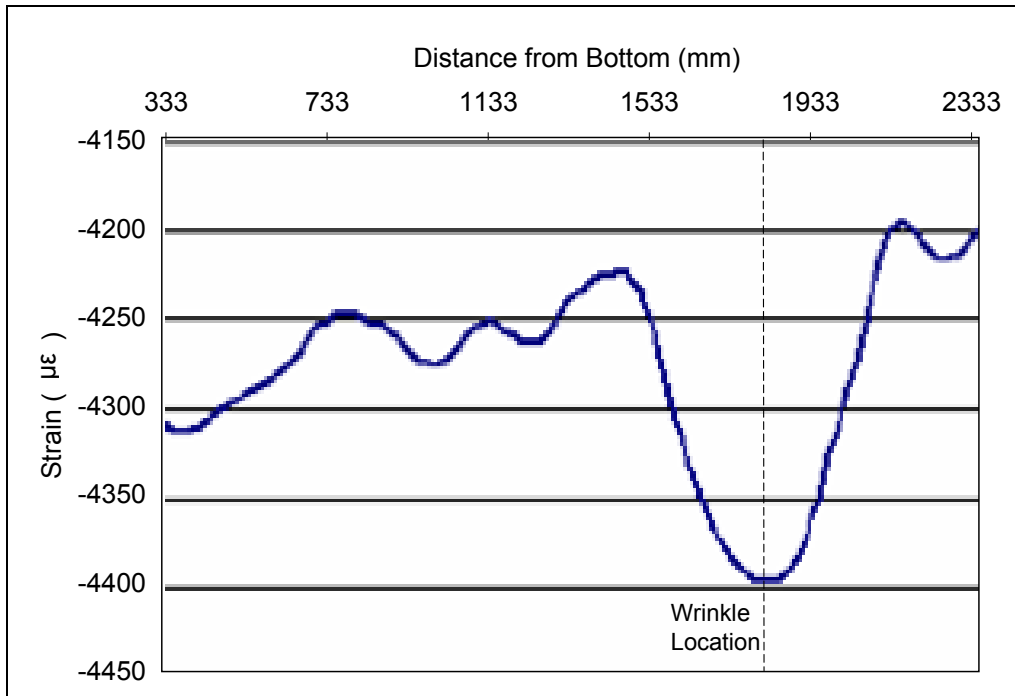
Figure 4.7 Compressive Strain Distributions at 75% of the Peak Moment for Specimen Pipe#14
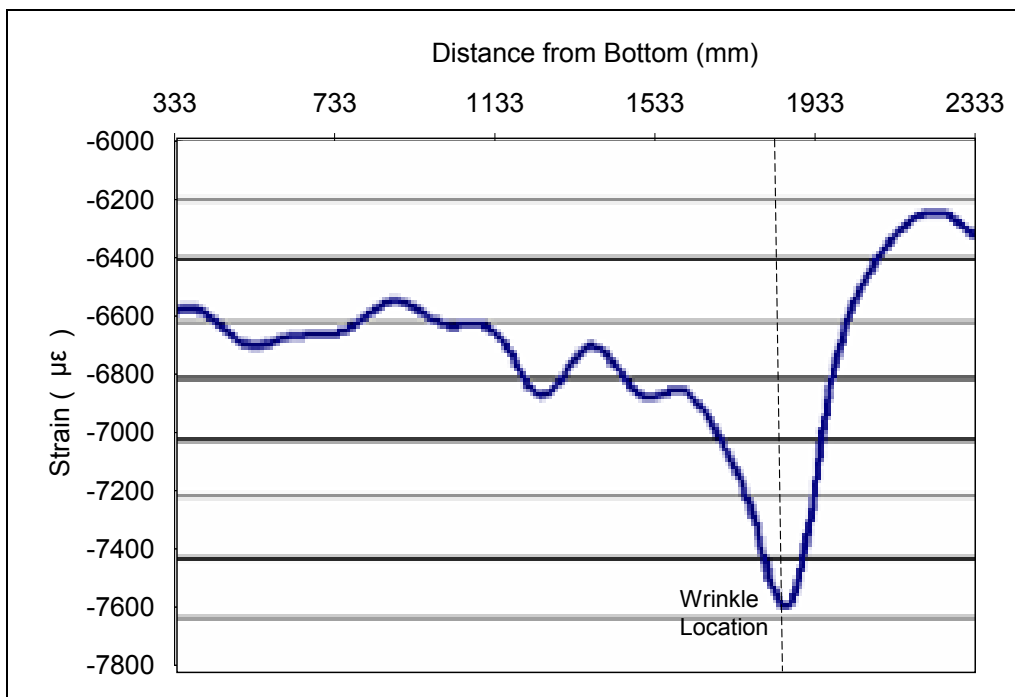
Figure 4.8 Compressive Strain Distributions at 86% of the Peak Moment for Specimen Pipe#14
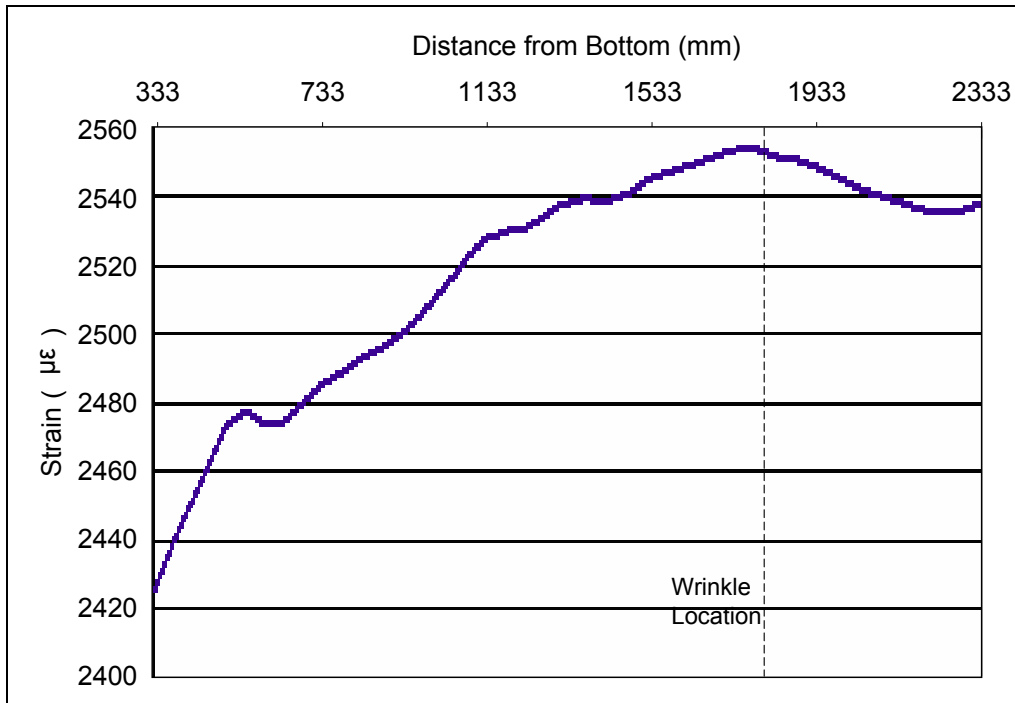
Figure 4.9 Tensile Strain Distributions at 75% of the Peak Moment for
Specimen Pipe#14
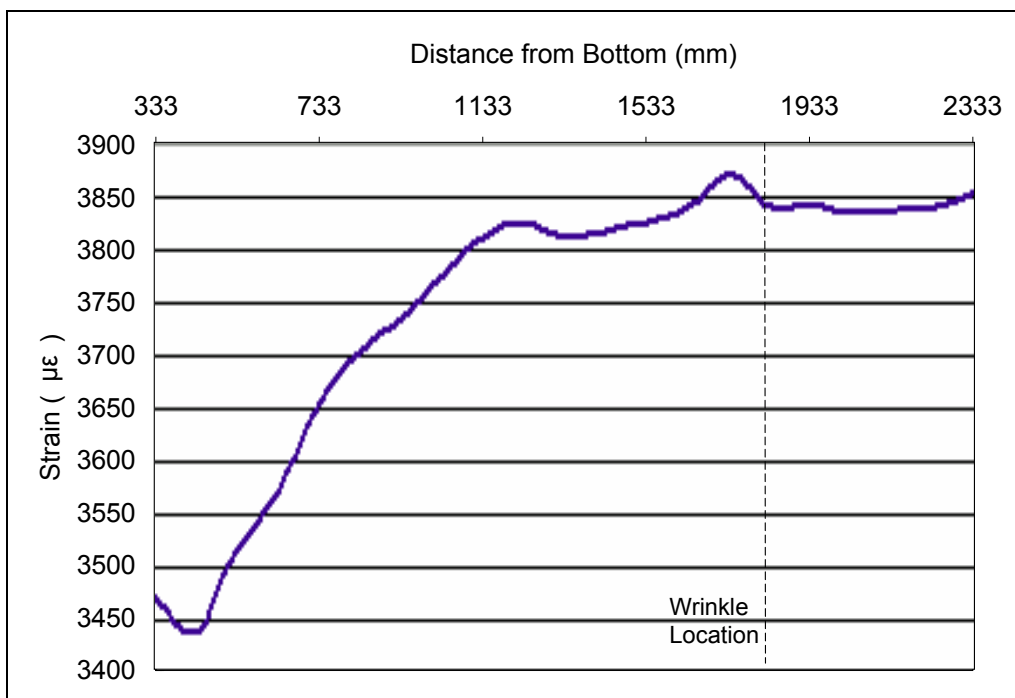
Figure 4.10 Tensile Strain Distributions at 86% of the Peak Moment for
Specimen Pipe#14
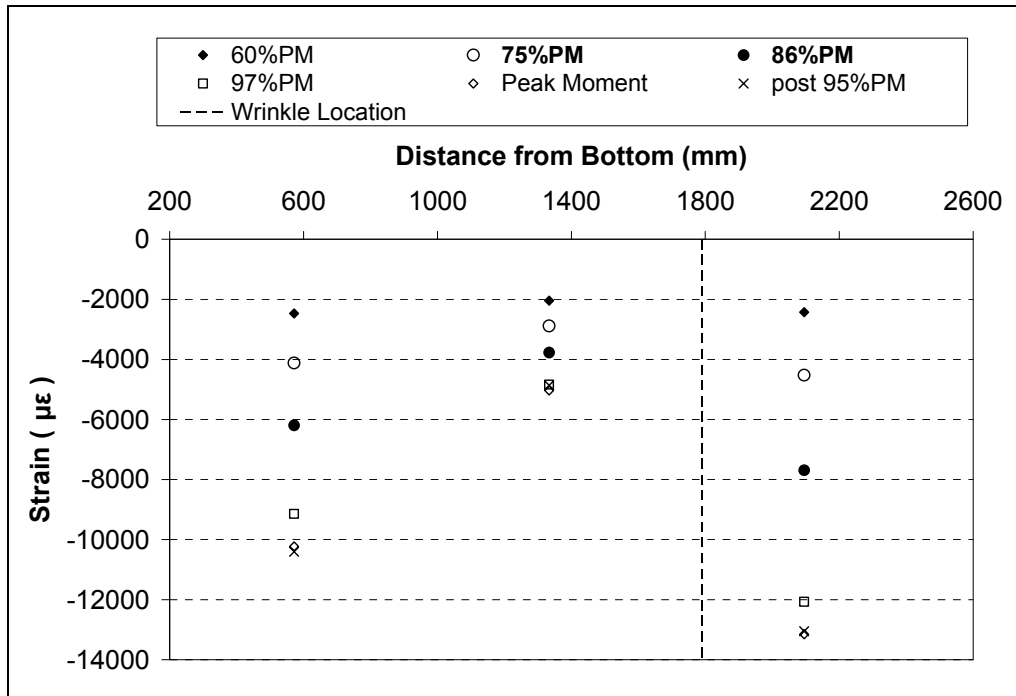
Figure 4.11 Strain Gauge Readings on the Compression Side for Specimen Pipe#14
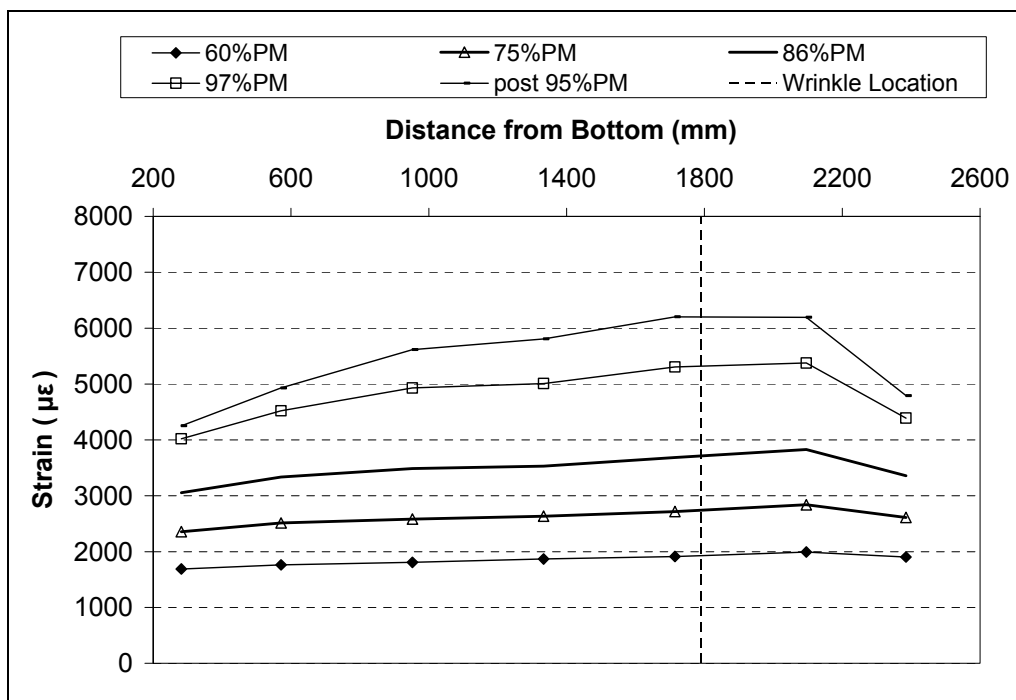
Figure 4.12 Strain Gauge Readings on the Tension Side for Specimen Pipe#14
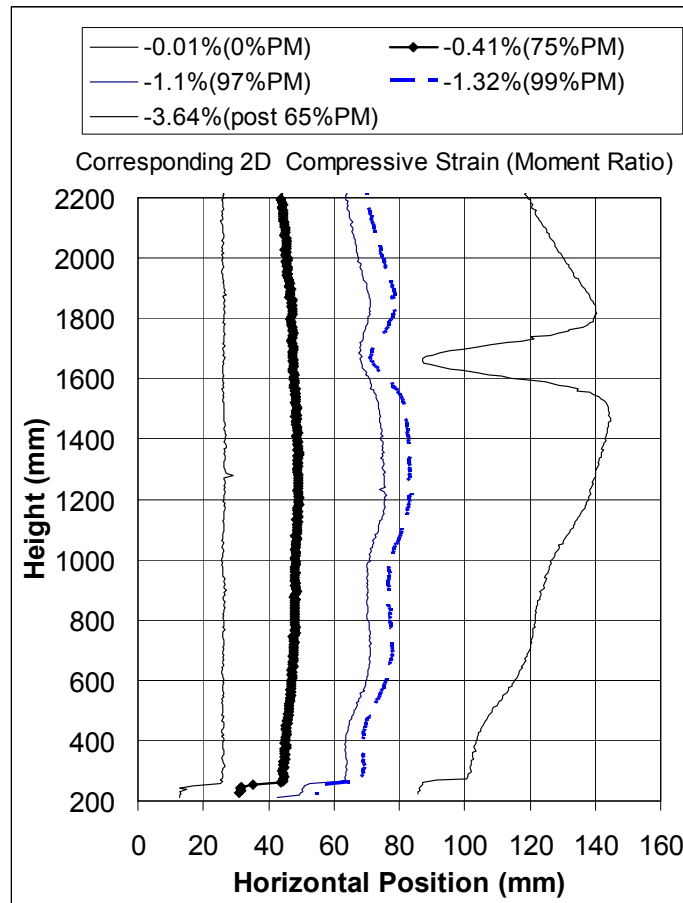
Figure 4.13 Deformation Profile for Specimen Pipe#14

Figure 4.14 Measuring Imperfection Device
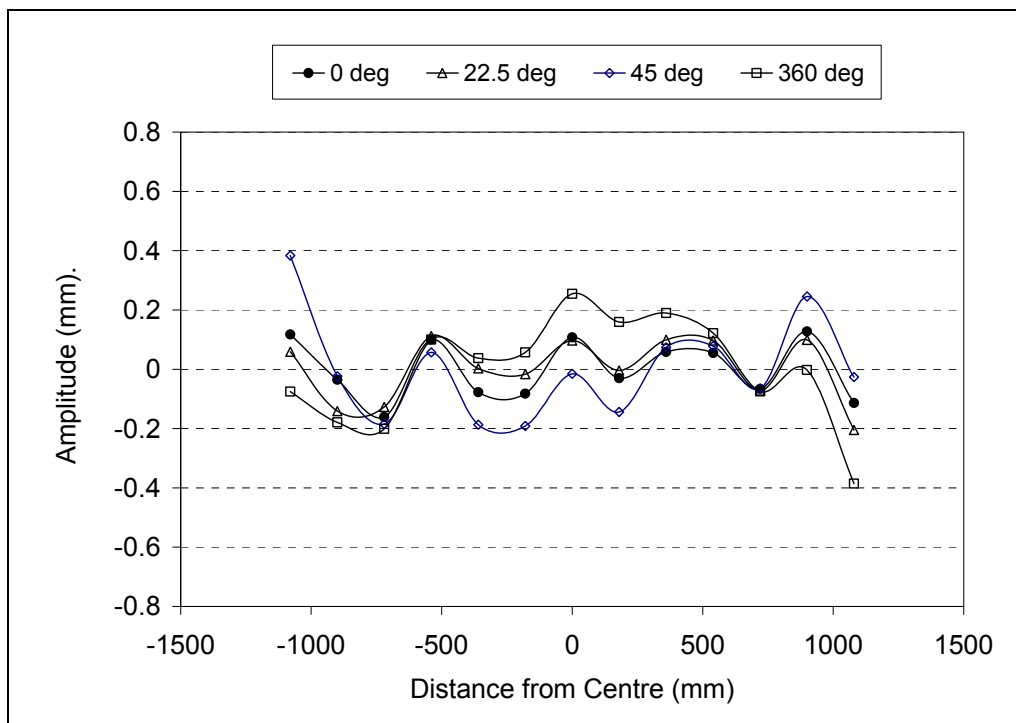
Figure 4.15 Initial Imperfection Measured on Specimen UofA#2
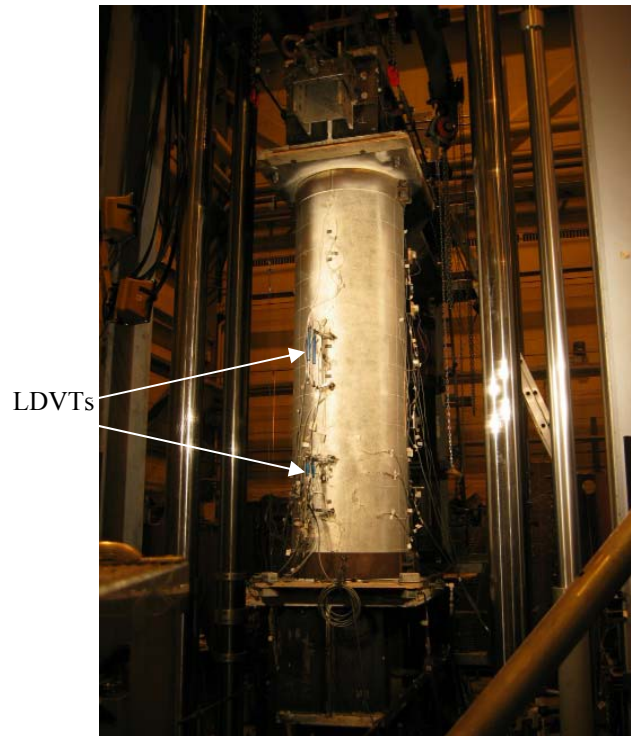
(a) Test Set-up
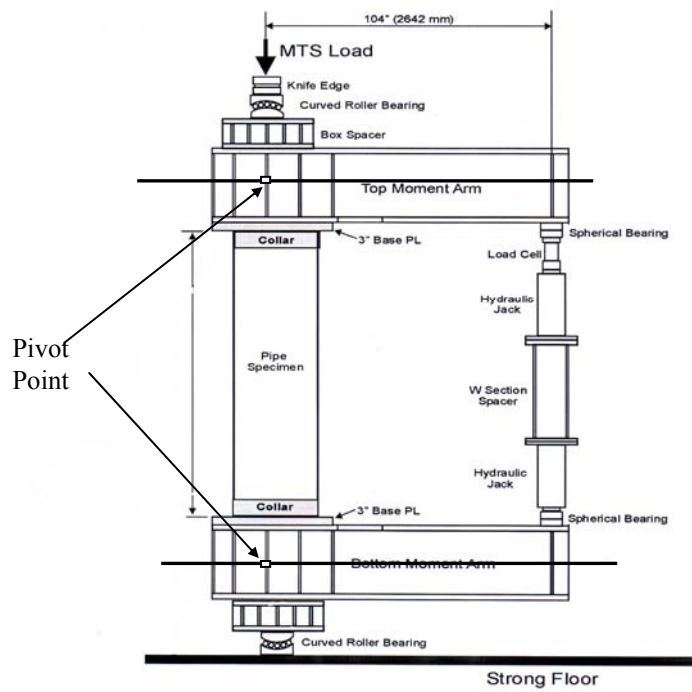
(b) The Components of the Test Set-up

Figure 4.16 Test Set-up for UofA#2 Experiment

An angled shim plate and an offset between the roller and moment arm
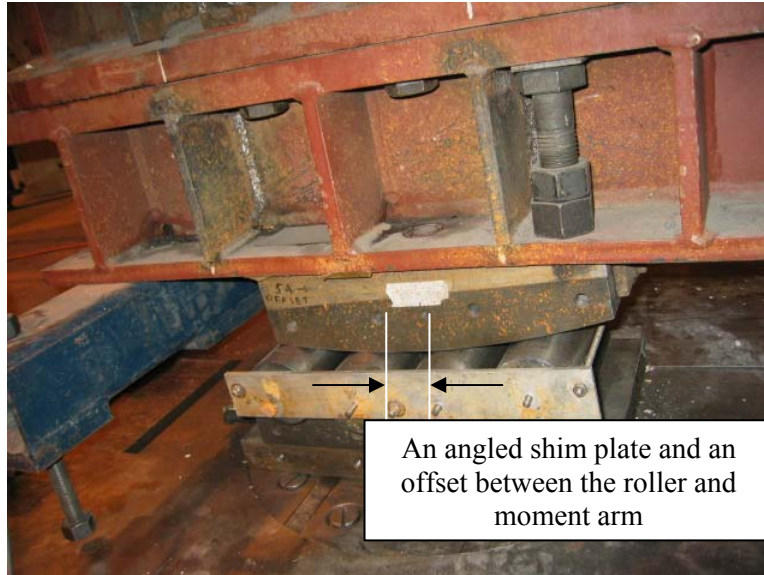
Figure 4.17 Angled Shim Plate and Offset Used in Curve Roller Bearing System
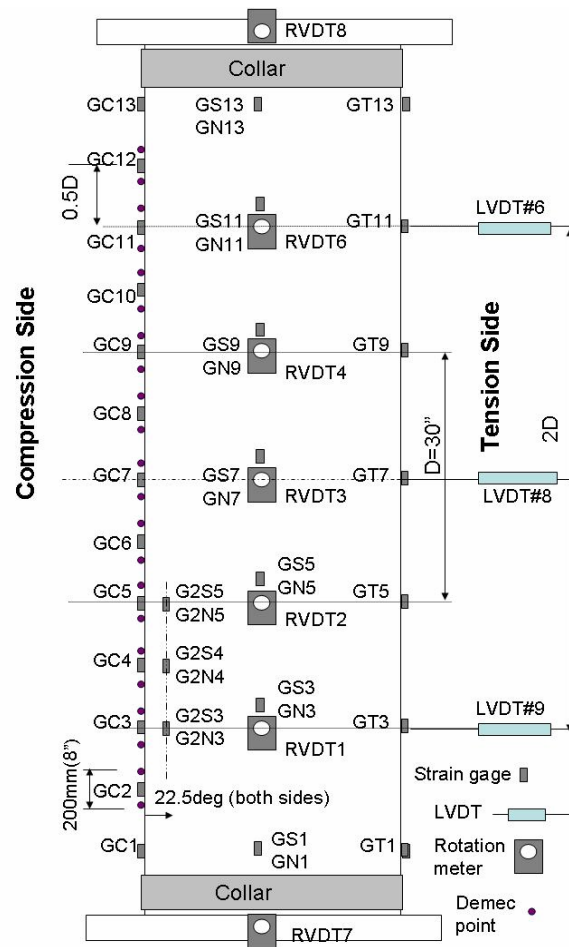
Figure 4.18 Instrument Layout for UofA#2 Experiment

96
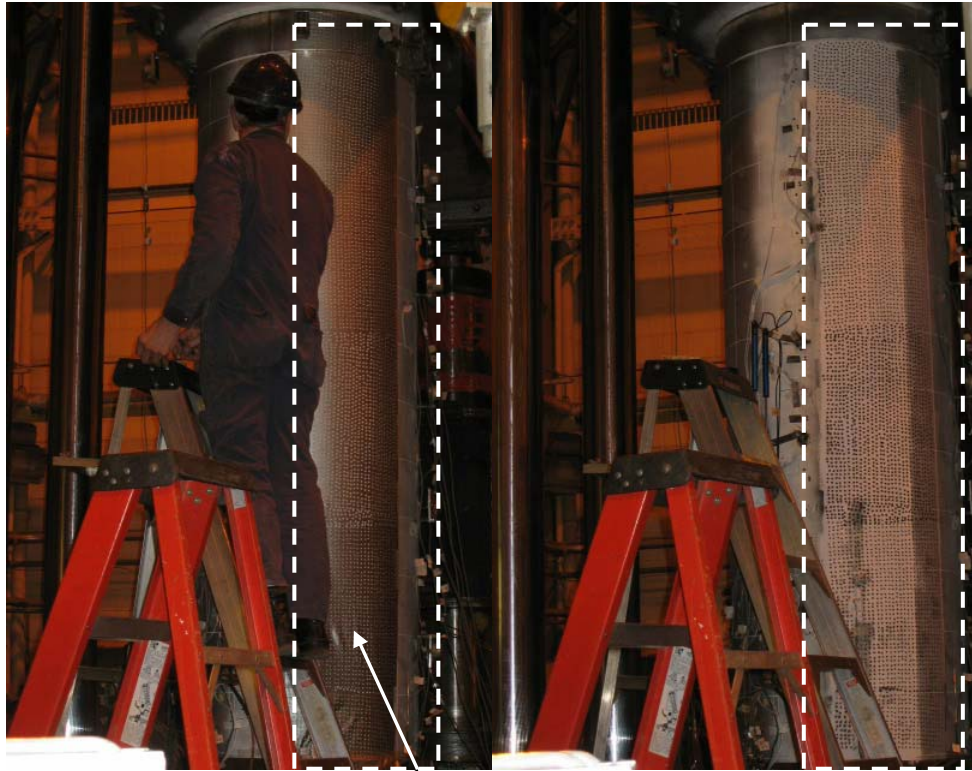
Template of sparkle pattern

Figure 4.19 Before and After Spraying Sparkles on the Pipe

Template board
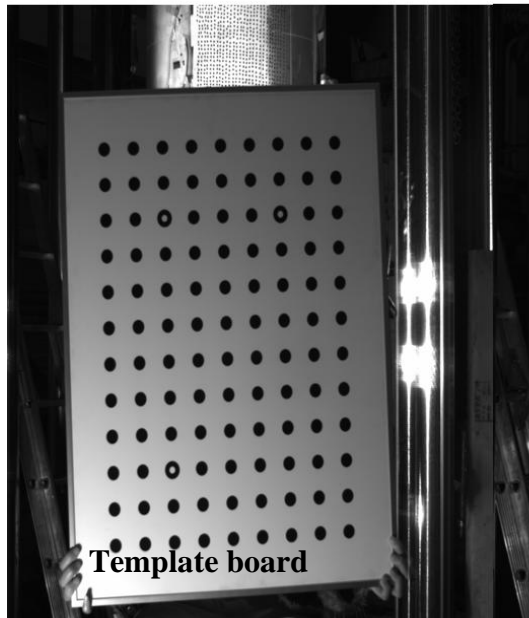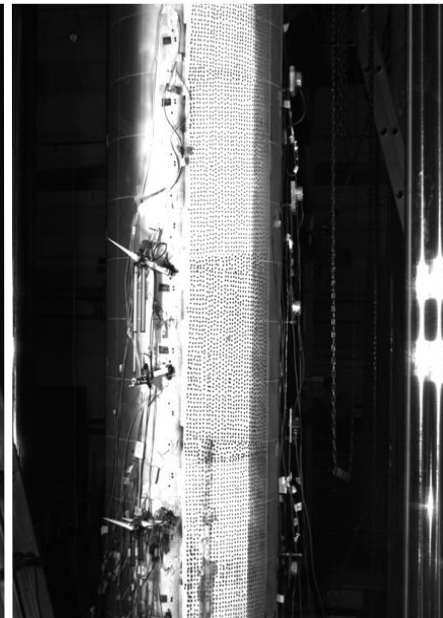
View from Camera 1   View from Camera 2

Figure 4.20 Camera Calibration

97
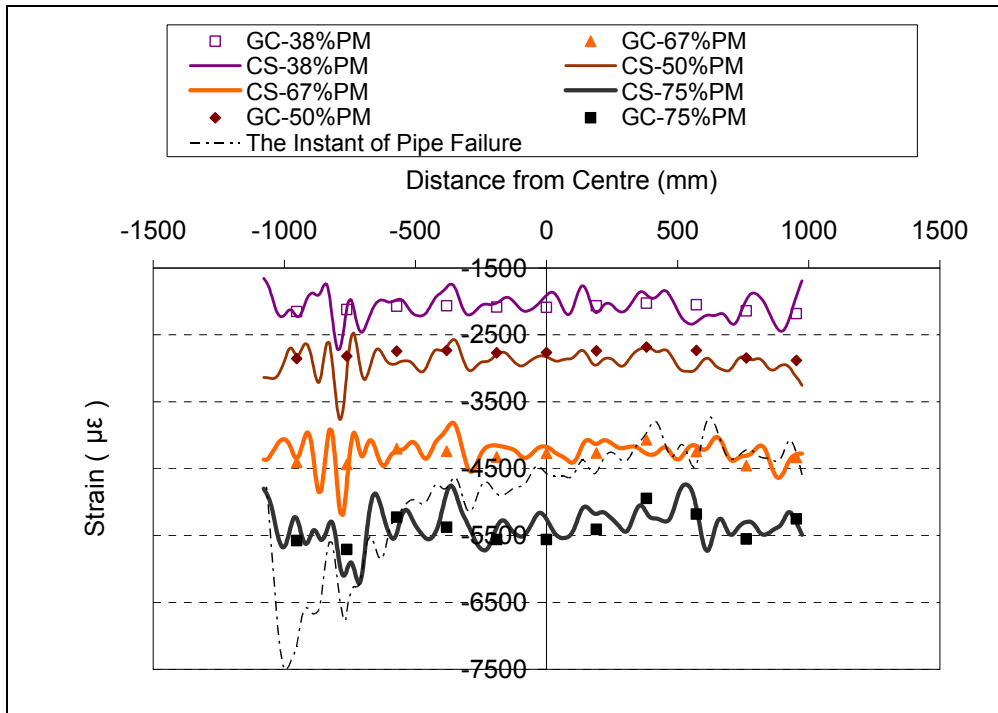
Figure 4.21 Strain Readings and Camera Strains Comparison for Specimen UofA#2
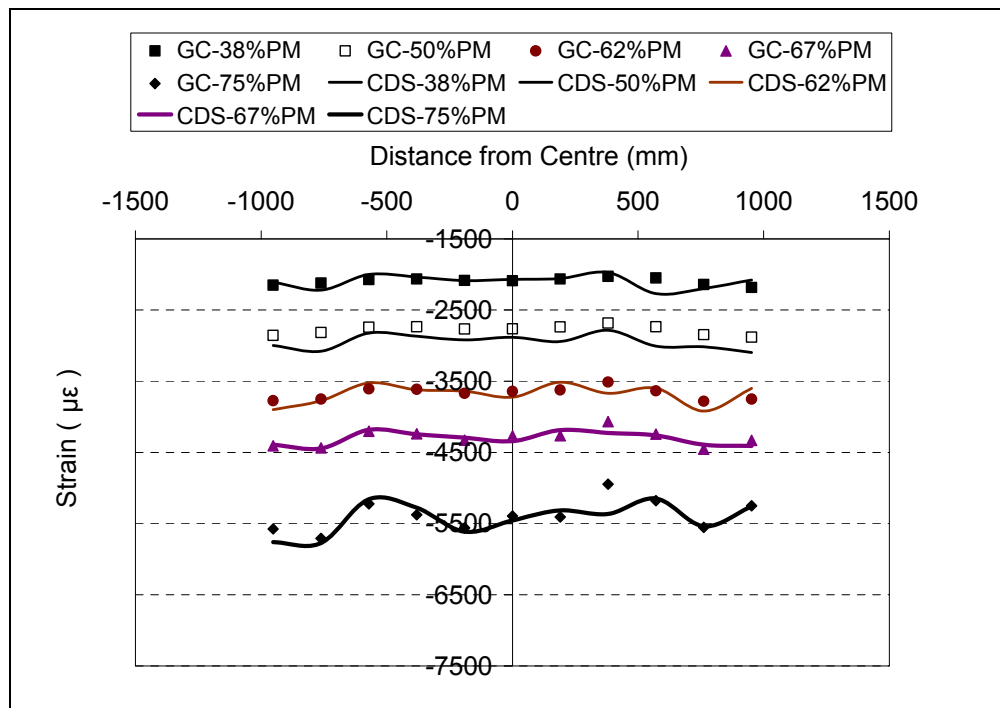
Figure 4.22 Strain Readings and Camera Demec-Strains Comparison for Specimen UofA#2

98
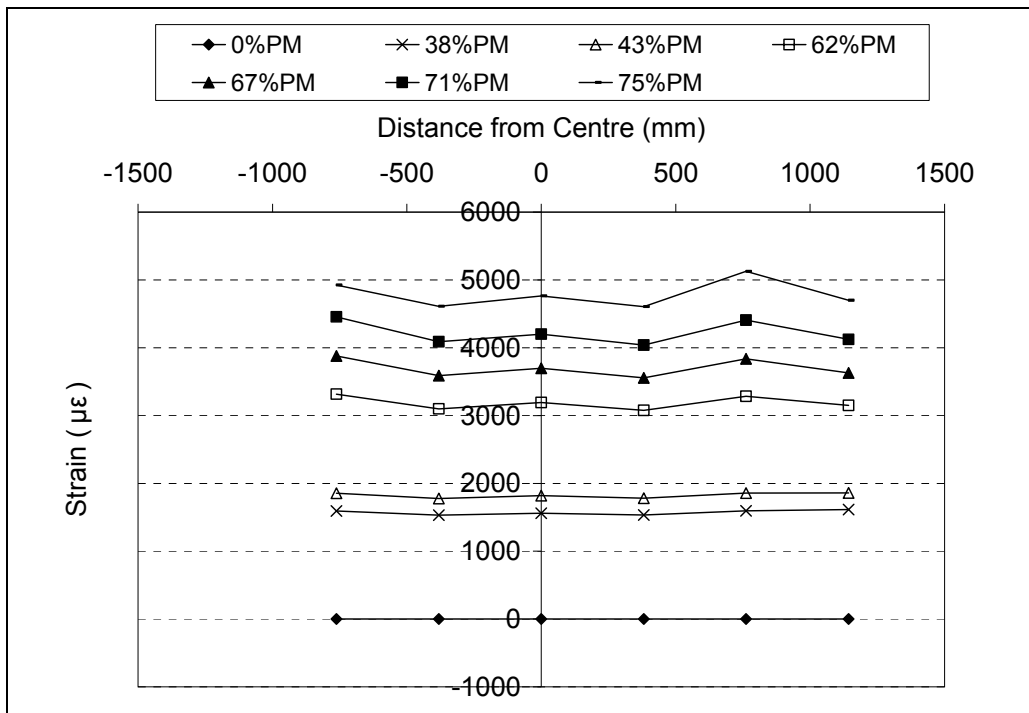
Figure 4.23 Tensile Strain Distributions for Specimen UofA#2
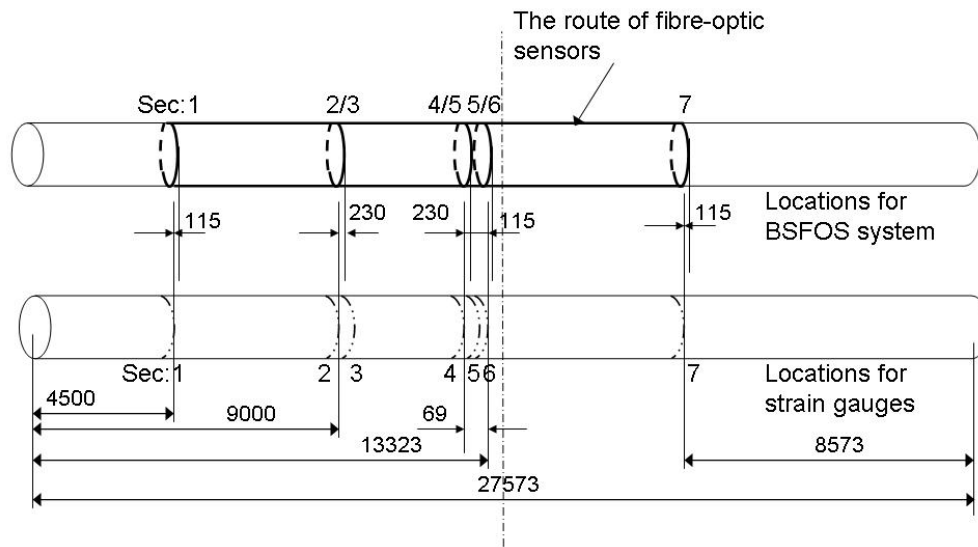
Figure 4.24 Main Route for BSFOS Measurement on the
Line-Pipe

Figure 4.25 Surface Clean-up for the Field Line-Pipe

100

Figure 4.26 Optical Fiber Setup for the Field Line-pipe Experiment
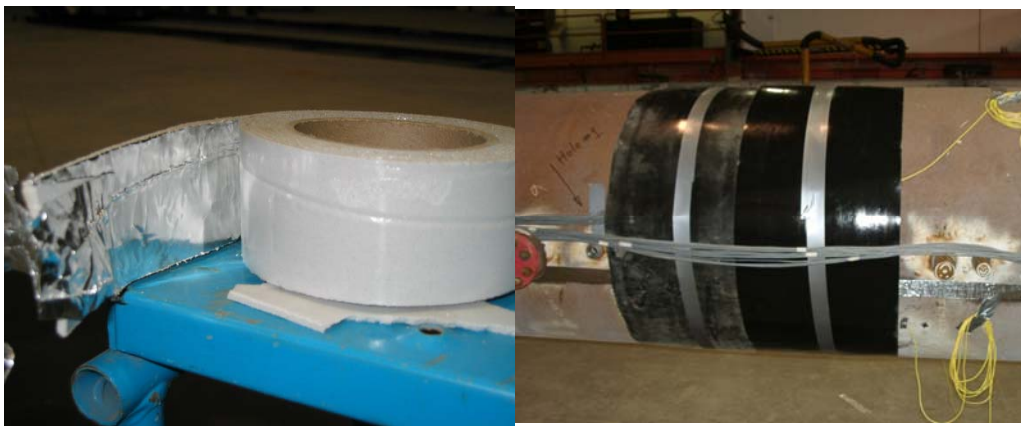
(a) Foam Tape   (b) Silicon Material

Figure 4.27 Fibre-protecting Materials Used in the Field Line-Pipe Experiment
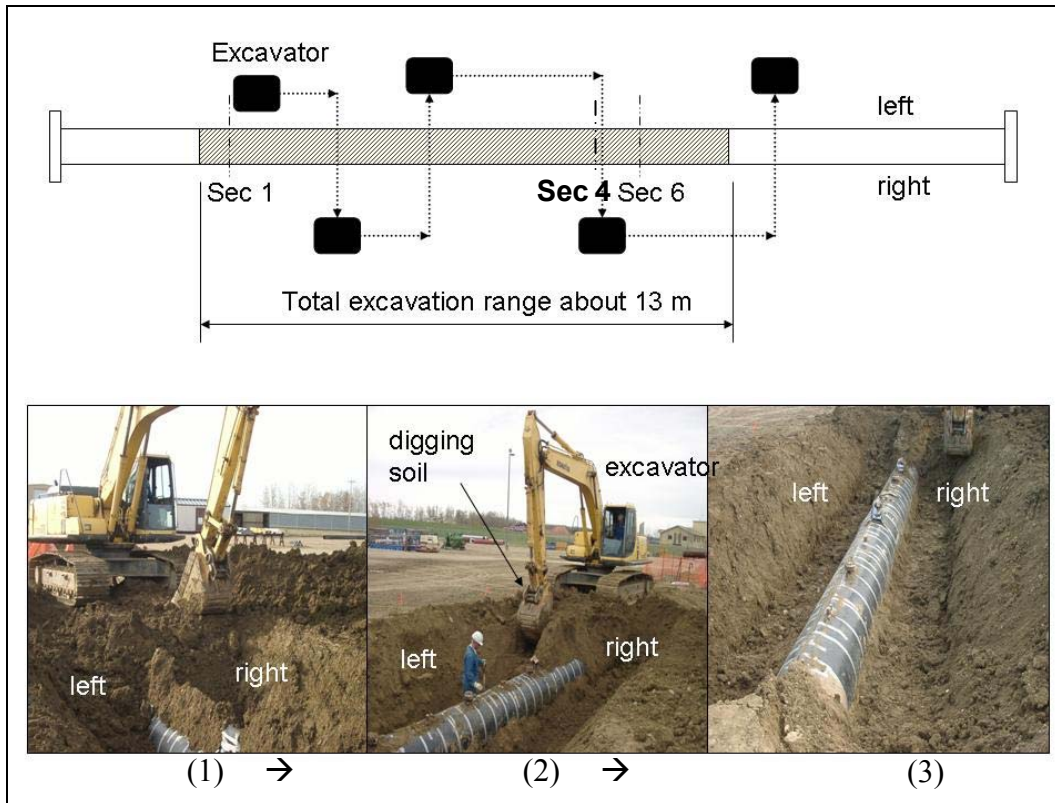
Figure 4.28 Excavation Procedure in the Field Line-Pipe Experiment
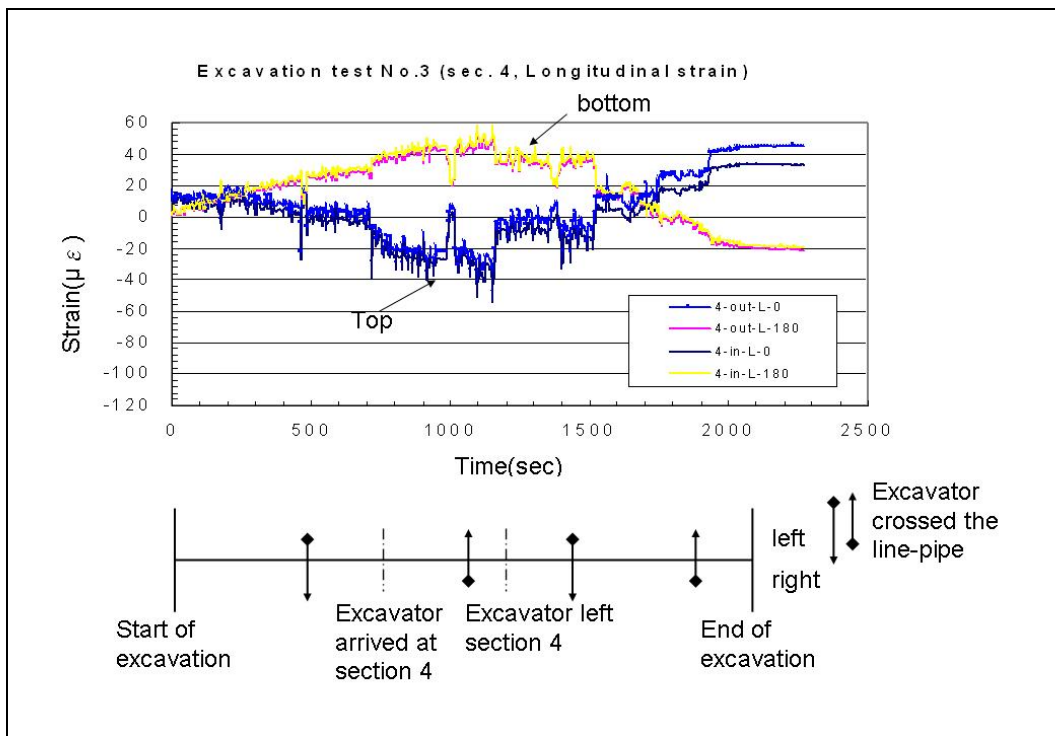
Figure 4.29 Strain-Time History Graph for the Field Line-Pipe
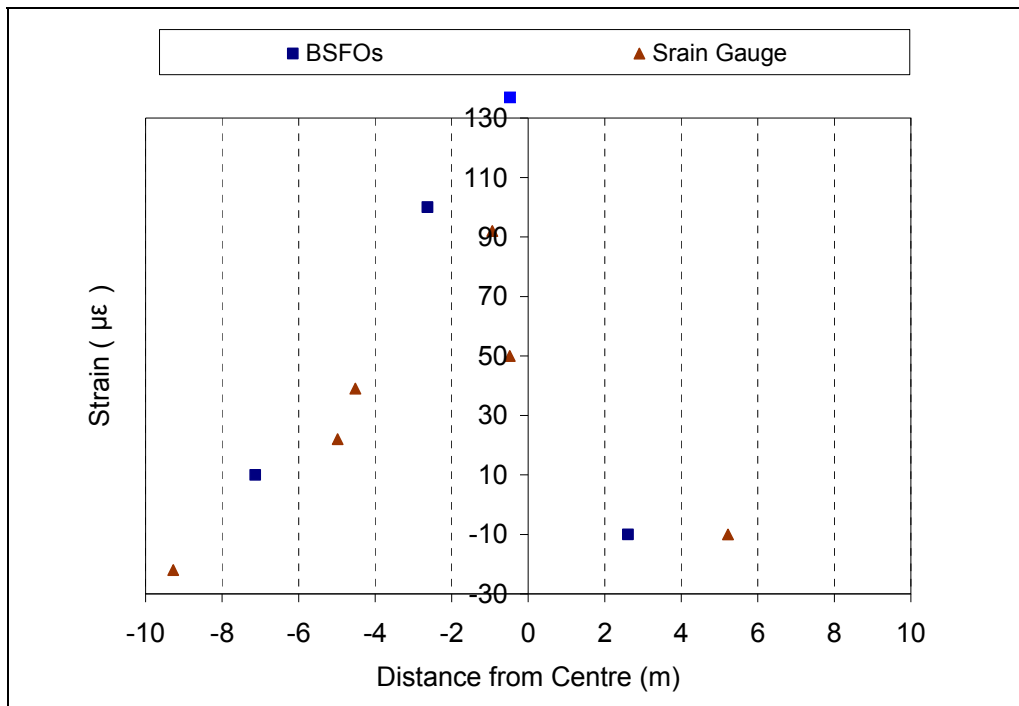
Figure 4.30 Longitudinal Strains on the Top of the Field Line-Pipe
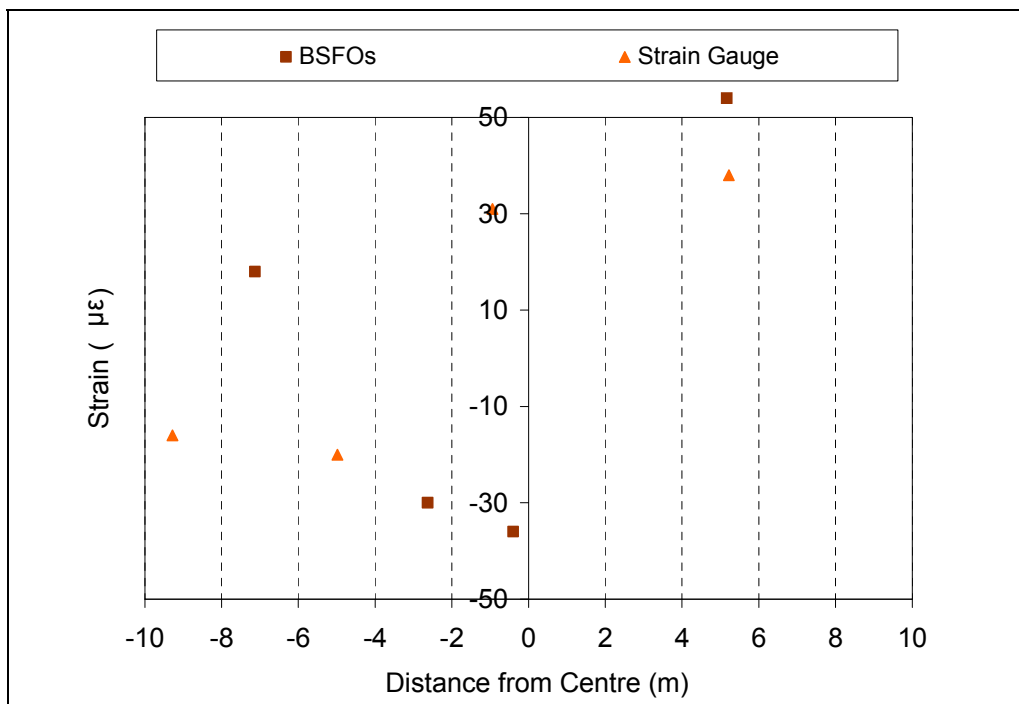
Figure 4.31 Longitudinal Strains on the Bottom of the Field Line-Pipe

103
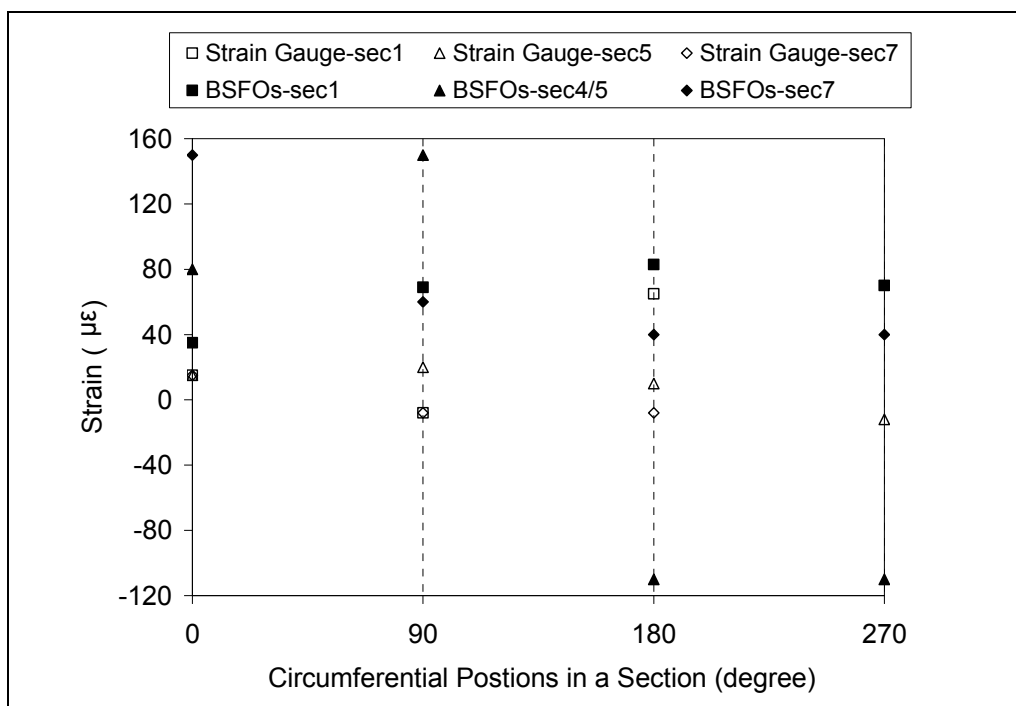
Figure 4.32 Hoop Strains on the Field Line-Pipe

104

5. BEHAVIOURAL PATTERNS (SIGNATURES) AND PREDICTION OF PIPE WRINKLING

5.1 Development of the Finite Element Models

Finite element (FE) simulation of line-pipe behaviour under combined loading has been well developed for several years at the University of Alberta (Zhou et al. 1993, Mohareb 1995, Dorey 2001, and Sen 2006). Nevertheless, previous FE models have not yet been validated by using the distributed strains along line-pipes. Therefore, the ability of FE models to simulate the distributed strains needs to be studied. In this project, the FE models were modified based on the concept of the previous numerical models (Dorey 2001 and Sen 2006), and validated by the test results obtained from the experiments on high-strength pipe buckling, as discussed in sections 3.2.4 and 4.1.

5.1.1 Purpose of the Finite Element Models

The developed models were expected to simulate the patterns (or signatures) of the strain distributions of pipe buckling under combined loading and to find the relationship among the strains at different locations.

Even though the distributed strains and curvatures of line-pipes under different loading have been widely studied, unfortunately, most of the previous studies do not provide enough information to allow this project to reliably identify the strain distribution patterns of pipe buckling and the behavioural signatures of these patterns. Instead of conducting more full-scale tests, developing reliable FE models to achieve the above purpose is more cost effective.

In addition, the models were used to generate a large amount of data pool of distributed strain patterns that will be employed to develop damage detection models in Chapter 7.

5.1.2 Finite Element Analysis (FEA)

5.1.2.1 Finite Element Models

The numerical models were developed by using ABAQUS/Standard Version 6.3 (Hibbitt, Karlsson, Sorenson Inc. 2002). ABAQUS/Standard is suitable for simulating large non-linear deformation and is able to apply varying loadings to a structure through multi-step loading procedures. After the results from the full model and the symmetric half model were compared, the results from the both models were found to be the same for the simulated conditions, where both loading and pipe section, as well as artificial imperfection, were symmetrical about the length of the pipe. Therefore, a symmetric half pipe model with a plane of symmetry along the length of the specimen was chosen to simulate the pipe tests. The main features of the FE models are explained in this section.

Elements

The pipe model used 4 node shell elements, S4R, with reduced integration. The S4R element is able to handle large strain problem and curved cross section, and has been used extensively by other pipeline researchers (Dorey 2001 and Sen 2006). There are two triangular elements, STRI3 and STRI65, available in ABAQUS/Standard. For STRI3 type, the Discrete Kirchhoff (DK) constraint is imposed analytically and involves no transverse shear strain energy calculation; while STRI65 is constrained numerically, and the transverse shear stiffness acts as a penalty enforcing the constraint. That is, STRI65 element is normally applied when the plate thickness approaches to very thin. In addition to no transverse shear, STRI3 element allows for relatively large rotations, but only small strains. Based on the above comparison, the 3-node triangular shell element, STRI3, was selected for simulating the 76 mm end plates, which were at the ends of the test pipe and remained elastic throughout the test.

A rigid beam element was used to connect the center of the pipe at the ends of the model to the pivot point (see Figure 4.16 (b)), on which loading was applied. This

element does not deform, therefore, the compressive load applied to the pipe is exactly equal to the compressive load applied to the pivot point. The pivot points at both ends of the pipe are free to rotate in all directions but prevented from lateral displacement; the pivot point at the bottom end allows free to displace in the longitudinal direction.

Element sizes

For element sizes used in the pipe models, Dorey (2001) studied six different sizes from 100 mm x 100 mm to 30 mm x 30 mm, and found 36 mm x 60 mm was the most effective one. Sen (2006) used finer sizes from 25 mm x 30 mm to 30 mm x 30 mm to exclude possible effect of mesh size on finite element results. Because the finite element (FE) models were used to simulate distributed strains along the pipes, the effect of mesh sizes on finite element results should be as low as possibly. The element sizes used in this project were from 25 mm x 30 mm to 30 mm x 30 mm, as shown in Figure 5.1(a). A finer mesh (one-third of the height of the pipe elements) was used around the girth weld of a girth welded pipe to capture the buckling mode triggered by the girth welds. In general, local buckling occurs near the girth weld location for the girth-welded pipes, but however in the high-strength pipe buckling tests, few girth-welded specimens failed away from the welds, such as Pipe#7. To compare FEA with test results in those cases, an additional finer mesh (half the height of the pipe elements) was used, as shown in Figure 5.1(b), to trigger a wrinkle at the correct location on the specific specimens.

Element thickness

In general, three element thicknesses were used for the finite element models. The thickness of the collar was modeled as twice the pipe thickness, and the thickness of the rest of the pipe was modeled as that measured from the test specimens. The thickness of the end plates in the models was 76 mm, the same as the thickness of the end plates used in the test set-up. For the test specimens manufactured from two segments of pipes by a girth weld, an extra 20% in wall thickness was considered at the girth-weld location.

Material models

An elastic–plastic material model was used for the pipe and collars in the finite element analysis. The material model employed in the FE models was the true stress – true strain curve derived from the engineering stress – engineering strain curve of the coupon tests of the longitudinal strips. A total of four longitudinal coupons were cut from both ends of the pipe specimens. The isotropic hardening model was used in the FE analysis since monotonic loading was applied in the tests.

Loading

A simplified loading procedure was used in this project. For the pressurized pipes, two loading steps were used. The first step was to apply uniform internal pressure around the circumference of the pipe to the level recorded during testing, and the Newton's approach was used for the loading-displacement analysis. The second step was to apply monotonic moments to the top and bottom pivot points. The Newton's approach cannot yield a converge solution when the loading-displacement curve after the peak moment is very flat or even in a negative slope. Therefore, the arc-length method, the Riks' method, was applied in the second loading step. In this method, an additional parameter, called arc length, is introduced into the static equilibrium, and, consequently, the approach can provide solutions regardless of whether the response is stable or unstable (ABAQUS theory manual 2003).

In the series of high-strength pipe buckling tests, the pipe specimens included both plain pipes and girth-welded pipes, and were either with or without internal pressure (see Table 5.1). Different imperfection patterns used in pipe models are explained in the following section.

5.1.2.2 Initial Imperfection Patterns

Plain pipes

Three most commonly used initial imperfection patterns in modeling the line pipes are ring pattern, blister pattern and thickness reduction. Dorey (2001) compared the ring pattern and blister pattern initial imperfections for their effect on the global behaviour and peak moment of line-pipes under combined loading. The blister pattern was found to be a better initial imperfection pattern than the ring pattern because of the random nature of an initial imperfection. Suzuki et al. (2006) used the reduction of the wall thickness of a pipe to model the initial imperfection in the FE models, and found that this method could reasonably predict the global behaviour, peak moment, and critical strain of the line-pipes.

To determine which initial imperfection patterns are most suitable for the distributed strain simulation, the blister patterns and the wall-thickness reduced patterns were compared by using two pipe examples, a pressurized pipe and a non-pressurized (NP) pipe. For a plain pipe, the assumed initial imperfection pattern was modeled by creating a smooth blister around one-fourth of the circumference, from the compression face to the neutral axis, and longitudinally over one-diameter of a pipe range (1.0D imperfection) centred at the wrinkle location (see Figure 5.2). The amplitude of the blister imperfection was chosen in accordance with experimental measurements, from 5% to 20% of the pipe wall thickness, in previous pipe experiments (Dorey 2001). The blister shape was simulated by a cosine function with the interval [-Π, Π] along the one-diameter range (see Figure 5.2), and by the other cosine function with the interval [0, 0.5Π] around the one-fourth of the circumference of the pipe section (see Figure 5.2). Two different values of the wall thickness reduction (1% and 5%) were used in wall thickness reduction pattern in the comparison with the results from the blister patterns.

No significant difference was found in the global behaviour, peak moment, and critical strain of the line-pipes before and during pipe buckling, as shown in

Figure 5.3 and Figure 5.4. However, the post-buckling behaviour of the pipe using the wall-reduced initial imperfection pattern exhibited faster deterioration in load carrying capacity. By studying the distributed stains, which is essential for SHM model development, from each model, as shown in Figures 5.5 and 5.6, reveals the differences between the blister and wall-reduced patterns. For the pressurized pipe, as shown in Figure 5.5, while the blister imperfection caused vivid fluctuation around the wrinkle location, the wall-reduced imperfection formed only an overstated strain concentration at the wrinkle location. Figure 5.6 shows the same results for the NP pipe. The local strain concentration for the wall-reduced imperfection pipe probably resulted from the abrupt change of the pipe wall thickness rather than from the localization of deformation during pipe wrinkling. Therefore, the blister imperfection pattern will be used in one-diameter range for simulating the strain distribution of plain pipe buckling; and 20% of wall thickness is used for the peak amplitude of the blister imperfection.

Girth welded pipes

For a girth welded pipe, the initial imperfection pattern is created by the different roundness at the joint between the two segments, and the offset imperfection is around the pipe circumferentially. Consequently, girth-welded pipe wrinkling is triggered by this imperfection.

In this project, a FE model with an offset imperfection pattern was used to simulate a girth-welded pipe (GW pipe) and 18% of the wall thickness was adopted for the peak amplitude of the imperfection. This amplitude was chosen based on the maximum experimental initial imperfection, 2.24 mm, recorded in different test series conducted in the University of Alberta, and the maximum allowable value of 1.6 mm specified in CAN/CSA Z662-03. In addition, the extra 20% of the wall thickness was used at the middle of the three-ring weld elements, which had one-third of the height of element size, i.e. the weld size was about 8.5 mm.

5.1.3 Comparison of Experimental and FEA Results

The ten pipe specimens shown in Table 5.1 were selected from the experiments on high-strength pipe buckling conducted in C-FER testing facility by TCPL for this study. The ten test specimens have different loading conditions and material properties. Therefore, the developed FE models can be validated for various pipe conditions, and the strain distributions of the ten pipe specimens measured from the tests and obtained from the finite element models can be used to find the signature patterns of the pipe wrinkling. The overall pipe behavioural characteristics such as the deformed shape, the global moment - curvature curve, the global moment – averaged strain curve, and the local distributed stain behaviour along a line-pipe are compared and discussed based on the test and FEA results. The comparisons of the deformed shapes generated from the experiment and FE models are interpreted by four pipes, Pipe#1, #3, #6, and #12, as shown in Figures 5.7 (a) to 5.7(d) and Figures 5.8(a) to 5.8(d).

Figures 5.7(a) to 5.7(d) present the comparisons of the deformed shapes of the non-pressurized (NP) plain pipe, Pipe#1, and the NP girth welded (GW) pipes, Pipe#3. For the GW pipe, Pipe#3, as shown in Figures 5.7(a) and 5.7(b), the girth-weld area forms a relatively rigid ring that restrains the development of a diamond wrinkle shape in this region, and the outward wrinkle is intercepted in the girth-weld location. The FE model is in good agreement with the test results. On the other hand, for the Pipe#1, a more apparent diamond shape and more symmetric outward bulges, a V-form shape, occur around the wrinkle location. The FE model also agrees with the test results, as shown in Figures 5.7(c) and 5.7(d).

Figures 5.8(a) to 5.8(d) present the comparison of the pressurized pipes without girth weld, Pipe#6, and with girth weld, Pipe#12. In the pressurized pipes, the deformed shapes differ greatly in the girth-welded pipe and the plain pipe, and the wrinkle is intercepted in the girth welded location for the Pipe#12. The FE models' results agree with the test results for both pipes.

5.1.3.1 Global Moment vs. Curvature Curves

For the selected ten pipes, the results from the FE models agree with the test results for the global moment and overall curvature curves. Five of the pipes, Pipe#1, #3, #6, #8, and #12, are presented here.

The overall curvature, κ_o, of the pipes was calculated using the top and bottom rotations, θ_t and θ_b respectively, measured in two-diameter, 2D, range of a pipe. The computing formula is as follows:

$$\kappa_o = (|\theta_b| + |\theta_t|) / 2D \tag{5.1}$$

For Pipe#1, the non-pressurized line-pipe with X80h high strength steel material, the model and test results closely agree in the elastic region, and are similar in the inelastic range. The critical overall curvature for the model is 0.009 rad/m compared with 0.008 rad/m for the test. The peak moment for the model is 4162 kN-m compared with 4034 kN-m for the test. The finding results in a percent error of 12.5 % and 3.2%, respectively. The moment-curvature curve is shown in Figure 5.9.

For Pipe#3, the non-pressurized girth-welded line-pipe with X100h high strength steel material, the model and test results are in very good agreement in both the elastic region and inelastic range. The critical overall curvature for the model is 0.018 rad/m compared with 0.020 rad/m for the test. The peak moment for the model is 4780 kN-m compared with 4725 kN-m for the test. The finding results in a percent error of 10.0% and 1.1%, respectively. The moment-curvature curve is shown in Figure 5.10.

For Pipe#6, the pressurized line-pipe with X80h high strength steel material, the model and test results are very similar in both the elastic region and inelastic range. The critical overall curvature for the model is 0.015 rad/m compared with 0.014 rad/m for the test. The peak moment for the model is 2520 kN-m compared

with 2660 kN-m for the test. The finding results in a percent error of 7.1% and the 5.5%, respectively. The moment-curvature curve is shown in Figure 5.11.

For Pipe#8, the pressurized line-pipe with X80 high strength steel material, the model and test results are closely agree in both the elastic region and inelastic range. The critical overall curvature for the model is 0.017 rad/m compared with 0.020 rad/m for the test. The peak moment for the model is 3524 kN-m compared with 3461 kN-m for the test. This finding results in a percent error of 17.6% and 1.8%, respectively. The moment-curvature curve is shown in Figure 5.12.

For Pipe#12, the pressurized girth-weld line-pipe with X100h high strength steel material, the model and test results are in excellent agreement in both the elastic region and inelastic range. The critical overall curvature is 0.009 rad/m for both the model and the test. The peak moment for the model is 3474 kN-m compared with 3376 kN-m for the test, which results in a percent error of 2.9%. The moment-curvature curve is shown in Figure 5.13.

5.1.3.2 Global Moment vs. Compressive Strain Curves

For the selected ten pipes, there is good agreement between the results from the finite element models and the test results in the global moment and averaged compression strain curves. A summary of the comparison of the models and the test results is presented in Table 5.2 and Figures 5.14 to 5.21. The averaged compressive strain ε_c of the specimen shown here was computed according to equation 5.2 (Zimmerman et al. 2004):

$$\varepsilon_c = \varepsilon_t - \kappa \times D \qquad (5.2)$$

In this equation, ε_t was measured tensile strain on the tension side of the buckled region; the curvature κ was calculated according to equation 5.1 by using the gauge length of 2.0 diameters (2D) of the specimens, centered at the mid-height of specimens, as shown in Figure 4.1. Except for Pipes #7, #8, #9, and #11, the

curvature of the pipe was obtained by using a gauge length of 2.25D in order to include the buckled region. D is an outside diameter of a pipe section.

Except for Pipes #7 and #8, the tested pipes are new generation high-strength steel pipes. For a conventional high-strength steel pipe, Pipes #7 and #8, although the model and test results are in excellent agreement in both the elastic region and inelastic range, the model is slightly more rigid than the test specimen throughout the whole loading stage (see Figure 5.17). The average compressive strain from the model is 0.91% compared with 1.05 % from the test. This critical compressive strain from the model is smaller with a percent error of 13.3%. The peak moment for the model is 3524 kN-m compared with 3461 kN-m for the test, which yields a percent error of 1.8%. Similar results were obtained for Pipe#7, which is a conventional X80 steel pipe with a girth weld. The critical compressive strain measured from the model is 87% of the strain obtained from the test result. The peak moment is 4% higher for the model than for the test result.

Figures 5.14 to 5.21 reveal that the peak moment and initial stiffness have a good agreement between the FEA and test results, and that the worst ratio of the FEA prediction to the test result is close to 0.95 for the peak moment of Pipe#6. For the peak moment, the averaged error is around a percent error of 2.0% with a very low standard deviation, i.e., 0.029, as shown in Table 5.2. Most of the critical compressive strains calculated by FEA are larger than those obtained from the tests. For the critical compressive strains, the averaged ratio of the prediction to the test is around 1.05 with an acceptable standard deviation of 0.178. The largest errors of over 20% occur in Pipe#1 and Pipe#11.

The main reason for a larger discrepancy in the critical compressive strength between the model and test results is probably due to the material model used in the FE model. As mentioned in section 3.2.4, the new generation high-strength steel pipes have much different yielding strengths in the longitudinal and transverse directions. For an example, for the X100h high strength steel, the yielding stress in the longitudinal direction is around 90% of the specific

114

minimum yielding stress (SMYS), the yielding stress in the transverse direction is about 1.1 times the SMYS, while the ultimate tensile stresses in both directions are almost same, about 1.2 times the SMYS. Thus, the high strength steel material is not really isotropic in the inelastic range. However, the FE model used the isotropic material model in the simulation of the pipe buckling. The anisotropic material behaviour of the high strength steel probably increases the strength of the pipe buckling and decreases the critical compressive stain in the longitudinal direction due to the Poisson's effect. As a result, the model predicted a larger critical compressive strain in the inelastic range.

5.1.3.3 Distributed Strain Plots

The main purpose for monitoring pipelines is to prevent pipeline failure due to wrinkling during pipeline operation. The behavioural signature of a pipe can effectively provide a warning signal before this kind of anomaly occurs. To achieve this purpose, the model needs to be calibrated with the experimental results at various loading stages with sufficient agreement. The developed FE models are examined by comparing the compressive strains at the locations near the wrinkle locations, and also by comparing distributed strains along a line-pipe between the models and the tests. The compared results are summarized in Table 5.3 and shown in Figures 5.22 to 5.34.

The strain distribution results from the experiments and the FEA show that the anomaly of a pipe normally occurs around 70% to 90% of the peak moment, before wrinkling being initiated. In this period, a meaningful sign of the pipe wrinkling can be found from the compression-side strain distribution. Therefore, in Table 5.3, this loading range is selected from 70% to 90% of the peak moment (PM). In the loading range from 70% to 80% of the peak moment, the average strain ratio of model's prediction to the test is 1.05 with a standard deviation of 0.117. Consistent results are also shown for the loading range from 85% to 90% of the peak moment. The slightly higher standard deviation in this range resulted mainly from the worse than average prediction of Pipe#14, where the strain gauge

115

readings are more deviant. The deviation can be confirmed by comparing them with the BSFOS results in Figures 4.7 and 4.8, and with FEA in Figure 5.30. If the results from Pipe#14 are excluded, the standard deviation of the prediction to the test decreases to less than 0.091.

Table 5.3 reveals a good correlation between the behaviour of the model and the test in the specific loading stages where the wrinkle is initiated. The strain distributions obtained from the FE model are further compared with discrete strain gauge readings. Two sets of the complete distributed strains on the compression side were obtained from the strain gauge readings and the BSFOS system for Pipe#9 and Pipe#14, respectively; and they will be used to investigate the reliability of the strain distribution patterns generated from the FE models.

Distributed strains on the compression side

The developed FE models generated the compression-side strain distributions for the pipes with various loading conditions. For the distributed strains of the NP pipes, a diamond shape wrinkle resulted in continuous short-wave strain distribution forming over the wrinkle location, as shown in Figures 5.22 and 5.29. A very similar trend occurred in the distributed strain for the models and the test results. The strain distributions along the pressurized pipes are presented in Figures 5.24, 5.25, 5.26, 5.27, and 5.30. For the pressurized pipes, a single outward shape wrinkle caused strain localization and concentration at the wrinkle location. The similar trends for the distributed strains can be found from the models and the test results. Moreover, the strain distributions of the pressurized pipes provide two important findings.

First, better simulation of the distributed strain was found for the pipes whose wrinkle occurred in the middle of the segments than the ones whose wrinkle occurred closed to the end of the pipes. For the pipes failed at the end, there was more fluctuation along the strain distribution from the test results than from the models, as the results for Pipe#9 revealed in Figure 5.26. This difference between the models and the test results can be attributed to the initial imperfection. While

116

various initial imperfections are present over the line-pipe, the FE model uses only the potentially dominant one to trigger pipe wrinkling, and, consequently, a relatively flat distribution is assumed in the outside of wrinkle area. In addition, secondary moment gradient and internal pressure fluctuation along the pipe probably result in strain fluctuation in some local areas. This effect is more apparent on the group of the pipes where wrinkling occurred at the end of the line-pipe due to the effects of the end plates.

Second, the other finding is obtained by comparing the strain distributions between Pipe#8 and Pipe#9. These two pipes have almost the same geometric and loading conditions except for their materials. As discussed previously, for the stress-strain curve of the X80, unrestricted plastic deformation occurred almost immediately after the attainment of material yielding stress (a very flat yield plateau as shown in Figure 3.36), while new generation X80h has a lower yielding stress and a much lower yielding ratio. Consequently, when the load approached to 92% of the peak moment, a slightly higher strain concentrated at the wrinkle location was observed for Pipe#9 than Pipe#8. However, a similar strain concentration was observed at the wrinkle location when the load approached the peak moment. This observation indicates that the material should not significantly affect the strain distribution patterns.

For Pipe#14, the strain distributions are compared for the model, the strain gauge readings, and the BSFOS results. The results of the model and BSFOSs show very good agreement in both the magnitude and strain distributions around the wrinkling location, and the distributed strain developments in both the BOSFS and FEA have a similar trend as well. Only three discrete measurements from the strain gauges were collected (see Figure 5.30). Figures 4.7 and 4.8 and Figure 5.30 show that not all strain gauge results are in agreement with the results from the BSFOSs and FEA. However, all the results are in the same order of magnitude.

For the girth-welded pipes, the strain distribution patterns were generated for the non-pressurized Pipe#3 and the pressurized Pipe#12 by the FE models. The

distributed strains are shown in Figures 5.23 and 5.28, respectively, which reveal an excellent correlation between the behaviour of the model and test. For Pipe#3, during the initiation of the pipe wrinkling, the strain distribution presents a single outward pattern wrinkle rather than a diamond pattern wrinkle. The lagging of the inward deformation was resulted from the additional rigid zone created by the girth weld at the wrinkle location. The girth weld not only intercepts the development of the outward bulge, but also restricts the inward wrinkle from forming. Pipe#12 presents a typical strain distribution for a girth-welded pressurized pipe during the pipe wrinkling, and the strain distribution is consistent with those observed in previous strain data collected from pigs, as shown in Figure 3.7 for the NP30. Figures 5.7(a), 5.8(c), 5.23, and 5.28 reveal that as pipe wrinkling was initiated, the dominant concentrated strain was triggered and intercepted by the girth weld.

Distributed strain on the tension side

The tension-side distributed strains were investigated for Pipes #3, #12, #13, and #14. Figures 5.31 to 5.34 show that a better simulation occurred for the NP pipes, such as Pipe#3 and Pipe#13, than for the pressurized pipes. For the pressurized pipes, Pipe#12 and Pipe#14, relatively flat strain distribution patterns were generated by the FE models. Secondary moment gradient and internal pressure disturbance might have influenced the deviation in the results from the models. In addition, The models yielded an exaggerated strain concentration at the girth weld location in Pipe#12. This phenomenon was not resulted from the pipe's behaviour, but from the numerical computing problem due to a sudden discontinuity at the girth weld location.

The comparison of strain distribution patterns

As mentioned, a cross-correlation concept was used in pattern matching for two-dimensional images, and, based on the same concept, the correlation coefficient can be used to examine pattern matching for a pair of strain distributions in a two-dimensional coordinate where a set of distributed strains was obtained from the test results and another set was obtained from the FEA. The correlation, often

118

measured as a correlation coefficient, indicates the strength and direction of a linear relationship between two random variables. The correlation reflects the noisiness and direction of a linear relationship, but not the slope of that relationship; thus, the identification of correlation in two distribution sets is made in accordance with the similarity of the distribution patterns rather than the difference in the strain magnitudes over the strain distributions. The correlation coefficient is calculated by using the following equation:

$$C(x, y) = \frac{\sum (x - x_m)(y - y_m)}{\sqrt{\sum (x - x_m)^2 \sum (y - y_m)^2}} \tag{5.3}$$

where x_m and y_m are mean strains respect to the two compared strain distributions; x and y are a pair of strains respectively on these two distributions at the same location. If the two distributions are proportional linear relation, the correlation coefficient $C(x, y)$ is 1. Table 5.4 presents the comparison of the compression-side distributed strains.

The correlation of distributed strains of Pipe#9 between the model and the test result is very low, while Pipe#14 has very good correlation with the BSFOS result. Figures 5.26 and 5.30 show that the wrinkle locations of the two specimens are very different. The wrinkle location is at the very end for Pipe#9, but is close to the middle of Pipe#14. As mentioned, relatively flat strain distribution occurred over the outside of the wrinkle location in the simulation of the Pipe#9. . However, Table 5.4 reveals that the distributed strains over the wrinkle locations have near 90% of correlation between the models and the test results for both Pipe#9 and Pipe#14. In addition, the comparison of the tension-side distributed strains by using the correlation coefficient confirmed the results from the previous observation of the tension-side distributed strains on both the experimental specimens and the FE models. Table 5.4 shows a low correlation between the tension-side distributed strains for the FEA and the test results because developing lag of the strain distribution patterns on the tension side probably occurred in the FE models. Table 5.4 reveals that the tension-side strain

distributions at the latter loading stage, i.e. at 96% of the peak moment in post-buckling rang simulated by the FE models (Pipe#13 and Pipe#14), have more than 80% of correlation with the test results measured during inception of pipe wrinkling, e.g. 84.9% of correlation at 86% of the peak moment for Pipe#14.

From the above comparison of the FE models and the test results, it can be concluded that the finite element models are capable of simulating the distributed strains during the initiation of wrinkling in a pipe, and for the distribution pattern, better simulation occurred on the compression-side strains than on the tension-side strains.

5.2 Signature Patterns of Pipe Wrinkling

5.2.1 Distributed Strain Patterns of Pipe Wrinkling

Since the loading on a buried pipeline can be very complex and unpredictable, monitoring a structural behaviour should be based on the qualitative behavioural signature change rather than the magnitude of the pipe response. For example, unless the complete load history of a line pipe is known, the measured strains represent only the relative measurements rather than the true accumulated strains. Therefore, the strain distributions obtained from field measurements are not necessary to give the true accumulated strain distributions at the critical location. Consequently, the measured magnitude of the strains along the pipe does not sufficiently represent the current strain status of the buried pipeline and cannot be compared directly with the critical buckling strain of the pipe. On the other hand, the investigation of the strain distributions in Chapters 3 and 4 revealed that if the behavioural pattern (or signature) of a wrinkled pipe can be identified from the distributed strains along the line pipe, the pipe wrinkle can be detected by monitoring the changes in the distributed strains. The postulate above is further verified by using the example of Pipe#14 under a bending load.

Figure 5.35(a) shows the use of the FE model to simulate the distributed strains on the compression side (regarded as zero degree position) of the Pipe#14 at

different loading stages. Each load stage shown in Figure 5.35(a) represents a specific time of loading on the pipe. The figure clearly shows distinct strain distribution development for the pipe buckling.

Figure 5.35(a) also shows that the phenomenon of localized strain concentrated around the wrinkle location (at 170 cm in Figure 5.35(a)) gradually becomes apparent as the loading/deformation increases. As shown in Figure 5.35(a), the compression strains at 37% of the peak moment remain relatively constant along the compression side of the pipe; but when the moment reaches 74% of the peak moment, the strain distribution shows a wave-shaped distribution and dominating strain localization begins. This wave pattern in the strain distribution can be used as a warning sign for pipe wrinkling. With an increase in load, the dominating strain localization becomes more serious at 86% of the peak moment. The imperfection in the pipe triggers deformation localization and results in strain concentration and eventual wrinkling at the imperfection location. Even though the behavioural pattern (or signature) of a wrinkled pipe is identified from the compression strain distributed strains along the line pipe, relying on only the distributed strains along the compression face (the critical buckling position) may not be sufficient to predict the trend of the pipe wrinkling. The longitudinally distributed strains at other circumferential positions, as shown in Figure 5.35(b) (45° to critical buckling position) and Figure 5.35(c) (67.5° to critical buckling position), can be used to further validate the development of pipe wrinkling. As Figures 5.35(b) and (c) reveal, the distributed strains at these two positions present a similar behavioural pattern of pipe wrinkling at the zero degree position. However, the signature revealed by the distributed strains becomes more unclear as the measured position becomes farther away the critical buckling position.

Moreover, as pipe wrinkling occurs, the behavioural signature is also revealed in the distributed strains along the tension side (regarded as the 180 degree position) at different loading stages. As Figure 5.36 shows, the tension strains remained relatively constant until the peak moment. After the limit point, when the moment decreased to 96% of the peak moment, the strain distribution showed a convex

121

shape distribution, which resulted from the increased secondary moment on the centre of the line-pipe. The distribution strain pattern change occurred on the tension side can also be used as a sign of pipe wrinkling. However, the behavioural signature revealed by tension-side strains is present in the latter loading stage, around the limit point, but still before the visible wrinkle (illustrated in Appendix B) occurred. Thus, it can be used as a secondary signature, like a fuse, to increase the reliability of the monitoring system.

5.2.2 The Derivative Signatures from Distributed Strains:

The more behavioural signatures a system can monitor, the more reliable the system will be. Therefore, in addition to the above behavioural signatures, some signature indices derived from the distributed strains were investigated in the following subsections.

5.2.2.1 The Correlation Index of Tension-side Strain Distributions

As mentioned in the section 5.1.3.3, the correlation coefficient can be used in pattern identification, but because the correlation coefficients are very sensitive to bias data (Asuero et al. 2006), this coefficient should provide a more promising analysis for simple smooth distribution patterns, such as tension-side strain distributions, than for complicated distribution patterns, such as compression-side strain distributions. Therefore, the correlation coefficient, computed from the tension-side strain distributions during specific loading stages, probably can be a valuable index of the behavioural signature of a wrinkled pipe. The correlation coefficient was computed by comparing the strain distribution pattern with the reference pattern. Eleven pipes were investigated to evaluate the feasibility of this index. These pipes have different material properties, sectional properties, and loading conditions (see Table 5.5). The reference distribution patterns used the tension-side strain distributions during the loading range from 30% to 40% of the peak moment of the analyzed pipes. This loading range was used because the experimental and the FEA results showed that the tension-side strains remained

122

relatively uniform before the load reaches 40% of the peak moment. The analytical results for the correlation index of tension-side strain distributions are presented in Figure 5.37 and Table 5.5.

In Figure 5.37, the loading ranges of the pipes are from 45% of the peak moment before pipe buckling to 95% of the peak moment after pipe buckling. The distributed strains in Figure 5.37 were obtained from the test results, and the strains, measured by seven strain gauges, were uniformly distributed along the 2500 mm range for Pipe#12 to Pipe#20, while 15 measurements were evenly distributed along the 6000 mm range for TCPL1 to TCPL3. Every scan run shown on the X-axis represents a specific time of loading on the pipe. As Figure 5.37 shows, a few inflection points, or slope change points, occurred in each correlation coefficient curve, but only one of them is relatively apparent. Recalling the calculation of the correlation coefficient of the strain distribution and the reference pattern, a relatively uniform distribution, as a strain distribution becomes apparently non-uniform, the correlation coefficient deviates away from 1. When localized strains present on the strain distribution, the correlation coefficient rapidly drops down and a dominant inflection point occurs on the correlation coefficient curve. Taking TCPL1 pipe as an example, though the correlation coefficient curve deviated from 1 at the 7th scan run in Figure 5.37, the dominate inflection point presented at the 8th scan run. According to the discussion above, the dominant inflection point could be regarded as a signature index to detect pipe wrinkling.

The loading stages corresponding to the dominant inflection points are summarized in Table 5.5. It reveals that the occurrence of the signature index cannot be defined by a consistent loading stage, and cannot also be used in an earlier loading stage. However, this signature index can provide a warning of pip winkle in time before an evidently visible wrinkle appears in the pipe segment. Moreover, it is independent of the behavioural signature revealed on the compression side, but is relevant to the pipe wrinkling behaviour.

123

5.2.2.2 The Strain Ratio Index on the Compression Side

As buckling is initiated, a pipe undergoes a rather abrupt increase in lateral deflection under small loading increments; and the pipe stiffness significantly decreases (or pipe softens). Previous researchers (Yoosef-Ghodsi 1994, Dorey 2001, Sen 2006) determined the initiation of pipe wrinkling by searching for the softening points through the global curvature versus the local curvature plots, or the global curvature versus the local strain plots for a whole loading history. This concept of finding the incipient wrinkling of the line-pipe could be applied to the monitoring of the development of the pipe wrinkle in the field. Since the strains from field measurements may be not the true accumulated strains at the critical location, the softening point was determined in this project by monitoring a dimensionless strain-ratios curve for the loading history. The strain ratio is the ratio of the local maximum strain to the average strain of the distributed strains along the pipe segment at a specific loading stage. As a slope significantly changes at a point along the strain-ratio curve, this point is considered the softening point. Nine pipes were investigated to understand the feasibility of the strain ratio index, and their properties and conditions were shown in Table 5.1.

In Figure 5.38, the loading range of the pipes is from 45% of the peak moment before the pipe buckling to 95% of the peak moment after the pipe buckling, and the compression-side strain distributions are obtained from the FEA. Figure 5.38 shows that approximately bi-linear curves occurred during specific loading stages. The apparent slope changed at the intersection of the two linear segments for each curve is considered the softening point. The loading stages corresponding to the slope change points (or the softening points) are summarized in Table 5.6. The table shows that the softening points occurred in the loading stages from 85% to 99% of the peak moment of the different pipes analyzed. The loading range is well defined although this range is close the attainment of the peak moment. In some loading conditions, the pipes are essentially under axially compressive loads, as discussed in section 3.2.3. In these cases, the behavioural signature of the pipe

wrinkling cannot be found through the tension-side strain distributions, the strain ratio index will become very important.

5.2.2.3 The Normalization of the Compression-side Strain Distributions

Though both the experimental and analytical results showed that monitoring strain distribution patterns on the compression side can provide a warning of a pipe anomaly during an early loading stage, e.g. at 74% of the peak moment for Pipe#14. This warning will allow prompt actions against the initiation of pipe wrinkling. However, if the detection of the anomaly can be make even earlier, e.g. at 50% of the peak moment, it will provide more robustness to the system. A statistical method is presented here to achieve this purpose and used to transform the measured compressive strains into a dimensionless index, X_n:

$$X_n = \frac{(x - x_m)}{\sigma} \tag{5.4}$$

This transformation is a standardization procedure, called normalization, in which x is a strain on a strain distribution, x_m is an average of the distributed strains, and σ is standard deviation for the distributed strains. Thereby, any distribution is transformed into a standard distribution with the mean = 0 and variance = 1. Through this transformation, the standard distribution is independent of the strain magnitude, and depends only on the distribution pattern. Furthermore, as a strain localized at the wrinkle location, the strain differences over wrinkle range are exaggerated during the very early loading stage, e.g. 50% of the peak moment; while the amplitude of a dominant strain is restrained at the maximum loading range, e.g. 100% of the peak moment.

Figures 5.39 and 5.40 show the distribution normalization for Pipe#1 and Pipe#6, respectively. As shown in Figure 5.22, the distributed strains of Pipe#1 remained relatively constant and presented a relatively flat linear distribution before 73% of the peak moment. After normalization, the locally dominating amplitude occurs during 43% of the peak moment. On the other hand, the amplitude of the

distributed strains at the peak moment, shown in Figure 5.22, is condensed into a specific range, as shown in Figure 5.39. Comparing Figure 5.24 and Figure 5.40, a similar result as Pipe#1 can be found for the pressurized pipe, Pipe#6. After normalization, the locally dominating amplitude occurs at wrinkle location around 48% of the peak moment for Pipe#6.

Another example, shown in Figure 5.41, explains that different distribution patterns resulting from different damage events can retain their own characteristics after normalization. In Figure 5.41(a), the strain distribution patterns during wrinkle damage and dent damage were collected respectively from the experimental data for Pipe#14 and the field data for NPS 36. Large global bending strains were simulated by a sinusoidal function and the relative strains on the strain distribution designated as "37% to 75% PM" are obtained from strain difference between two loading stages, 37% and 75% of the peak moment, for Pipe#14. Figure 5.41(b) reveals that different damage events can be distinguished by observing these standardized distribution patterns. Moreover, the dimensionless strain distribution can correctly locate wrinkling for a relative strain distribution pattern. In Figure 5.41(a), the signature of the relative strain distribution pattern is more unclear than that of the true accumulated strain distribution, designed as 75%PM, but after normalization the two distribution patterns are almost identical (see Figure 5.41(b)).

The application of normalization in monitoring pipe buckling will be studied in Chapter 7.

5.2.3 The Relation of Strains at Different Circumferential Positions

Practically, the distributed sensors can only be installed on a pipeline at a few specific positions. Hence, the maximum strains measured on these sensors may not be the true maximum strains on the monitored pipe. This concern can be illustrated in Figure 5.42. In Figure 5.42(a), sensors are installed along a line-pipe at 8 different circumferential positions, numbered from 1 to 8, but the maximum

strains are located between the 6th and 7th positions circumferentially. The relation of the longitudinal strains along the pipe at different circumferential positions must be studied to ensure that important behavioural signatures will not be missed due to the limitation of the measured positions. To study the effect of the sensor positions, the positions 22.5° and 45° circumferentially away from the maximum strain position (or the critical buckling position) were selected for studying the strain correlation in different circumferential positions. In addition, because wrinkle patterns are different for pressurized and non-pressurized pipes, the strain correlation in different circumferential positions was separately investigated for these two pipe groups and the results are shown in Table 5.7. In this table, a range of loading stages from 70% to 90% of the peak moment was selected, because both the experimental results and FEA showed that wrinkling signature revealed on the strain distributions usually after the loading stage approached 70% of the peak moment. Also, this project is concerned mainly with the patterns on the loading range prior to the limit point. By selecting a specific loading stage, the strain ratios between the selected position and the critical buckling position can be obtained. The relation of strains at different positions with the critical buckling position is shown in Table 5.7. In this table, the strain ratio represents the ratio of the maximum longitudinal strain at the 22.5°or 45° position to the true maximum strain, which occurred at the 0° position. The average strain ratios and the corresponding standard deviations are also presented in Table 5.7.

As can be seen in Table 5.7, the strain ratios are similar for different pipes that have different pipe geometries, material properties, and loading conditions. The strain ratios at a specific position relative to the critical buckling position remain relatively constant regardless of the loading stage. As expected, when the specific position closer to the critical buckling position, the strain ratios are approaching unity. The table also indicates that a better prediction will be obtained if the specific position is closer to the critical buckling position; i.e. the strain ratios at the 22.5° position yielded better agreement than those at the 45° position for all pipes at selected loading stages.

In Table 5.7, Pipe#12 presents much lower strain ratios at the selected loading stages and positions because the exaggeratedly concentrated strain was simulated by the FE model at the critical buckling position. Accordingly, the strain ratios of Pipe#12 should be excluded. In the way, Table 5.7 reveals the average of the strain ratios of the maximum longitudinal strains at the 22.5° position to the true maximum strains is 91.8% and 91.1% with respect to the pressurized pipes and the non-pressurized pipes. For a perfect circular section, as shown in Figure 5.43(a), if the critical longitudinal strain (ε_{cr}) occurs at the zero degree position, and the sectional plane remains plane, the ratios between the strains (ε_n) at different positions (n degree away from the zero degree position) and the critical strain can be calculated by using the following equation and represented by a strain diagram shown in Figure 5.43(b):

$$\varepsilon_n = (1 - \cos(n)) \, \varepsilon_{cr} \tag{5.5}$$

From equation 5.5, the ratio of $\varepsilon_{22.5}$ to ε_{cr} is 92.4%, and the ratio of ε_{45} to ε_{cr} is 70.7%. These numbers are similar to the above analytical results shown in Table 5.7, except for the strain ratios of the inward-wrinkle pipe on the 45° position. The average strain ratio for the inward-wrinkle case is 57.1%. In addition to resulting from the diamond-shaped wrinkle, the lower ratio occurs because of ovalization in the pipe section for the non-pressurized pipe. The ovalization effect is less evident for the pressurized pipes than for the non-pressurized pipes, as the internal pressure can counteract the transverse components in the pressurized pipes. The above hypothesis is consistent with the observations in previous researches (Mohareb 1995 and He 2007). However, when the pipe is in the pre-buckling loading stages, the curvatures induced from bending are so small that ovalization has limited effect on the relation of strains at different circumferential positions.

Based on the above investigation, a distributed strain sensors in the monitoring system can be installed along a line-pipe at 8 different positions with a 45° circumferentially interval spacing, as shown in Figure 5.42. The 45° interval

spacing represents the possible maximum deviated position to the critical buckling position of 22.5°. Therefore, along the designated measured positions, even if the monitoring system cannot exactly capture the strain distribution in the true maximum strain direction, more than 90% of the strain ratios to the true maximum strain distribution are sufficient to be used in predicting the pipeline wrinkling.

5.2.4 Effect of Sensor Spacing

The spacing of sensors and the operating of a monitoring system are usually in conflict. Decreasing the sensor spacing in strain measurement increases the measuring precision, but increases the operating time and cost. Therefore, the effect of spacing of sensors has to be discussed. Two examples, a non-pressurized pipe, Pipe#1, and a pressurized pipe, Pipe#6, are used to illustrate the effect of measuring frequency on data diagnosis. As shown in Figures 5.44 and 5.45, a decreasing resolution of the behavioural signature occurred as the measurement spacing increased. In addition, it is possible that the sensor spacing can be too large to detect pipe wrinkling before loading reaches the peak moment, e.g. the loading stages at 90% of the peak moment, as shown in Figure 5.44. However, as shown in Figures 5.46 and 5.47 for a monitoring system with larger measurement spacing, e.g. 250 mm, though the system probably cannot distinguish pipe wrinkle from other damage events, it can provide a warning for winkling before catastrophic wrinkling occurs by monitoring the global trend, fluctuant curve, and strain distributions.

5.3 The Prediction of Buried Pipe Wrinkling

5.3.1 Development of Structural Health Monitoring (SHM) System

As mentioned before, for the thousands of kilometer buried pipelines in remote Canadian North, it is very difficult to reliably and cost-effectively detect the damages. Therefore, the structural health monitoring (SHM) system has become a promising technology to solve the problem. The components of the health

monitoring system are proposed in this section and the studies of the system will covered in the following chapters.

5.3.1.1 The proposed scheme of the SHM system

An integrated SHM system for buried pipelines using distributed strain sensors contains a data acquisition system, a centralized control computer and server, database system (DBS), terminal computers, a diagnostic program (or a damage detection model), and communication equipment, as shown in Figure 5.48. The calibrated behavioural patterns (or signatures) of local buckling (wrinkling) of buried pipelines should be identified before they are employed by the damage detection model. These calibrated signatures can be found not only from the observations in the field and the laboratory experiment, but also from the Finite Element Analyses (FEA). FEA technology will be used to perform behavioural simulations and parametric studies of behavioural signatures for line-pipes under combined loading. The proposed SHM system is expected to allow engineers to reliably diagnose the pipe behaviour without interrupting the normal operation of buried pipelines, and actively monitor pipe wrinkling before reaching the critical condition, as shown in Figure 5.49. The methodology of the proposed SHM system and its framework will be explained in the following sections.

5.3.1.2 The features for the SHM system

In this project, the following components of the SHM system are studied and integrated.

5.3.1.2.1 <u>Monitored signatures used in the SHM system</u>

The investigation of strain and curvature distributions in Chapters 3 and 4 concluded that strain distribution patterns and their development can be used as reliable signatures for monitoring pipe buckling. Although the curvature distribution patterns and their development could be used in detecting pipe wrinkling, but the behavioural signature of the curvature distribution pattern

probably cannot locate a wrinkle during an early loading stage as effective as the strain distribution patterns. In addition, the curvature distribution patterns currently obtained from Geopigs provide only a snap shot of the current status of the pipe, but cannot provide real time, continuous, on-demand information. Therefore, the strain distribution patterns will be used as the main health diagnosis tool for pipe buckling in this study. Due to the nature of pipe buckling, compression-side strains always provide a better signs of pipe wrinkling and wrinkling location during an earlier loading stage than the strains at the other positions. Therefore, the distributed strain patterns on the compression side become the main criterion for detecting pipe wrinkling, and their derived signature index such as strain ratio index can be another criterion to further detect the pipe wrinkle growth. In addition, as a line-pipe approaches its limit point, i.e., its peak moment, the progress of the tension strains speeds up over the wrinkle location. This sign can be used as an additional criterion for the health monitoring of pipe buckling. Also, tension-side strain is independent of compression-side strain, and, hence, the behaviour signature revealed on the tension side can increase system reliability in detecting pipe wrinkling.

However, because a large amount of distributed curvature data has been created by Geopigs in the pipeline industry, the developed SHM system should be capable of identifying the behavioural signature revealed by the curvature distribution patterns during pipe buckling. In this project, because of limited accessibility of Geopigs' curvature data, the applicability of the developed SHM system to the curvature distribution patterns will not discussed. However, the framework of the decision-making system developed here for predicting pipe wrinkling should be compatible with the existing curvature data obtained from field pipelines.

5.3.1.2.2 <u>Monitoring technologies used in the SHM system</u>

Since the BSFOS system was validated in Chapter 4, the framework of the monitoring system is established based on the BSFOS system. However, the

131

framework is expected to fit with other distributed sensing systems, such as varied pig tools, through a minor modification. The BSFOS system has some unique features for pipeline monitoring, such as distributed measurements along optical fibers and average measurements in a specific resolution.

5.3.1.2.3 Data simulating technology used in the SHM system

Previous experiments and field work have shown that measuring or collecting the distributed strain and curvature data is difficult. Also, to build and to validate the health monitoring system, a large amount of data is needed. Therefore, Finite Element Analysis (FEA) is used to solve the problem of the lack of distributed strain data. The FE models have been verified in the previous sections, and they can appropriately simulate distributed strains along the monitored pipeline. A strain data base will be created by the developed FE models and used in Chapters 6 and 7.

5.3.1.2.4 Decision model used in the SHM system

An indiscriminating health diagnostic program is needed to provide an early warning of the wrinkling damage in pipelines. The framework of the diagnostic program (or a damage detection model) will be built by using trained Artificial Neural Networks (ANN) with the data base analyzed through a parametric study. The ANN system is validated by the data simulated with FE models and by real measuring data. The parametric study and the establishment of the ANN system are discussed in Chapters 6 and Chapter 7, respectively.

5.3.2 Methodology of Predicting Pipe Wrinkling

The behavioural signatures and signature indices of the pipe wrinkling were investigated in the previous sections, and some practical issues relating to the installation of the distributed sensors were studied as well. The procedure for predicting pipe wrinkling by using the proposed SHM system can be summarized as follows. The operating procedure of the developed damage detection model of

the SHM system will be explained in Chapter 7.

1. Install distributed strain sensors along a buried pipeline at multiple positions, e.g., at eight different positions around the circumference of the pipe, as shown in Figure 5.42. A 45° interval between the positions should be used.

2. Before the pipeline operation, record the initial distributed strains as the reference strain distributions.

3. Using the developed FE models, establish the strain distribution patterns and threshold patterns. Use the thresholds and signature indices to develop the deterioration detection criteria for the pipeline buckling under different loading conditions. The threshold patterns will be discussed in the next two chapters.

4. Establish an automatic damage detection algorithm based on the built-in buckling behavioural patterns and signature indices. Install a real-time distributed strain monitoring system to measure the distributed strains from the distributed sensors at different positions. Check the distributed strains against the established deterioration criteria for pipe buckling.

5. Monitor the buried pipelines segment by segment. Based on the damage sequence during pipe buckling, the warning signs will be revealed during different pipe loading stages with respect to the different criteria. For instance, by monitoring the behavioural signatures of the compression-side strain distribution patterns, the monitoring system will provide warning for the pipeline anomalies and the inception of the pipe wrinkling; or by detecting the strain ratio index throughout the pipeline's operating life, unacceptable wrinkles can be prevented.

6. Once the pipe wrinkle has been detected, a warning system will inform the pipeline operator to take appropriate action.

Table 5.1 Pipe Dimensions and Conditions

Specimen No.	Grade (MPa)	D (mm)	D/t	Length (mm)	Girth weld	Internal Pressure (%SMYS)
Pipe#1	X80h (550)	762	59	2667	No	0
Pipe#3	X100h (690)	762	58	2667	Yes	0
Pipe#6	X80h (550)	610	39	2667	No	77
Pipe#7	X80 (550)	762	57	2667	Yes	76
Pipe#8	X80 (550)	762	57	2667	No	76
Pipe#9	X80h (550)	762	57	2667	No	77
Pipe#11	X100h (690)	914	69	2667	No	77
Pipe#12	X100h (690)	762	58	2667	Yes	77
Pipe#13	X100h (690)	762	55	2667	No	0
Pipe#14	X100h (690)	762	55	2667	No	77
UofA#2	X100h (690)	762	59	2588	No	20

Table 5.2 Critical Strains and Peak Moment for Experimental Results and FEA

Specimen No. Pipe# (Gauge length)	Critical strains (%) (Averaged in the gauge length)			Peak Moment (kN-m)		
	Test	FEA	FEA/Test	Test	FEA	FEA/Test
1 (2D)	-0.92	-1.15	1.25	4034	4162	1.03
3 (2D)	-0.74	-0.81	1.09	4725	4780	1.01
6 (2D)	-2.87	-3.10	1.08	2660	2520	0.95
7 (2.25D)	-1.31	-1.14	0.87	3467	3598	1.04
8 (2.25D)	-1.05	-0.91	0.87	3461	3524	1.02
9 (2.25D)	-1.71	-1.72	1.01	2878	2918	1.01
11 (2.25D)	-0.86	-1.23	1.43	5322	5369	1.00
12 (2D)	-0.91	-0.85	0.93	3376	3474	1.03
13 (2D)	-1.08	-1.08	1.00	5226	5481	1.05
14 (2D)	-1.26	-1.17	0.93	3659	3816	1.04
Averaged Ratio			1.05	**Averaged Ratio**		1.02
ST. Deviation			0.178	**ST. Deviation**		0.029

Table 5.3 Compressive Strains at the Vicinity of Wrinkle Location for Experimental Results and FEA

Specimen No. Pipe# (wrinkle location)	Strains: (Measured at the nearest Location of wrinkle)				Strains: (Measured at the nearest location of wrinkle)			
	Load Stage (%PM)	Test (%)	FEA (%)	$\frac{FEA}{Test}$	Load Stage (%PM)	Test (%)	FEA (%)	$\frac{FEA}{Test}$
1 (middle)	73	0.34	0.34	1.00	89	0.61	0.66	1.08
3 (middle)	75	0.32	0.34	1.06	86	0.37	0.45	1.21
6 (middle)	80	0.93	1.09	1.17	90	1.23	1.29	1.05
8 (top)	74	0.37	0.36	0.97	85	0.63	0.54	0.86
9 (bottom)	81	0.80	0.82	1.03	92	0.15	0.14	0.93
11 (bottom)	79	0.44	0.46	1.05	89	0.61	0.65	1.07
12 (middle)	76	0.33	0.32	0.96	96	0.57	0.64	1.12
13(middle)	77	0.41	0.38*	0.93	88	0.58	0.59**	1.02
14 (middle)	74	0.27	0.35	1.30	86	0.38	0.48	1.26
Averaged Ratio				1.05	**Averaged Ratio**			1.07
ST. Deviation				0.117	**ST. Deviation**			0.125

*: measurement in the loading stage, i.e., at 74%PM.

**: measurement in the loading stage, i.e., at 84%PM.

Table 5.4   Correlation of Experimental and FEA Strain Distribution Patterns

Specimen No. (strain position)	Loading Stages (% of peak moment)	Pattern Correlation Coefficient	
		Evaluation over distributed strains	Evaluation only in wrinkle area
Pipe#9 (compression)	80	-0.160	0.833
Pipe#9 (compression)	92	0.210	0.919
Pipe#14 (compression)	75	0.845	0.883
Pipe#14 (compression)	86	0.888	0.903
Pipe#13 (tension)	84	0.895	N.A.
Pipe#13 (tension)	92	0.737	N.A.
Pipe#14 (tension)	86	-0.186	N.A.
Pipe#14 (tension)	100	0.133	N.A.
Pipe#13 (tension)*	84	0.938	N.A.
Pipe#13 (tension)*	92	0.858	N.A.
Pipe#14 (tension)*	86	0.849	N.A.
Pipe#14 (tension)*	100	0.912	N.A.

N.A.: not available

* the distribution patterns of the FE models used the tension-side strain distributions during the loading stage, 96% of the peak moment in post-buckling rang

Table 5.5 Correlation of Tension-Side Strain Distributions during the Referenced
Loading Stage and Pipe Wrinkling

Specimen No.	Grade	D/t	Internal Pressure (%SMYS)	Pipe Condition	Loading Stages (%of the peak moment)	Correlation Coefficient
Pipe#12	X100h	58	76	GW	99*	0.927
Pipe#13	X100h	55	0		80	0.836
Pipe#14	X100h	55	77		89	0.746
Pipe#15	X100h	66	0		90	0.943
Pipe#16	X80h	55	77		95	0.929
Pipe#17	X100h	55	77		76	0.657
Pipe#20	X80	59	0		75	0.904
UofA#2	X100h	59	20		74	0.937
TCPL1	X65	93	80	Cold bend	100	0.983
TCPL2	X65	93	0	Cold bend	70	0.746
TCPL3	X65	93	80	Cold bend	100	0.970

The diameters of pipes are 762 mm, except for Pipe#15 with 914 mm diameter
The referrence distribution patterns used the tension-side strain distributions on the
FE models during the loading range from 30% to 40% of the peak moment

* the loading stage is during the post-buckling range

Table 5.6 Ratios of Maximum Strains to Average Strains on the Compression Side
during Pipe Softening

Model No.	Loading Stages (% of the peak moment)	Strain Ratio
Pipe#1	99	1.14
Pipe#3	94	1.46
Pipe#6	94	1.13
Pipe#8	92	1.19
Pipe#9	92	1.19
Pipe#11	89	1.11
Pipe#12	88	1.66
Pipe#13	85	1.06
Pipe#14	86	1.48

Table 5.7   The Relation of Strains at Different Circumferential Positions with the
Critical Buckling Position on Pipes

Specimen No. (wrinkle shape)	Loading stages (% of the peak moment)	Strain ratio (%)	
		Strain on 22.5° / Strain on 0°	Strain on 45° / Strain on 0°
Pipe#6 (outward)	82	93	74
Pipe#6 (outward)	91	92	74
Pipe#7(outward)	86	91.7	70.7
Pipe#7 (outward)	91	91.9	71.4
Pipe#11(outward)	76	92	73
Pipe#11(outward)	86	92	75
Pipe#12(outward)	86	78	57
Pipe#12(outward)	91	78	56
Pipe#14(outward)	75	92**	66*
Pipe#14(outward)	81	90	68
Pipe#14(outward)	86	94**	82*
Pipe#14(outward)	86	90	67
UofA#2(outward)	76	91.5*	63.8*
Averaged Ratio		**91.8**	**71.4**
ST. Deviation		**1.14**	**5.10**
Pipe#1(inward)	73	91.1	35.5
Pipe#1(inward)	89	90.5	35.4
Pipe#3(inward)	75	92.0	69.1
Pipe#3(inward)	86	91.9	69.1
Pipe#13(inward)	78	90.5	66.7
Pipe#13(inward)	85	90.6	66.6
Averaged Ratio		**91.1**	**57.1**
ST. Deviation		**0.70**	**16.78**

* test results

** interpolation of test results
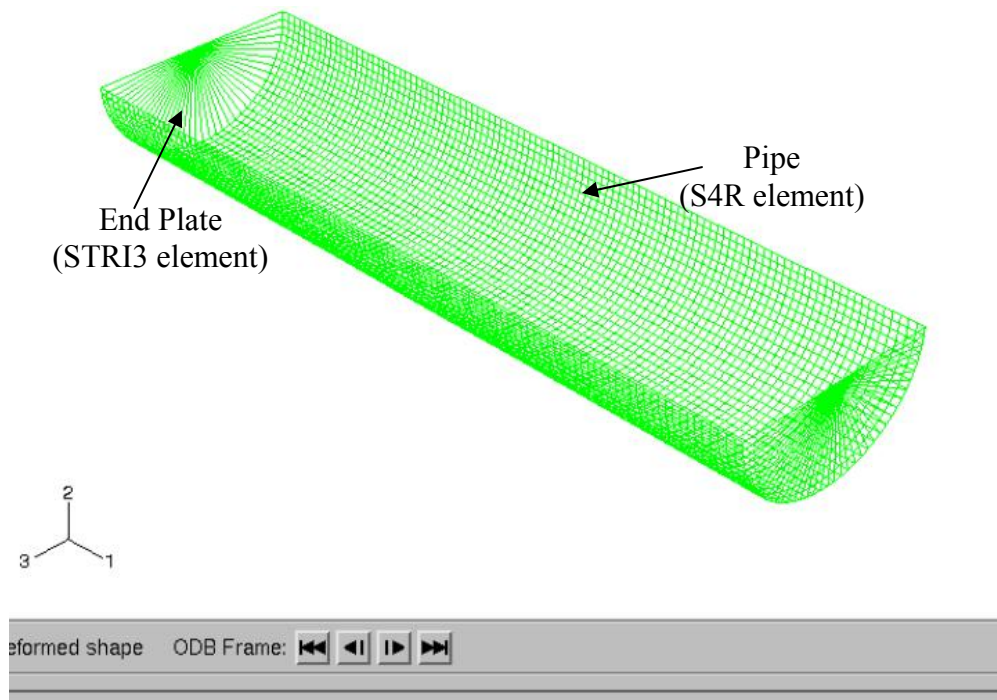
Pipe
(S4R element)

(a) Finite Element Model for a Plain Pipe
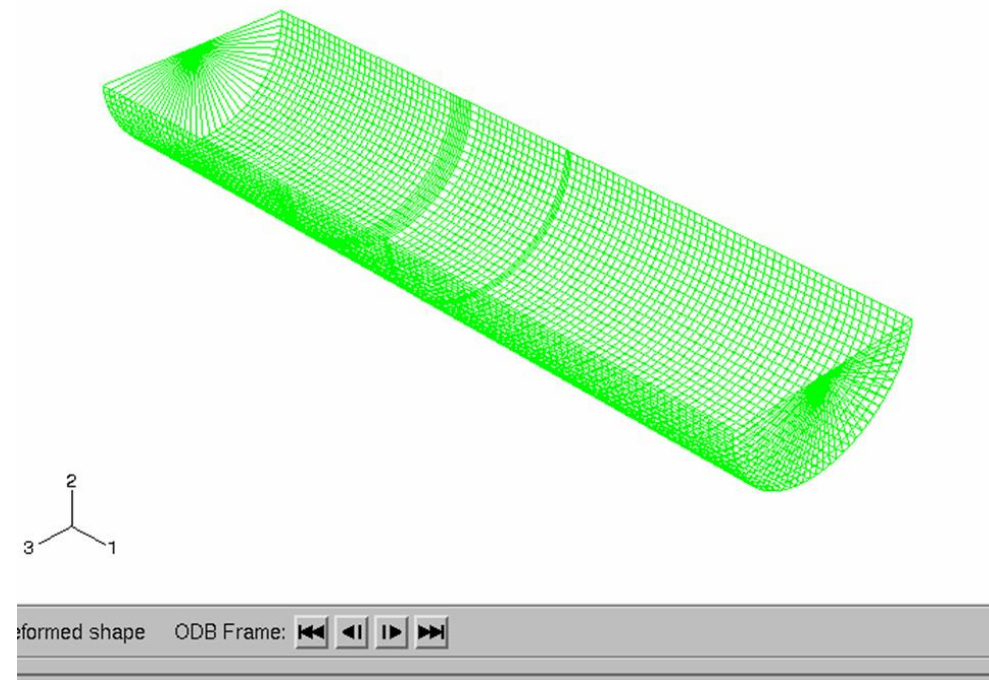
(b) Finite Element Model for a Girth-Welded Pipe

Figure 5.1 Finite Element Models
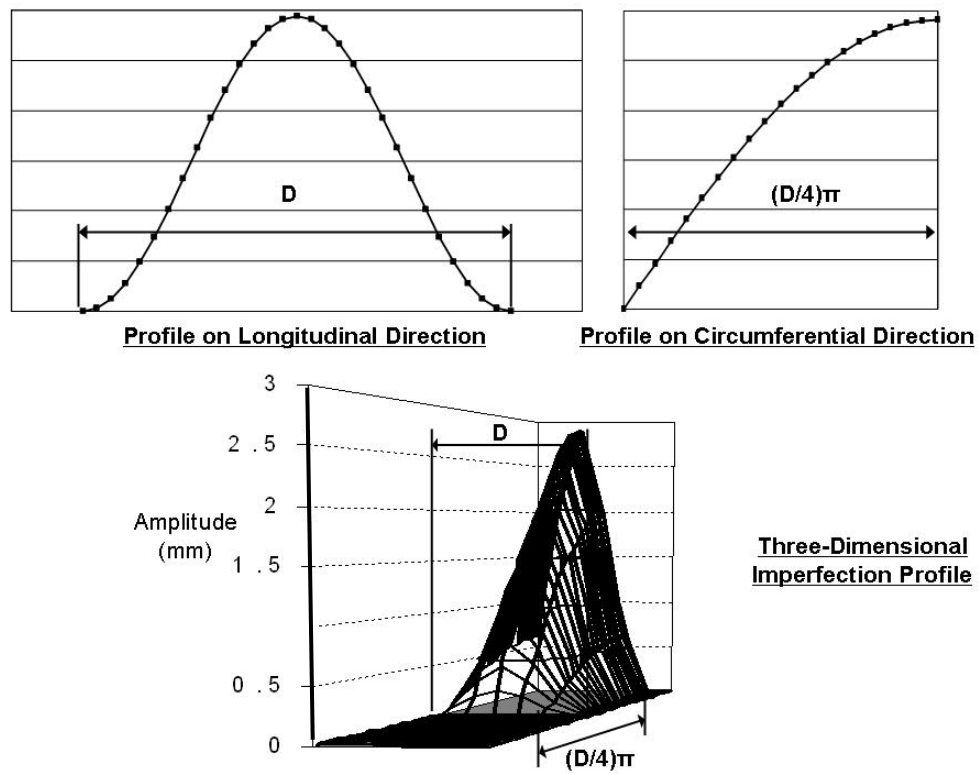
Figure 5.2 Example of Blister Pattern Initial Imperfection
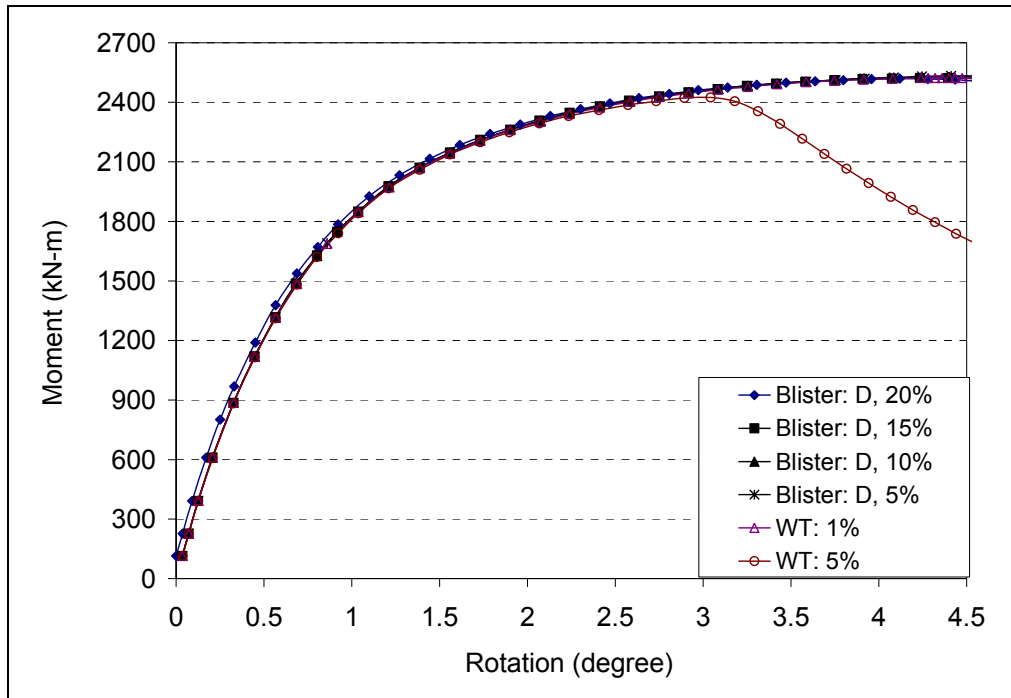
Figure 5.3 Imperfection Pattern Effect on Global Behaviour for a Pressurized
Pipe
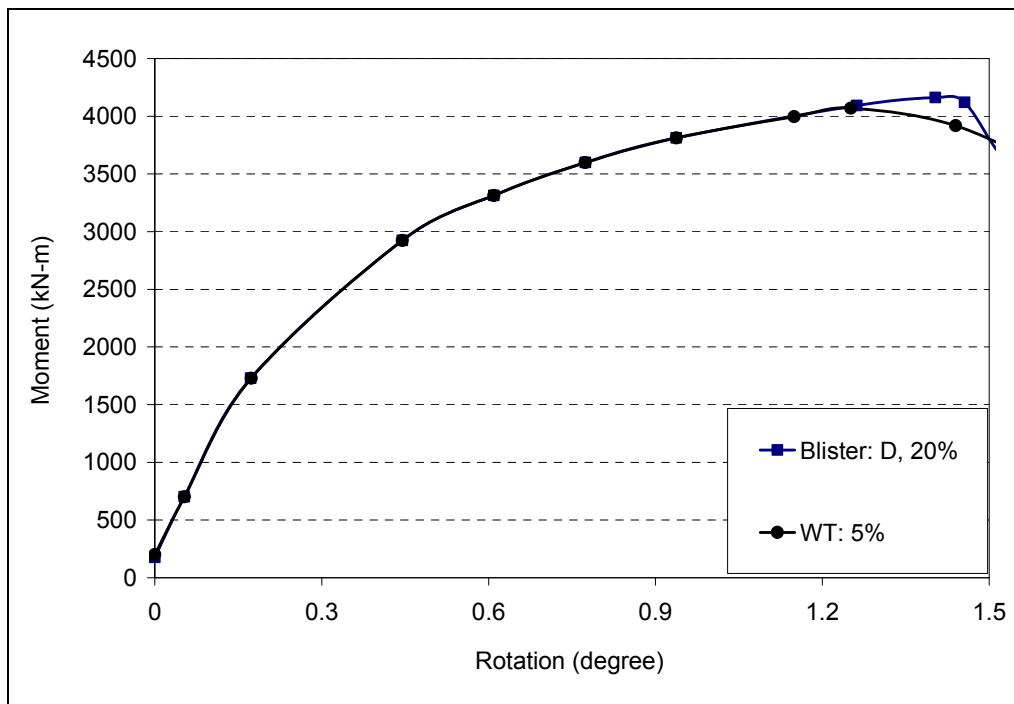
Figure 5.4 Imperfection Pattern Effect on Global Behaviour for a
Non-pressurized Pipe

142
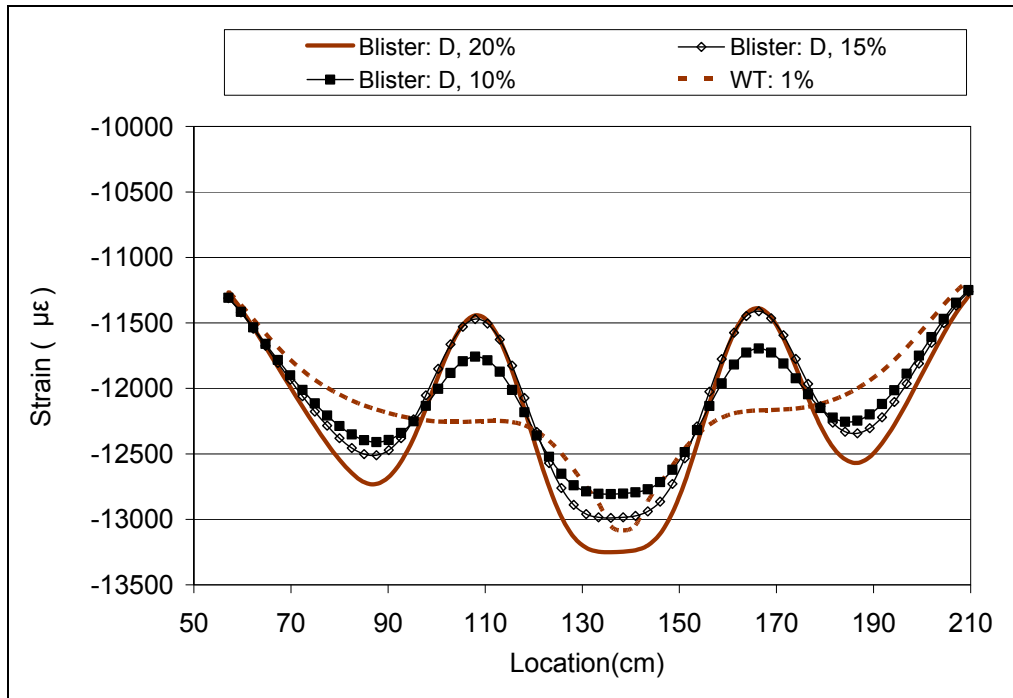
Figure 5.5 Imperfection Pattern Effect on Strain Distributions for a Pressurized Pipe
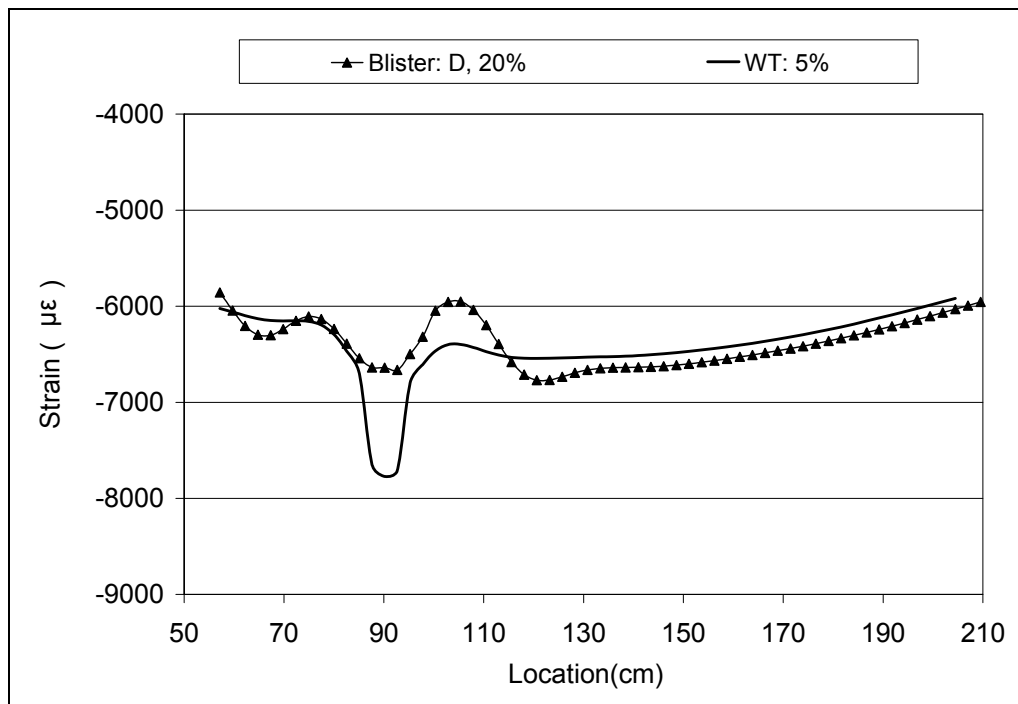
Figure 5.6 Imperfection Pattern Effect on Strain Distributions for a Non-pressurized Pipe

143
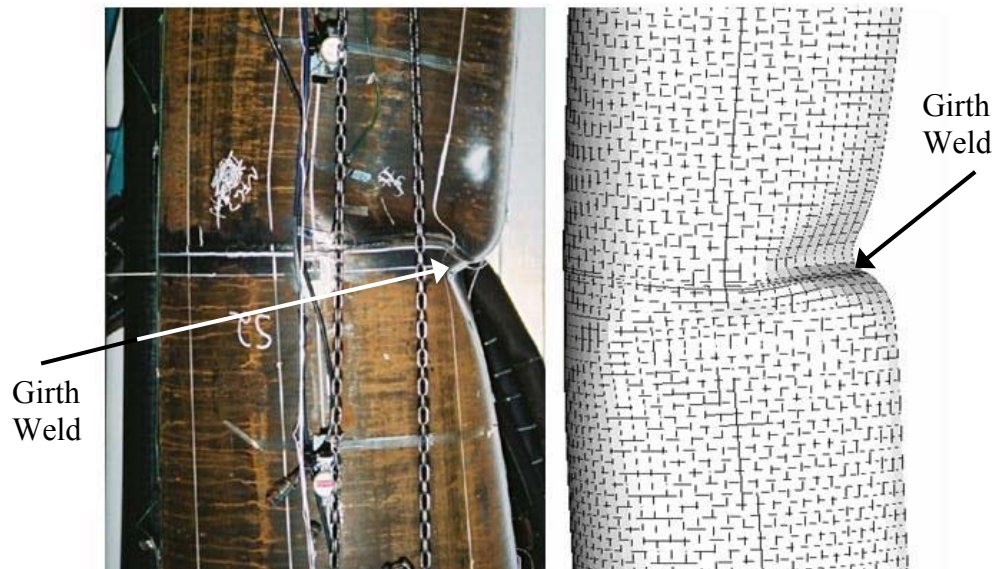
(a) Experimental Result for Pip#3 (b) Analytic Results for Pipe#3
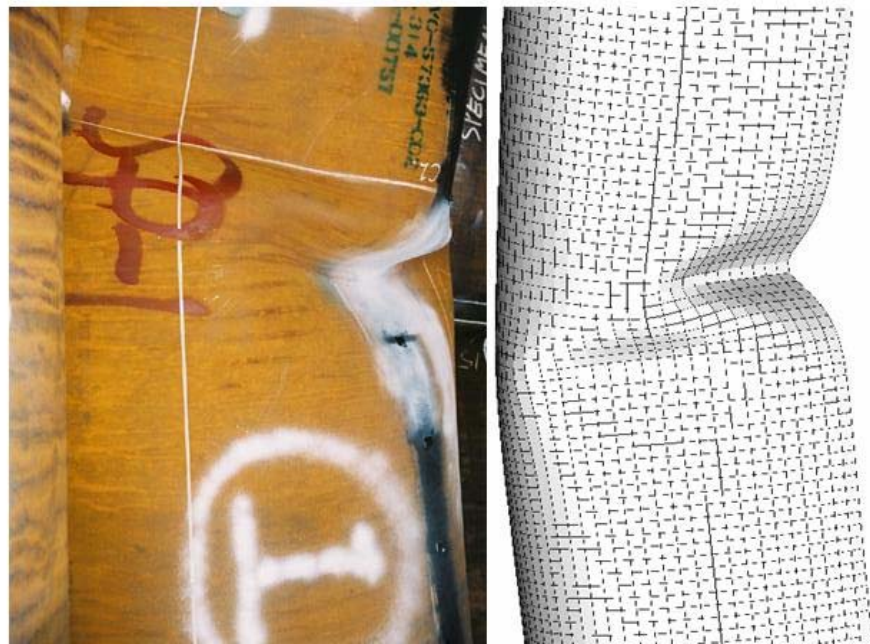
(c) Experimental Result for Pip#1   (d) Analytic Results for Pipe#1

Figure 5.7 Deformed Shape for Non-pressurized Pip#1 and Pipe#3:
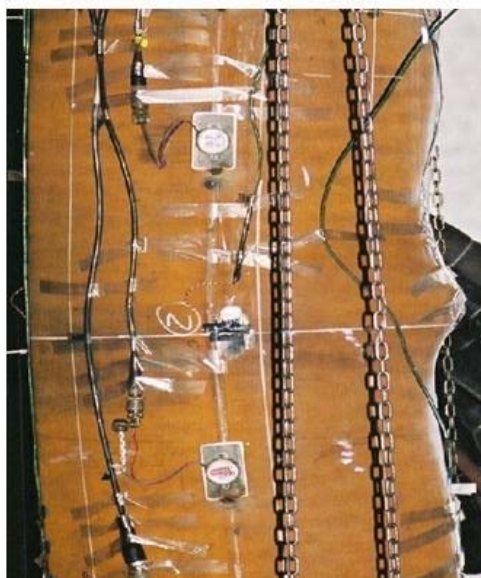
(a) Experimental Result for Pip#6   (b) Analytic Results for Pipe#6
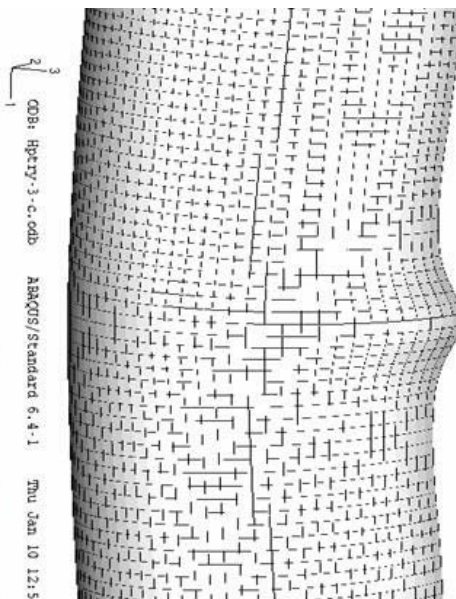
Girth
Weld

Girth
Weld
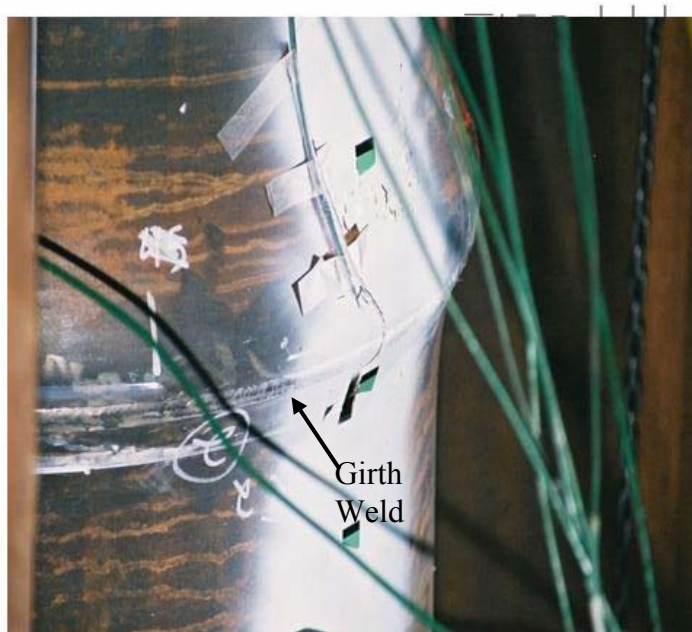
(c) Experimental Result for Pip#12   (d) Analytic Results for Pipe#12
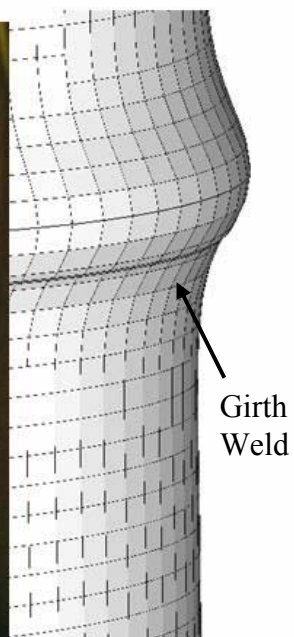
Figure 5.8 Deformed Shape for Pressurized Pipe#6 and Pip#12:

145
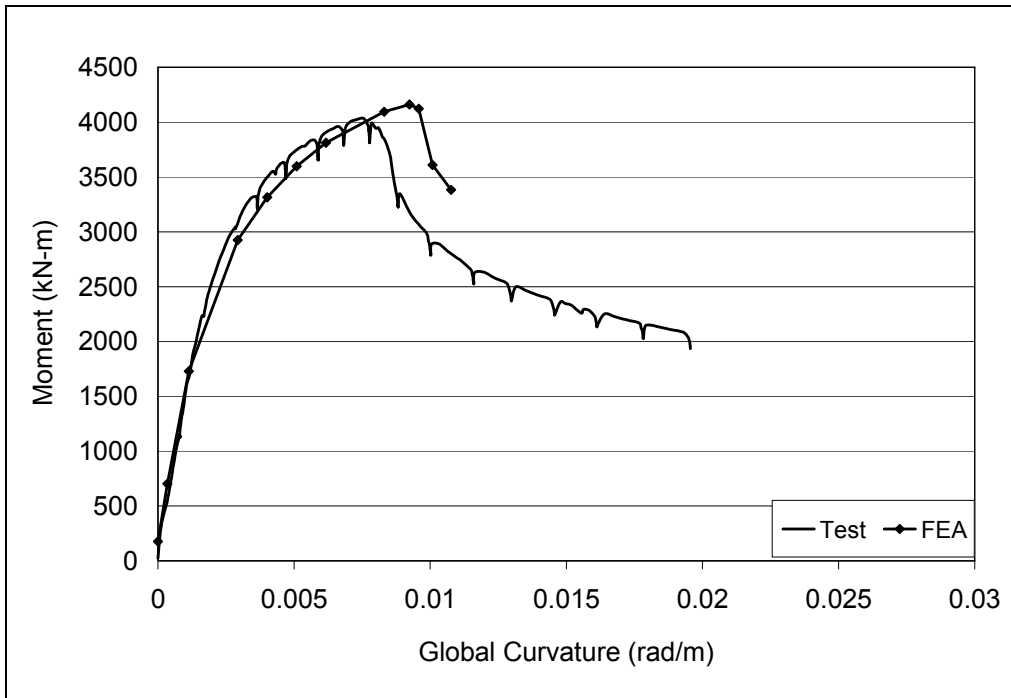
Figure 5.9 Global Moment versus Curvature Comparison for Specimen Pipe#1
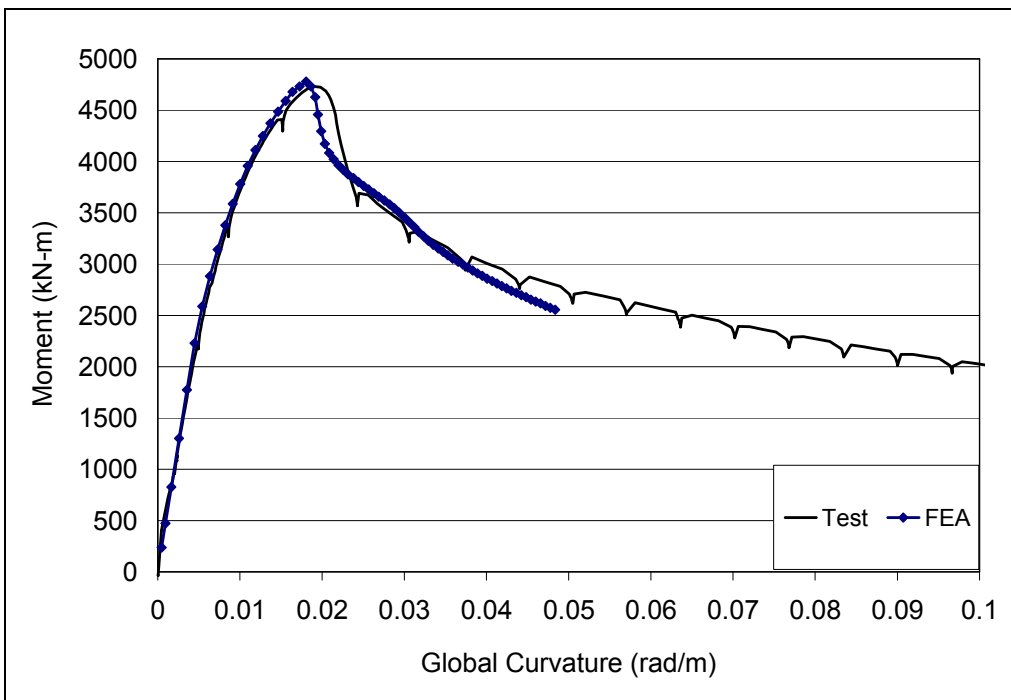
Figure 5.10 Global Moment versus Curvature Comparison for Specimen Pipe#3

146
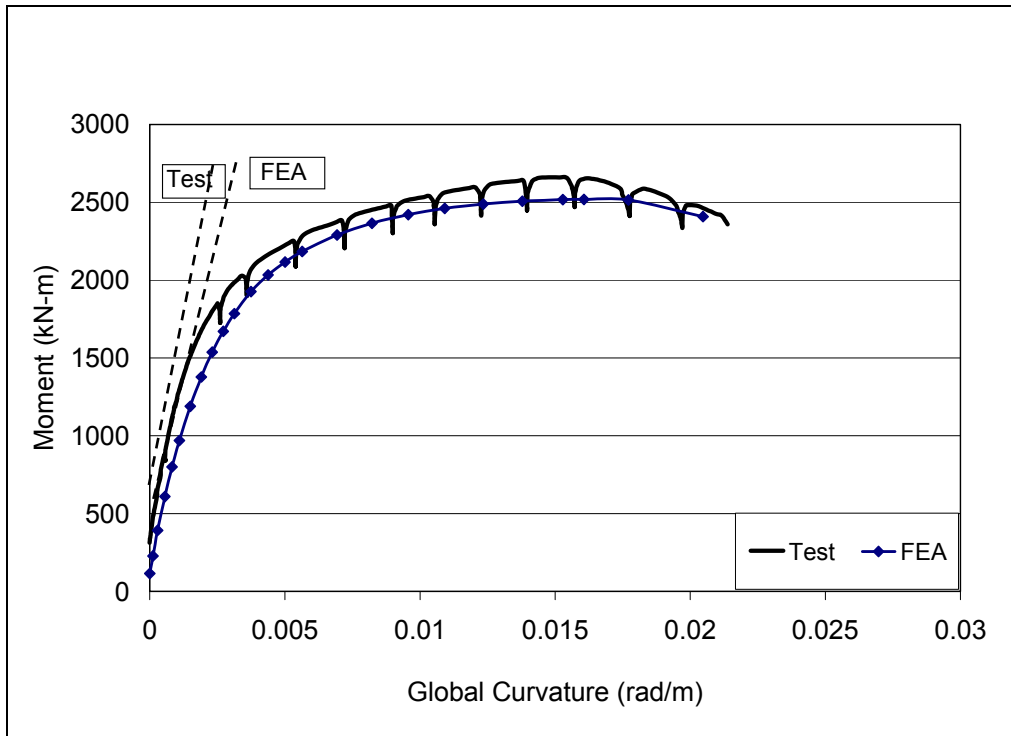
Figure 5.11 Global Moment versus Curvature Comparison for Specimen
Pipe#6
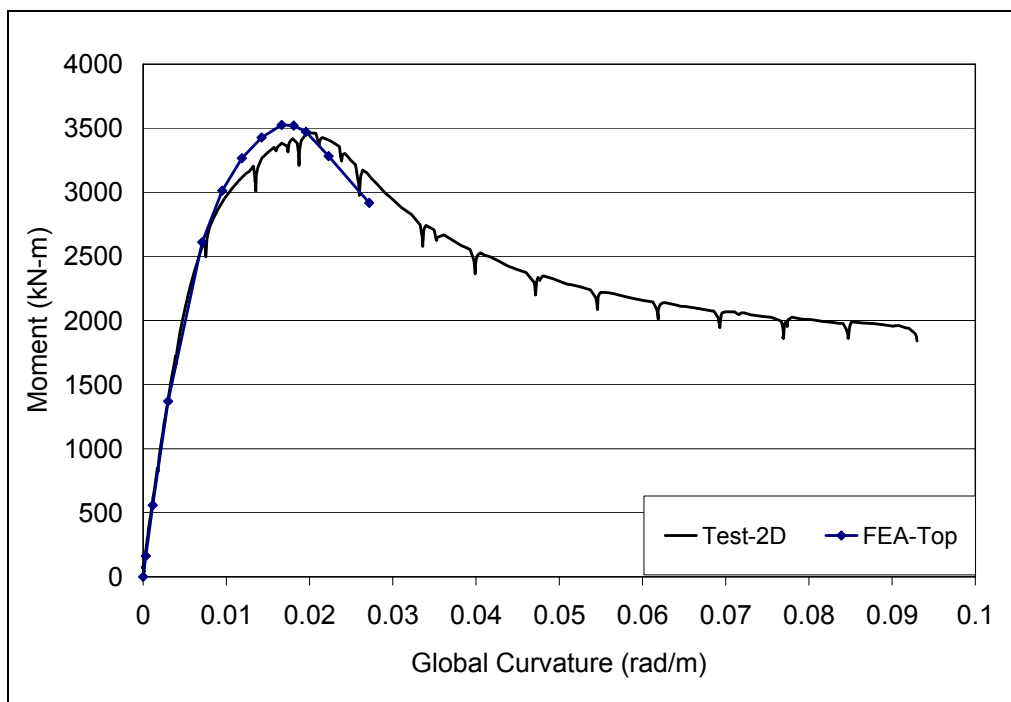
Figure 5.12 Global Moment versus Curvature Comparison for Specimen
Pipe#8

147
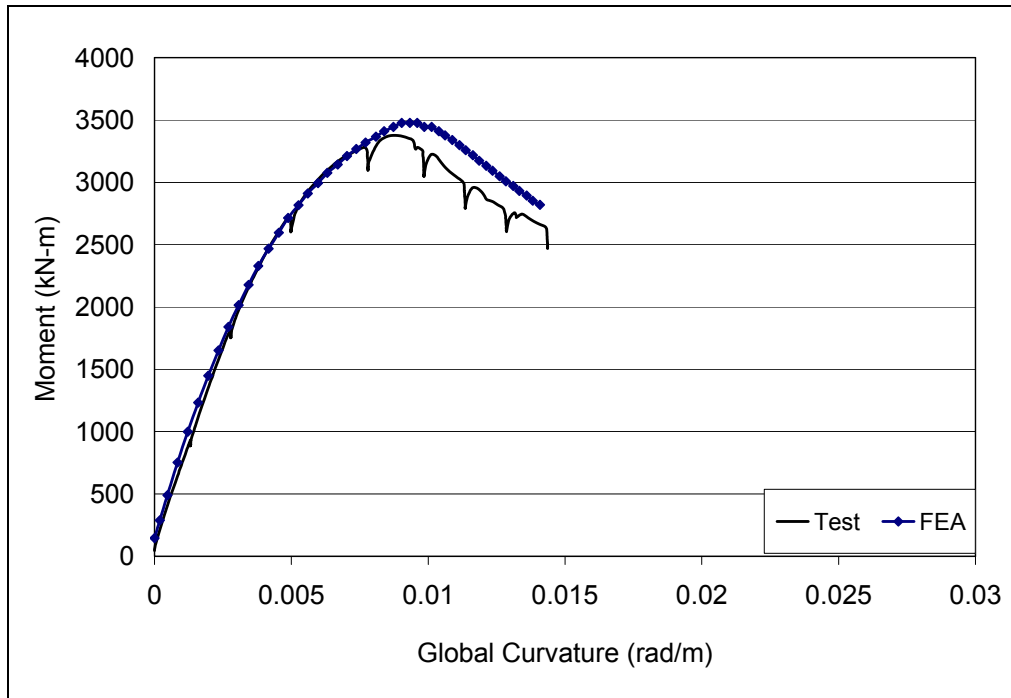
Figure 5.13 Global Moment versus Curvature Comparison for Specimen
Pipe#12
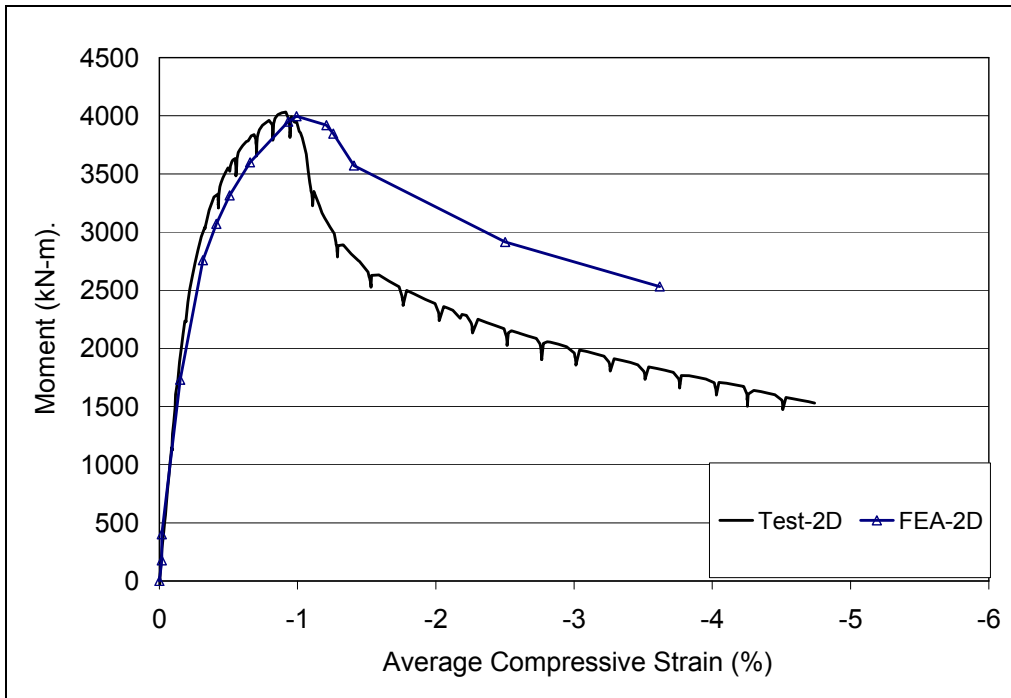
Figure 5.14 Global Moment versus Averaged Strain Comparison for
Non-pressurized Pipe#1
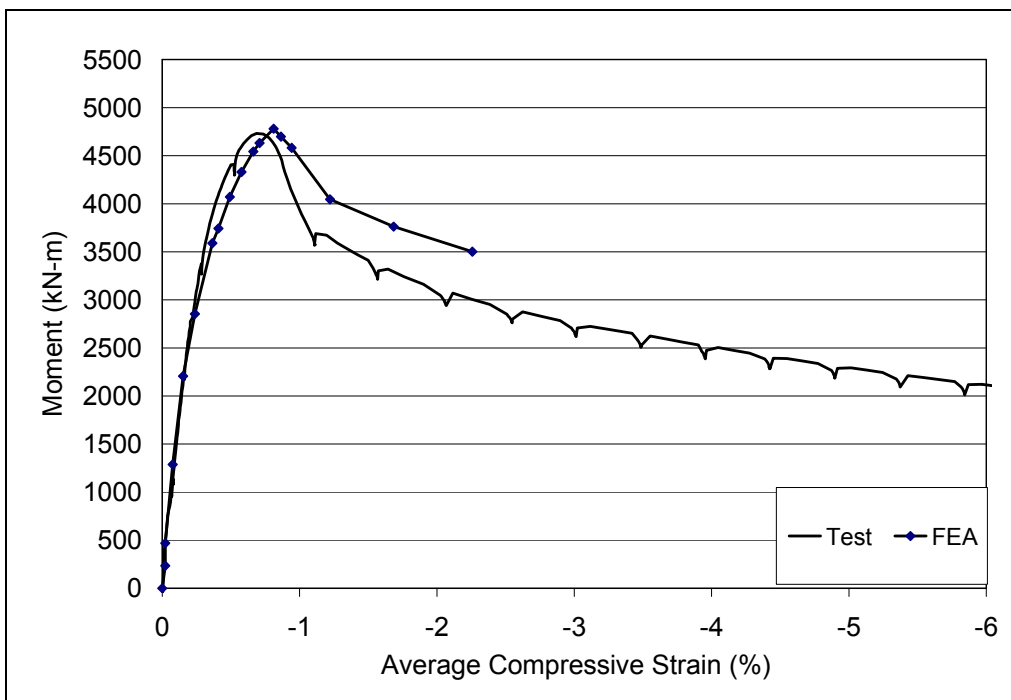
Figure 5.15 Global Moment versus Averaged Strain Comparison for
Non-pressurized Girth-welded Pipe#3

149
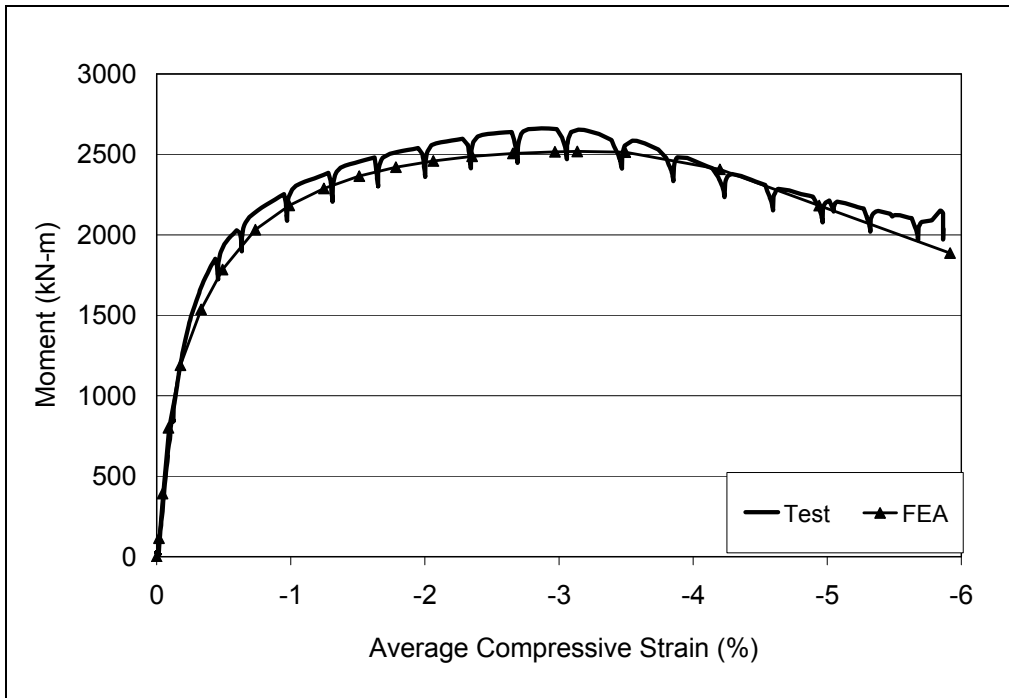
Figure 5.16 Global Moment versus Averaged Strain Comparison for
Pressurized Pipe#6
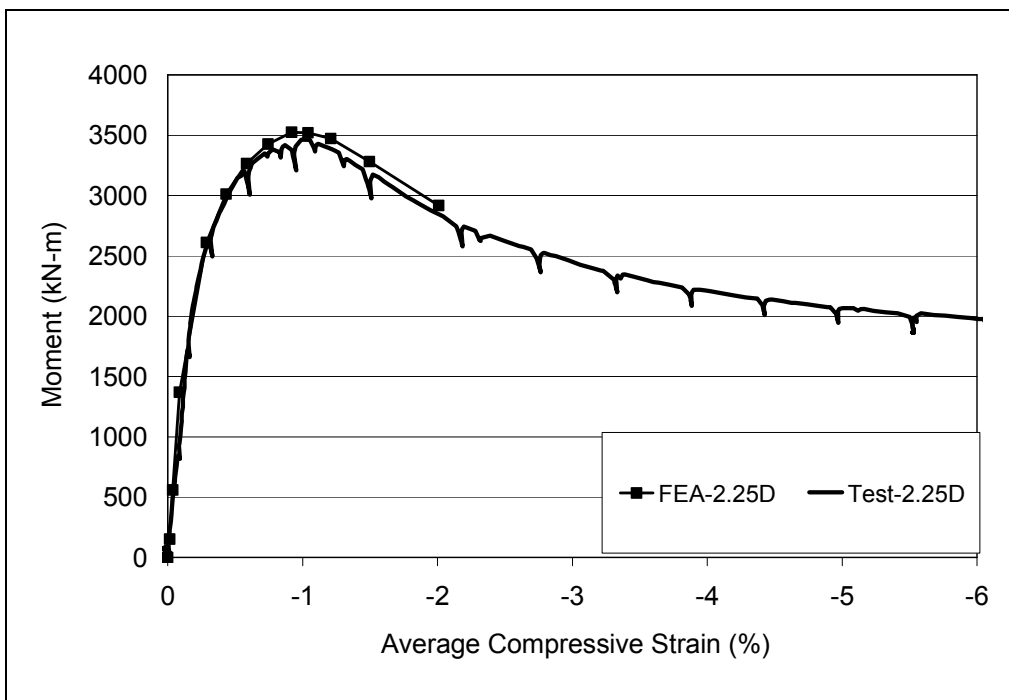
Figure 5.17 Global Moment versus Averaged Strain Comparison for
Pressurized Pipe#8

150
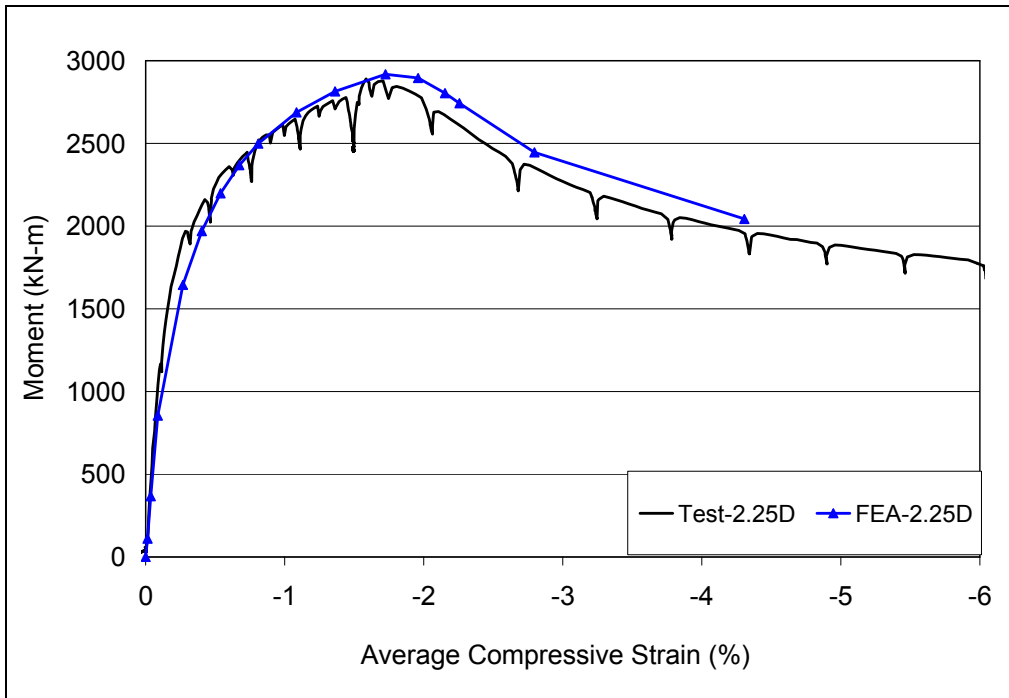
Figure 5.18 Global Moment versus Averaged Strain Comparison for
Pressurized Pipe#9
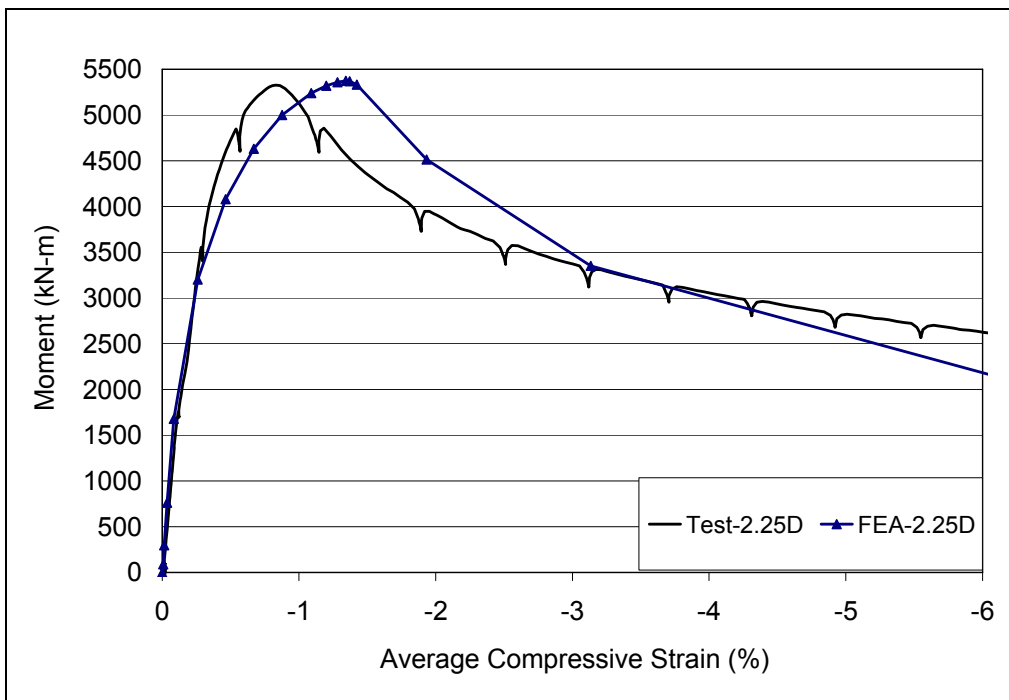
Figure 5.19 Global Moment versus Averaged Strain Comparison for
Pressurized Pipe#11

151
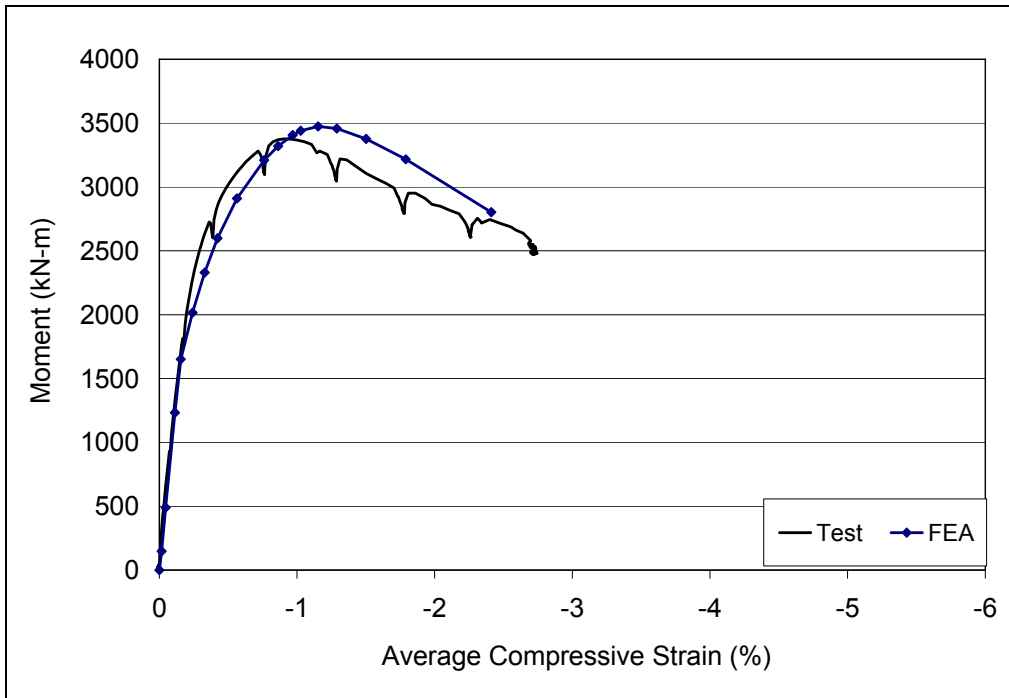
Figure 5.20 Global Moment versus Averaged Strain Comparison for
Pressurized Girth-Welded Pipe#12
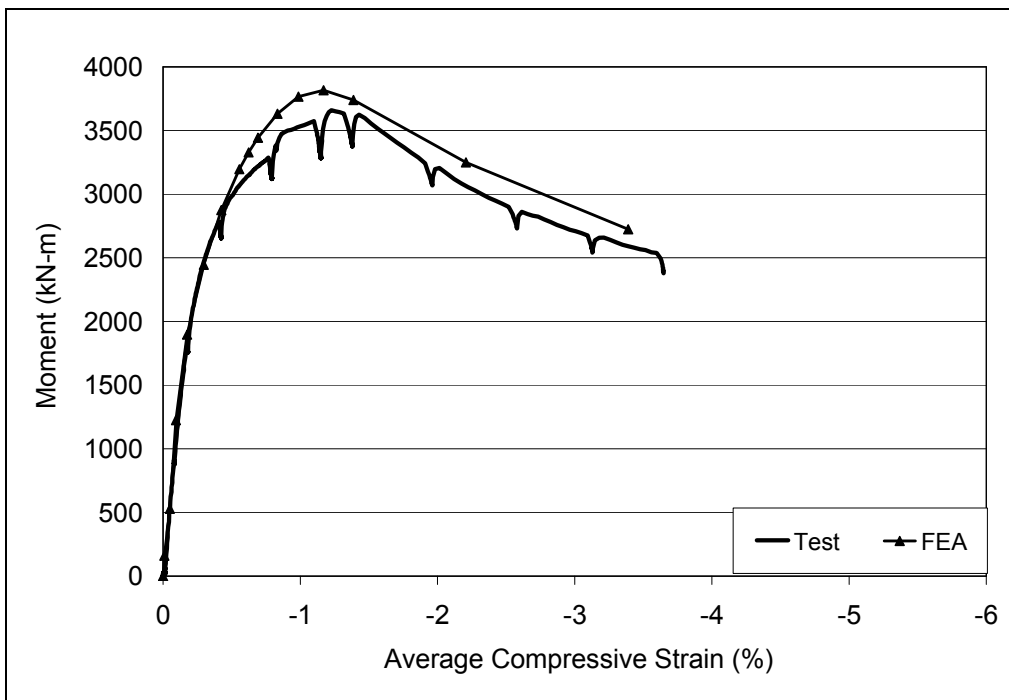
Figure 5.21 Global Moment versus Averaged Strain Comparison for
Pressurized Pipe#14

152
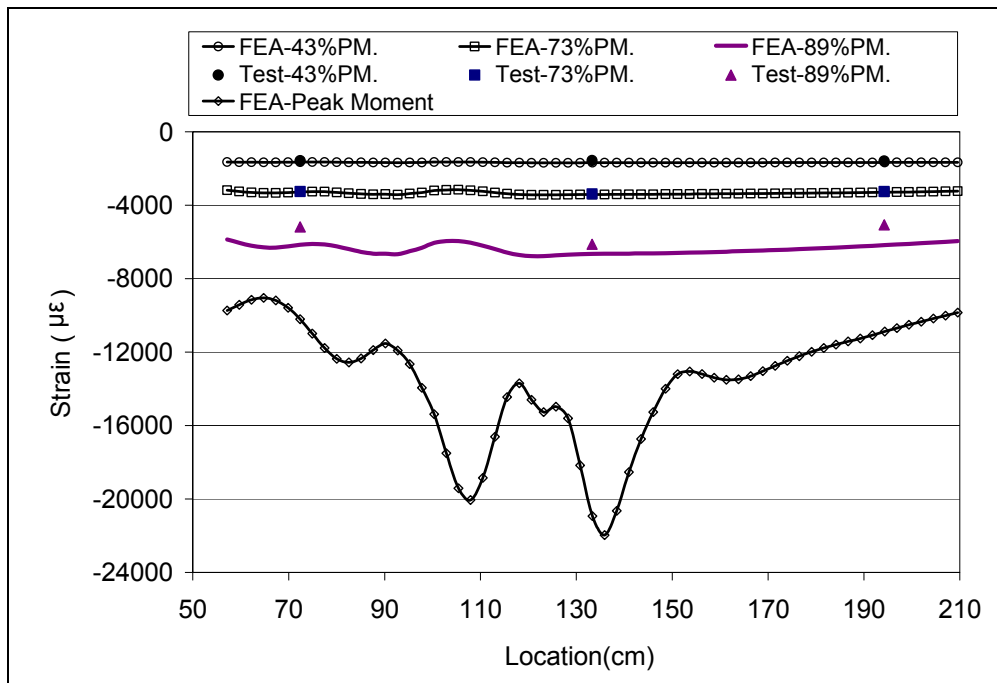
Figure 5.22 Compressive Strain Distributions Comparison for Specimen Pipe#1
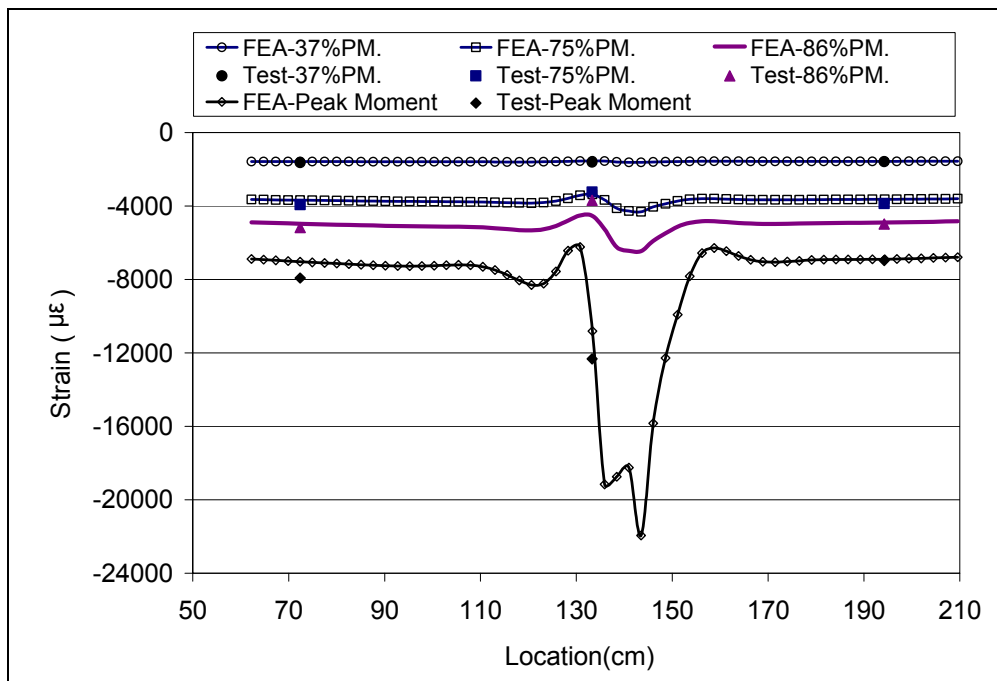
Figure 5.23 Compressive Strain Distributions Comparison for Specimen Pipe#3

153
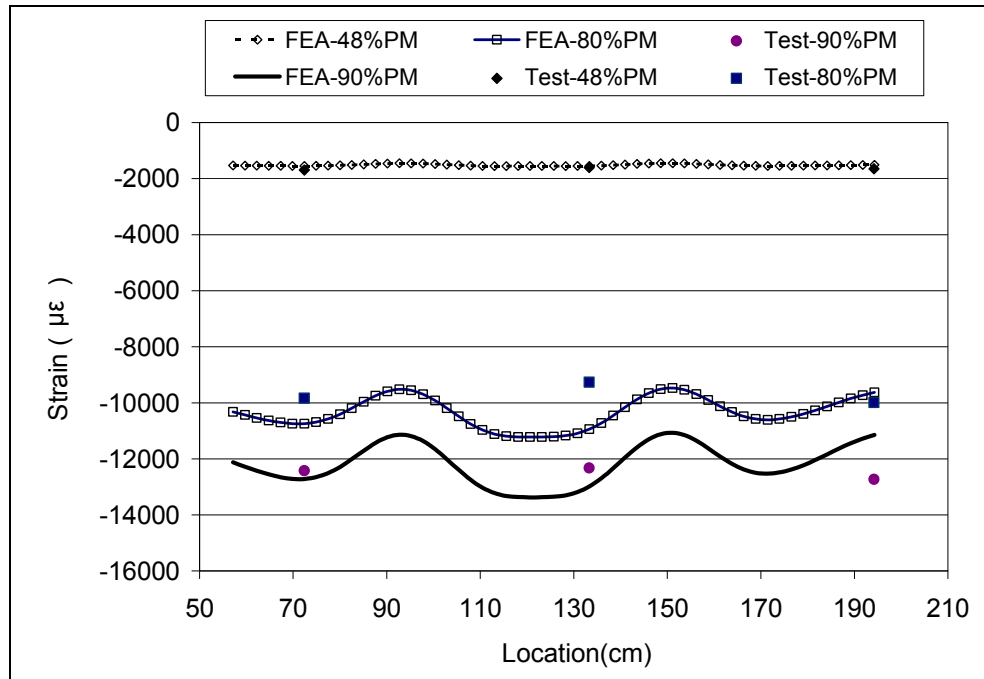
Figure 5.24 Compressive Strain Distributions Comparison for Specimen
Pipe#6
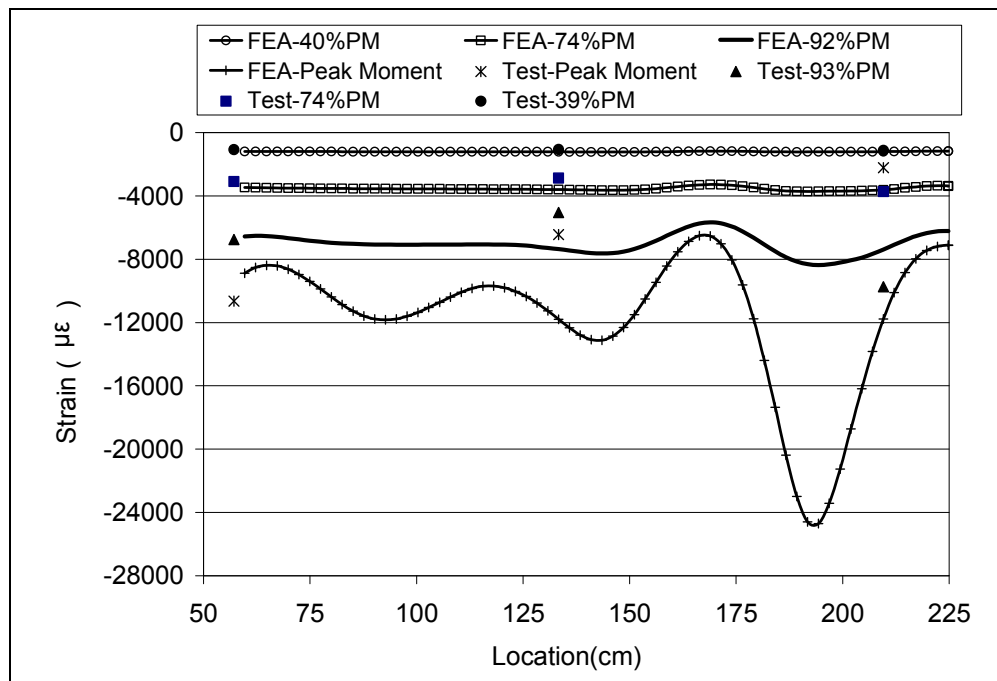
Figure 5.25 Compressive Strain Distributions Comparison for Specimen
Pipe#8

154
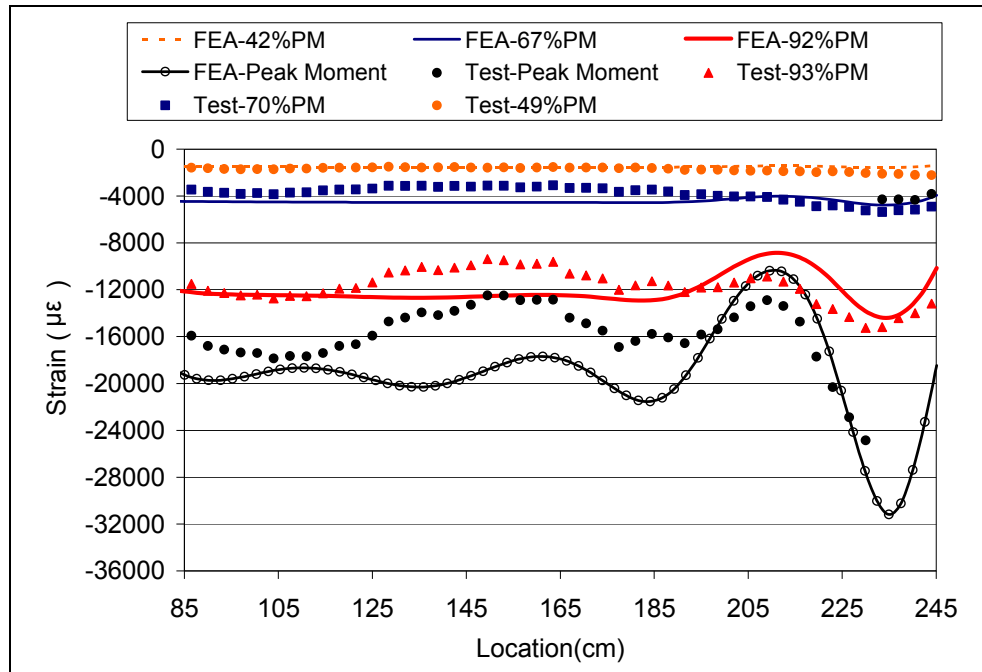
Figure 5.26 Compressive Strain Distributions Comparison for Specimen Pipe#9
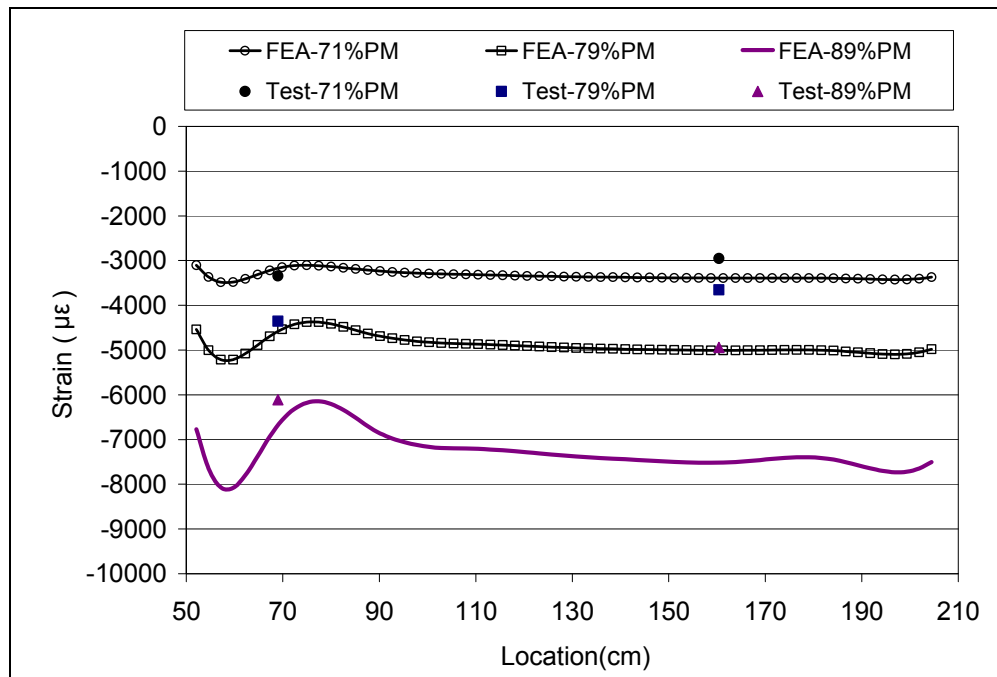
Figure 5.27 Compressive Strain Distributions Comparison for Specimen Pipe#11

155
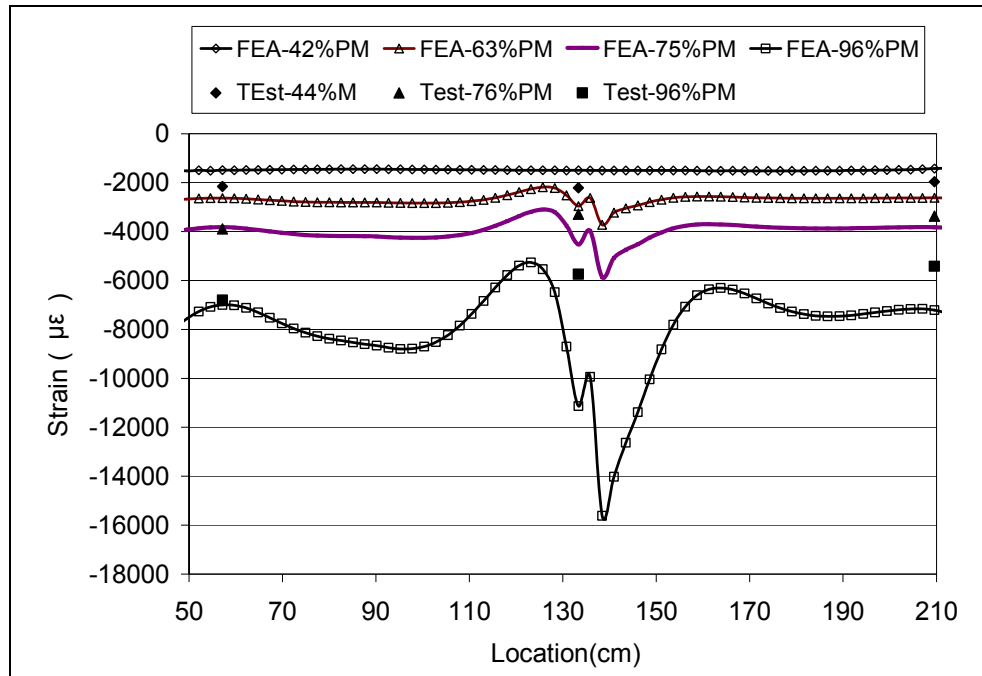
Figure 5.28 Compression Side Strain Distributions Comparison for
Specimen Pipe#12
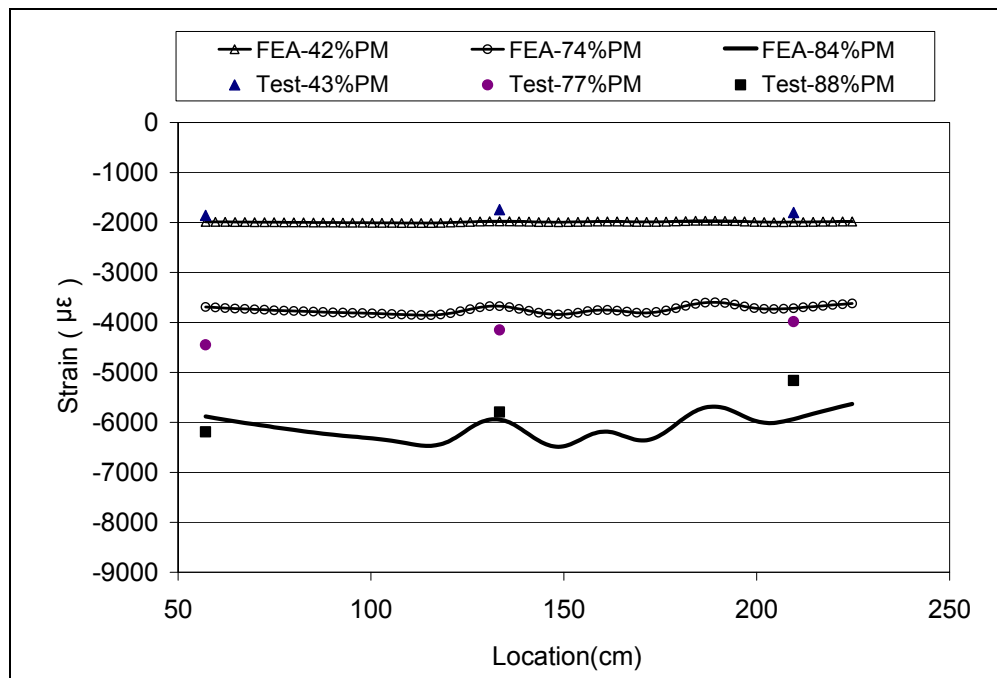
Figure 5.29 Compression Side Strain Distributions Comparison for Specimen
Pipe#13

156
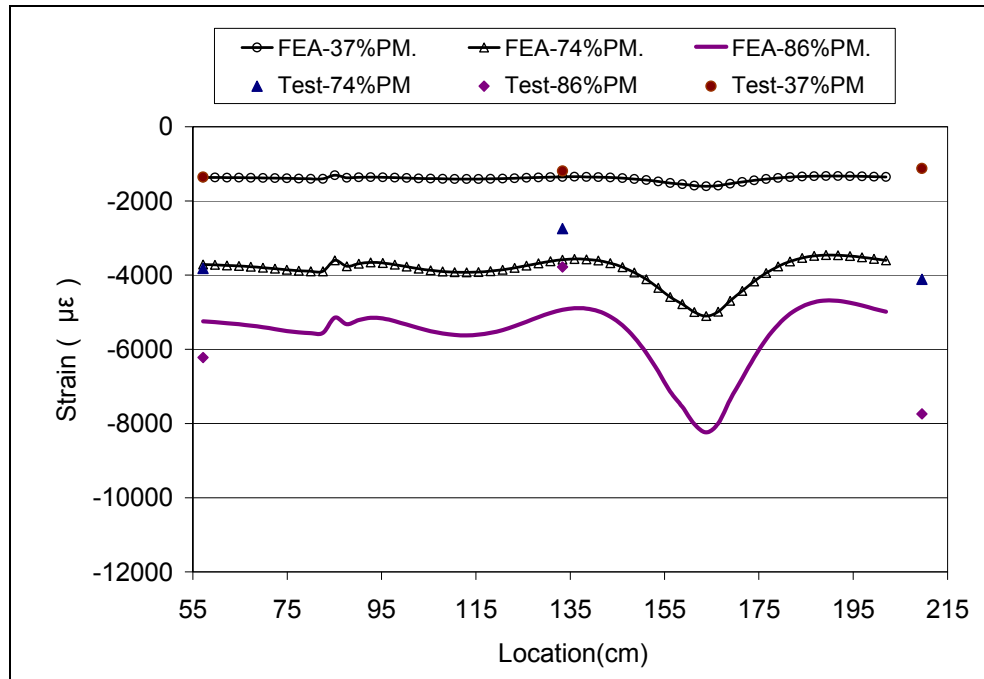
Figure 5.30 Compression Side Strain Distributions Comparison for
Specimen Pipe#14
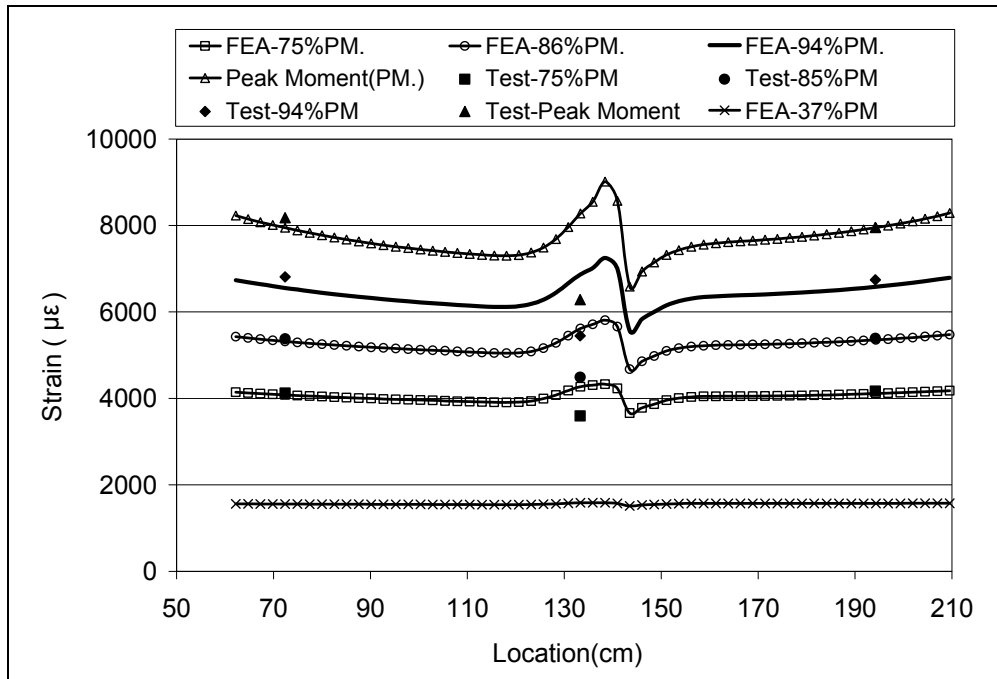
Figure 5.31 Tensile Strain Distributions Comparison for Non-pressurized
Girth-welded Pipe#3
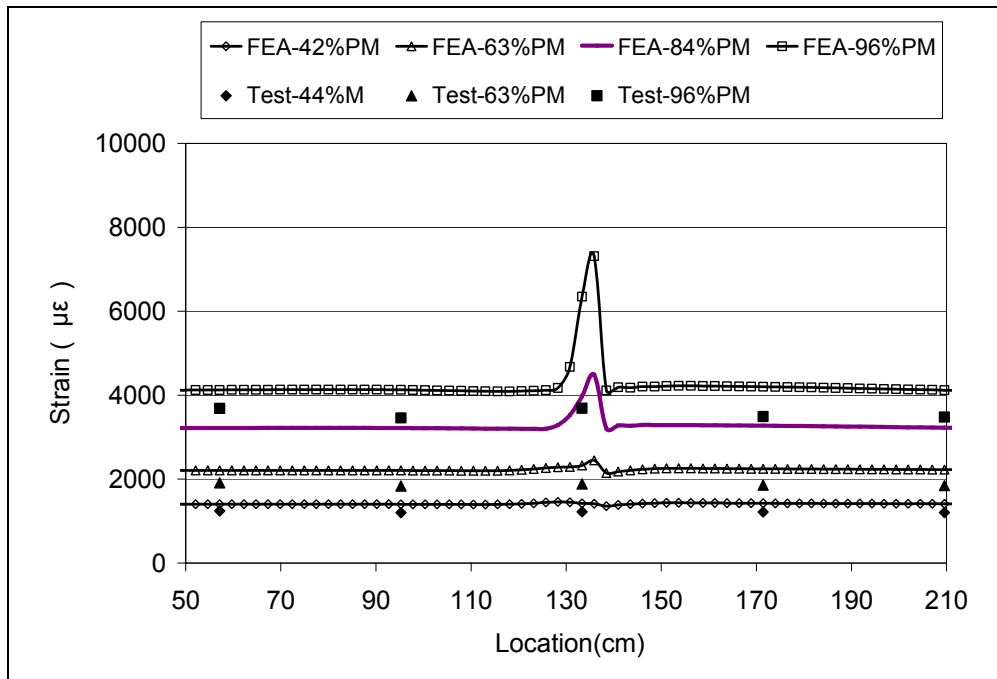
Figure 5.32 Tensile Strain Distributions Comparison for Pressurized
Girth-welded Pipe#12

158
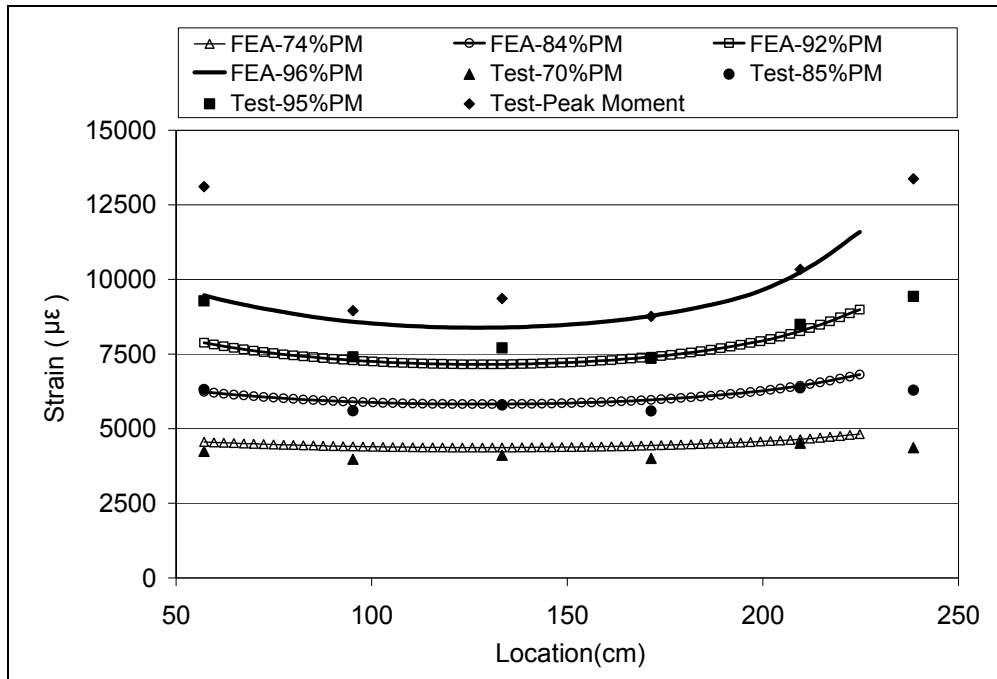
Figure 5.33 Tensile Strain Distributions Comparison for Non-pressurized
Plain Pipe#13
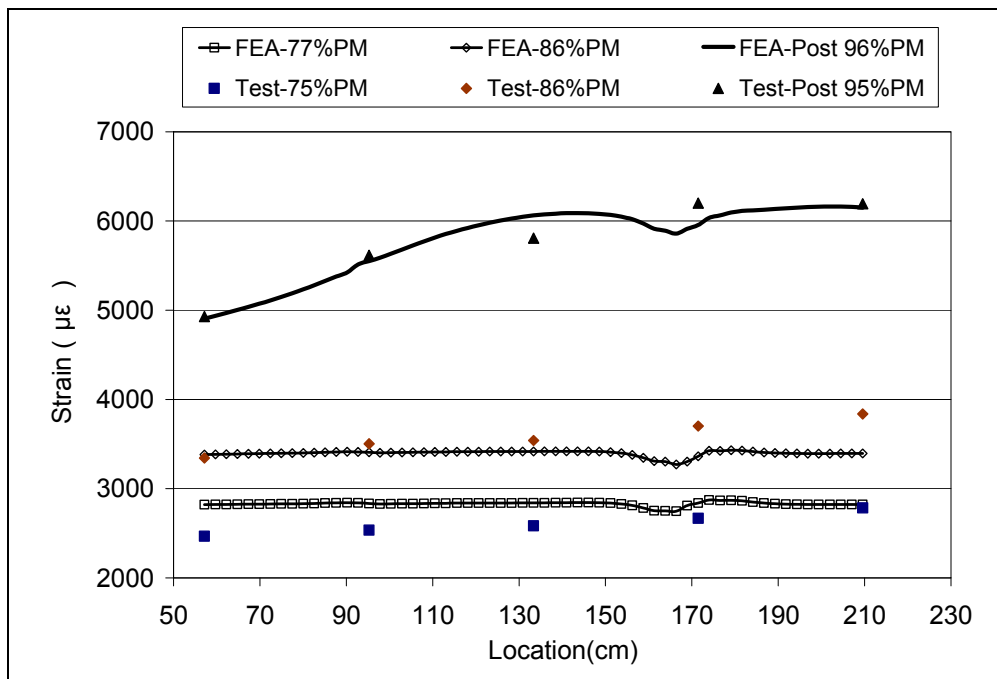
Figure 5.34 Tensile Strain Distributions Comparison for Pressurized Plain
Pipe#14

159
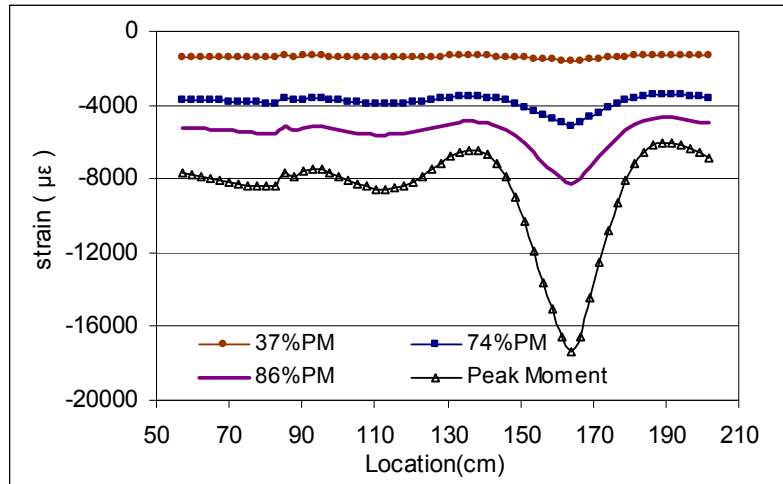
(a) Longitudinal Strains on 0° Position
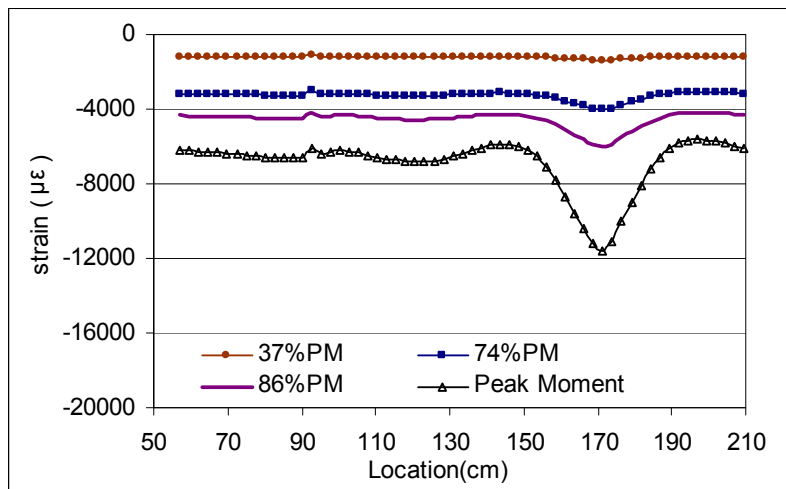
(b) Longitudinal Strains on 45° Position
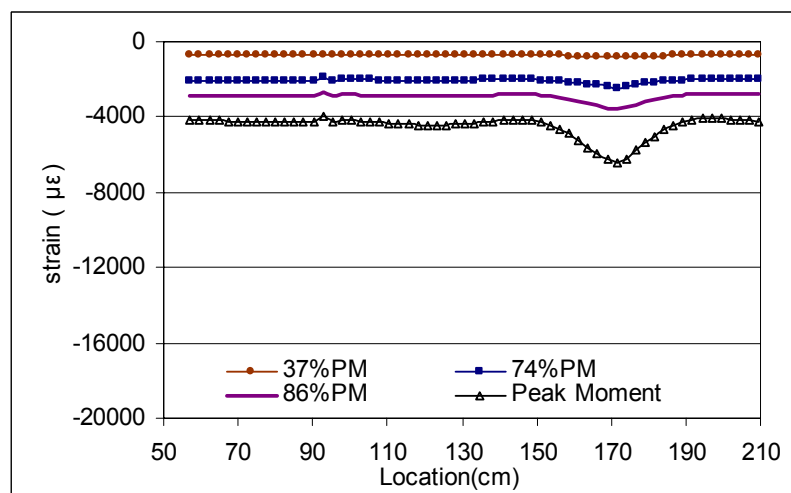
(c) Longitudinal Strains on 67.5° Position

Figure 5.35 Longitudinal Strains History during Pipe Buckling

160
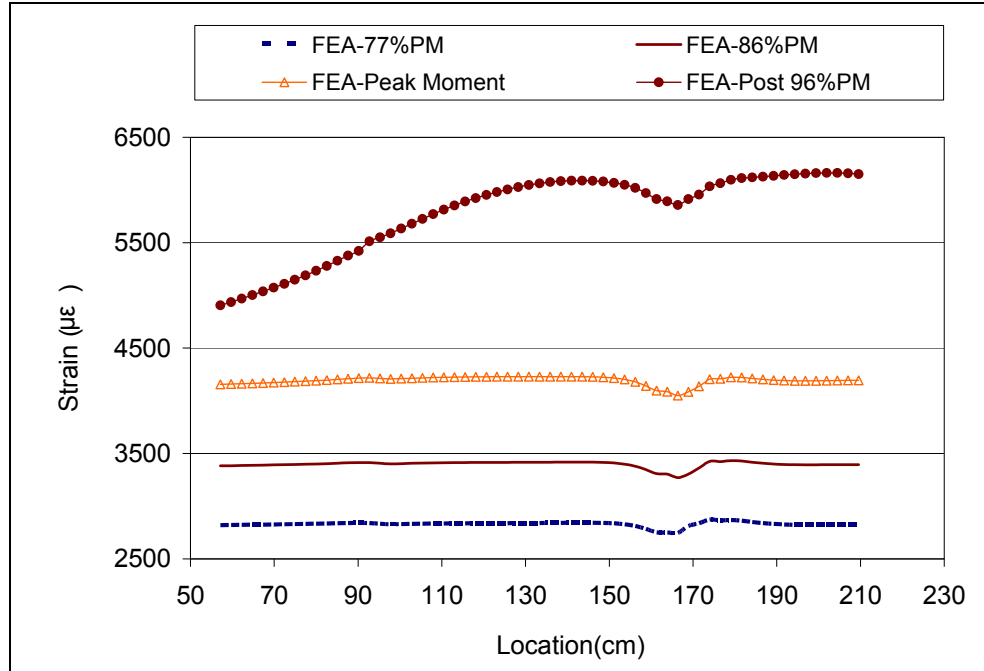
Figure 5.36 Longitudinal Strains History on 180° Position during Pipe
Buckling
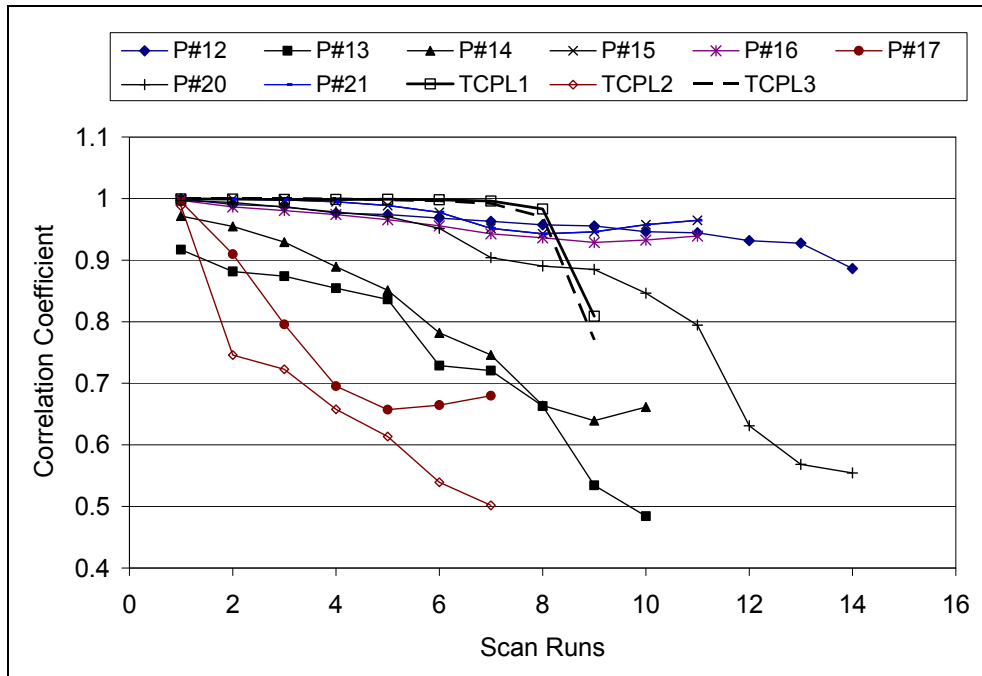
Figure 5.37 Correlation Coefficients of Tension-Side Strain Distributions
during Various Loading Stages
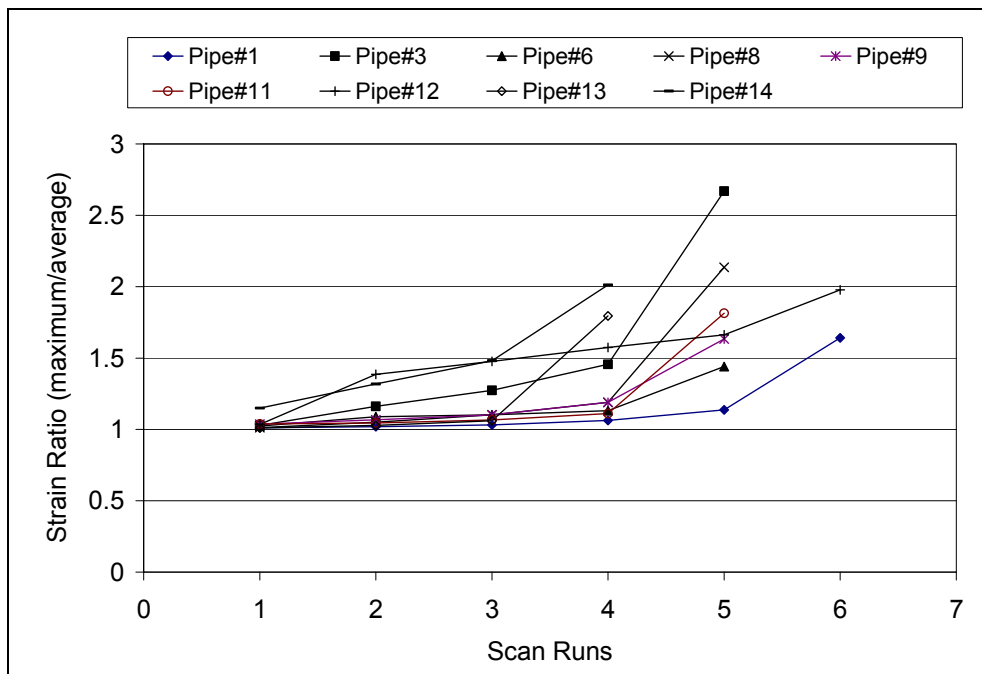
Figure 5.38 Ratios of Maximum Strains to Average Strains on Compression
Side during Various Loading Stages

162
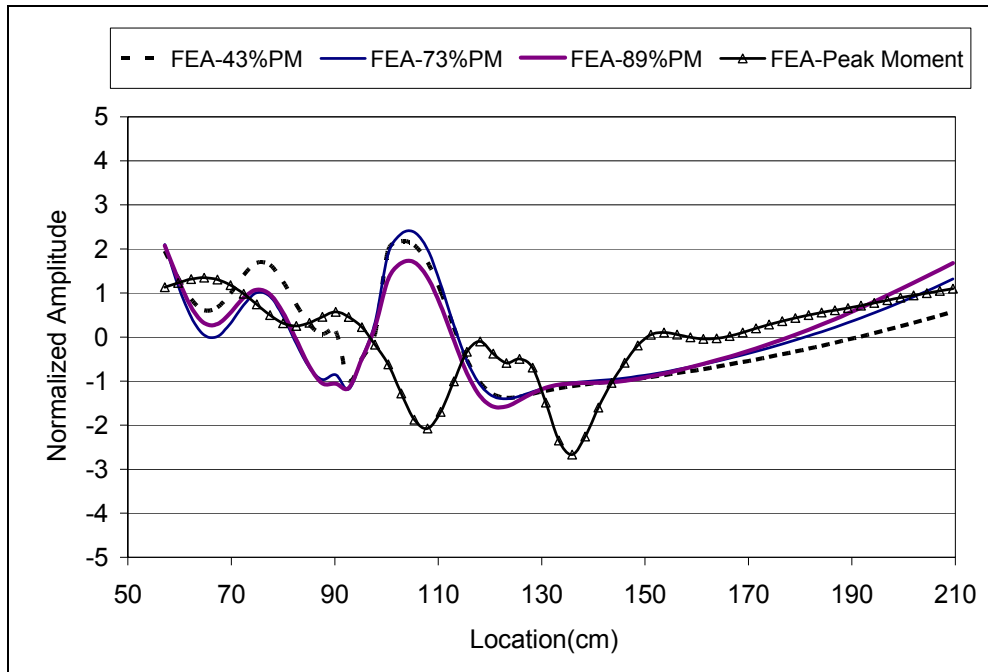
Figure 5.39 Normalized Strain Distributions for an Non-pressurized Pipe
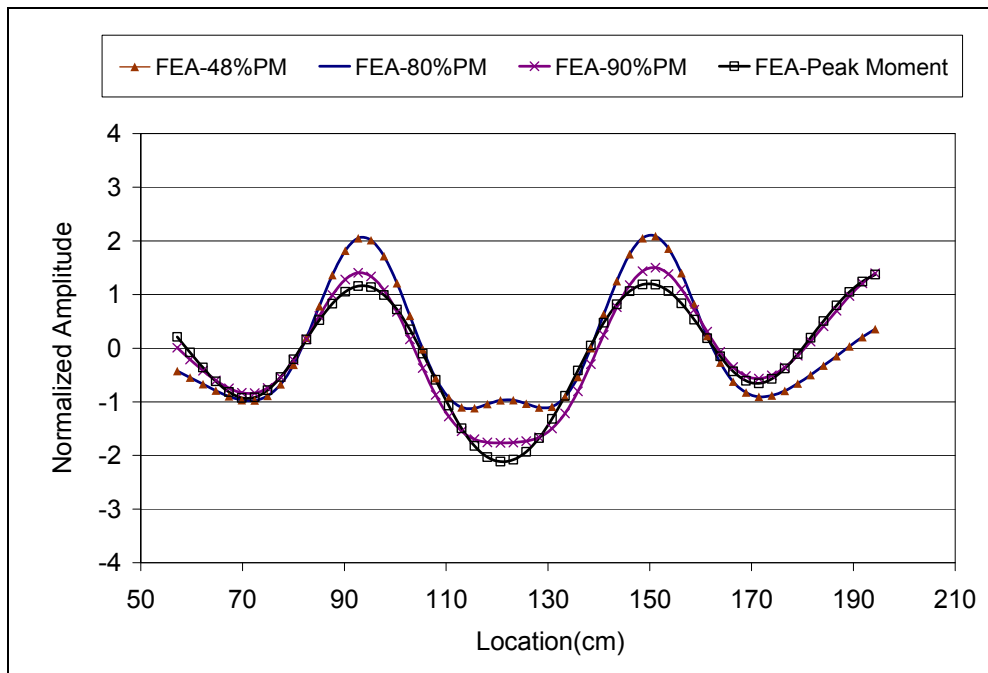
Figure 5.40 Normalized Strain Distributions for a Pressurized Pipe

163
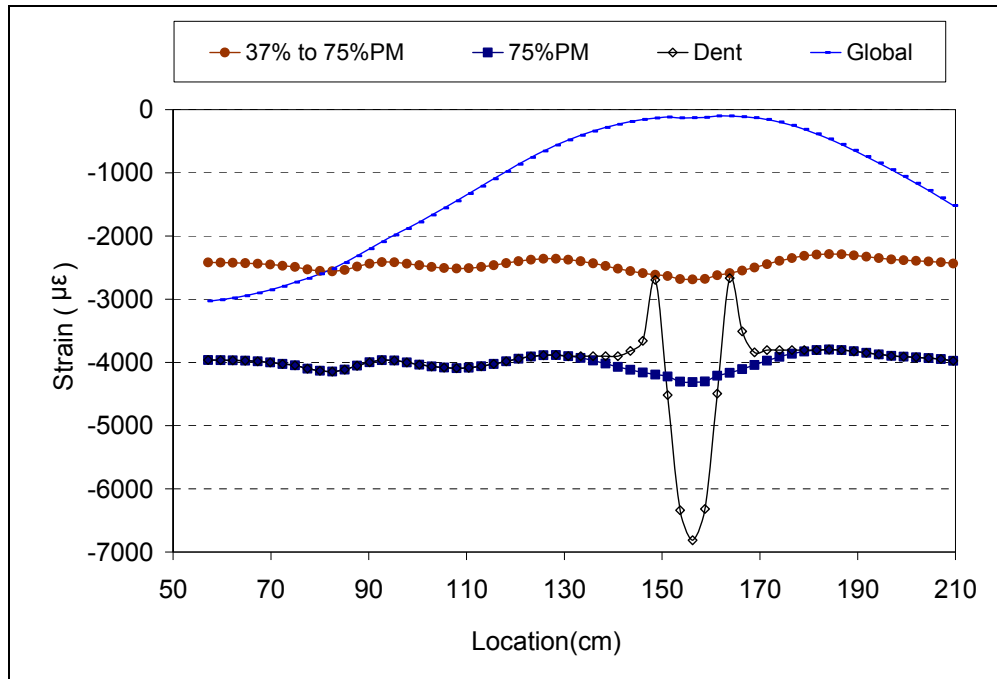
(a) Before Normalization
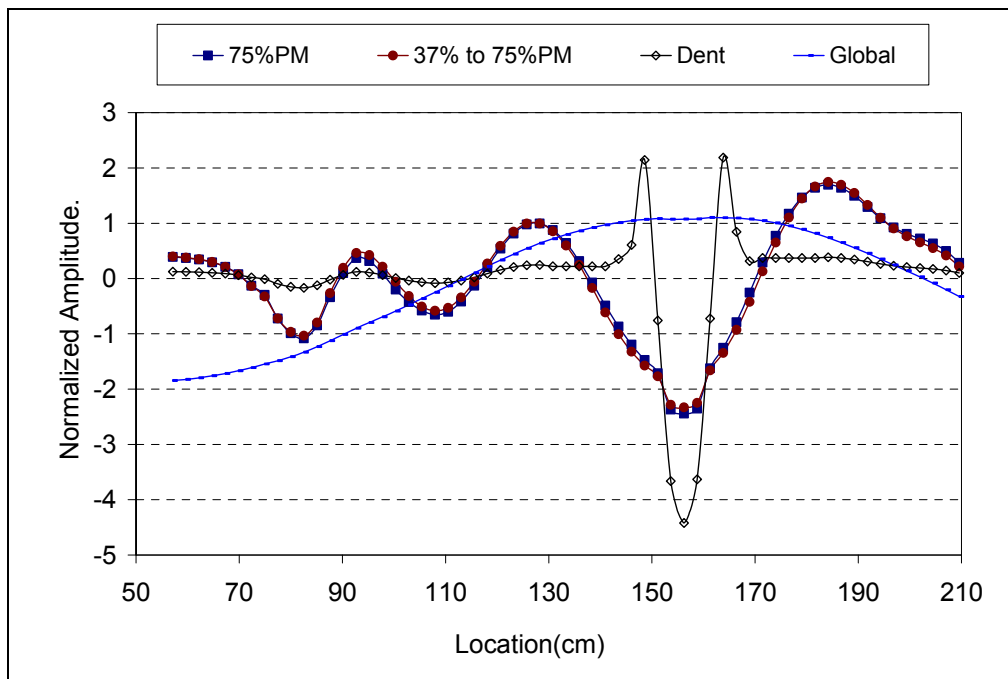
(b) After Normalization

Figure 5.41 Normalization Effect on Strain Distribution Patterns for Different
Damage Events

164
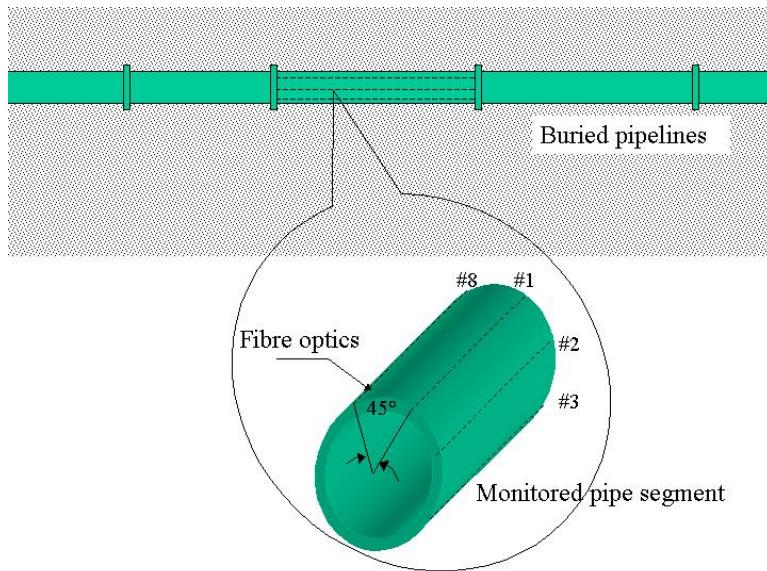
(a) Positions of Distributed Strain Sensors
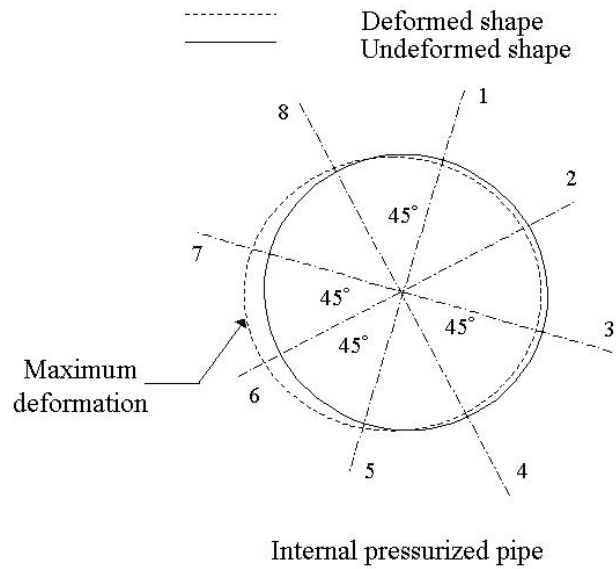
(b) Pipe-Sectional Configurations Before and After Pipe Deformation

Figure 5.42 Installations of Distributed Strain Sensors for a Field Pipeline

165
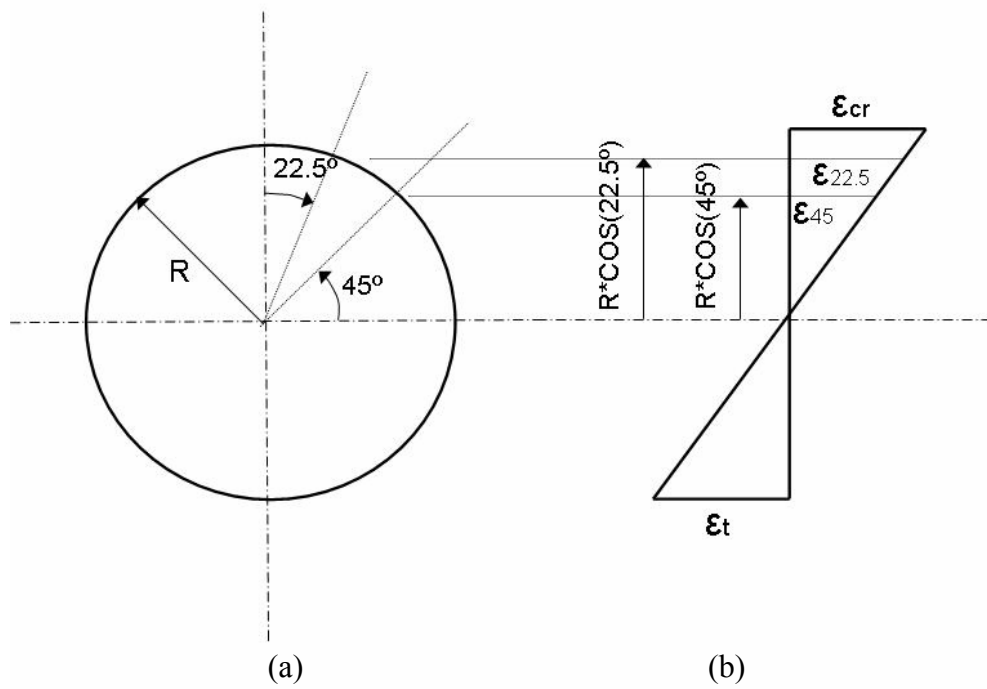
Figure 5.43 Strain Diagram in a Perfect Circle Section
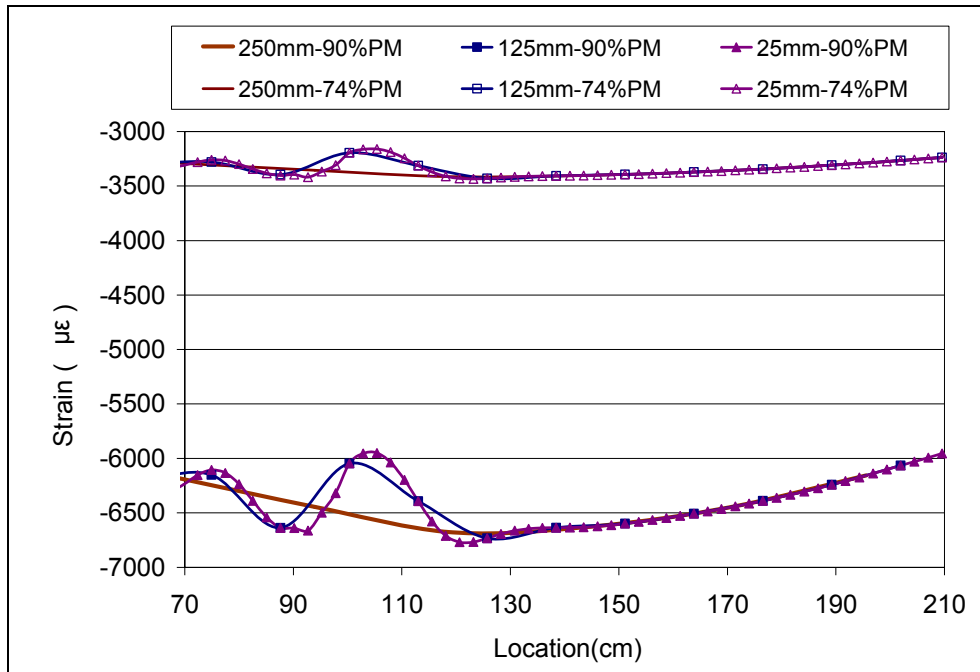
Figure 5.44 Strain Distributions in Different Measuring Spacings for
a Non-pressurized Pipe
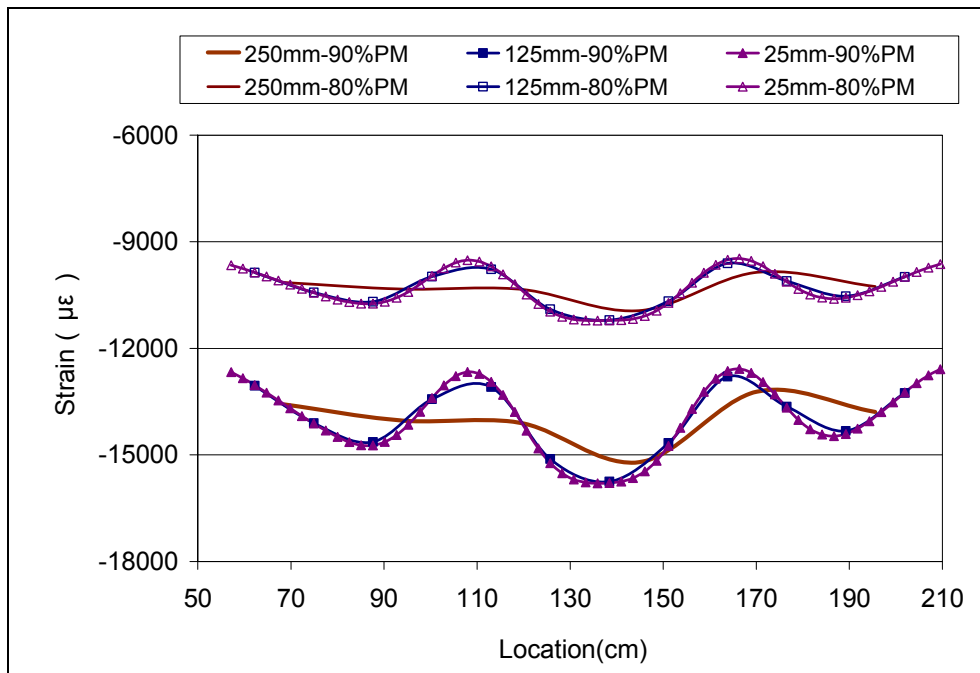
Figure 5.45 Strain Distributions in Different Measuring Spacings for
a Pressurized Pipe

167
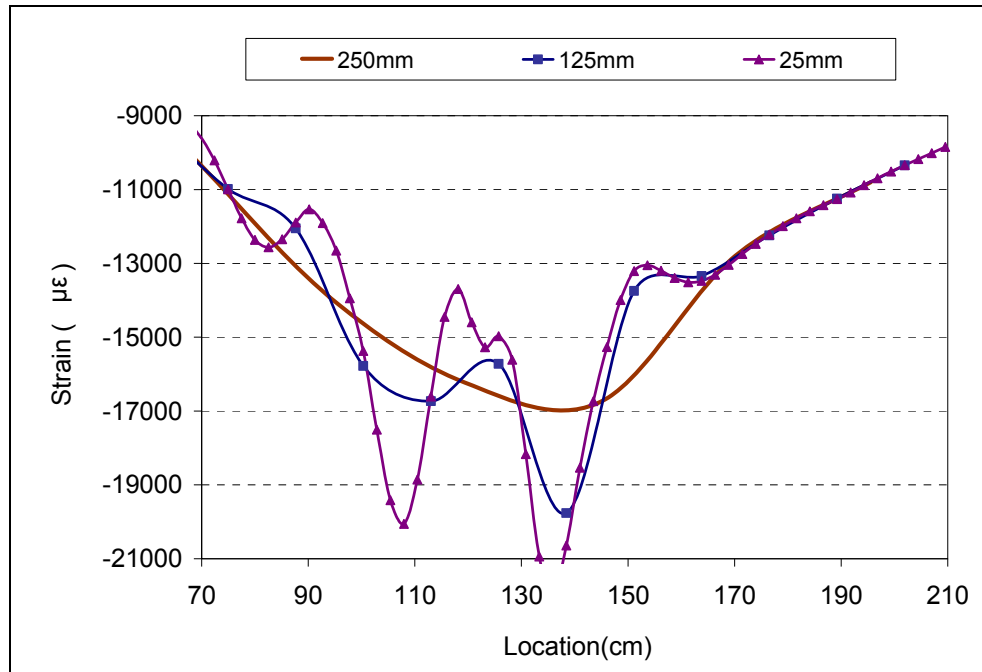
Figure 5.46 Strain Distributions in Different Measuring Spacings for a
Non-pressurized Pipe at the Peak Moment
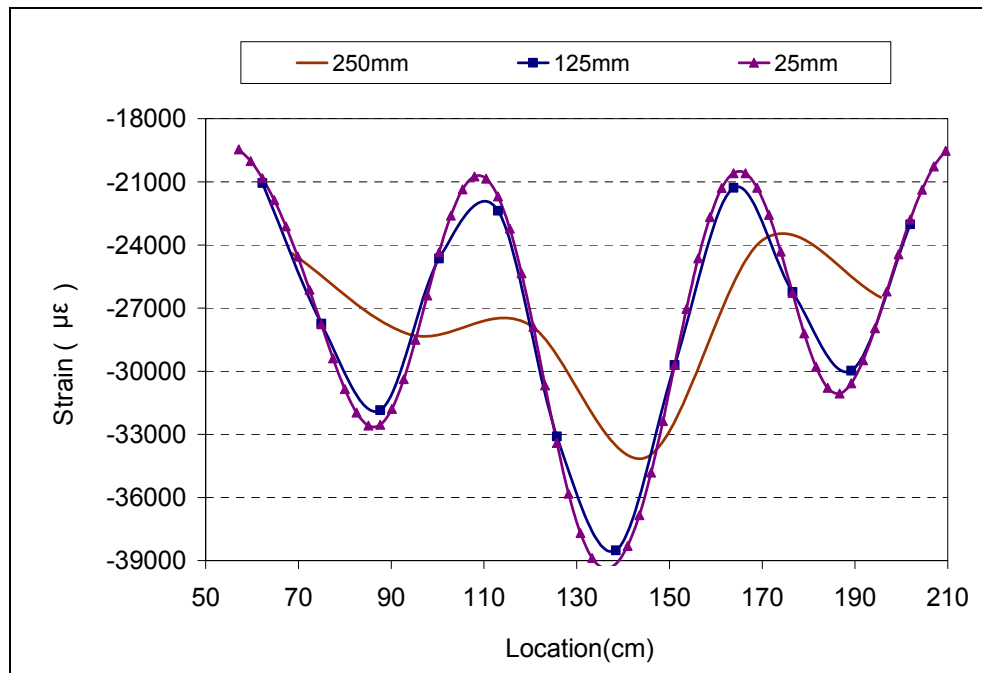
Figure 5.47 Strain Distributions in Different Measuring Spacings for a
Pressurized Pipe at the Peak Moment

168
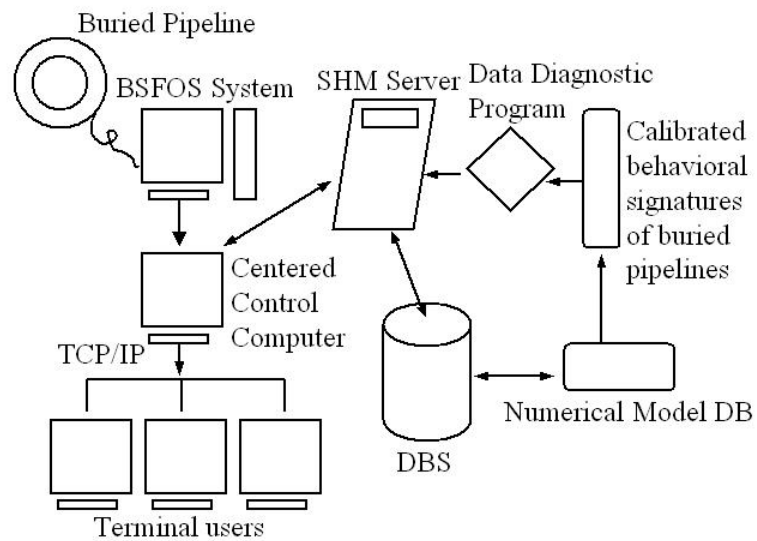
Figure 5.48 Scheme of the Developing SHM System for Buried Pipelines Buckling
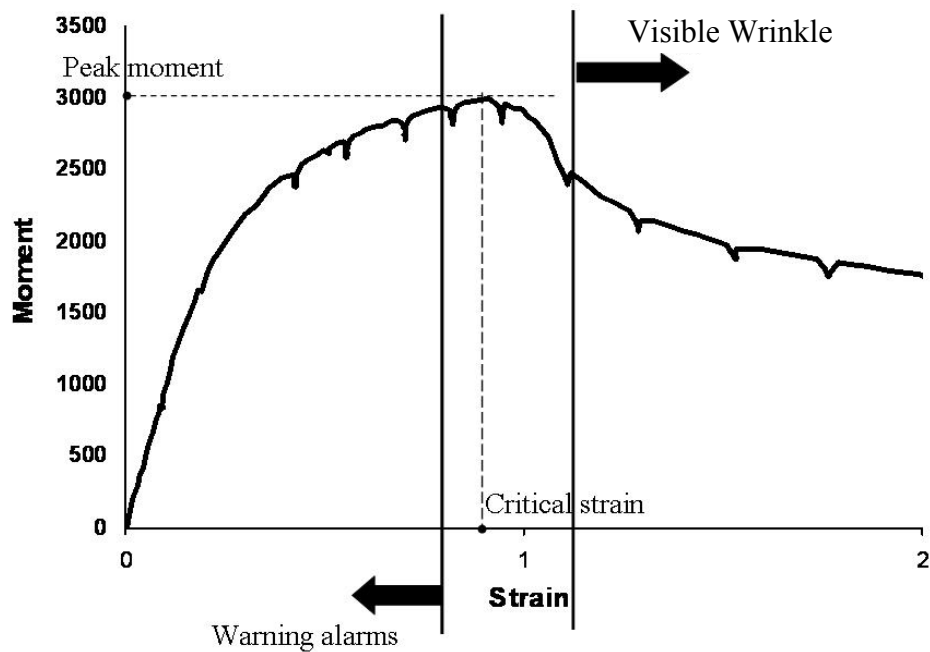
Figure 5.49 Schematic of Using the SHM System to Provide Early Warning for Pipe Wrinkling

6. PARAMETRIC STUDY

The validated FE models from Chapter 5 are used in the parametric study with different parameters. The parametric study has two purposes: to understand the effect of various parameters on the distributed strain patterns; the other is to search for appropriate threshold patterns of strain distributions in order to develop a damage detection system with an artificial neural network (ANN).

6.1 Determination of the Parameters

A total of 81 sets of FE models with different materials, pipe sizes, and loading conditions (see Table 6.1) were studied to expand the data base of the distributed strain patterns of pipe buckling. The parameters, including the material grade, D/t ratio, operating pressure, and girth weld condition, were studied. In addition, because the data base will be employed by an ANN to predict the initiation of pipe wrinkle and the ANN usually gives a better prediction in interpolation than in extrapolation, the assumptions and the selections of these parameters should be carefully considered to include all the practices by pipeline industry. Tables 6.2 and 6.3 show the material properties and geometric properties used in the parametric study, and the choice of the range for each parameter is explained in the following subsections.

The designations of the different pipe models are defined here and are used to identify the pipe models used in this chapter and in Chapter 7. The pipe models are designated as XmmTdtnnLppw.

Xmm indicates the pipe material grade. "mm" represents the steel specified minimum yielding stress (SMYS) in ksi. For instance, X80 indicates the SMYS is 80 ksi (550 MPa).

T indicates the material type. h represents new generation high-strength steel; otherwise, the material is normal strength steel.

dtnn   indicates the ratio of the outside pipe diameter to the pipe wall thickness (the D/t ratio). For example, dt40: the D/t ratio is equal to 40.

L   indicates the pattern of loading. U is the bending load and C is the axially compressive load.

pp   indicates the level of the hoop stress induced by the internal pressure as a percentage of the SMYS.

w   indicates a girth-welded pipe.

For example, X80hdt60U40w represents a new generation high-strength steel of 80 ksi, girth-welded pipe with D/t = 60, and under an internal pressure that induces 40% of SMYS in hoop stress and a bending load; X65dt40C00 represents a normal strength steel of 65 ksi, plain pipe with D/t = 40, and without internal pressure but under an axially compressive load.

6.1.1 Material Properties

Three material grades, X65 (448 MPa), X80 (550 MPa), and X100 (690 MPa), were selected, because the FEA models developed in Chapter 5 were validated within this range. In addition, as mentioned in the previous chapter, distributed strain patterns are affected by the stress-strain curve shape rather than the material strength, therefore X65 steel is considered as normal strength steel while X80 and X100 are considered as new generation high strength steel, as shown in Table 6.2. The material models employed by the FE models are the regression of the experimental data and are shown in Figures 6.1 to 6.3.

6.1.2 Geometric Properties

D/t ratios of 40, 60, and 80 were used, mainly for the same reason as that for the selection of the material properties. That is, the validated FE models were limited to the range of 39 < D/t < 79. The other reason is that this range is usually used in the pipeline industry, especially for the gas pipelines. The pipe length of at least 3.5 times the pipe diameter was used in the analysis (see Table 6.3). The length

171

chosen was to minimize the boundary condition effect and enable the wrinkle to occur away from the end of a pipe.

6.1.3 Loading Conditions

Operating pressure: Internal pressure producing hoop stresses equal to 80% of the SMYS were chosen as the upper bound of the operating pressure based on the upper limitation in CAN/CSA Z662-03 (2003). While bulge wrinkling shapes are normally observed in pressurized pipes; a diamond shape wrinkling is commonly occurred in empty or low-pressurized pipes. Therefore, in order to identify the strain distribution patterns of the diamond shape wrinkling, 0% operating pressure was selected as the lower bound of the internal pressure.

External loading conditions: two loading conditions, bending and axially compressive loads, were selected to generate distributed strain patterns. In the real world, the buried pipes always undergo extremely complicated loading conditions throughout their life cycle. These external loadings induced bending moment, shear force, and axial loads onto the line-pipe. In this study, only bending moment and axially compressive load will be considered since both of these loads generate compressive stresses in pipe walls that eventually cause the pipe buckle. Other loading conditions, such as moment gradient along a line-pipe, were not simulated in the pipe models, but were considered in developing the damage detection system in Chapter 7.

6.1.4 Manufacturing Conditions

Girth weld and cold bend are usually needed for pipe segments along a pipeline route. Earlier studies of girth-welded pipes (Yoosef-Ghodsi 1994, Dorey 2001) showed that the pipe wrinkle was found to occur either at exactly the girth weld location or in its vicinity, depending on the D/t ratio and internal pressure of the pipes. Dorey found that for a larger D/t ratio, i.e. D/t = 92, the wrinkle generally located right at the girth weld location. Both experimental and FEA results showed that girth-welded pipes and plain pipes have different strain distribution

172

patterns. Therefore, the girth weld is considered as a parameter. In addition, as shown before, the strain distribution pattern along a cold-bend pipe is unique. Therefore, the cold-bend effect will be examined for the development of the damage detection system in Chapter 7.

6.2 Effects of Parameters on the Distributed Strain Patterns

In this section, the distributed strain patterns were generated by the FE models with different parameters. The FE models include three groups of pipes, plain pipes under an external bending moment, girth-welded pipes under an external bending moment, and plain pipes under an axially compressive load (see Table 6.1). The different material grades, D/t ratios, and internal pressures were considered in each case and presented in Table 6.1. Typically, fifteen loading stages were applied in each of the 81 FE models, from 35% of the peak load before buckling to 95% of the peak load after buckling with an interval of 5% of the peak load.

The strain distributions of the three groups of pipes at selected loading stages are shown in Figures 6.4, 6.5, and 6.6, respectively. The strain distributions in all three FE models showed that the behavioural patterns (or signatures), such as a non-uniform strain distribution and a dominating strain, became more apparent when the loading approached 70% of the peak moment. Also, since the project is concerned mainly with the patterns at the different loading ranges prior to the limit point, the strain distributions shown in the parametric study, as summarized in Appendix C, are from only the loading stage of around 75% to 95% of the peak load.

As shown in Figures 6.4 to 6.6, the loading stages were not exactly at the designed loading stages with the 5% loading ratio interval, i.e. 75%, 80%, 85%, 90%, etc. The differences resulted from the limitation of the loading procedure (Riks method) in the ABAQUS. The Riks method computes the static equilibrium by considering an additional parameter, called the arc length, to solve the

relationship between the load and the deformation during an entire loading history. Consequently, users cannot exactly set the desired loading stages in the loading steps. Instead, approximate loading stages are obtained by decreasing the loading increment. The trade-off from using this method is that some FE models will have difficulty converging around the limit point because of the restriction of the maximum loading increment. This increment limitation can cause the equilibrium path to be trapped in an ill- condition in which the slope of the curve is either zero (the so-called singular point problem), or infinitely small (the so-called unstable problem). Therefore, when the user-defined loading increments do not allow the FE models to converge, the automatic loading increments set by the software were used. In these cases, the models could not yield the strain results exactly at the desired loading stages. As discussed in Chapter 5, a blister initial imperfection with peak amplitude of 20% of the wall thickness was used to model the plain pipes. However, it was found that 20% of the wall thickness for the blister imperfection was not large enough to trigger every pipe buckles at the correct (middle) locations, especially for the pipes under an axially compressive load. Tutuncu and O'Rourke (2006) used an initial imperfection up to 100% of the pipe wall thickness for plain pipes under an axial load, so that FE models could converge and produce the wrinkle at the middle of the pipe. Seven out of the 27 pipe models under an axial load were not completed successfully, two of the 7 models had wrinkles at the end of the pipes, and the rest of the models could not converge. Therefore, only 20 pipe models are available for the distributed strain patterns of the pipes under an axially compressive load.

6.2.1 Effects of Girth Weld, Loading Conditions, and Operating Pressure on Strain Distribution

Approximate 900 strain distributions were generated by the FE models for the parametric study. In this study, the strain distribution patterns affected by different parameters are the main concerns, rather than the strain amplitude. The effects of the girth weld, external loading conditions, and operating pressure on the behavioural patterns of the distributed strains are discussed below.

174

Girth weld:

Because of the apparently discontinuous surface across the girth-welded location, a dramatically fluctuating wrinkle shape occurred at this location. This type of initial imperfection caused a much earlier strain concentration at the wrinkle location that led to a large localized deformation starting in a very small curvature along the pipe. Consequently, a flat strain distribution occurred along the outside of the wrinkle location, as shown in Figures 6.5(a) and 6.5(b). This similar trend continued throughout the loading stages, e.g. from 33% of the peak moment.

Axially compressive load:

As an axially compressive load was applied in the straight pipe, before the load reached a certain level, the line-pipe remains almost straight, and the global curvature induced into the pipe was very small even during the onset of the wrinkle. Such pipe behaviour caused the distributed strains to be relatively constant in the outside of the wrinkle area along the line-pipe, as shown in Figures 6.6(a) and 6.6(b). Moreover, compared to the distributed strains along a bent pipe as shown in Figure 6.4, the wrinkle of the axially compressively loaded pipe had a sharper outward bulge, but the wrinkle shapes caused by the bending load and axial compressive load cases were not significantly different.

Operating pressure:

Regardless of the pipe geometry, material grade, and applied loads, the strain distribution patterns had the same signature. With increase in the internal pressure, the wrinkle shape changed from diamond shape (multiple bulges) for zero or low internal pressure to a single outward bulge shape for medium to high internal pressure, as shown in Figure 6.7. In Figure 6.7, an example using the X65dt60 pipes under an external bending load shows that the internal pressure acted against the inward deformation of the pipe but increased the outward bulge growth. Consequently, the corresponding strain distributions changed in wrinkle range from short-wave shape during zero internal pressure (see Figure 6.7(a)) to a dominating curve during high internal pressure, e.g., an internal pressure inducing 80% of SMYS hoop stress (see Figure 6.7(c)). The transition shape of the strain

175

distribution is shown in Figure 6.7(b) in which internal pressure induces 40% of SMYS hoop stress.

6.2.2 Effects of D/t Ratio on the Wrinkle Patterns of the Girth-welded Pipes

Due to geometric discontinuity at the girth weld location, the D/t ratio could meaningfully affect the distributed strain patterns along a girth-welded pipe. Different D/t ratios disturbed the strain distribution shape (see Figures 6.8(a) to 6.8(c)) as well as the wrinkle development along the pipes (see Figures 6.9(a) to 6.9(c)), especially for pressurized pipes.

The buckling of a girth-welded pipe is triggered by the eccentricity at the weld joint (see Figure 6.10). The eccentricity induces additional local moment and local compressive circumferential membrane stresses on the compression side of the pipe. The local moment triggers pipe winkle near the girth weld; the compressive circumferential stresses squeeze the pipe to further the inward deformation in the weld-depression. However, the inward deformation effect was reduced by the internal pressure of the pipe. Rotter studied the above effect on cylindrical shell strength, and Singer discussed ring confine effect on the strength of the pipe buckling (Teng et al. 2004). These researchers concluded that the D/t ratio was a key parameter for the local strength of the cylindrical shell structure and for the boundary conditions over the circumferentially welded zone during pipe buckling. In addition, Dorey (2001), through the observation of the experimental and FEA results, pointed that the high D/t ratio specimens had less rigid body rotation at the end caps.

The above D/t ratio effects were also revealed in the strain distributions. With an increase in the D/t ratio, three significant findings are explained as follows:

- Since local strength of the pipe decreased in the circumferentially welded area, the pipe yielded earlier in this area resulting eventually strain localization. At the loading stage 74% of the peak moment, the differential strains between maximum and minimum strains were 1500 $\mu\varepsilon$ and 2000 $\mu\varepsilon$

176

for the pipes, respectively, with the D/t ratio of 40 (see Figures 6.8(a)) and with the D/t ratio of 80 pipe (see Figure 6.8(c)).

• Since the capacity of the ring confine decreased at the girth-welded joint, more significant inward deformation in the weld-depression attracted the wrinkle to be developed closer to the girth weld location (see Figure 6.9(c)). As a result, the D/t ratio of 80 pipe had a narrower strain distribution and larger curvatures over the wrinkling area than that of the D/t ratio of 60 pipe (see Figures 6.8(c) and 6.8(b)).

• Since the pipe with the larger D/t ratio had less significant rotation at the end of the pipe than that of the pipe with the smaller D/t ratio, the smaller global curvature occurred in the larger D/t ratio pipe during pipe buckling. As a result, the overall strain distribution became flatter for the D/t ratio of 80 pipe than for the D/t ratio of 40 pipe (see Figures 6.8(a) and (b)).

6.3 Determination of the Thresholds of Monitored Signature Patterns

In this section, the main focus is on searching the threshold patterns in order to train a developed ANN. Although it was shown in the previous chapter that by monitoring strain distribution patterns, operators can track the progress of pipe buckling and detect the initiation of pipe wrinkle. The question of how to monitor the progress of buckling automatically remains an issue. The first step of automation is to provide correct and effective information, which is organized data pool for pipe wrinkling. Therefore, the data pool created from the FE models has to be analyzed and filtered. During this process, the desired data are extracted from the data pool. Through the observation of the experimental results in Chapters 3 and 4, and the studies of the strain distribution patterns in Chapter 5, three types of strain distribution patterns are considered as signature patterns to identify the pipeline as being in the safe, warning, or wrinkling condition. The three patterns are shown in Figure 6.11. In the safe condition, the pipe segment presents a behavioural characteristic within the proportional limit (elastic) range. In the warning condition, the monitoring system reveals abnormal strains along the strain distribution to pipe operators. The wrinkling condition is defined as the

onset of wrinkle in the pipe segment. Accordingly, the threshold pattern for the safe condition can be determined by the following observations of the pipe behaviour and strain distribution:

- The observation of the moment (or axial load) versus strain curves showed that the maximum strain in the pipe was close to the proportional limit when the loading stage was near 40% of the peak load (see Figures 5.14 to 5.21).
- As the data pool of the distributed strains reveals, the ratio of the maximum strain in the pipe at the 40% of the peak moment (load) to the maximum strain at the peak moment (load) is less than 20%.
- The strains were relatively constant in the strain distribution along the line-pipe, and, thus, the distribution shape was relatively flat (see Figures 6.4(a) and 6.6(a)).

Therefore, the strain distribution at 40% of the peak load is used as the threshold patterns for the safe condition.

Because observation of the strain distribution patterns and the load versus the deformation curves alone cannot determine the distinct thresholds for the warning condition and wrinkling condition, the statistical analysis is used to determine the threshold patterns corresponding to these two conditions. The procedures to find the threshold patterns for these two conditions are explained here, and complete statistical analysis is presented in the following subsections.

First, the complicated strain distributions were converted into simple curves in the strain-ratio-versus-moment-ratio plots as shown in Figure 6.12(a), so that the loading stages corresponding to the possible threshold patterns as shown in Figure 6.12(b) can be selected for a pipe model. Next, the selected loading stages acquired from the different pipe models were analyzed statistically to find a reasonable loading range corresponding to the possible threshold patterns. Correlation analysis was processed for the possible threshold patterns in the subsequent step. Thereby, the threshold patterns of the warning condition and

178

wrinkling condition were determined for the three pipe groups: plain pipe under a bend load, girth-welded pipe under a bend load, and plain pipe under an axially compressive load. The calculations of the correlation coefficient and the strain ratios above were explained in Sections 5.1.3.3 and 5.2.2.2, respectively.

6.3.1 Determination of the Thresholds from the Strain Ratio versus Moment Ratio Plots

Strain ratio versus moment (or loading) ratio curves were produced by the results of the FEA for different pipe groups including the plain pipes under a bend load, girth-welded pipes under a bend load, and plain pipes under an axially compressive load, and shown respectively in Figures 6.13 to 6.15. Each strain ratio is the ratio of the local maximum strain to the average strain of the distributed strains on the compression side of the pipe model at a specific loading stage. The strain ratio shown in these figures had processed baseline adjustment referring to the strain ratio at the first loading stage (or called initial strain ratio) as 1.0, and the strain ratios at the other loading stages were divided by this initial strain ratio. The investigation of the thresholds began by focusing on plain pipes under a bending load, shown in Figure 6.13. The possible threshold patterns were determined from the strain ratio versus moment ratio curves by searching for slope-change points. As can be seen in Figure 6.12, when the strain distribution remains relatively constant, the strain ratio is equal approximately to a unit, and a trend line over the earlier loading stages, e.g. from 38% to 50% of the peak moment shown in Figure 6.13, is approximately linear. As strains develop non-uniformly along the pipe segment, a point representing the strain ratio in this situation starts to deviate from the trend line on the plot. This point is called the first slope-change point (or the first point) as shown in Figure 6.12(a).

In addition, once the pipe starts wrinkling, the local strain at the wrinkling location increases more rapidly than does the average strain on the pipe. A significant slope change occurs on the strain ratio versus moment ratio plot, and a point intersecting at two straight lines is defined as the second point, as shown in

179

Figure 6.12(a). Theoretically, occurrence of a dominating pipe wrinkle leads to the pipe softening; consequently, the capacity of the pipe starts to drop from the peak load (or the limit point), and the localized strain grows rapidly faster than ever at the wrinkle location. However, the pipe wrinkling initiates before the applied loading attains the limit point, and, at this time, the strain ratio growth has become evident. Accordingly, two lines were used to acquire the second point: the one is a tangent line starts from the first point; the other is a secant line connecting the last two stages before limit point.

The loading stages corresponding to the first point and second point were selected for a pipe model. The above procedure is applied to different pipe models in the group, i.e. plain pipes under a bending load. A loading range (or the range of the moment ratios) for this pipe group was determined by averaging the selected moment ratios of the different pipes and by computing their 95% of confident interval in the group, as shown in Tables 6.4. However, the first point cannot be determined for three of twenty-seven curves, and, therefore, a total of 24 results are shown in Table 6.4. The same procedures were applied to the other pipe groups: girth-welded pipes under a bending load and plain pipes under an axial load.

For the girth-welded pipes, the slope-change points were obtained from only 8 FE models. The reason is that for most of the pipe models, before apparent slope growth, the strain ratio versus moment ratio curve remains gradually changing, as shown in Figure 6.14. Thus, the first point and consequently the second point cannot be determined for these girth-welded pipe models. The strain ratio trend of the girth-weld pipes probably resulted from the occurrence of strain concentration in the very early loading stage and the absence of wave shape along the strain distribution prior to the rapid growth of the strain concentration. The first point occurs at the early stage, e.g., the loading stage at 69.8% of the peak moment, and shown in Table 6.4.

180

For the plain pipes under an axially compressive load, as shown in Figure 6.15, the strain ratio curve presents a relatively flat line until the slope rapidly grows at the onset of the pipe wrinkling. Thus, the first point and consequently the second point can only be determined for several pipe models. The trend of the strain-ratio development can be explained by observing the strain distributions in Figure 6.6. The strain distribution patterns show that the distributed strains remain relatively uniform along the line-pipe during the loading stages until the loading stage at 85% the peak load (see Figure 6.6(b)). As a result, the slope of the strain ratio grows very slowly before wrinkle initiates. In addition, the second point occurs in the loading stage closer to the limit point for this pipe group than for the other groups, e.g. the loading stage at 92.8% of the peak load, as shown in Table 6.4.

In addition to the above method, the second points can be found from the U of A test database. The collected threshold ranges correspond to the inception of the pipe wrinkle or occurrence of the critical strain, and they are shown in Table 6.5.

The results from the above two databases are in agreement, and the test results show a higher threshold level for most cases except the girth-welded pipes. The reason that the FE simulation yielded higher threshold level for the girth-welded pipes is probably because the FE models generated the larger initial slope. The FEA is quite sensitive to sudden discontinuity in the pipe geometry at the girth-welded location. The real initial imperfections (or offset) are probably smaller and less sensitive. Consequently, the far earlier strain concentration occurring in the girth-welded pipe models probably can be mitigated in real pipes, and the initial slope growth can be smaller for the real pipes than for the FE models.

Through the analysis of the strain ratio versus moment ratio plots, Tables 6.4 and 6.5 shows that the ranges of the moment ratios corresponding to the possible threshold patterns was found to be from 67% to 81% of the peak moment for the warning condition and from 78% to 98% of the peak moment for the wrinkling condition.

181

6.3.2 Determination of the Thresholds from the Pattern Correlation Analysis

As mentioned, buried pipes' deterioration should be monitored based on the qualitative strain patterns rather than the magnitude of structural responses; moreover, the threshold patterns determined here are used to train ANN to identify pipe status. Therefore, the principle to determine the threshold patterns focus more on the distinction of the patterns, which increases ANN's ability to assess the pipe buckling conditions. Through the investigation for the strain ratio versus moment ratio curves, the preliminary threshold ranges for the warning and wrinkling conditions were determined to be from 70% of the peak moment to 95% of the peak moment. To determine the threshold patterns from the selected threshold ranges above, the other statistical method, correlation analysis, will be used. The Pearson product-moment correlation coefficient (Eq. 5.3) was used to examine the similarity of the strain distribution patterns in the selected threshold ranges. As mentioned, this correlation coefficient is used to evaluate the strength of the linear relationship between two variables and any departure of the two variables from independence. Therefore, it is reasonable to use the correlation coefficient to confirm the threshold patterns for the safe, warning, and wrinkling conditions and to preliminarily evaluate whether the threshold patterns are distinct from one another. In the correlation analysis, each pair of variables is a pair of strains, and the each pair of strains was acquired at the same location in respectively two strain distributions where a set of distributed strains was obtained from the reference strain distribution pattern, and the other set was obtained from the possible threshold patterns corresponding to these loading stages from 70% of the peak moment to 95% of the peak moment. The reference strain distribution patterns were the patterns at 40% of the peak moment which are referred to as being in the safe condition and within proportional limit range. As the applied loading increases during pipe buckling, a pipe behaviour changes from elastic behaviour to inelastic behaviour in some locations along the pipe. Consequently, the relationship between the each pair of the strains at these locations deviates from the previous linear relationship, and the deviation

182

becomes larger as the strains localization becomes more serious at these locations during pipe wrinkling. As a result, the correlation of these two strain distribution patterns will decrease. A smaller correlation coefficient represents lower correlation between two patterns and shows that these two patterns are more distinct. Researchers have not yet agreed about what guidelines should be used for interpreting a correlation coefficient. Cohen et al. (2003), for example, have suggested a coefficient from 0.1 to 0.3 represents a weak correlation, while a coefficient over 0.5 represents a strong correlation. On the other hand, Montgomery et al. (2006) pointed out that, in general, a correlation coefficient between 0.8 and 1.0 represents a strong correlation, and a coefficient smaller than 0.5 represents a weak correlation. According to these guidelines, when the coefficient is around 0.5, the correlation between two patterns should be weak enough.

For the 24 plain pipes under a bend load, the correlation between the selected threshold patterns and the strain distribution pattern in the safe condition is shown in Table 6.6. The strain distribution pattern in the safe condition presents a relative flat distribution shape. As expected, the dominant strain concentration becomes more apparent with increase of the deformation or loading, e.g. loading from 70% to 95% of the peak moment, the correlation coefficient decays from 0.64 to 0.48. The coefficients are close to 0.5, so that the ANN models could distinguish safe condition from other conditions, i.e. warning and wrinkle.

The previous method, strain ratio versus moment ratio plots, revealed that the threshold patterns for the warning condition should consider the patterns at the loading stages from 68% to 81% of the peak moment, and therefore, the patterns at 70%, 75%, and 80% of the peak moment are possible candidates. Further considering the lowest similarity between safe pattern and warning pattern, the pattern at 75% of the peak moment is best one, and the corresponding correlation coefficient is 0.52 (see Table 6.6).

To determine the threshold pattern for the wrinkling condition, the possible threshold patterns at from 80% to 95% of the peak moment were compared with the patterns at 75% of the peak moment. Table 6.6 shows that correlation coefficient is larger than 0.8 for all comparison. It means that there is a strong correlation between the warning pattern and wrinkling pattern if the strain distribution pattern at 75% of the peak moment is used to be as the threshold pattern of the warning condition. Consequently, ANN models can probably not be able to identify the difference between these two patterns. Because a strong correlation between the warning and wrinkling patterns needs to be prevented, the correlation coefficient needs to be smaller than 0.8. Therefore, the pattern at the earlier loading stage, i.e. 70% of the peak moment was chosen as the threshold pattern of the warning condition. Further examining the similarity of the patterns, Table 6.6 presents the results of the correlation analysis for the selected threshold patterns and the strain distribution pattern at 70% of the peak moment. Most of the coefficients are smaller than 0.8, and the pattern at 95% of the peak moment acquire smallest coefficient, 0.7.

Though the pattern at 95% of the peak moment is distinct from the warning pattern, it is expected that pipe wrinkling can be detected at an earlier loading stage, and, thus, three experimental results obtained from the previous experimental programs were used to do this examination. The moment (loading) ratio versus strain ratio plots from these experimental results are shown in Figures 6.16 to 6.18. The definition of the moment ratio is the same as that used in Figure 6.12, but the strain ratio was defined as the maximum compressive strain at a loading stage divided by the strain at the limit point (the critical strain). Figure 6.16 shows that the relationship of the moment ratios and strain ratios for a X100h pipe with the D/t ratio of 69 under a bend load. As a moment applied to 95% of the peak moment, the corresponding compressive strain ratio approached to 80% of the critical strain and grew in a much quick pace. Accordingly, the threshold moment (loading) ratio should be selected at an earlier loading stage. Table 6.6 shows that the pattern at 90% of the peak moment has the second

smallest coefficient, 0.76, and therefore this pattern is probably a good candidate. In addition to Figure 6.16, Figures 6.17 and 6.18 shows that strain ratios at this loading stage were less than 65% of the critical strain. Figures 6.17 and 6.18 were created respectively for an X70 pipe with the D/t ratio of 88 under an axially compressive load and for an X80 pipe with the D/t ratio of 55 under a bend load.

Based on the above studies, the threshold patterns were determined as the patterns at 40%, 70%, and 90% of the peak moment for the safe, warning, and wrinkle conditions, respectively. Figures 6.19 to 6.21 present these threshold patterns, which have been adjusted according to the baseline. In addition, Tables 6.7 and 6.8 reveals the strong correlation among the selected threshold patterns for the girth-welded pipes and axial loading pipes. This correlation probably influences the developed ANN models to classify the distributed strain patterns into the three pipe conditions. This issue will be discussed in Chapter 7.

The discussion in this chapter has shown that even though the possible threshold patterns were selected through using the moment ratios, the strain distribution patterns override the strain magnitude as the key signatures to be monitored in the developed decision-making system. Also, the ANN trained by the threshold patterns is expected to detect pipe wrinkling before the maximum strain on a pipe approaches 65% of the critical strain.

Table 6.1   Parameter Matrix

Pipe Models	External Loading Conditions	Steel Grade	D/t	Internal Pressure SMYS
Plain pipes	Bending moment	X65	40	0%, 40%, 80%
			60	0%, 40%, 80%
			80	0%, 40%, 80%
		X80h	40	0%, 40%, 80%
			60	0%, 40%, 80%
			80	0%, 40%, 80%
		X100h	40	0%, 40%, 80%
			60	0%, 40%, 80%
			80	0%, 40%, 80%
	Axially compressive load	X65	40	0%, 40%, 80%
			60	0%, 40%, 80%
			80	0%, 40%, 80%
		X80h	40	0%, 40%, 80%
			60	0%, 40%, 80%
			80	0%, 40%, 80%
		X100h	40	0%, 40%, 80%
			60	0%, 40%, 80%
			80	0%, 40%, 80%
Girth-welded pipes	Bending moment	X65	40	0%, 40%, 80%
			60	0%, 40%, 80%
			80	0%, 40%, 80%
		X80h	40	0%, 40%, 80%
			60	0%, 40%, 80%
			80	0%, 40%, 80%
		X100h	40	0%, 40%, 80%
			60	0%, 40%, 80%
			80	0%, 40%, 80%

186

Table 6.2 Pipe Material Models Used for Parametric Study

Grade	(A) Proportional Limit (MPa)	(B) Nominal Yield Stress (MPa)	(C) Model Yield Stress (MPa)	(A)/(C)	(C)/(B)	Young's Modulus (MPa)
X65	320.3	448	492.8	0.71	1.10	200000.0
X80h	277.0	550	510.22	0.54	0.93	196282.6
X100h	357.1	690	625.55	0.57	0.91	200016.7

Table 6.3 Pipe Geometry Used for Parametric Study

D/t	Diameters (mm)	WT (mm)	Length (mm)	L/D	L/r	Models Modified from
40	610	15.24	2667	4.4	8.8	Pipe#6 (D/t=39)
60	762	12.70	2667	3.5	7.0	Pipe#12(D/t=58)
80	508	6.35	2667	5.2	10.4	NPS20 (D/t=79)
r: radius of pipe section						

Table 6.4 Loading Stages (% of the Peak Load) Corresponding to Slope Change Points from FEA

	Plain Pipes under Bend		Girth-welded Pipes under Bend		Plain Pipes under Axial Compression	
	1st point (Warning)	2nd point (Wrinkle)	1st point (Warning)	2nd point (Wrinkle)	1st point (Warning)	2nd point (Wrinkle)
Available Samples	24	24	8	8	5	5
Average	72.0	85.2	69.8	84.9	79.2	92.8
St. D	4.107	3.279	2.252	0.534	2.168	2.588
95%CI	[70.4,73.6]	[81.4,88.9]	[67.2,72.3]	[83.4,84.6]	[76.7,81.6]	[89.9,95.7]

Table 6.5 Loading Stages (% of the Peak Load) Corresponding to Slope Change Points from the U of A Experimental Database

	Plain Pipes under Bend	Girth-welded Pipes under bend	Plain Pipes under Axial Compression	Cold-bended Pipes under Bend
	2nd point (Wrinkle)	2nd point (Wrinkle)	2nd point (Wrinkle)	2nd point (Wrinkle)
Available Samples	11	9	4	8
Average	88.5	83.3	97.2	96.8
St. D	7.100	9.430	0.960	1.890
95%CI	[84.3,92.7]	[77.1,89.5]	[96.3,98.1]	[95.5,98.1]

Table 6.6 Correlation Coefficient for the Threshold Patterns of Plain Pipes under Bend

	Compared with the Pattern at 40% of the Peak Load(PL.)		Compared with the Pattern at 70% of the Peak Load(PL.)		Compared with the Pattern at 75 % of the Peak Load(PL.)	
Loading Stage	Avg.	St D.	Avg.	St D.	Avg.	St D.
70%of the PL.	64.7%	0.343				
75%of the PL.	52.9%	0.336	78.7%	0.359		
80%of the PL.	56.2%	0.341	81.8%	0.327	95.1%	0.199
85%of the PL.	52.5%	0.339	78.0%	0.341	94.2%	0.204
90%of the PL.	52.2%	0.347	76.1%	0.337	89.9%	0.219
95%of the PL.	48.2%	0.345	70.8%	0.340	82.5%	0.330

Table 6.7 Correlation Coefficient for the Threshold Patterns of Girth Weld Pipes under Bend

	Compared with the Pattern at 40% of the Peak Load(PL.)		Compared with the Pattern at 70% of the Peak Load(PL.)	
Loading Stage	Avg.	St D.	Avg.	St D.
70%of the PL.	22.5%	0.125		
75%of the PL.	25.1%	0.161	96.9%	0.152
80%of the PL.	23.5%	0.141	99.3%	0.006
85%of the PL.	24.3%	0.151	98.4%	0.009
90%of the PL.	25.6%	0.160	96.8%	0.013
95%of the PL.	27.8%	0.173	93.8%	0.022

Table 6.8 Correlation Coefficient for the Threshold Patterns of Plain Pipes under Axial Load

Loading Stage	Compared with the Pattern at 40% of the Peak Load(PL.)		Compared with the Pattern at 70% of the Peak Load(PL.)	
	Avg.	St D.	Avg.	St D.
70%of the PL.	91.8%	0.177		
75%of the PL.	N.A.	N.A.	N.A.	N.A.
80%of the PL.	N.A.	N.A.	N.A.	N.A.
85%of the PL.	N.A.	N.A.	N.A.	N.A.
90%of the PL.	89.9%	0.169	98.6%	0.038
95%of the PL.	87.9%	0.146	96.4%	0.053
N.A.: not available				
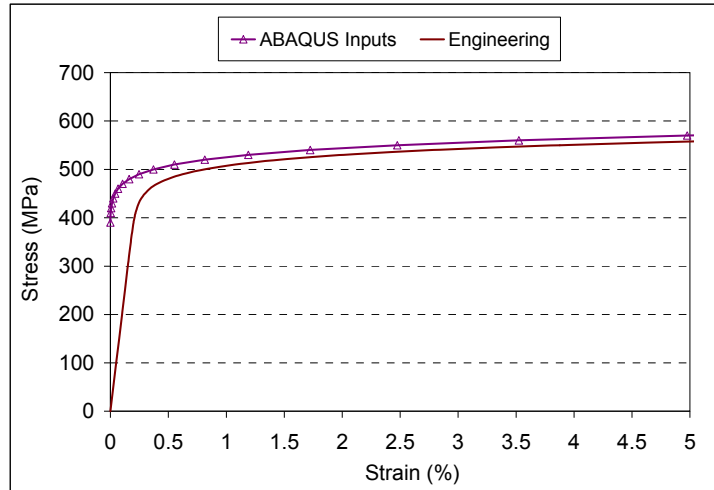
Figure 6.1 Stress-Strain Curves for Pipe Materials X65
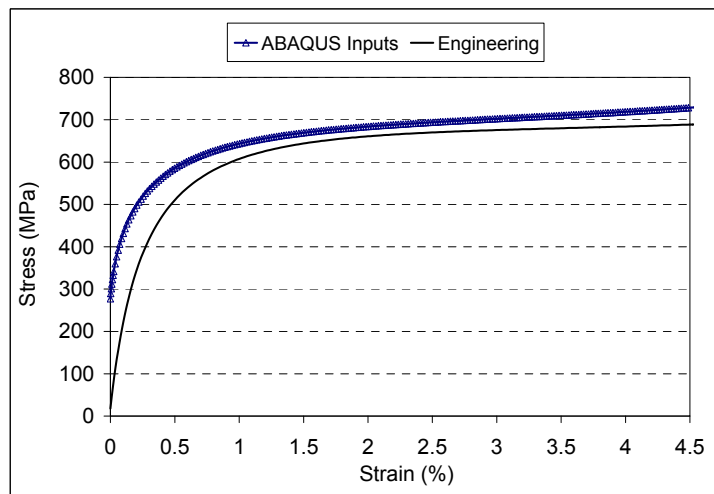
Figure 6.2 Stress-Strain Curves for Pipe Materials X80h
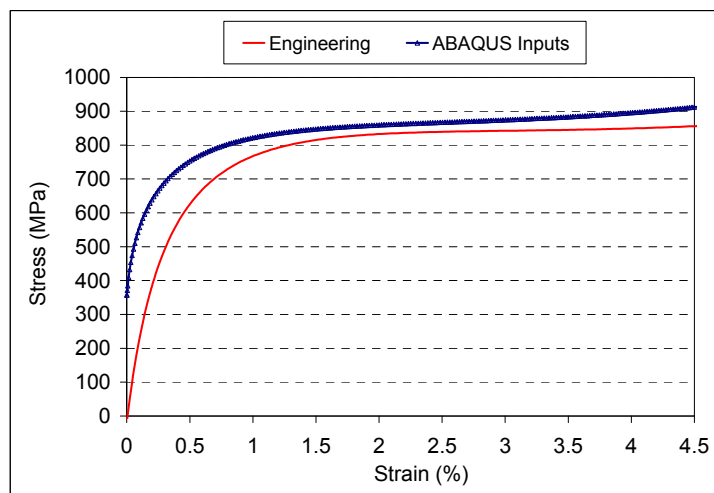
Figure 6.3 Stress-Strain Curves for Pipe Materials X100h
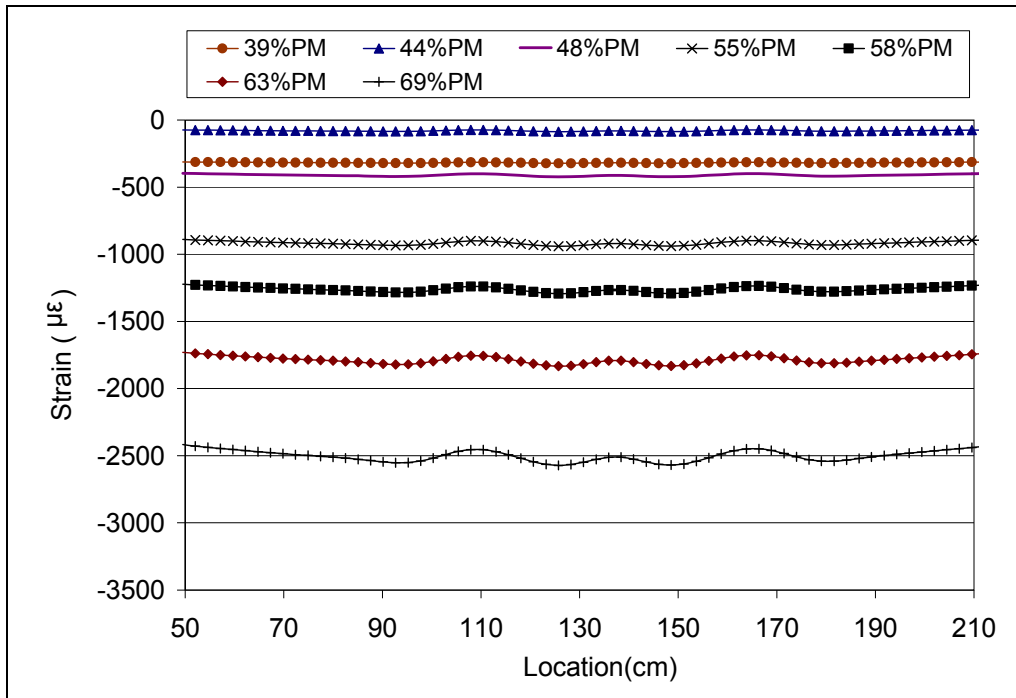
191

(a) Loading Stages before 70% of the Peak Moment
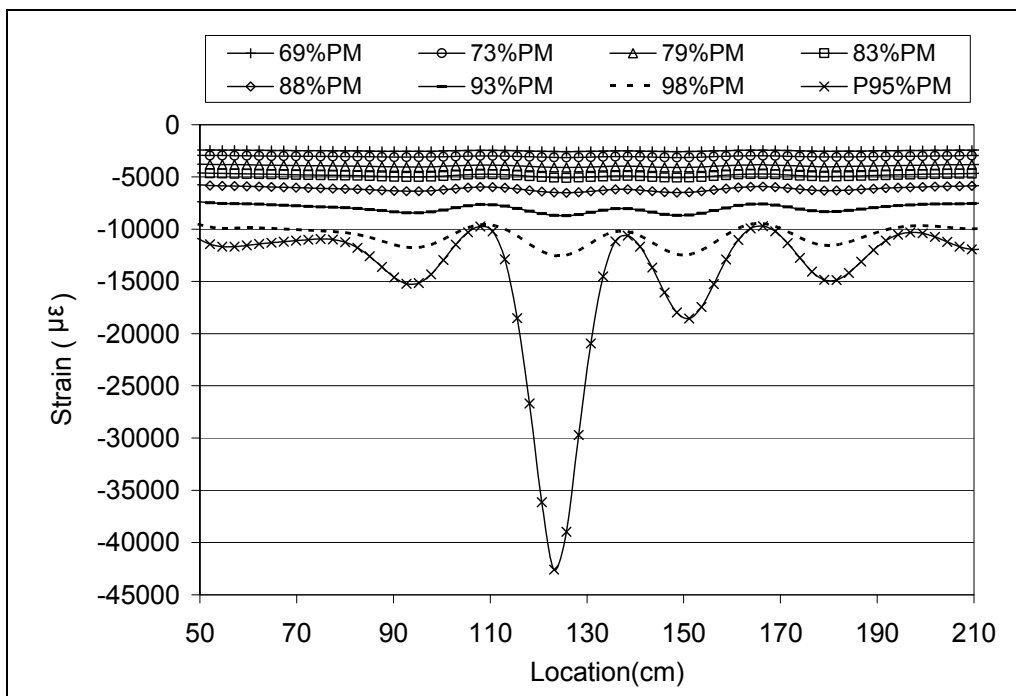
(b) Loading Stages after 70% of the Peak Moment

Figure 6.4 Strain Distributions for a Plain Pipe under Bend Load
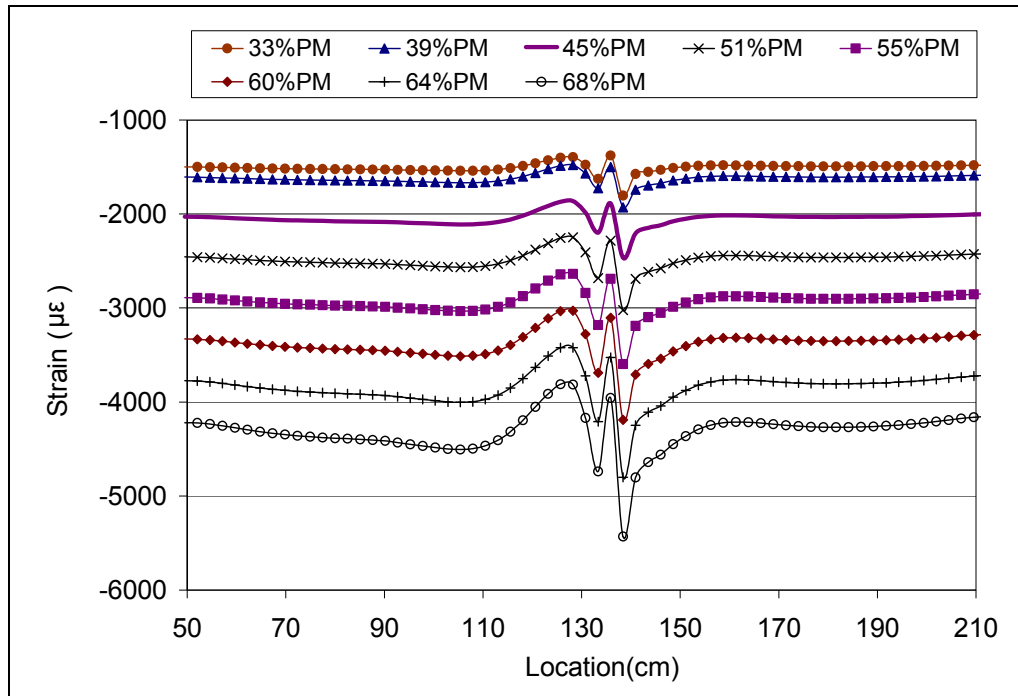
(a) Loading Stages before 70% of the Peak Moment
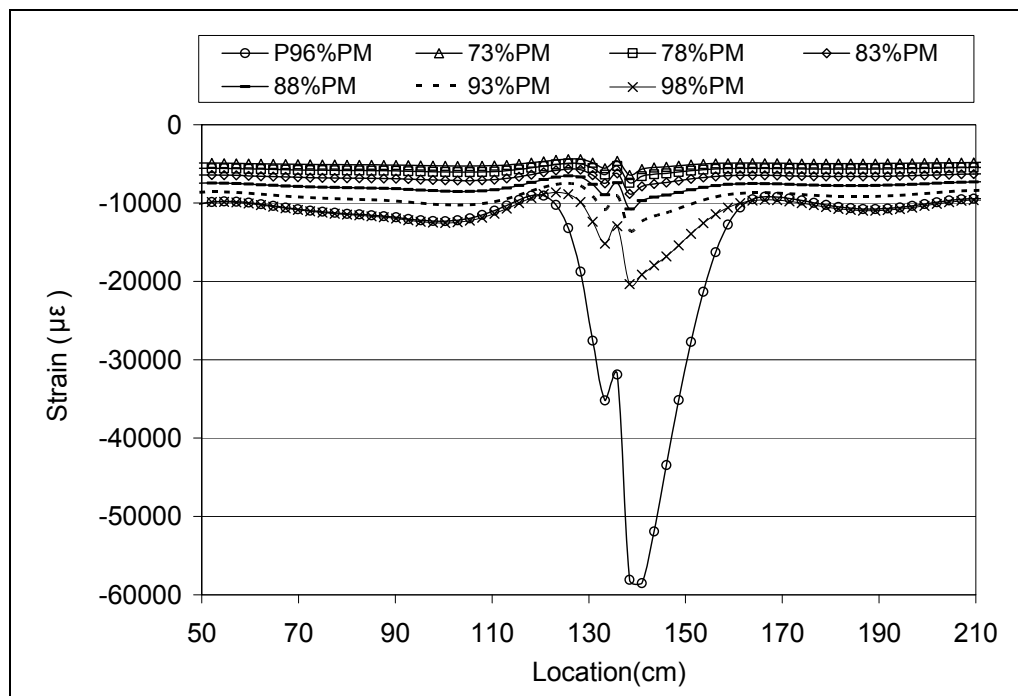
(b) Loading Stages after 70% of the Peak Moment

Figure 6.5 Strain Distributions for a Girth-welded Pipe under Bend Load
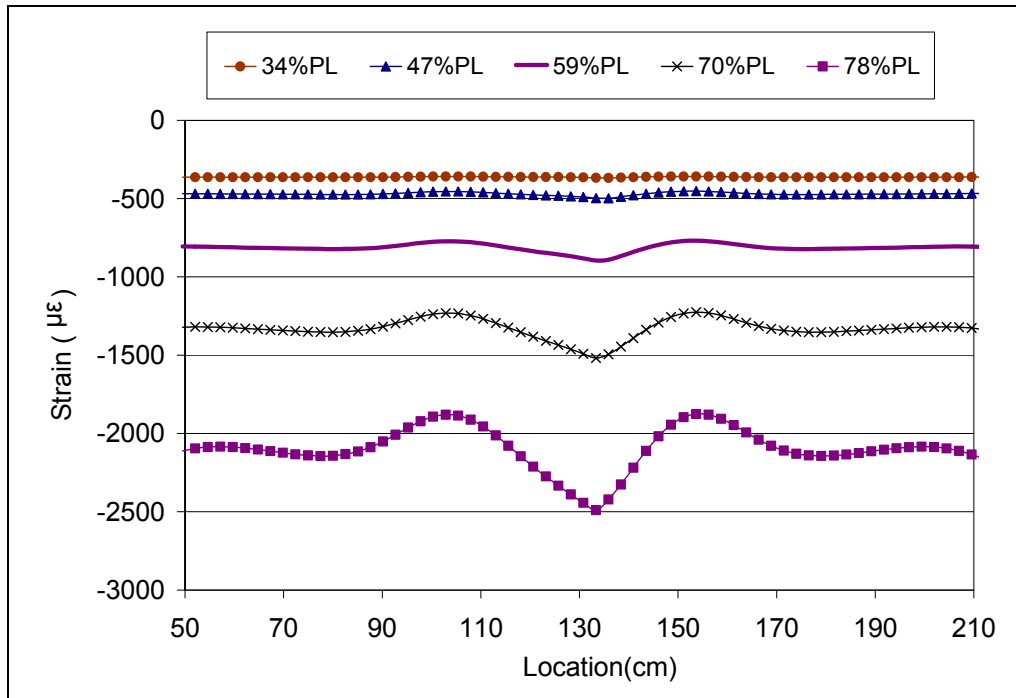
193

(a) Loading Stages before 70% of the Peak Moment
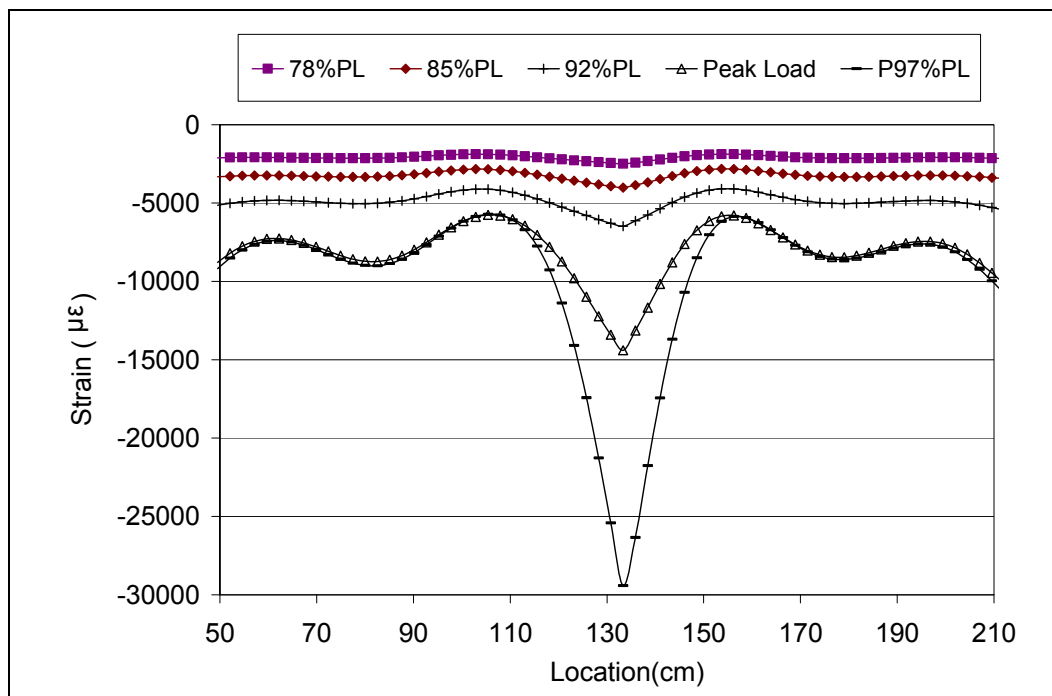
(b) Loading Stages after 70% of the Peak Moment

Figure 6.6 Strain Distributions for a Plain Pipe under Axially Compressive Load
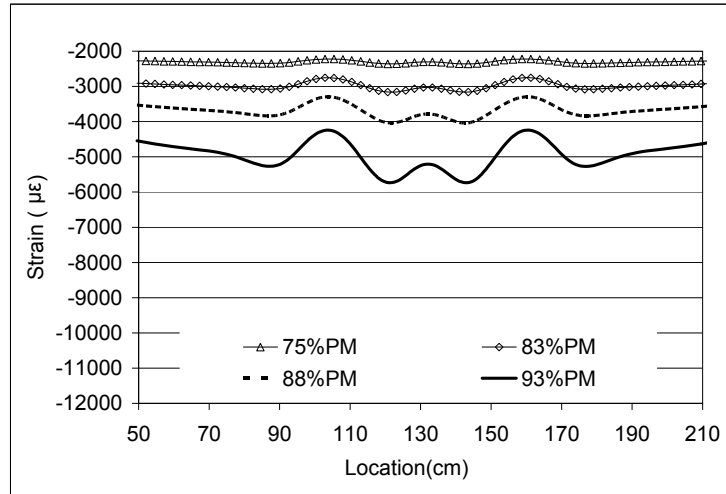
(a) Pipe Model X65dt60U00
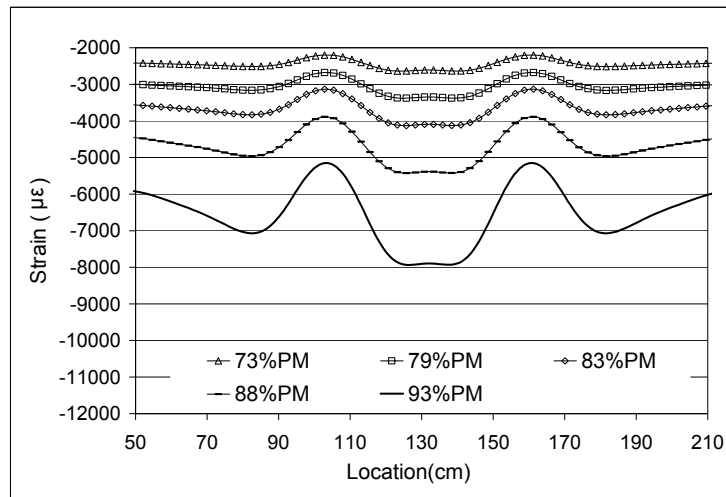
(b) Pipe Model X65dt60U40
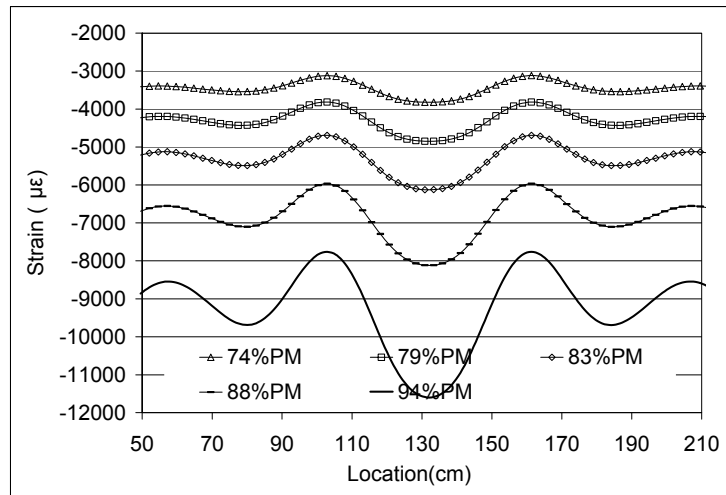
(c) Pipe Model X65dt60U80

Figure 6.7 Operating Pressure Effect on Strain Distributions for Plain Pipes

195
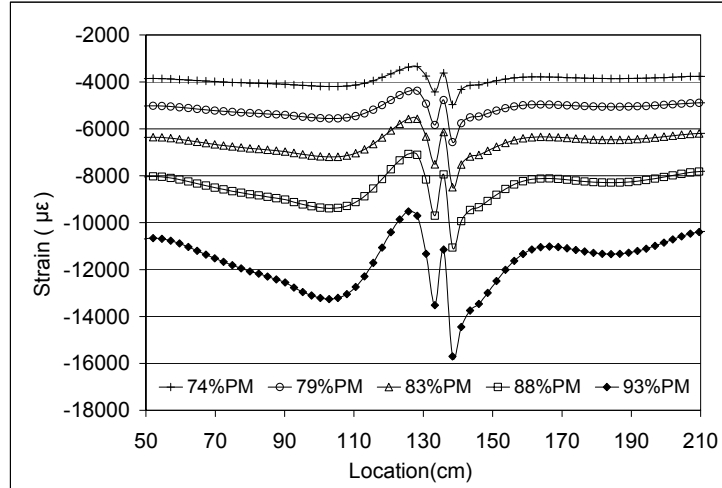
(a) Pipe Model X80hdt40U80w
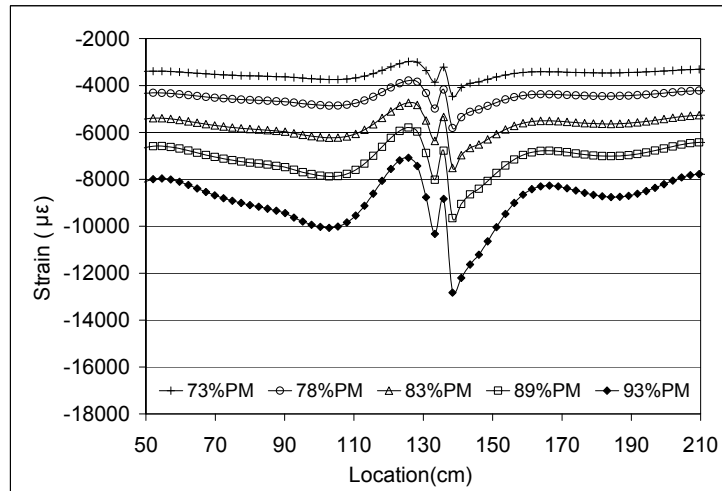
(b) Pipe Model X80hdt60U80w
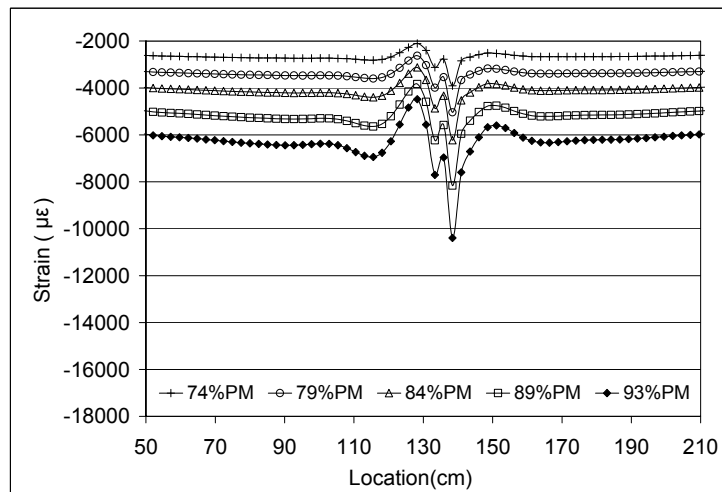
(c) Pipe Model X80hdt80U80w

Figure 6.8 D/t Ratios Effect on Strain Distributions for Girth-welded Pipes
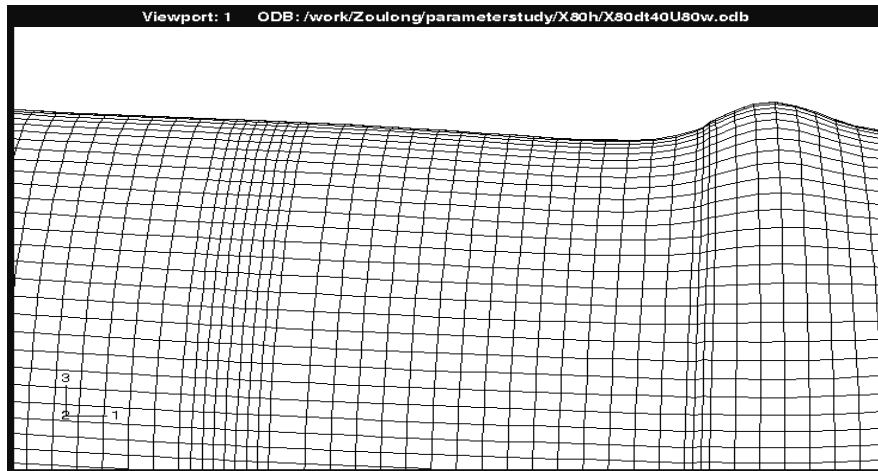
(a) Pipe Model X80hdt40U80w
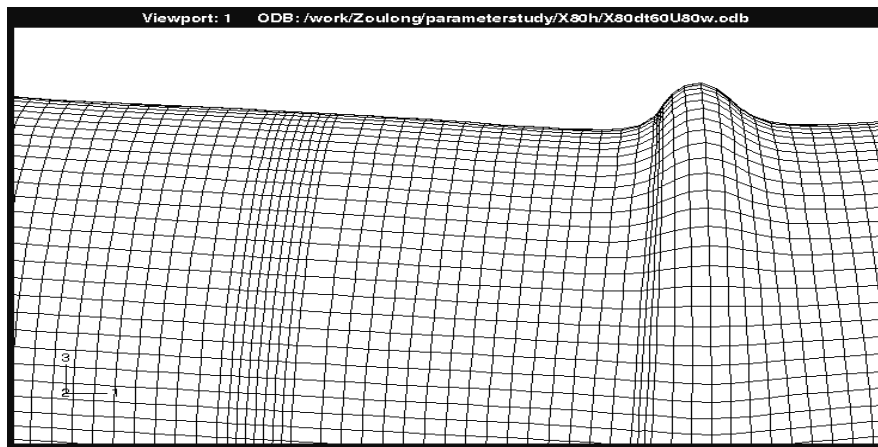
(b) Pipe Model X80hdt60U80w
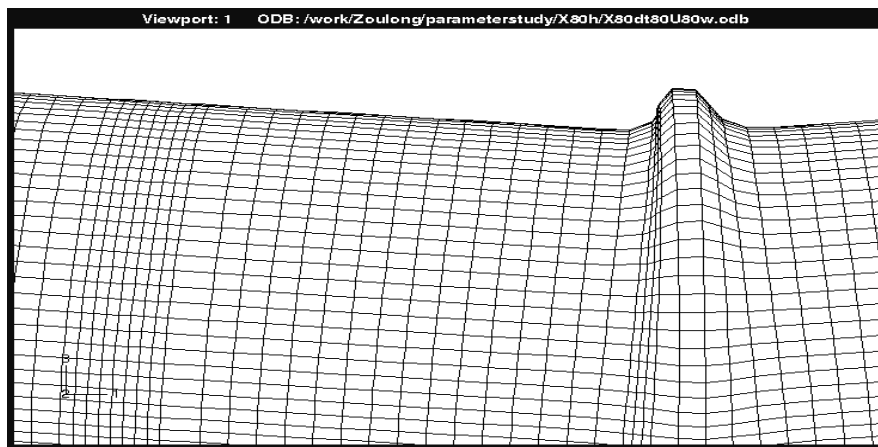
(c) Pipe Model X80hdt80U80w

Figure 6.9 D/t Ratios Effect on Wrinkle Development for Girth-welded Pipes

197
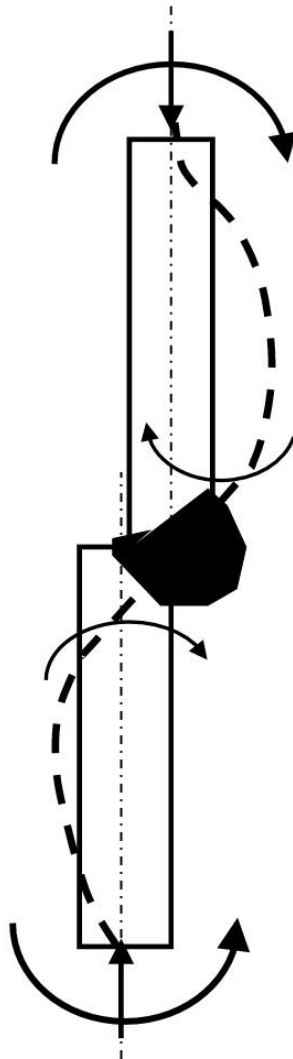
Figure 6.10 Mechanism for the Girth Weld Zone
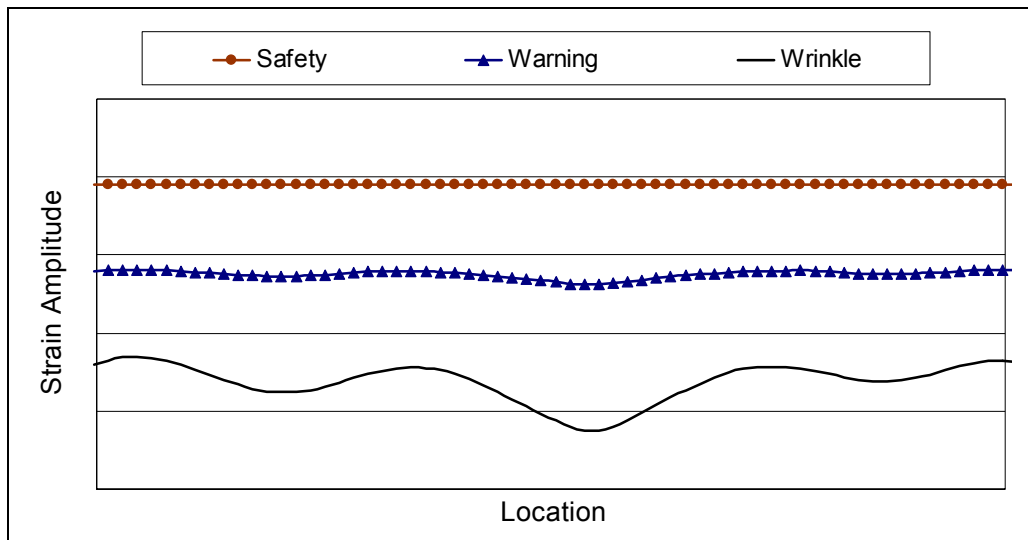
Figure 6.11 Example Patterns for Three Pipe Conditions
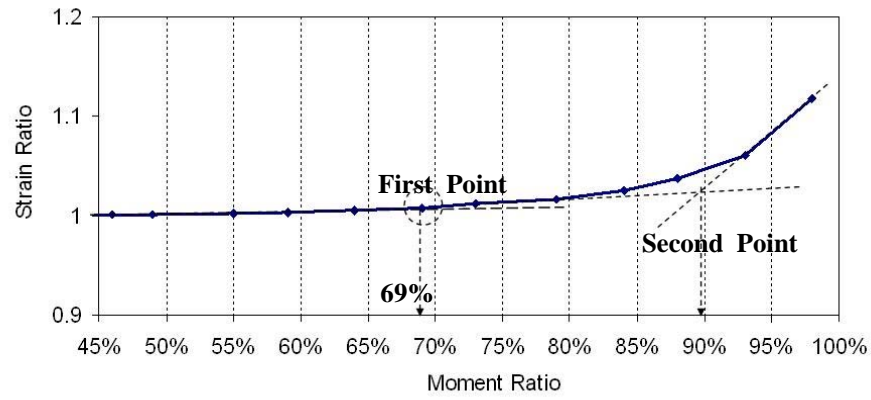
(a) Strain Ratio versus Moment Ratio Plot
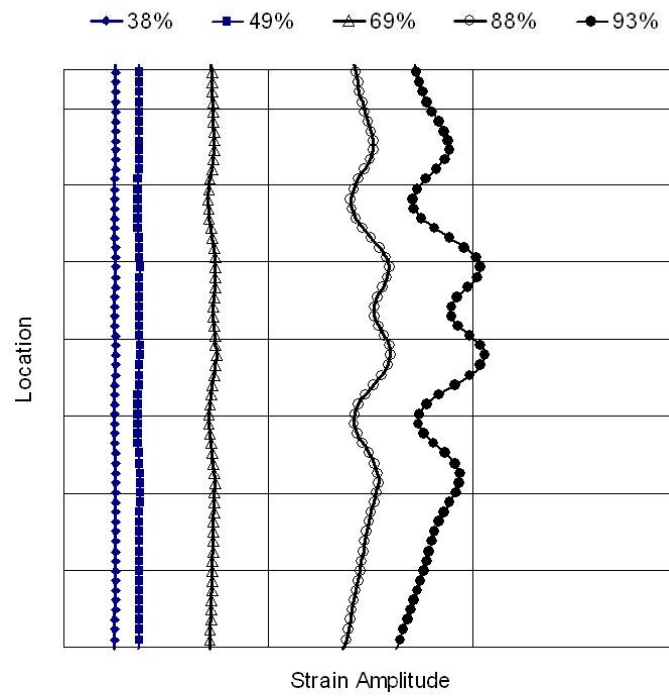
(b) Possible Threshold Patterns

Figure 6.12 Schematic to Determine the Possible Threshold Patterns
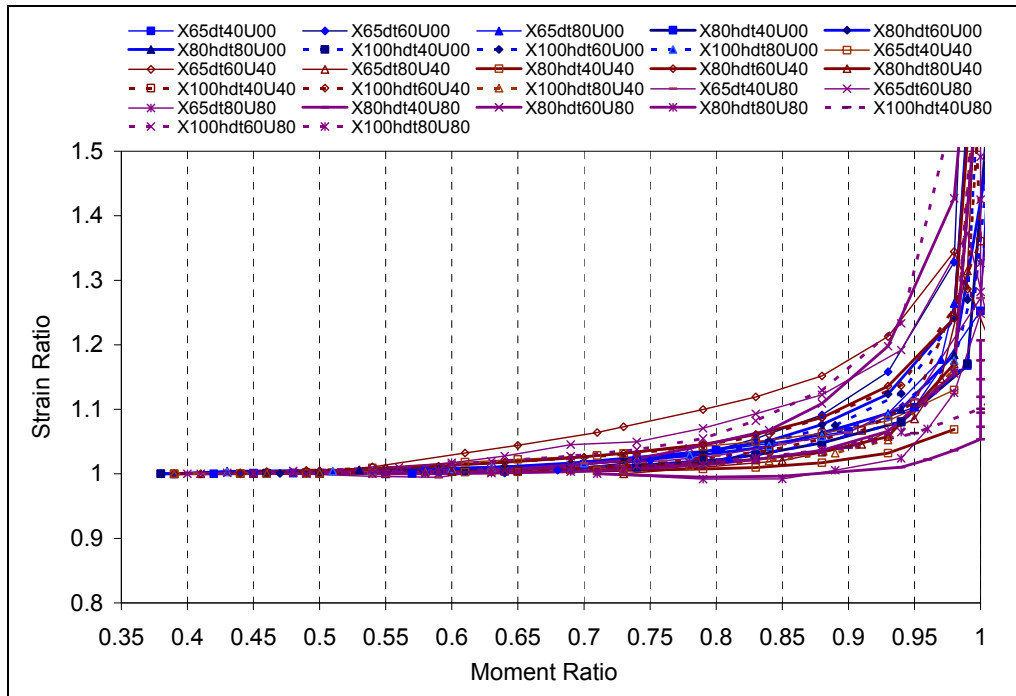
Figure 6.13 Strain Ratio versus Moment Ratio Plots for Plain Pipes under a
Bend Load
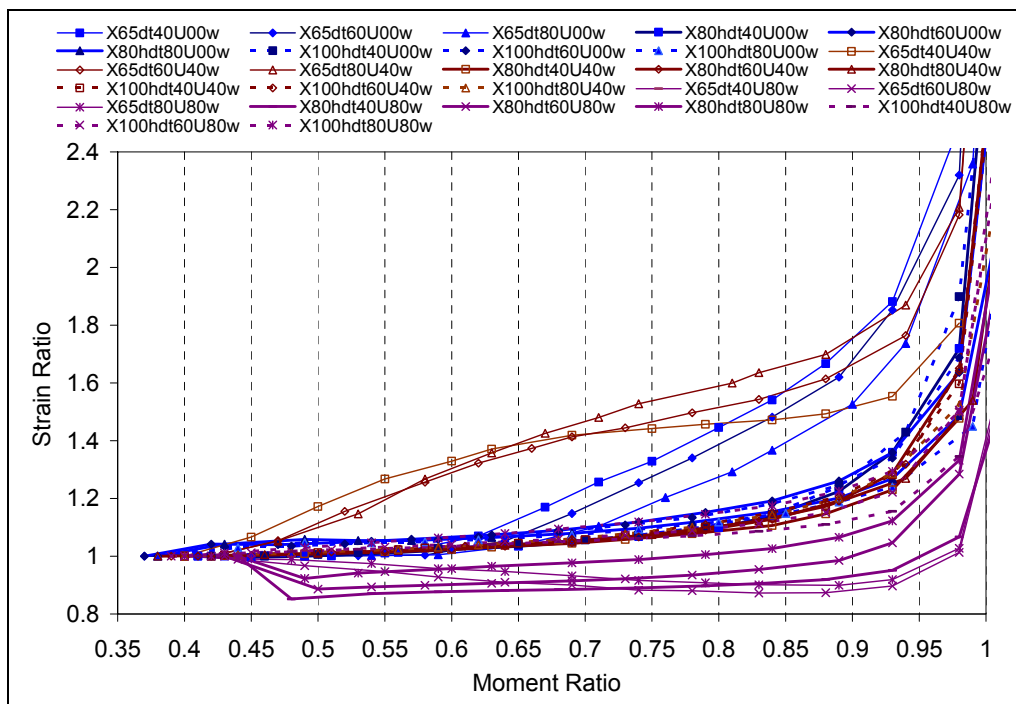
Figure 6.14 Strain Ratio versus Moment Ratio Plots for Girth-welded Pipes
under a Bend Load

201
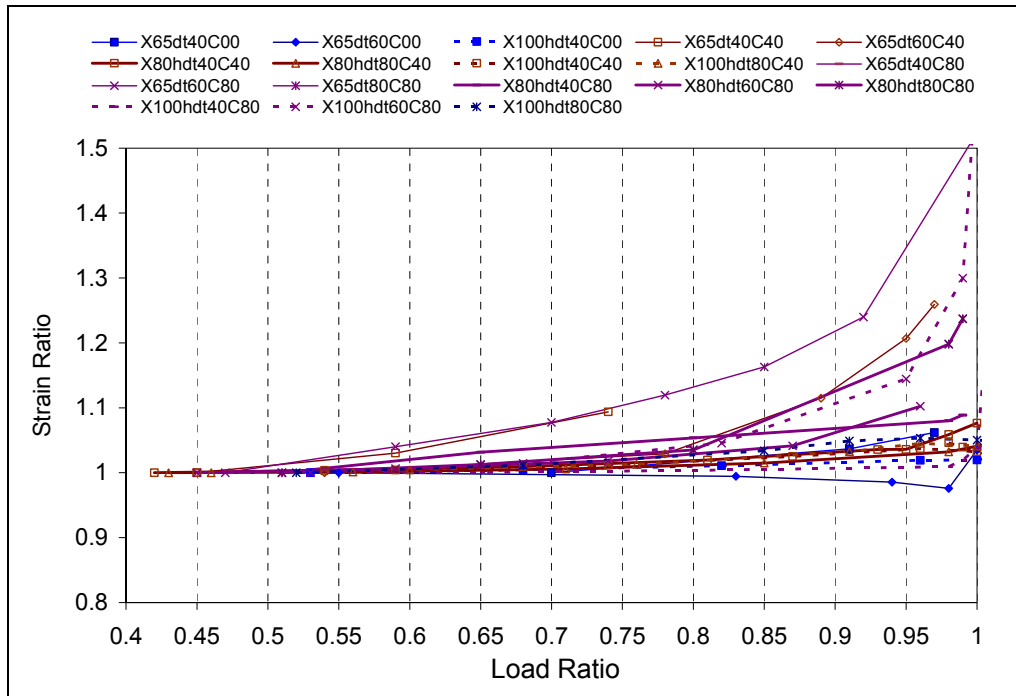
Figure 6.15 Strain Ratio versus Load Ratio Plots for Plain Pipes under an
Axially Compressive Load
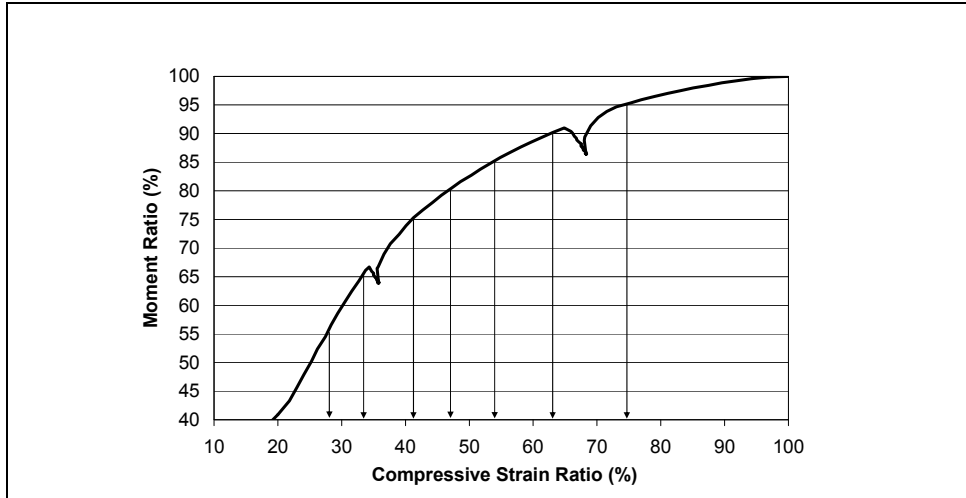
Figure 6.16 Moment Ratio versus Strain Ratio Curve for X100h Pipe with
the D/t Ratio of 69 under Bend Load
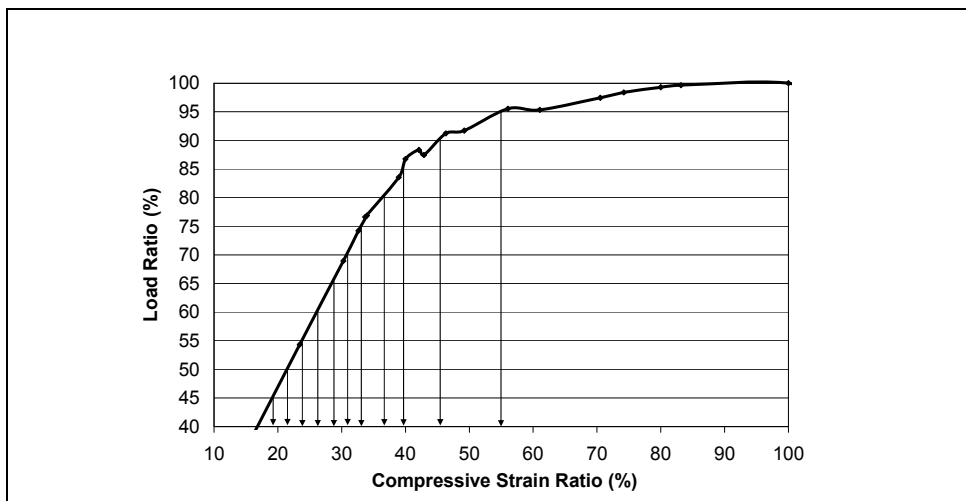
Figure 6.17 Load Ratio versus Strain Ratio Curve for X70 Pipe with the
D/t Ratio of 88 under Axially Compressive Load
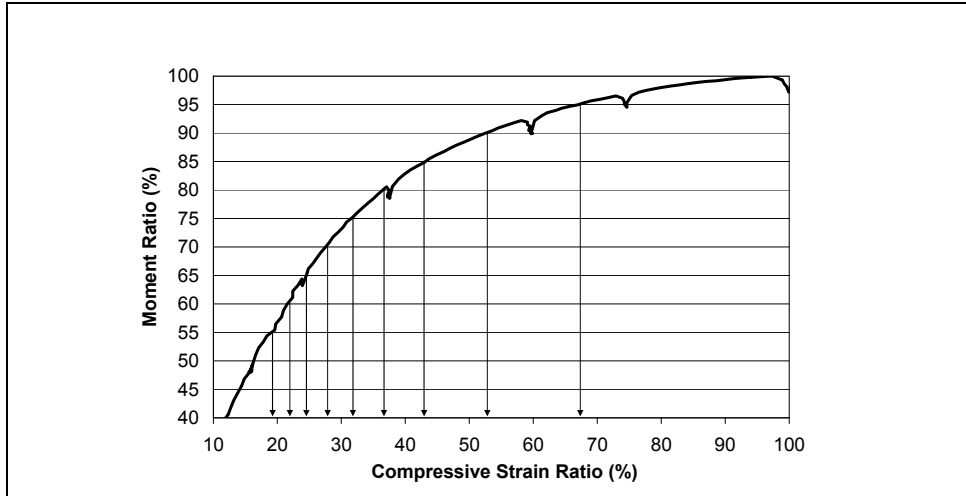
Figure 6.18 Moment Ratio versus Strain Ratio Curve for X80 pipe with the
D/t ratio of 55 under Bend Load
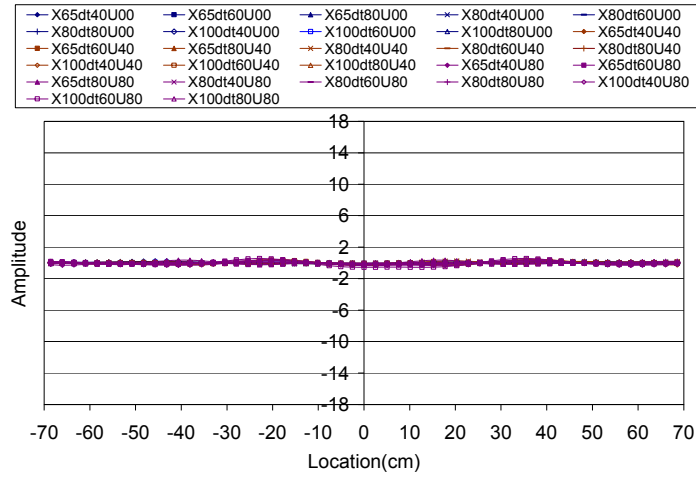
Figure 6.19 Threshold Pattern for Safe Condition
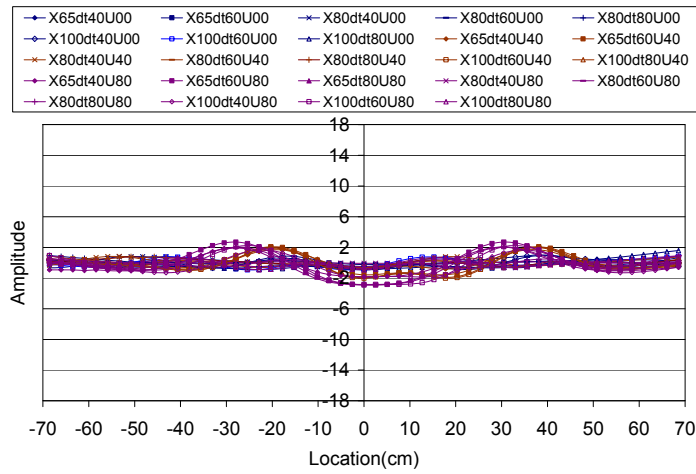
Figure 6.20 Threshold Pattern for Warning Condition
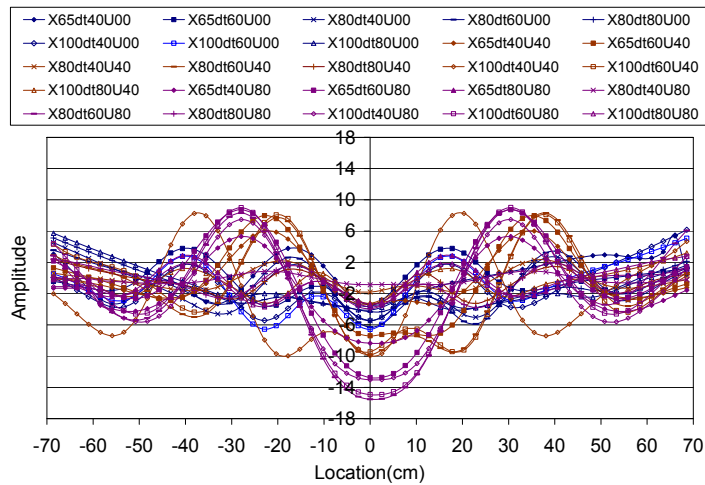
Figure 6.21 Threshold Pattern for Wrinkling Condition

7. DAMAGE DETECTION MODEL

The discussions in the previous chapters demonstrated the potential of the distributed sensors and the feasibility of using strain distribution patterns as a signature/damage indicator in the health monitoring of buried pipeline buckling. The threshold patterns for safe, warning, and wrinkling conditions, independent of the strain magnitude, were determined in Chapter 6. In this chapter, by integrating the above findings, a damage detection model is proposed.

7.1 Proposed Damage Detection Model

In this section, data processing for a damage detection model is explained first. In this procedure, the field raw data are processed, and the processed data are fed into the developed damage detection model (DDM). The DDM is used to assess extent of pipe deterioration during buckling. By using the data processing and the developed damage detection model, not only can the pipe deteriorating condition be identified, but also a large amount of data collected from field pipelines can be significantly reduced.

7.1.1 Framework of Data Processing for the Damage Detection Model

In general, field data recorded from distributed strain or curvature sensors include not only the pipe responses, but also some undesirable data, such as electronic noise, deviation, and sometimes errors. Before these data can be processed and analyzed, these undesirable data are first eliminated by using either digital filters built in Data Acquisition (DAQ) software, such as LabView, or mechanical filters. After the data are filtered, they are called raw data.

If the distributed strains (or curvatures) are recorded at a specific position along the monitored pipe by using inspection tools, such as Geopig, or distributed strain gauges, the data are called single-route data. The single-route data are processed according to the steps of the flow chart shown in Figure 7.1, and the procedure of data processing in the figure is called the single-route data processing. On the

other hand, if the distributed strains are collected by employing multiple positions sensors such as the BSFOS system, the collected data is called the multiple-route data. For the single-route measurement, it is assumed that the compression side of pipe buckling is known; and the sensors are installed on the compression side of the pipe. Thus, the raw data processed according to the flow chart in Figure 7.1 are compressive strains. However, because of complex loading conditions of the buried pipes, the final buckling conditions are generally unpredictable and the recorded strains are probably not exactly on the compression side, but on the other position or even on tension side. Although it is possible to develop DDM based on the strain distributions other than compressive strains, only the compressive strain data are considered in this study, as shown in Figure 7.1, due to insufficient experimental data. A conceptual procedure monitoring the signature of strain distributions on the tension side is provided in Appendix E.

In Figure 7.1, the single-route data are processed (or interrogated) at every 3 meter segment. The wrinkle shape of a pipe buckling can be either a bulge shape for pressurized pipes or a diamond shape for non-pressurized pipes. Moreover, extent of the profile of the buckled shapes is different for the pipes under different combined loading conditions and different manufacturing processes (such as girth welds). In general, the extent of a wrinkle is found to be within one diameter of a pipe. Therefore, a minimum length of 3D for each segment is required to cover at least 3 continuous waves, which is the minimum number of waves required for the signature patterns of distributed strains for wrinkling. A 3-meter segment was adopted in Figure 7.1 to cover the most practical sizes of gas pipelines, which normally range from 324 mm (12 in) to 914 mm (36 in).

The complete procedure for the single-route data processing, as shown in Figure 7.1, is summarized below, and illustrated graphically in Figure 7.2:

Step 1: Apply an interrogated window on a 3-m pipe segment.

Step 2: Search for the maximum strain within this window, and record the magnitude and location of the maximum strain.

Step 3: Center the maximum strain location in a 3-m interrogated window, i.e. the maximum strain now is located at the center of the 3-m interrogated window, as shown in Figure 7.2. This step is ensured that the processed data can be identified by the developed damage detection model (DDM), because the DDM was trained by the strain distributions where the maximum strain was located at the center of the strain distribution.

Step 4: Check that the maximum strain is still the maximum within the 3-m interrogated window. If not, repeat the Step 3; otherwise, go to the Step 5.

Step 5: Define the strain distribution pattern within the 3-m window as the processed data, and define the pipe type for this pipe segment. The pipe type is either the plain pipe or the girth-welded pipe. Feed the strain distribution and pipe type into the DDM for damage detection.

The data processing is continued for the next 3-m pipe segment until all the data have been processed.

Similarly, Figure 7.3 presents the flow chart of the multiple-route data processing. The advantages of the multiple-route monitoring had been discussed in Chapter 5. Contrast to the single-route monitoring, predetermination of the compressive side of a wrinkle is not necessary for the multiple-route monitoring. The procedure of the multiple-route data processing is essentially the same as the single-route, except for the steps finding the absolutely maximum compressive strain from the multiple positions and its corresponding location, as indicated in Step 2 to Step 5 in Figure 7.3. The absolutely maximum compressive strain is the largest compressive strain found at different multiple positions, i.e. 1st to 8th positions as shown in Figure 7.3.

7.1.2 Framework of the Damage Detection Model

In this section, only the profile of the damage detection model (DDM) is discussed. Each component of the DDM will be explained in detail later. The core of the DDM consists of artificial neural network (ANN), as shown in Figure 7.4. The ANN is trained to identify the strain distribution patterns on the compression side along the monitored pipe segment so that the initiation of pipe wrinkle can be early detected. Figure 7.4 shows that the strain distributions are extracted from the processed data in a 1.5-m range centered at the maximum strain location and then fed into the ANN protocols. The 1.5-meter range was selected because of most of the experimental data available only in around the 2-meter range, and, thus, the developed ANN was trained and validated by the strain distributions in a 1.5-meter range. In addition, to increase the system's adaptability in the health diagnosis for pipe buckling, the discriminate IF...Then is employed by the DDM. The discriminate IF...Then allows pipeline operators to adjust the timing of the warnings and the recognition rate of a wrinkling pattern. The procedure for operation of the ANN protocols in the DDM is shown in the flow chart in Figure 7.4 and summarized as follows:

(1)   Prepare input data for the ANN in the damage detection model. In this step, the processed data need to be interpolated and normalized, so that the normalized strain distribution patterns can be input to ANN.

(2)   Feed the normalized strain distribution patterns to suitable ANN protocols in accordance with the location of the distributed strains. If this location is near a girth weld location, the pipe type was defined as the girth-welded pipe, and a set of the ANN protocols, ANN(3) and ANN(4), are used to identify the strain distribution pattern for this pipe segment. Otherwise, the other set of the ANN protocols, ANN(1) and ANN(2), are employed.

(3)   Apply ANN(1) and ANN(3) to identify the distributed strain pattern as being in either safe or abnormal conditions for the different pipe types (plain or girth welded pipes), respectively.

(4)   If the pipe segment is identified as being in the abnormal condition, i.e. either the warning or the wrinkling condition, feed the strain distribution patterns into ANN(2) or ANN(4), respectively. ANN(2) and ANN(4) distinguish the onset of pipe wrinkling from the warning condition.

(5)   Once a pipe segment has been identified as being in the abnormal condition, the damage detection model will send an alarm to the pipeline operators. The pipeline operators will take action in accordance with the different pipe conditions, either pipe wrinkling or warning condition. As mentioned in Section 6.3.2, the pipe wrinkling can be detected before the largest strain on the pipe segment approaches 65% of the critical strain.

Theoretically, the DDM was developed for providing pipeline operators with a real-time, on-demand warning system for buckling monitoring of buried pipelines. The DDM identifies the monitored pipe as being in the safe, warning, or wrinkling condition and gives the pipeline operators warning for pipe's anomaly at a specific time. Therefore, the data are not needed to be saved in a database system (DBS). However, in the development of the DDM, most of the training data for the ANN were the simulated data by the FE models and calibrated by the limited field data. In order to increase the accuracy of DDM, the processed data of the abnormal conditions should be saved in the DBS for future calibration. For the pipe segments identified as being in the safe condition, which consists of majority of the processed data, pipeline engineers can select a portion of the data to be saved. In this way, most of the processed data can be eliminated, and the data stored are significantly reduced. Moreover, if the potentially dangerous segments of the pipeline are identified, the inspection can be focused only in a few specific locations, and, consequently, the operating time and collected data can be further reduced.

The developed DDM shown in Figure 7.4 cannot be used to track the growth of pipe wrinkling. Appendix D provides two secondary criteria to allow pipeline engineers to monitor the wrinkle growth. These criteria could be used to detect pipe wrinkle growth at different stages by identifying strain distribution patterns

on the tension side or by estimating strain ratio growth on the compression side. Because the behavioural signatures of the pipe wrinkle identified by these criteria appear during the latter loading stages, e.g. the loading stages after the peak loading, these criteria are more apparent to be used in detecting a visible or unacceptable wrinkle rather than the onset of the pipe wrinkling. These criteria had been discussed in Section 5.2.2, and only the conceptual frameworks were proposed for these two criteria in Appendix D, due to insufficient field and experimental data, as well as FE simulation results. To apply the proposed secondary criteria to track the pipe wrinkle growth, time series data are required. Therefore, a portion of the processed data, corresponding to the specific time, need to be saved in DBS.

7.2 Warning System for Pipe Buckling

Along with the algorithm, the procedure for developing the ANN models employed by the warning system is presented in this section. This section discusses the concept and background of the ANN, the selection of its optimal protocol, and the building of the reliable ANN models.

7.2.1 The Concept of Artificial Neural Network (ANN)

A damage detection model can be based on either theoretical or empirical basis, or both. A theoretical model can be extrapolated when data are not available; while an empirical model, which is based on experimental observations, cannot be reliably extrapolated beyond the range over which data have been collected. Nevertheless, when a theoretical model cannot provide reliable results, an empirical model is normally employed. Artificial intelligent (AI) technologies have been found to provide reliable empirical models for applications in various areas. They include the statistical method, expert system, fuzzy logic, and artificial neural network (ANN). The ANN uses a modeling technique that simulates the problem-solving processes in the human brain by learning previous sample solutions (data) and then developing the ability to correctly classify new

data. In many AI models, such as the expert system, knowledge is stored as a static copy of a pattern or represented by a criterion in the long-term memory. Retrieval parameters are then used to find the pattern and then copy the pattern into the working memory. However, for the ANN, the patterns themselves are not stored; rather, the connection strengths between units are stored and trained to enable these patterns to be re-created (Rumelhart 1987). Furthermore, the ability to re-create patterns enables the ANN to classify patterns that have not been previously presented. The ANN is probably more useful than the statistical method and the expert system in a damage detection model, because the ANN not only can do correlation learning (statistical regression and correlation), but also can process competitive learning (parameter competition).

The history of ANNs is dated back to 1943, when McCullough and Pitts (1943) invented the first artificial neuron model for networks based on their understanding of neurology. Rosenblant (1958) designed and developed a learning method for McCullough and Pitts' neuron model. Subsequently, Widrow and Hoff (1960) proposed the use of the least mean squares (LMS) filter adaptive algorithm, which helped in the development of the subsequent learning technique, the backpropagation learning rule. Minsky and Papert (1969) published a pivotal paper which demonstrated that perceptrons are not computationally universal, and, consequently, this paper drastically reduced the needs of researches on the multi-layer perceptrons (now being used in the most common ANNs). The use of multi-layer perceptrons became the most popular ANN technique after Rummelhart et al. (1986) proposed the backpropagation learning rule in their famous work about parallel distributed processing. After the publication of this paper, researchers overcame most of the limitations of neural networks, and now ANNs are broadly applied in civil engineering applications (Adeli et al. 2001).

7.2.2 ANN Package and Advantages of ANN Models

This project used the Neuroshell2 software to develop ANN models. This software can reduce the amount of time needed for programming and increase

efficiency when studying an optimal ANN model. This software not only has adequate functions, such as various learning algorithms, activation functions, and perceptron types, but also provides statistical analysis of ANN parameters and output results by using a graphic user interface (GUI). Moreover, through Runtime facilities of NeuroShell2, the completely trained ANN models can link MS Excel with dynamic link library (DLL). The components of the ANN are explained in Appendix E.

Due to the complexity of the distributed strains along a buried pipe segment, it is difficult to find statistical functions, such as multiple regression and cross-correlation, to reliably identify strain distribution patterns independently of the strain magnitude. Some statistical algorithms have been successfully developed for pattern recognition, such as spike sorting (Lewicki et al. 1998) and piecewise linear recognition (Morlier et al. 2005). The former focuses only on the local pattern (spike shape), but not on the whole distribution pattern; while the latter (like the well-known wavelet-based functions) may be good for distributed parameter simulation (NI manual and Dinc et al. 2007), but cannot provide automatic damage diagnosis for the strain distribution patterns measured in the buried pipes. In contrast, an ANN model can identify a pattern in the local characteristics as well as the global trends, and also automatically evaluate pipe conditions by appropriately training and then generalizing the model (Mehrotra 2000) in advance. In addition, as mentioned, ANN models can simplify programming and reduce the use of logical discriminates.

7.2.3 Application of ANN in Monitoring of the Strain Distributions

Very few studies have been published on the identification of the distributed strains by using ANN models. Hegazy et al. (1998) used ANN models to simulate distributed strains on concrete slabs, and Kesavan et al. (2006 and 2008) monitored the distributed strain patterns in order to detect the delamination of composite members by using ANN models.

Hegazy et al. (1998) concluded that the forward feed and backpropagation learning algorithm of an ANN model is suitable for predicting strain patterns; and Kesavan et al. (2006 and 2008) found that the increasing curve function, i.e. hyperbolic tangent function, is an excellent activation function for identifying the distributed strain patterns, and also validated the generalization capacity of the ANN. These findings were used in the development of the ANN models in this study.

7.2.4 The Features of ANN Used in the Research Program

The pipeline researchers have not yet used ANN models in pattern identification for the buckling behaviour of line-pipes. Thus, this study is a pioneer study in establishing a framework for predicting pipe wrinkling by using ANN models. The backpropagation algorithm (Beale and Jackson 1990), explained in Appendix E, was used in the network since this algorithm has been proven effective in a variety of projects (Teh et al. 1997, Hegazy et al. 1998, Mehrotra et al. 2000, Amali et al. 2006, and Kesavan et al. 2008), and the mathematical and statistical concepts involved in this algorithm are concise. Thereby, researchers can efficiently evaluate the advantages and disadvantages of the ANN protocols when searching for the optimal ANN models during the establishment of the framework.

In this study, ANN models were employed to classify the distributed strain patterns into three groups: safe condition, warning condition, and pipe wrinkling. Three distributed strain patterns were selected as the inputs for the ANN: a relatively constant strain distribution, a wave shape distribution, and a wave shape

along with apparent strain localization, as shown in Figure 6.11. In addition, because the strain distribution patterns are quite different in low and high pressurized pipelines and are also affected by the material and sectional properties of a pipe, the preliminary input parameters of the ANN include also internal pressure, steel grade, and D/t ratio. The input used as few parameters as possible to retain all meaningful information and to promote the accuracy of the ANN models. A total of 17 parameters were used to monitor the distributed strains in a 1.5-meter range. A preliminary ANN profile for identifying the distributed strain patterns is shown in Figure 7.5.

7.3 The Development of an ANN for Monitoring Distributed Strain Patterns

A framework that integrates a distributed sensory system with the ANN decision-making tool is used in health monitoring for buried pipe buckling. The ANN model developed is explained below.

7.3.1 Preparation of Input Data for the Proposed ANN

Before structuring an optimal ANN protocol, two tasks need to be completed in advance: data preparation to suit the model input but not to miss the behavioural signatures of the monitored pipes, and the study of a variety of ANN protocols. In the following subsections, these two tasks are explained in detail.

Yu et al. (2006) systematically studied and described an integrated data-preparation method. This study provided some valuable information for this research program. A comprehensive data-preparation method not only includes data processing but also data analyzing. The data-preparation scheme for the ANN model is shown in Table 7.1.

Data preparation contains three steps: data analysis, data processing, and data post-analysis. The main task in data analysis is to select relatively important parameters (variables) from all possible variables influencing the ANN

215

prediction/classification. Most of the data analysis was completed in the previous parametric study.

The data processing in this stage focused on finding the reasonable number of measurements and solving the multi-scale data issue. To find the number of measurements, an investigation of the numerical models used in the previous experiments was carried out. The data obtained from the results of the 9 sets of FEA showed that the data inputs of an ANN could use a total of 17 measurements, spread evenly over a 1.5-m interval, and centered at the maximum strain location. It can be realized that rationally describing half a sine curve needs at least 5 points, and the strain distributions probably include two sine curves in the 1.5-m range. Hence, when 17 measurements are used, the strain distribution patterns can retain their behavioural signature, and the number of neurons and weights can be reduced as well. However, the spacing for data measurement differs for different instruments. Different instruments use different measuring intervals to eliminate (filter) measurement noise. Take the BSFOS system and the Geopig system for examples: the former presents distributed measurements at 100 mm intervals; while the latter describes the strain/curvature profile usually at much longer intervals, e.g. 500 mm. It was expected that the ANN models should be applied to both monitoring systems, and, hence, the data from different sensing systems should use different interpolating methods to generate consistent input data for the ANN models.

In order to solve the multi-scale data issues, which includes relative strain measurement, different attributive parameters, and different data sampling range, the following solutions were proposed.

- **Normalization:** The strains measured in the field can be either the relative strains or the absolute strains. When using distributed sensing systems to measure the field strains along the buried pipelines, the measured strains (or curvatures) are usually a relative value; the true deformation of the buried pipe is probably underestimated. Consequently, some important signs for

216

pipe wrinkle are possibly missed. This phenomenon is presented in Figure 7.6. In this figure, it was assumed that the instrumentation was installed right after the pipeline was buried, and the absolute strains were able to obtain in the subsequent measurements, e.g. in 90% and 95% of the peak moment (see Figure 7.6). On the other hand, if the instrumentation was installed in a specific time after the pipeline had been under operation, e.g. in the time when the loading inducing the pipeline had reached 90% of the peak moment, the relative strains would be acquired in the next measurement, e.g. in 95% of the peak moment. In Figures 7.6 and 7.7, the dash line, TC3-95-90%PM, represents the relative strains measured between the two runs, and the solid curves, TC3-90%PM and TC3-95%PM, represent the true accumulated strain distributions measured in these two runs. As can be seen that the magnitude of the strains in the relative strain distribution is misleading, and, moreover, the strain distribution is smoother for the relative strains (the dash-line curve) than for the accumulated strains in the second run (the solid-line curve with square points). To overcome this problem, as mentioned, the data need to be normalized. Normalization has been found to influence the success of the classification and prediction in an ANN model (Sola et al. 1997, Yu et al. 2006, and Bezerra et al. 2007). Figure 7.7 shows that the above results can approach agreement after data normalization. In addition, data normalization can sometimes eliminate the measuring noise from the temperature effect, as the strains caused by temperature change are usually uniformly distributed in a specific pipe-segment until the wrinkle is triggered.

- **Scale:** The strain, operating pressure, material property, and D/t ratio were measured in different scales. It is not necessary to use the exactly same numerical range for the multi-source parameters, but they should be in similar scale to prevent the ANN from giving them different weights based on a judgment biased by the different scale ranges among these parameters. In this present study, all the parameters were scaled to a similar order, i.e. to one to two digits before a decimal point. In addition, the current ANN model

217

was trained and validated by using large amounts of FE data and experimental data. Most of them were available from around a 2-meter measuring range (in the ANN models, a 1.5-m interrogated window was used), and, hence, the Geopig data had to be modified in scale to fit into this ANN model. For example, the range of dominant strains distribution along Geopig data is usually more than 3-times the diameter of the monitored pipe, but experimental observation evidenced that the dominant strains were concentrated in one-diameter range during pipe wrinkling. Based on the different ranges of dominant strain distribution, the Geopig data were adjusted by ¼ scale in location and kept at the same scale in amplitude. Figures 7.8 and 7.9 provide examples of the original and adjusted strain distribution from the Geopig system, respectively.

Data post-analysis is a heuristic procedure for the preliminary design of ANN protocols. The heuristic procedure is usually a cyclic procedure to find an optimal solution by experimental methods and especially trial and error. During this procedure, the importance of the selected parameters (variables) can be reviewed, the ANN architecture can be established, and the ANN performance can be examined. Table 7.1 shows that the ANN performance could be under fitting or over fitting. If the ANN is under fitting, the accuracy of the ANN is not good enough; while if the ANN is over fitting (or over learning), the generalization capacity of the ANN will be restricted. The generalization capacity of the ANN will be further discussed in the latter section. The steps of the heuristic procedure are shown in Appendix E; the complete procedure of developing the ANN protocols will be presented in the following subsections.

7.3.2 The Development of the Proposed ANN

During the heuristic procedure for a backpropagation ANN, the ANN parameters, including the number of neurons and layers, scaling and activation functions, learning rates and momentums, learning epochs (iterative cycles), and the methods of data extraction, are studied. Most of these parameters affect the

accuracy as well as the generalization capacity of the ANN models, but the method of data extraction is used to examine the stability of the ANN. During the ANN learning process, the different learning rates and momentums affect the speed and correction of convergence; in addition, the more the learning epochs, the better the accuracy will be, but the worse the generalization capacity may be. The number of learning epochs recommended by Neuroshell2 is 20,000 to 40,000.

Furthermore, during ANN's learning processes, the learning data are separated into two groups: the training data and the test data. In general, the processes are completed as the minimum error has reached for the test-data sets after certain learning epochs. The above learning process is also called the training process. After the ANN is trained, additional data are used to verify capacity of the ANN. These additional data are different from the data used in the training processes and called validating data.

After studying the results obtained from the previous researches and the information provided by Neuroshell2, only the more significant parameters of the ANN involved in this project were considered (see Table 7.2). Theoretically, thousands of trial protocols seem to be needed based on the number of the parameters listed in Table 7.2, but because of the heuristic procedure, some parameters such as the number of layers, the number of neurons, and the number of data sets do not have to be changed, so the trial runs of the protocols can be reduced significantly. In addition, some features such as the initial bias weight, learning rate and momentum, and learning epochs were not the focus of the parametric study in the proposed ANN. Therefore, they were used according to the Neuroshell2's recommendations. Several cases in the 2nd heuristic cycle, the ANN cannot converge under the learning rate of 0.1 and the momentum of 0.1 recommended by the Neuroshell2, the learning rate of 0.05 and momentum of 0.5 was used. A total of 78 protocols were studied in five heuristic cycles, as shown in Table 7.2, but only eight representative protocols, Protocols 1 to 8, will be

extracted from the 78 protocols to explain the significant findings from the heuristic procedure.

Before the studies of protocols are presented, two statistical indicators, the coefficient of multiple determination (R^2) and correlation coefficient (r), are interpreted. They were provided by Neuroshell2 and used to evaluate the overall performance of the ANN prediction. The coefficient of determination, R^2 can be used in multiple regression models whose purpose is the prediction of future outcomes; the correlation coefficient, r, was used to evaluate the overall trend of the correlation between the expected and predicted outputs. As mentioned, the capacity of ANN is trained through correlation learning (multiple regression and correlation analyses), and, thus, if R^2 is close to 1, the capacity of the ANN prediction is good. Similarly, as the r is close to 1, the set of expected outputs and the set of predicted outputs have approximately positive linear relationship. In addition, ANN outputs are expected to be classified distinctly into two groups, either "0" or "1", in each output neuron, but however ANN outputs are probably not exactly in either "0" or "1" due to the predicting error. Therefore, another statistical indicator, mean squared error (MSE) was also used to see the performance of the ANN prediction. MSE is the mean of the square of the expected output minus the predicted output of all patterns in the output file.

Protocol 1:

In the five heuristic cycles, Protocol 1 was studied in the 1st heuristic cycle to study the feasibility of the ANN with 3 outputs neurons. In Protocol 1, 3 layers of neurons with 20 input neurons, 17 hidden neurons, and 3 output neurons were employed. The number of hidden neurons used the default of Neuroshell2. Even though a single output is usually used for the optimal ANN model, the 3-output neurons were used to classify the three conditions simultaneously.

Thirty seven strain distribution patterns, in which 29 training patterns and 8 testing patterns were randomly extracted from these 37 patterns, were created from the parametric study. While all training and test sets were generated from

220

the finite element models, the 3 validating sets were collected from an artificial data and two experimental data, as shown in Figure 7.10, where the pipe properties and loading conditions are different from those in the training and test sets. For the artificial strain distribution pattern, a strain distribution shape resulting from the moment gradient was simulated by a sine curve.

Table 7.3(a) shows that the overall results from the ANN prediction are acceptable, but that a contradictory classification occurred for the artificial strain distribution pattern. In this protocol, the desired outputs, 1-0-0, 0-1-0, and 0-0-1, represent the safe condition, warning condition, and wrinkling condition, respectively. The artificial distribution pattern was used to simulate the large strains resulted from the over bend rather than from the local pipe wrinkling along the line-pipe, Thus, the ANN model was expected to warn operators about a pipe anomaly but not a pipe wrinkle, so the desired output should have been 0-1-0. The trained ANN model provided a completely opposite output, 1-0-1, that is, the model predicted pipe wrinkling, but on safe side. This prediction does not make sense for wrinkle detection. Therefore, the 3-output protocol was eliminated.

Protocol 2:
Based on the observations in the 1st heuristic cycle and probably because the similarity between the patterns for the warning and wrinkling conditions led to the contradictory results, in the 2nd heuristic cycle, the protocols took out the warning patterns from the training data and used only 2 neurons in the output layer for the safe condition and wrinkle condition, respectively. The generalization of the ANN was anticipated to assist the models in distinguishing the warning condition from the safe and wrinkling conditions for the monitored line-pipe.

The data used in the 2nd heuristic cycle were normalized by using Equation 5.4. The training and test data used 52 threshold patterns for the safe and wrinkling conditions, and these patterns were obtained from the data pool of the FEA of the plain pipes under a bend load. Twenty-seven patterns were used to validate the protocols, including the experimental and field data, such as the cold-bended pipe

221

data, field Geopig data, BSFOS data, and artificial strain data. These validating data were measured in pipes under different conditions, such as different material properties, pipe properties, loading conditions, moment gradients, soil conditions, manufacturing procedures, and operating conditions. Protocol 2 is extracted from 37 protocols in this heuristic cycle to explain some findings.

The results from the protocol 2 show that the overall performance of ANN classification was better than that from the protocol 1, but that the prediction of the wrinkle condition was worse (see Table 7.3(a)). For protocol 2, the mean squared error was less than 0.10 and a more than 80% correlation occurred in the relationship between the ANN predictions and desired outputs. In this ANN, the desired outputs, 1-0, 0-0, and 0-1, represent the safe condition, warning condition, and wrinkling condition, respectively. Ten out of the 27 validating patterns have a more than 20% error in the ANN prediction. In most of these errors, the ANN predicted a wrinkling condition for a pattern that belonged to the warning condition. These errors were not surprising because of the similarity of normalized patterns in these two conditions. However, it was not expected that the ANN would classify 4 of these 10 patterns into the wrinkling condition rather than correctly into the safe condition. The results predicted by the ANN protocol 2 are safe, but do not sufficiently meet the purpose of the warning system. In the further study of these misclassifications, which are shown in Figure 7.11, it was found that these safe patterns were much more equivocal patterns that were either the relative smooth curve along with a dominant strain concentration or the vivid arc curve in the interrogated window. Moreover, Figure 7.11 reveals that as the dominant strain of the misclassified pattern becomes more apparent, the ANN output is closer to 0-1. That is, the pattern classification is more inclined to the wrinkling condition. The relative constant strain distribution is defined as the pattern in the safe condition, while a dominant strain concentration occurs on the wrinkling pattern. Therefore, the protocol made reasonable classifications according to the characteristics of the patterns, but the capacity of its generalization was not good enough to identify the never experienced patterns

which had been collected from the cold-bended pipe experiments and the field data.

The investigation of the all 37 protocols in the 2nd heuristic cycle also revealed some disadvantages of the data normalization. For some strain patterns, the amplitude of the maximum strain was not significantly different from rest of the strains, but the normalization made the difference significant. Consequently, the concentration-like strains misled the judgment of the ANN models. This problem will be further addressed and discussed a in Section 7.3.3.

The parametric sensitivity was also examined in the 37 protocols by observing the histograms of the parametric contributions, as an example shown in Figure 7.12. It was found that the D/t and the steel grade had not affected the classification of the distributed strain patterns significantly. Therefore, these two parameters were removed from the input layer in the subsequent studies.

Protocol 3:
In accordance with the findings in the 2nd heuristic cycle, the redundant parameters (D/t and steel grade) and the threshold patterns of the safe condition were taken out in the 3rd heuristic cycle. In a total of 52 patterns, 20% and 15% of the 52 patterns were extracted as test patterns and validating patterns, respectively. Protocol 3 was selected from the 10 protocols studied in this cycle to explain the predicting capacity of the ANN with 18 inputs neurons. As Table 7.3(a) reveals, the protocol's ability to identify pipe wrinkle was improved; but the identification of the safe patterns became worse because of the absence of the training patterns for the safe condition.

This heuristic cycle provided the following significant findings:
- Adding experimental and field strain data to the training and test sets improved the performance of the ANN model.

223

- Dividing the model into two models with only one neuron in the output layer for each model, one for the safe condition and the other for the wrinkling condition, should produce better results.

Protocol 4 and Protocol 5:

Protocol 4 was modified from Protocol 2 by adding a hidden layer into a 4-layer ANN, while the 4-layer ANN, Protocol 5, was modified from protocol 3. Protocols 4 and 5 were used to investigate the effect of the 4 layers of ANN, and the results from these two protocols are shown in Table 7.3(a). There are very similar results of the ANN predictions by the 3-layer and 4-layer models. The 4-layer model slightly improved the accuracy of the ANN models' predictions when the desired outputs were correctly predicted. However, when the model predicts the outputs incorrectly, the actual outputs from the 4-layer model give the worse outputs than the 3-layer model. In addition, the 4-layer ANN makes it difficult to determine the "IF…Then" discriminant in the post process of the ANN models. Therefore, the 3-layer protocol was used in this research program.

After completing the 3 heuristic cycles, it was found that it would be suitable to apply the logistic scaling function (or sigmoidal scaling function) to the input neurons of the proposed ANN models, and using the bell shaped curve function (Gaussian function) as the activation function in hidden neurons could mitigate the effect of normalization on the ANN's prediction for pipe wrinkling. The selection of the activation and output functions was further studied throughout the 4th and 5th heuristic cycles. In addition, the data obtained from the FEA of the girth-welded pipes were added into the training sets of the ANN protocols.

Protocol 6 and Protocol 7:

In the 4th heuristic cycle, Protocol 6 and Protocol 7 were used to investigate the effect of the number of test patterns on the ANN prediction of the wrinkle condition. Because the ANN was trained until the best test error was obtained, too few test patterns would decreased the accuracy of the ANN model's predictions. To clarify this concern, a total of 86 patterns including 12 validating patterns were

224

used in both Protocols 6 and 7. To retain sufficient number of the training patterns in these protocols, 18 test patterns were used in Protocol 6; while 12 test patterns were used to train Protocol 7, so that the number of the test patterns was not less than the number of the validating patterns. The overall results were similar for both protocols, and are shown in Table 7.3(b). The table shows that even more test sets were used in Protocol 6, the test patterns in these two sets would have been almost the same for Protocols 6 and 7. Thus, increasing the number of the test sets but retaining the similar test patterns probably cannot improve the ANN's capacity.

Protocol 8:

The last cycle, the 5th heuristic cycle, focused mainly on determining the optimal ANN protocol to identify the pipe condition to be safe or abnormal. The protocol studies in the 2nd heuristic cycle revealed that the internal pressure did not contribute to ANN prediction for identification of the safe patterns. It can be realized that the relatively constant strain distribution for the safe patterns probably will not be influenced by different internal pressure conditions. Therefore, the input neuron corresponding to the internal pressure could be removed. This heuristic cycle was processed to investigate the predicting capacity of the ANN with 17 input neurons. Protocol 8 reveals the ANN with 17 input neurons can distinguish the safe patterns properly from the abnormal patterns, as shown in Table 7.3(b).

Proposed Protocols:

According to the comparison of the protocols in the last two heuristic cycles, the most feasible model for monitoring the health of pipeline buckling by identifying the distributed strain patterns could be made by integrating two ANN protocols, ANN(1) and ANN(2), with 3 layers of neurons, as shown in Figures 7.13(a) and 7.13(b), respectively. ANN(1) uses 17 input neurons, 17 hidden neurons, and 1 output neuron to examine if a monitored pipe segment is the safe condition, while ANN(2) uses 18 input neurons, 18 input neurons, and 1 output neuron to distinguish pipe wrinkle events from the abnormal condition. Different scaling

and activation functions were applied in these two ANN models: ANN(1) used logistic functions (sigmoidal functions) for all layers, and ANN(2) used logistic functions in input scaling, and Gaussian function as the activation function in both the hidden and the output neurons.

The capacity of the integrated ANN protocols, ANN(1) and ANN(2), was examined through two stages in this project. The first stage is to test the capacity of the ANN prediction for the patterns have occurred during the ANN's training processes, and is discussed here. The second stage is to verify the capacity of the ANN prediction for the patterns that have not appeared during the ANN's training processes, and this capacity is called generalization capacity or generalization power of ANN. The second stage, the validation of the integrated ANN protocols, is discussed in Section 7.4.

The capacity of the ANN(1) was estimated first. Twelve data were extracted from a total of the 52 data to examine if the ANN(1) protocol can successfully identify the safe patterns among the distributed strain patterns. For the overall performance of the ANN(1), the coefficient of the multiple determination, R^2, was equal to 0.72, and the correlation coefficient, r, was 0.85. Therefore, the ANN(1) can correctly identify these testing data, as shown in Table 7.4.

Next, it was examined how well ANN(2) had distinguished the wrinkling patterns from the distributed strain patterns. The success of ANN(2) was shown by the results of the pattern-recognition test shown in Table 7.5. The table shows that the overall performance of ANN(2) was good: R^2 and r was as high as 0.86 and 0.93, respectively, and most of the input parameters contributed to the ANN prediction (see Figure 7.14). The percentage error of the ANN prediction for most of the distributed strain patterns is lower than 5%, and the errors occurred mainly in the cold-bended pipes and the girth-welded pipe. The most critical one is the incorrect recognition in the strain distribution patterns of the girth-welded pipe.

Based on the above findings from evaluation of the capacity of the ANN(1) and ANN(2), the ANN protocols in the damage detection model need to be further improved by adding ANN protocols to cope with the strain distribution patterns of the girth-welded pipes. In order to improved the performance of the ANN prediction, more training data could be needed for ANN(1) and more data of the cold-bended pipes should be collected as training data for ANN(2).

The studies of the protocols above have provided useful information to develop ANN protocols for the girth-welded pipes. The ANN protocols for girth-welded pipes used similar architecture of ANN(1) and ANN(2) for identification of the safe condition and wrinkling condition, and they are named ANN(3) and ANN(4), respectively. During the procedure of searching the optimal protocols for ANN(3) and ANN(4), the parameters of ANN such as scaling, activation, and output functions were the main concerns, and different training data were estimated as well. The most feasible protocols for monitoring the girth-welded pipe buckling were acquired as follows: ANN(3) uses 17 input neurons, 17 hidden neurons, and 1 output neuron to identify a girth-welded pipe segment as being in safe or abnormal condition; ANN(4) uses 18 input neurons, 20 hidden neurons, and 1 output neuron to distinguish pipe wrinkle events from the abnormal condition for the girth-welded pipes. Both the ANN(3) and ANN(4) used logistic functions for all layers. For the overall performance of the ANN prediction, R^2 was equal to 0.89 and r was as high as 0.95 for ANN(3); R^2 was equal to 0.70 and r was 0.86 for ANN(4). In addition, the experimental data of the girth-welded pipe HGAW at 49% of the peak moment and at 95% of the peak moment were included in the test data sets to examine the performance of ANN(3) and ANN(4). The percentage errors of both ANN(3) and ANN(4) predictions for the distributed strain patterns are lower than 6%. Therefore, ANN(3) and ANN(4) should be capable of identifying the strain distribution patterns of the girth-welded pipes.

The developed ANN protocols, ANN(1) to ANN(4), were further verified by 26 sets of strain distribution patterns extracted mainly from the experimental data of

cold-bended pipes, girth-welded pipes, and from the field Geopig data. The validation of these protocols is discussed in the latter section.

7.3.3 The Discriminate Thresholds for the ANN(1), ANN(2), ANN(3), and ANN(4)

As can be seen in Tables 7.4 and 7.5, ANN outputs are not exactly in either "0" or "1", and, thus, thresholds were used in the "IF…Then" discriminant to filter the outputs of the ANN(1) to ANN(4) in the post process of ANN. The reasonable thresholds were determined by estimating the predictions resulted from the four ANN protocols. In ANN(1) and ANN(3), the ANN output "1" represents that the pipe condition is the safe condition, while the output "0" represents the pipe being in abnormal condition, either the warning condition or the wrinkling condition. In ANN(2) and ANN(4), the outputs "0" and "1" represent that the pipe conditions are the warning condition and pipe wrinkling, respectively. By setting a threshold number of the ANN, the ANN outputs can be classified distinctly into the two groups, either "0" or "1". The principles of selecting the threshold number are as follows:

- If the ANN protocol identifies a set of strain distribution pattern as being in safe condition, the pipe has to be safe.
- It is expected that the ANN protocol will not miss to detect pipe wrinkling. That is, the strain distribution patterns from pipe wrinkling cannot be misclassified into the warning condition.
- The accuracy of the integrated ANN protocols is expected to be as high as possible

The following procedures were used to establish an evaluation table (see Table 7.6) in order to determine the thresholds for ANN(1) to ANN(4):

(1) Test data were extracted from every fifth data set for each protocol, and the rest of the data sets were used to train the ANN protocol. For example, ANN(1) had a total of 319 sets of data, so 63 sets of the data were

228

extracted as test data, and 256 sets of the data were used to train the ANN. This extraction method can acquire appropriate number of test data sets and retain sufficient data sets to train the ANN. After training, the ANN was used to predict the pipe condition for the test data.

(2)   The outputs of the ANN prediction were filtered to either "0" or "1" by using a threshold number in the "IF…Then" discriminant. The threshold numbers were designed from 0.5 to 0.9 with the 0.05 interval. If the output was larger than the threshold then it was "1"; otherwise, it was "0".

(3)   After applying a threshold to these outputs, the filtered outputs of ANN prediction were compared with the desired outputs. If the predicted output was different from the expected output, the ANN misclassified this test data set. The same procedure was used for all thresholds

(4)   These misclassified data were separated into two groups respective to two pipe conditions, the safe and abnormal conditions, under each threshold, and the error of the misclassification was computed respectively for each group. Taking ANN(1) as an example, in a total of 63 sets of the test data, 18 sets were safe patterns, and 45 sets were abnormal patterns, which were either warning or wrinkling patterns. When the threshold was set as 0.60, ANN(1) misclassified three sets of the test data: two safe patterns were classified into the abnormal condition, and an abnormal pattern was classified into the safe condition. Therefore, the error of misclassification for the safe patterns was 0.11, and the error of misclassification for the abnormal patterns was 0.02, as shown in Table 7.6. The same procedure was used for all thresholds.

The above steps were applied to all ANN protocols, and the results are presented in Table 7.6.

Based on the principles of selection of the thresholds, the threshold for each ANN protocol can be determined by observing the error of misclassification under different thresholds in Table 7.6. For instance, ANN(1) is employed to identify the safe patterns among the distributed strain patterns. Therefore, as a strain

distribution pattern is identified by ANN(1) as being in safe condition, the pipe have to be safe. That is, no abnormal pattern is allowed to be misclassified in ANN(1). Under this requirement, the thresholds 0.65 to 0.90 are qualified. However, the accuracy of ANN(1) is expected to be higher; thus, the threshold 0.65 is chosen here, and the corresponding accuracy of ANN(1) is 0.89.

Following the above procedures, the thresholds, 0.65, 0.70, 0.85, and 0.60, were chosen for ANN(1), ANN(2), ANNN(3), and ANN(4), respectively.

7.4 Validation of the Damage Detection Model

The developed damage detection model, which includes an integration of ANN(1) to ANN(4), for diagnosing buried pipeline buckling was discussed in the previous sections. The model's operating procedure was explained along with the flow charts shown in Figures 7.4. The integrated damage detection model's ability has been proven by test data sets, and the generalization capacity of the developed ANN protocols was partially verified by validating data sets during the development of the ANN protocols. In the following subsection, 26 strain distribution patterns that had not appeared in the training process of these ANN protocols were used to verify the generalization capacity of these ANN protocols and the ability of the integrated damage detection model. The generalization and limits of these ANN were also discussed.

7.4.1 Validation of Capacity of the Damage Detection Model

A total of 26 sets of strain distributions on the line-pipes were acquired from the experimental results and field data. The diameters of the pipes ranged from 203 mm (8 in) to 762 mm (30 in), the material strengths were from 359 MPa (X52) to 550 MPa (X80), and the D/t ratios from 51 to 93. These strain distributions were normalized, and are shown in Figures 7.15 and 7.16 for plain pipe segments and for girth-welded pipe segments, respectively. The non-normalized strain distributions of the 26 data sets had been discussed in Chapter 3. The legends of the two figures show the loading stages corresponding to the strain distributions

230

and the ANN trainer's judgment for these pipes' condition based on the definition of strain distribution patterns respective to the three pipe conditions, as discussed in Sections 5.2 and 6.3.

By following the operating procedure of the damage detection model shown in Figure 7.4, the conditions of the 26 strain distributions were identified by the ANN model and summarized below.

(1)   According to locations of the distributed strains, the 26 sets of the normalized strain distributions were separated into 2 groups: 16 sets of the strain distributions occurring on the plain pipes were fed into ANN(1) and ANN(2); the other 10 sets of the strain distributions were fed into ANN(3) and ANN(4) for the girth-welded pipes.

(2)   For the 16 sets of the strain distributions occurring on the plain pipes, they were examined with ANN(1) first. By using the threshold of 0.65, most of them were identified correctly, except for one strain distribution that was misclassified into the abnormal condition as it should be the safe condition, and the results are shown in Table 7.7.

(3)   The strain distributions identified as being in abnormal condition by ANN(1) were fed into ANN(2). By using the threshold of 0.70, all strain distributions were identified correctly either warning or wrinkling condition, and the results are shown in Table 7.7.

(4)   For the 10 sets of the strain distributions occurring on the girth-welded pipes, they were identified by ANN(3) first. By using the threshold of 0.85, only one strain distribution was misclassified into the safe condition as it should belong to the warning condition, and the results are shown in Table 7.7.

(5)   The strain distributions identified as being in abnormal condition by ANN(3) were fed into ANN(4). By using the threshold of 0.6, no strain distribution was identified incorrectly, and the results are shown in Table 7.7.

The reason for the incorrect recognition of ANN(1) and ANN(3) on those strain distributions will be explained in the next subsections. The validation reveals that pipe wrinkling can be predicted reliably with the damage detection model before the maximum strains reach the critical strain. However, it is possible for false warning to be reported. For the plain pipes, the percent error of the damage detection model was 6%; while the percent error was 10% for the girth-welded pipes. It is noted that the above validating strain distributions were recognized by the generalization capacity of these ANN protocols, and the rate of correct recognition of the integrated damage detection model approached to 90%.

7.4.2 The Generalization of ANN for Recognition of the Strain Distribution Patterns

Though the above results are good for the prototype of the damage detection model, further investigation is needed to understand why ANN misclassified couple of the validating data sets. In this section, the investigation focuses on the pattern recognition of ANN for the validating strain distributions. That is, what kind of distribution patterns does the ANN consider safe, warning, or wrinkling pattern?

While ANN(3) and ANN(4) were trained by simply feeding the strain distributions obtained from the FE models of girth-welded pipes; about 10% and 35% of training data respectively for ANN(1) and ANN(2) were acquired from the experimental results. Therefore, it can be realized that the strain distribution patterns representing the three pipe conditions recognised by the trained ANN(1) and ANN(2) may be different from the threshold patterns conducted in Chapter 6, because these threshold patterns were generated by the FE models. Accordingly, the study of the generalization of ANN focuses on ANN(1) and ANN(2).

Comparing ANN(2) with ANN(1), ANN(2) had the higher ratio of the real data to the simulated data. Thus, the results of ANN(2)'s outputs were studied first. The

outputs of ANN(2) prediction, as shown in Table 7.7, for the validating patterns were classified into a high score group (or outputs from 0.7 to 1.0) and a low score group (or outputs from about 0.3 to 0.0). The high score and low score groups of the validating strain distributions were presented in Figures 7.17 and 7.18, respectively. As an output of the ANN(2) was closer 1.0, the strain distribution patterns would be more likely identified as the wrinkling pattern, as shown in Figure 7.17. On the other hand, Figure 7.18 shows the strain distribution patterns that were most unlikely to be identified as being in the pipe wrinkling by ANN(2). These two figures reveal a global trend and local characteristics of the wrinkling patterns recognised by ANN(2) as follows:

- The global trend is a relatively symmetrical distribution centered at the wrinkling location.
- The local characteristics are that a spike shape without serious fluctuation occurs at the center of the distribution and the curvatures decreases gradually from the vicinity of the wrinkling area to the location far away the wrinkling range, e.g. from the 8th node to 5th node in Figure 7.17.

As can be seen in Figure 7.17, when the strain distributions agree with the behavioural characteristics described above, they acquired highest score, i.e. 1.0. On the other hand, the unsymmetrical distributions along with an unclear dominating strain acquired very low score, as shown in Figure 7.18. The serious fluctuation occurred (or curvature suddenly changed) at the vicinity of the dominating strain area on the strain distribution of the dented pipe also resulted in a very low score in ANN(2)'s output.

The behavioural characteristics of the strain distribution recognised by ANN(2) and ANN(1) are similar. ANN(1) identified the evidently unsymmetrical distributions along with an unclear dominating strain or the strain distribution without localized strains as the safe patterns, and, hence, gave them a higher score, as shown in Figure 7.19. Figure 7.19 shows that the strain distribution pattern, TCPL2 (46%), acquired the highest score 1.0, and it presented extremely

233

unsymmetrical distribution along with a flat distribution on the right side of this pattern.

Based on the above findings, the misclassified pattern, the relative strain distribution between loading stages 36% and 39% of the peak moment on TCPL3 pipe, was discussed here. Figure 7.20 shows that this relative strain distributions, the strain distribution at loading stage 39% of the peak moment, and the strain distribution at loading stage 88% of the peak moment before normalization; Figure 7.21 shows that the relative strain distribution and the strain distribution at 88% of the peak moment after normalization. The magnitude of the relative strains was amplified to 10 times the original amount in Figure 7.20. Figure 7.20 shows that a dominating strain had not yet concentrated at the wrinkle location but at the other location during the loading stage 39% of the peak moment. Therefore, a spike shape on the relative strains distribution between loading stages 36% and 39% of the peak moment confused ANN(1)'s prediction. However, the output of ANN(1) prediction still identified this relative strain distribution pattern as most likely being in the safe condition, and gave it 0.63 of output value, because the normalized pattern of this strain distribution presented evidently unsymmetrical distribution, as shown in Figure 7.21. On the other hand, ANN(2) gave this pattern a very low score, 0.02 of output value, and it was identified as being in the warning condition. This particular strain pattern resulted from the cold-bend pipe's manufacturing process. As mentioned in Chapter 3, residual strain and initial imperfection already significantly exist in the cold-bended pipes before they are buried underground. Consequently, the strain localization exists at the cold bend region before wrinkle initiates. Therefore, at the earlier loading stage, e.g. 39% of the peak moment, the wrinkle-like pattern aroused from the cold bend has been fed to the damage detection model. This problem is further discussed in the next subsection.

Thorough the above studies, the main advantages of using ANN for this research project were highlighted and are verified. The trained ANN protocols can identify

a pattern's local characteristics as well as the global trends and detect pipe wrinkling reliably.

7.4.3 The Limitations of the Damage Detection Model

The main limitation of the developed damage detection model is the alarm timing by the ANN protocols. Although the three threshold patterns used to train ANN are based on three specific loading stages, i.e. loading stages at 40%, 70%, and 90% of the peak moment, the ANN cannot report the exact loading stage or strain ratio. The reason is that ANN recognises patterns based on the distinction among the patterns, not a specific magnitude of loads or strains. Consequently, the developed damage detection model report a pipe condition once the strain distribution reveals the behavioural signatures corresponding to the pipe condition on the monitored pipe. The ranges of the loading stages (or strain status), during which the damage detection model report one of the three pipe conditions, were discussed here. A total of 26 and 39 sets of the stimulated data by the FE models at three loading stages of 50%, 60%, and 80% of the peak moment were used to investigate the ranges of the loading stages for plain pipes and for girth-welded pipes, respectively. Using the thresholds determined in Section 7.3.3, the investigated results are presented as follows:

ANN(1)
The strain distributions at the loading stage of 50% of the peak moment (or about 25% of the critical strain) have 50% probability to be classified as the safe condition; no strain distributions at the loading stage of 80% of the peak moment (or 35% to 50% of the critical strain) was classified as the safe condition. As applied loading at about 60% of the peak moment, the strain distributions have 40% probability to be identified as the safe pattern.

ANN(2)

The strain distributions at the loading stages of 80%, 60%, and 50% of the peak moment have 40%, 20%, and 0% probability to be classified as the wrinkling condition, respectively.

ANN(3)

The strain distributions at the loading stages of 50%, 60%, and 80% of the peak moment have 50%, 15%, and 0% probability to be classified as the safe condition, respectively.

ANN(4)

No strain distributions at the loading stages of 50% and 60% of the peak moment were classified as the wrinkling condition; the strain distributions at the loading stage of 80% of the peak moment have 36% probability to be classified as the wrinkling condition.

The above results were obtained based on the selected thresholds in subsection 7.3.3. As the thresholds adjusted, the timing of the warnings would be changed. For example, if the threshold of ANN(1) is set as 0.90, the probability decreases from 40% to 10% for the strain distributions at the loading stage of 60% of the peak moment to be identified as the safe pattern. In addition, the limitation also caused ANN(3) misclassified the strain distribution pattern of the non-pressurized girth-welded pipe UGAw at 61% of the peak moment as the safe condition.

The other limitation of the damage detection model is the range of strain distribution. Due to the limited available data sets, the strain distribution range input to the ANN protocols is limited at 1.5-meter range. This range satisfied most of the pipes used in the validation of the damage detection model, but, however, it is probably not long enough for the cold-bended pipes. This potential limitation has been revealed in the example of the relative strain distribution on TCPL3 at between 36% and 39% of the peak moment, as shown in Figure 7.20. The longer range, e.g. a range equal to 3 times diameter, would be better for the

recognition of strain distribution patterns, because the longer range could include more behavioural signatures revealed on the strain distribution. As can be seen in Figure 7.20, the strain distribution patterns at 39% of the peak moment in the 3-m range from -2500 mm to +500 mm is very distinct from the pattern at 88% of the peak moment in the range from -1750 mm to +1250 mm. The former pattern belongs to the safe condition; while the latter belongs to the wrinkling condition.

Table 7.1 Integrated Data Preparation for the ANN Used in Monitoring Distributed Strain Patterns

Step	Task	Solution
Data Analysis	Input variable selection	Parametric study
Data Processing	The reasonable number of measurements	Data sampling or linear interpolation
	Multi-scale data	Normalization or scaling
Data Post-analysis	Under-fitting	Increase in data sets and decrease in learning rate
	Over-fitting	Decrease in data sets and increase in learning rate
	Parameter contributions (sensitivity)	Elimination for the one with much less contribution

Table 7.2 Parameters of the ANN Protocols in Different Heuristic Cycles

Heuristic Cycle	1st	2nd	3rd	4th	5th
Perceptrons	2	2	2	2	2
		3(P4)*	3(P5)*		
Neurons (input, output)	(20, 3)	(20, 2)	(18, 2)	(18, 1)	(17,1)
Scaling Functions	Linear [-1,1]	Non Linear [-1,1]	Linear [-1,1]	Logistic	Logistic
		Logistic	Logistic		
Activation Function	Logistic	Logistic	Logistic	Logistic	Logistic
		Tanh function	Tanh function	Tanh function	Tanh function
		Gaussian function	Gaussian function	Gaussian function	Gaussian function
Output Function	Logistic	Logistic	Logistic	Logistic	Logistic
		Tanh function	Tanh function	Tanh function	Tanh function
		Gaussian function	Gaussian function	Gaussian function	Gaussian function
Initial Bias Weight	0.3	0.3	0.3	0.3	0.3
Learning rate and Momentum	0.05/0.5**	0.05/0.5	0.1/ 0.1**	0.1/ 0.1**	0.1/ 0.1**
		0.1/ 0.1			
Data sets: Training-Test-Validating	29-8-3	36-16-27	34-10-8	62-12-12(P7)*	32-9-10
				56-18-12	
Learning Epochs	20,000 to 40,000	20,000 to 40,000	20,000 to 40,000	20,000 to 40,000	20,000 to 40,000
Extract Methods: Test Data / Validating Data*	Random/ Sequence	Random/ Sequence	Intervals/ Intervals*	Random/ Sequence	Random/ Sequence
			Jump/ Jump*		
			Random/ Sequence		
The Number of Trial Protocols	1	37	21	10	9
Representatives of the Trial Protocols	Protocol 1	Protocols 2 & 4	Protocols 3 & 5	Protocols 6 & 7	Protocol 8
** the amount was used by the recommendation of Neuroshell2; * the parameter was applied only in the representatives of the protocols (P)					

Table 7.3 (a) Comparison of ANN Prediction for Protocols 1 to 5

Representative Protocols	1			2		3		4		5	
Normalization	Non-normalized			Normalized to [-1,1]		Normalized to [-1,1]		Normalized to [-1,1]		Normalized to [-1,1]	
Input Neurons	20			20		18		20		18	
Hidden Neurons	17			20		16		10-10		8-8	
Output Neurons	3			2		2		2		2	
Scaling Func.	Linear [-1,1]			Linear [-1,1]		Linear [-1,1]		Linear [-1,1]		Linear [-1,1]	
Activation	Logistic			Logistic		Logistic		Logistic		Logistic	
Output Func.	Logistic			Logistic		Logistic		Logistic		Logistic	
Significantly Contributed Inputs	N.A.			11		8		13		10	
Learning Rate	0.1			0.05		0.1		0.1		0.1	
Momentum	0.1			0.5		0.1		0.1		0.1	
Patterns Processed	40			78		52		78		52	
Patterns Validated	3			27		8		27		8	
Output Conditions	s	w	r	s	r	s	r	s	r	s	r
R^2	0.54	0.70	0.81	0.83	0.59	0.50	0.83	0.84	0.61	0.54	0.85
r^2	0.59	0.72	0.82	0.83	0.64	0.54	0.83	0.83	0.62	0.60	0.85
r	0.77	0.85	0.90	0.90	0.80	0.74	0.91	0.88	0.80	0.77	0.92
MSE	0.05	0.074	0.05	0.04	0.10	0.04	0.03	0.02	0.12	0.03	0.02
Percentage for High-error Patterns*	33%			37%		14%		37%		14%	
Percentage for Misclassification Patterns**	33%			15%		14%		15%		14%	

N.A. : not available

s, w, and r: Safe, warning, and wrinkling conditions

*: the percentage was computed by high-error patterns divided all patterns for validating patterns, and the high-error patterns have an actual-to-desired output ratio lager than 1.2

**: the percentage was computed by misclassified patterns divided all patterns for validating patterns,

Table 7.3 (b) Comparison of ANN Prediction for Protocols 6 to 8

Representative Protocols	6	7	8		
Normalization	Normalized to [-1,1]	Normalized to [-1,1]	Normalized to [-1,1]		
Input Neurons	18	18	17		
Hidden Neurons	16	16	15		
Output Neurons	1	1	1		
Scaling Func.	Logistic	Logistic	Logistic		
Activation	Gaussian	Gaussian	Logistic		
Output Func.	Gaussian	Gaussian	Logistic		
Significantly Contributed Inputs	16	17	3		
Learning Rate	0.1	0.1	0.1		
Momentum	0.1	0.1	0.1		
Patterns Processed	86	86	51		
Patterns Validated	12	12	10		
R^2	0.83	0.86	0.89		
r^2	0.83	0.86	0.89		
r	0.91	0.93	0.94		
Percentage for High-error Patterns*	33%	33%	10%		
Percentage for Misclassi-fication Patterns**	17%	17%	0%		
*: the percentage was computed by high-error patterns divided all patterns for validating patterns, and the high-error patterns have an actual-to-desired output ratio lager than 1.2 **: the percentage was computed by misclassified patterns divided all patterns for validating patterns					

Table 7.4 ANN(1) Prediction Results

File Name	18-6r1			
Neuron Number (input-hidden-output)	17-17-1			
Data Number (total-Test-Validating)	52-12-0			
Coeff. of Multi-regress: R^2	0.72			
Correlation Coeff. : r	0.85			
Desired Outputs (1)	ANN Outputs (2)	Error [(1)-(2)]	Mark	Pipe Data (%of the Peak Moment)
0	0	0	T	FEA
1	0.740742	0.259258	T	FEA
1	0.935858	0.064142	T	FEA
1	0.980333	0.019667	T	FEA
1	0.957419	0.042581	T	FEA
1	0.864739	0.135261	T	FEA
1	1	0	T	FEA
1	0.761862	0.238138	T	FEA
1	0.924734	0.075266	T	FEA
1	1	0	T	FEA
0	0.786218	-0.78622	T	FEA
0	0	0	T	Geopig 1
T: Test sets				

Table 7.5 ANN(2) Prediction Results

File Name	18-5r1			
Neuron Number (input-hidden-output)	18-18-1			
Data Number (total-Test-Validating)	113-30-0			
Coeff. of Multi-regress: R^2	0.86			
Correlation Coeff. : r	0.93			
Desired Outputs (1)	ANN Outputs (2)	Error [(1)-(2)]	Mark	Pipe Data (%of the Peak Moment)
0	6.03E-05	-6E-05	T	FEA
0	7.66E-07	-7.7E-07	T	FEA
0	2.43E-05	-2.4E-05	T	FEA
0	2.98E-05	-3E-05	T	FEA
0	0.014064	-0.01406	T	FEA
0	0.056734	-0.05673	T	FEA
0	0.00324	-0.00324	T	FEA
0	0.052331	-0.05233	T	FEA
0	1.96E-05	-2E-05	T	FEA
0	0.001558	-0.00156	T	FEA
1	5.41E-06	0.999995	T	FEA
1	0.998718	0.001282	T	FEA
1	0.906342	0.093658	T	FEA
1	0.90013	0.09987	T	FEA
1	0.983627	0.016373	T	FEA
1	0.996624	0.003376	T	FEA
1	0.571607	0.428393	T	FEA
1	0.986653	0.013347	T	FEA
0	0.007217	-0.00722	T	TCPL3 (39)
1	0.899146	0.100854	T	TCPL3 (95)
0	0.021153	-0.02115	T	TCPL2 (64)
1	0.886083	0.113917	T	TCPL2 (100)
0	0.082389	-0.08239	T	TCPL2 (46to90)
0	0.000903	-0.0009	T	TCPL1 (69)
1	0.110266	0.889734	T	TCPL1 (100)
1	0.886396	0.113604	T	Pipe#9 (70)
0	0.000212	-0.00021	T	Dent
1	0.887453	0.112547	T	Geopig4
0	0.178535	-0.17853	T	TCPL3 (88)
1	0.001025	0.998975	T	HGAw (95)

243

Table 7.6   Thresholds versus Error of Misclassification

ANN		ANN(1)		ANN(2)		ANN(3)		ANN(4)	
Neuron Number (input-hidden-output)		17-17-1		18-18-1		17-17-1		18-20-1	
Scaling and Activation Functions		L-L-L		L-G-G		L-L-L		L-L-L	
Number of Total Data Sets		319		120		54		54	
Pipe Condition		s	w	w	r	s	w	w	r
The Number of Data		18	45	12	12	5	5	5	5
Thresholds		Error (Number of Misclassified Data / Number of Data)							
	0.90	0.33	0	0	0.17	0.20	0	0	0.40
	0.85	0.27	0	0	0.17	0	0	0	0.40
	0.80	0.22	0	0	0.17	0	0	0	0.40
	0.75	0.22	0	0	0.17	0	0	0	0.20
	0.70	0.17	0	0	0	0	0	0	0.20
	0.65	0.11	0	0	0	0	0	0	0.20
	0.60	0.11	0.02	0	0	0	0	0	0
	0.55	0.11	0.02	0	0	0	0	0	0
	0.50	0.05	0.04	0	0	0	0	0	0

s, w, and r: Safe, warning, and wrinkling conditions

Table 7.7 Validation of ANN Generalization Capacity

ANN		ANN(1)	ANN(2)	ANN(3)	ANN(4)
Neuron Number (input-hidden-output)		17-17-1	18-18-1	17-17-1	18-20-1
Scaling and Activation Functions		L-L-L	L-G-G	L-L-L	L-L-L
Threshold		0.65	0.70	0.85	0. 60
The Number of Validating Data		16	11	10	9
Pipe Data (% of the peak moment)	Expected Pipe Condition	(s):1, (w,r): 0	(s, w):0, (r): 1	(s):1, (w,r): 0	(s,w):0, (r): 1
Geopig (Dent)	(w)	0.000	0.000		
Geopig1 (wrinkle near joint)	(r)			0.000	1.000
Geopig2 (settlement)	(s)	0.933			
Geopig3 (wrinkle:upheaval)	(r)	0.032	0.989		
Geopig4 (wrinkle near girth weld)	(r)			0.000	1.000
Geopig5 (wrinkle: slope unstable)	(w)	0.292	0.662		
TCPL3 (36 to 39)	(s)	*0.628 (M)*	0.018		
TCPL3 (71)	(w)	0.513	0.302		
TCPL3 (88)	(r)	0.000	0.977		
TCPL1 (33)	(s)	1.000			
TCPL1 (95)	(r)	0.033	0.992		
TCPL1 (85*)	(r)	0.000	0.933		
TCPL2 (30)	(s)	0.972			
TCPL2 (46)	(s)	0.675			
TCPL3 (71to73)	(w)	0.260	0.690		
TCPL3 (90to95)	(r)	0.000	0.985		
Pipe#9 (36)	(s)	0.994			
Pipe#9 (70)	(r)	0.152	1.000		
UGAw (61)	(w)			*1.000 (M)*	0.000
UGAw (86)	(r)			0.760	1.000
UGAw (100)	(r)			0.000	1.000
DGAw (100)	(r)			0.126	1.000
DGAw (87*)	(r)			0.820	1.000
HGAw (49)	(s)			1.000	
HGAw (95)	(r)			0.000	1.000
HGAw (87*)	(r)			0.000	1.000

*: Post-buckling Loading Stage;   s, w, and r: Safe, warning, and wrinkling conditions
M: Misclassified patterns
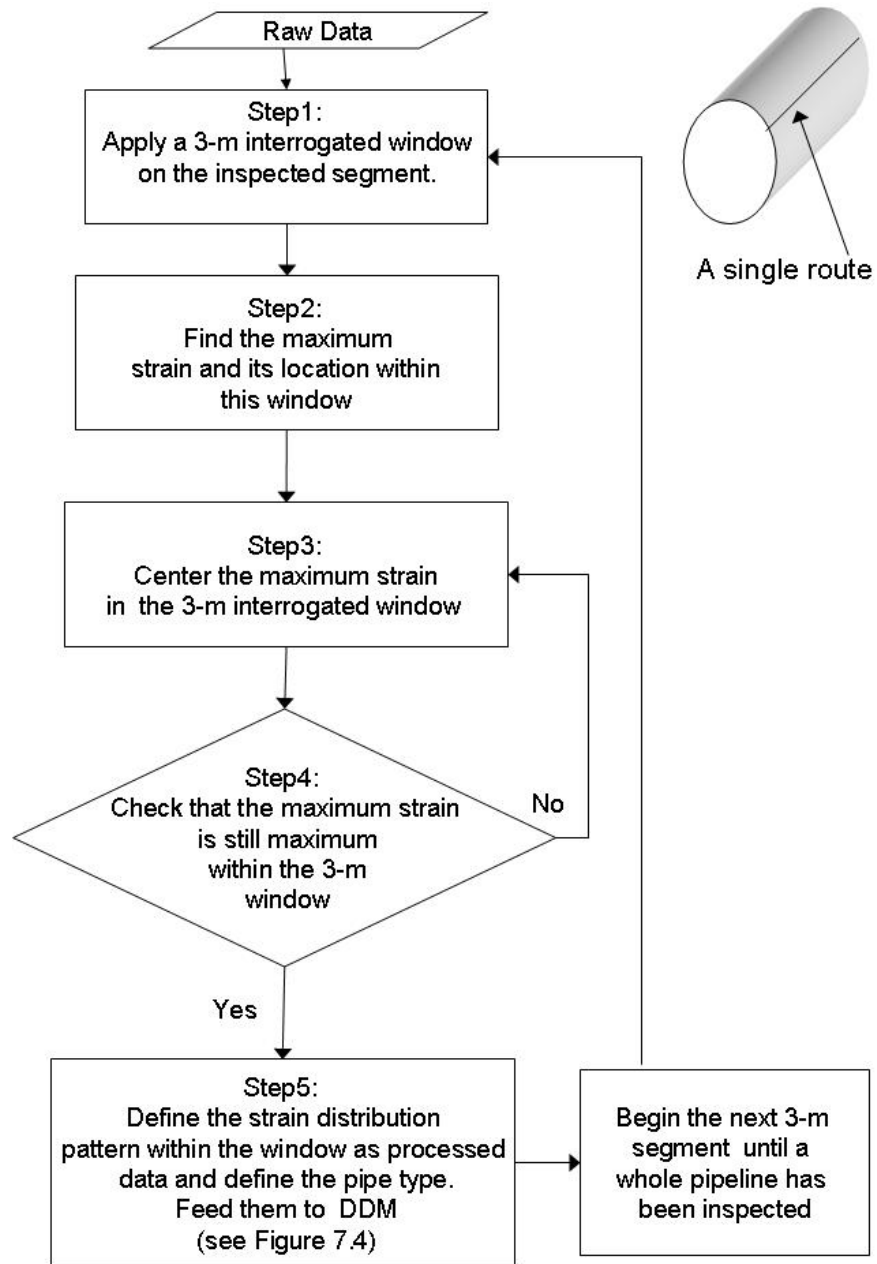
Figure 7.1 Flow Chart of the Single-route Data Processing for the Damage
Detection Model
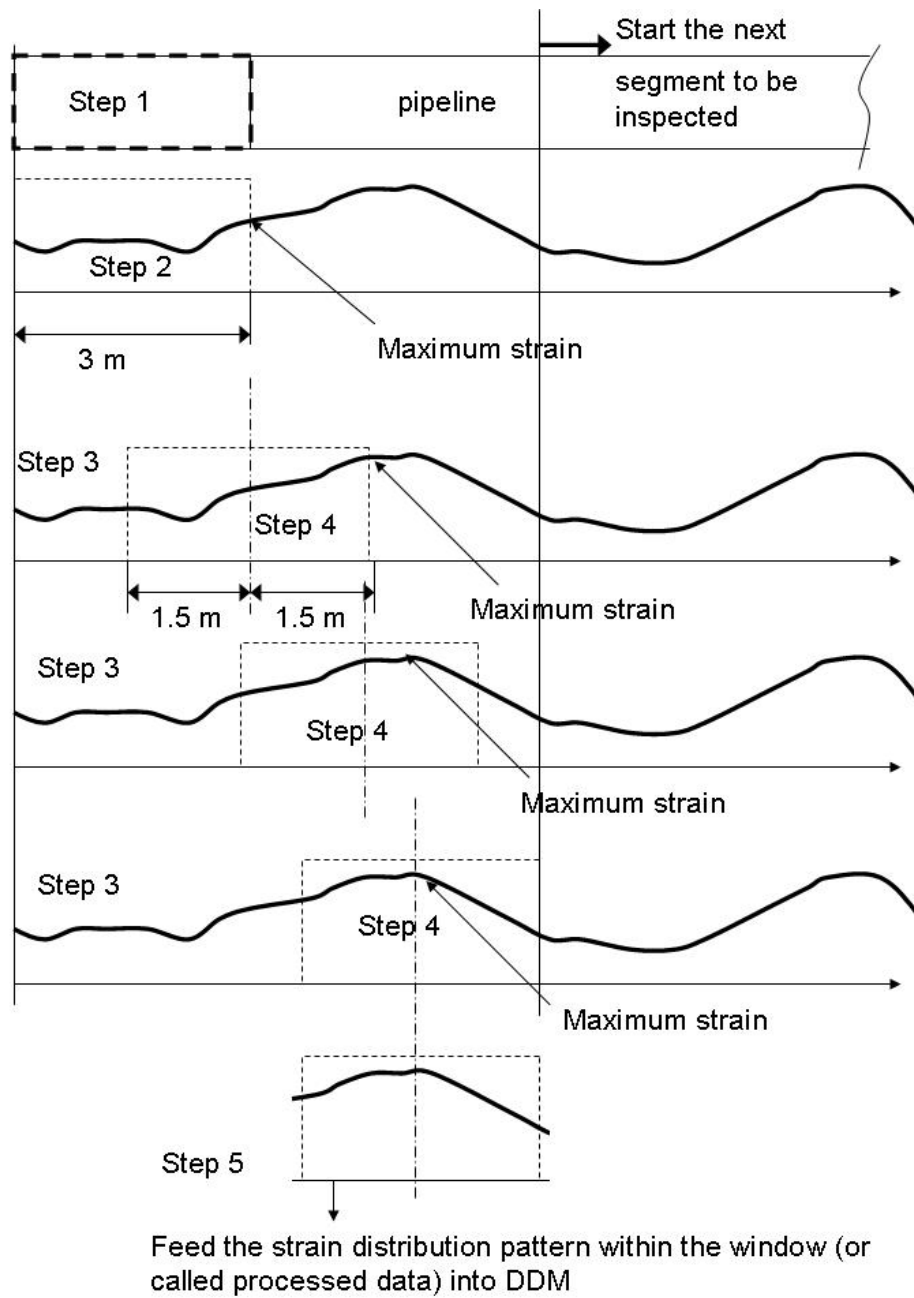
Figure 7.2 Schematic of Data Processing for the Damage Detection Model
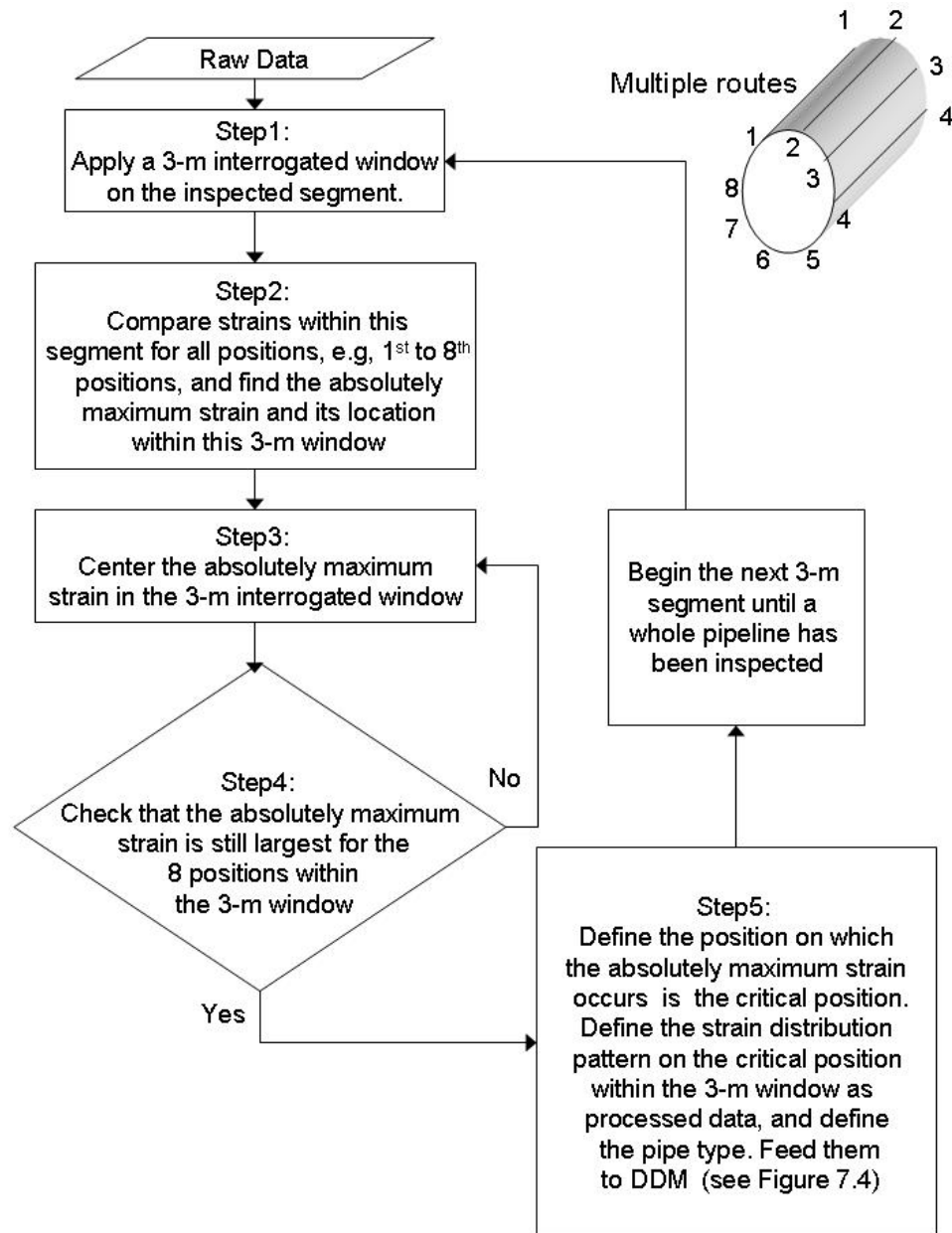
Figure 7.3 Flow Chart of the Multiple-route Data Processing for the Damage Detection Model

Strain distribution pattern extracted in 1.5-m range centered at the maximum strain location from the processed data

For plain pipes | Pipe Type | For girth-welded pipes

ANN(1) | ANN(3)

IF…Then | IF…Then

No | Safe condition | No
ANN(2) | Safe condition | ANN(4)

Yes | Yes

IF…Then | S | S | IF…Then

Wrinkling Condition | No | W | W | No | Wrinkling Condition

Yes | Yes

R | R

Send an alarm to pipe operators | Send an alarm to pipe operators

Save selected processed data to DBS | Save processed data to DBS

S; Pipe safe**; W:** Warning Condition**; R:** Pipe wrinkling

Figure 7.4 Flow Chart of Wrinkling Detection Using the Damage Detection Model
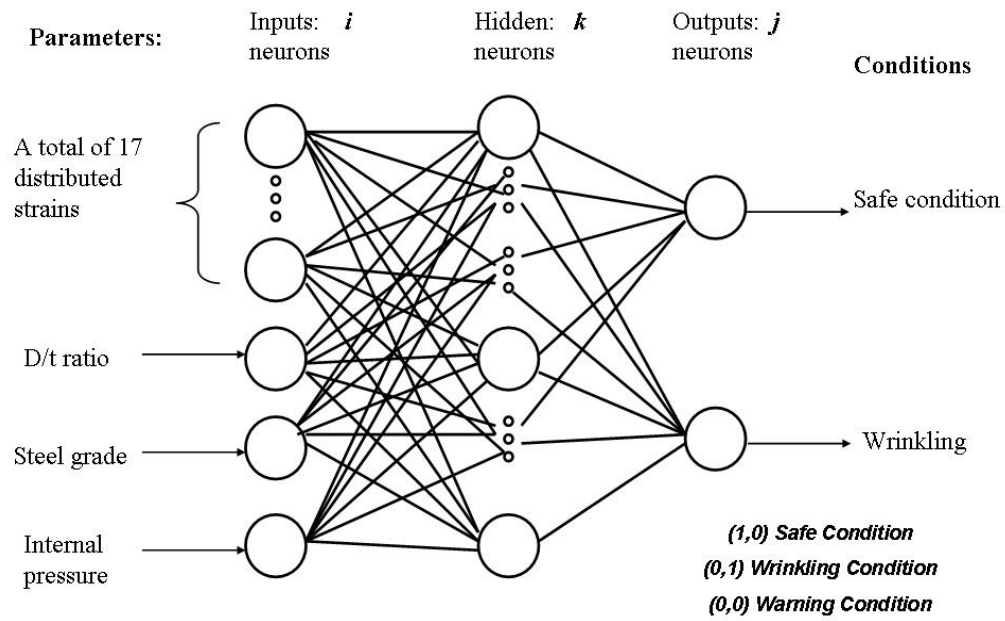
Figure 7.5 Profile of a Preliminary ANN for Monitoring Strain Distribution
Patterns

250
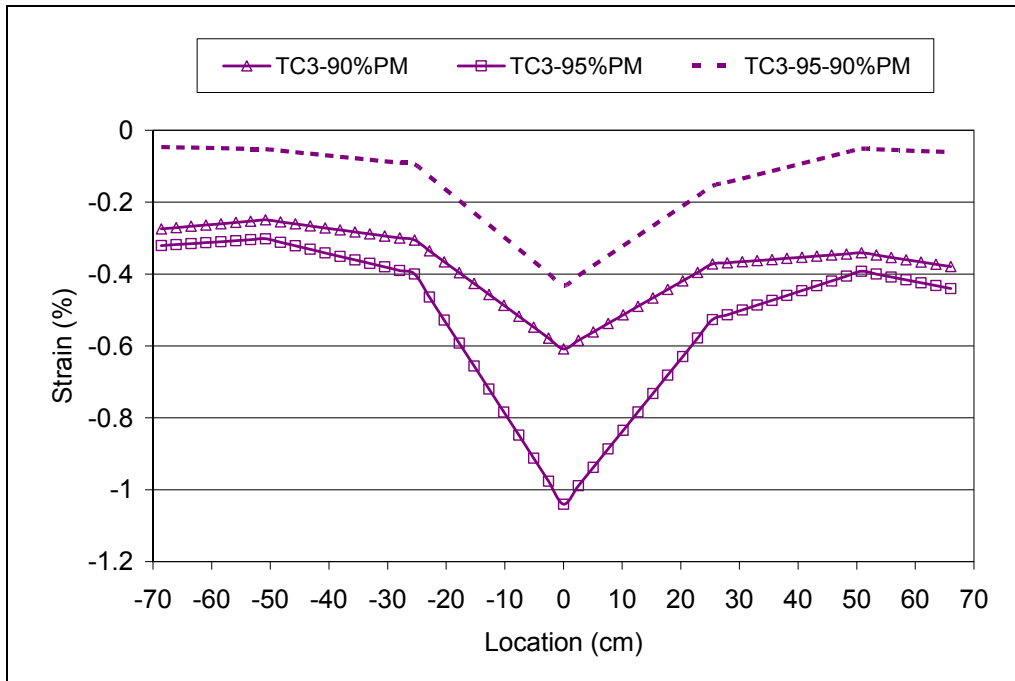
Figure 7.6 Comparison of Accumulated Strain and Relative Strain distributions
Before Normalization
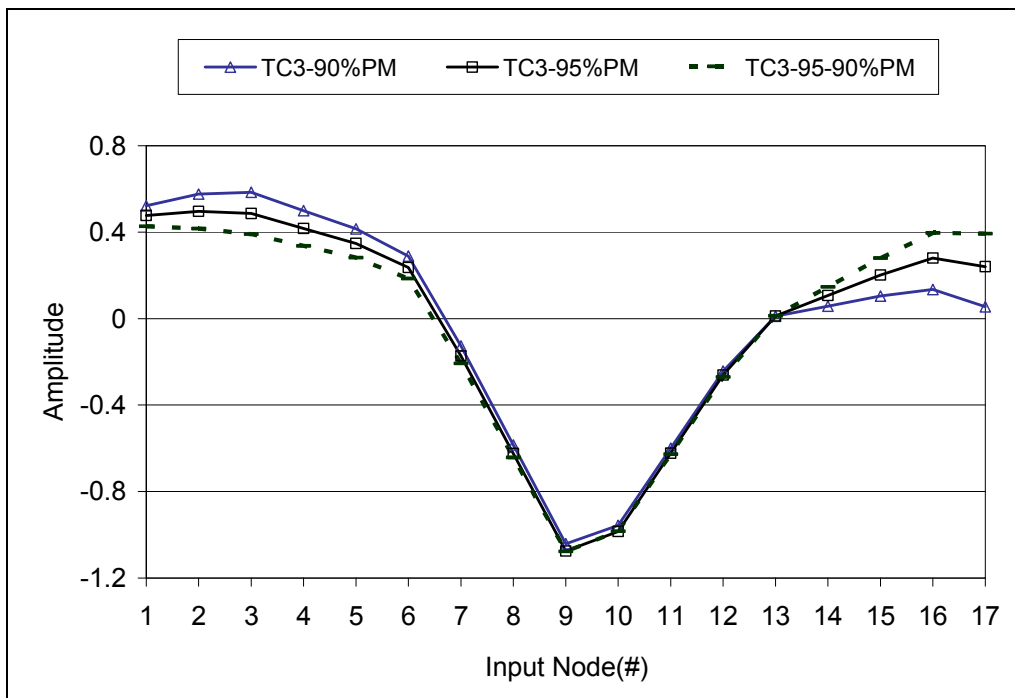
Figure 7.7 Comparison of Accumulated Strain and Relative Strain distributions
After Normalization
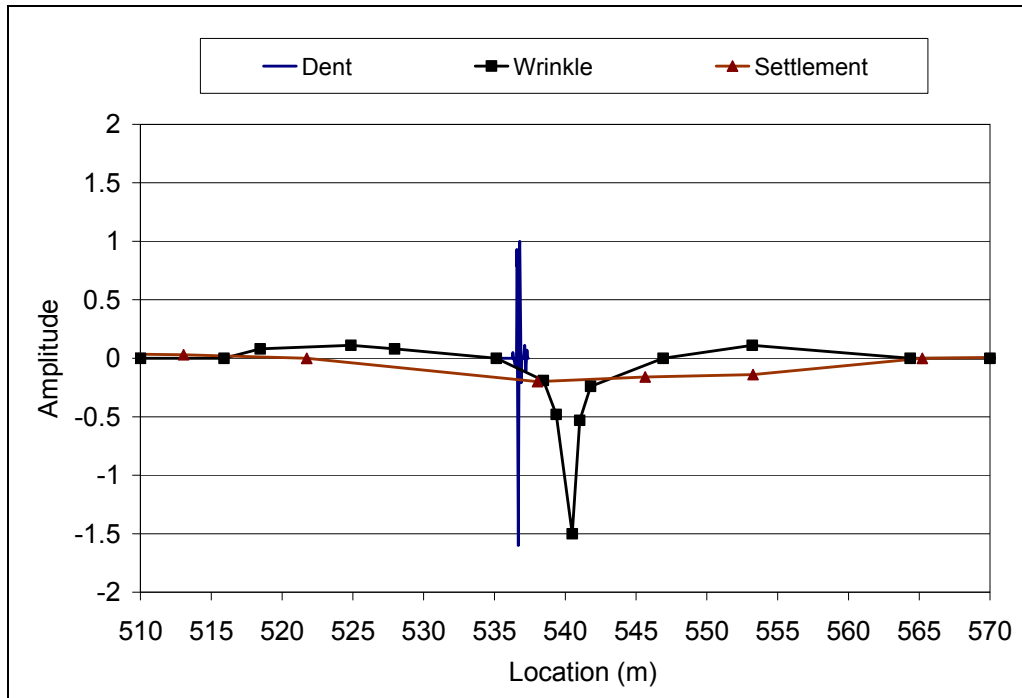
Figure 7.8 Strain Distribution Patterns of Geopig Data Before Scaling
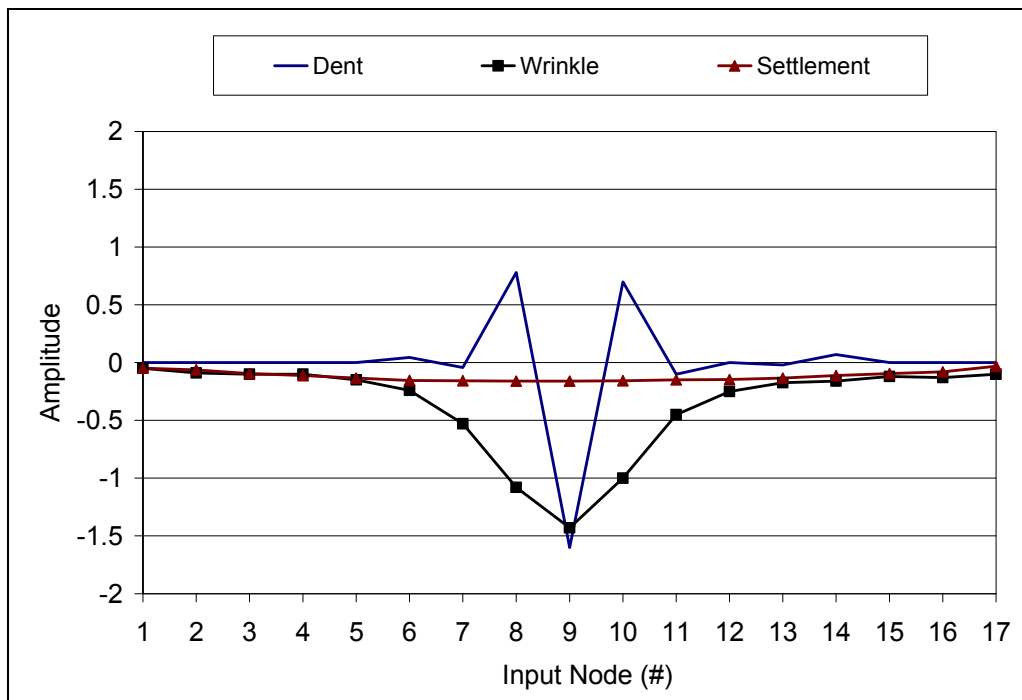
Figure 7.9 Strain Distribution Patterns of Geopig Data After Scaling

252
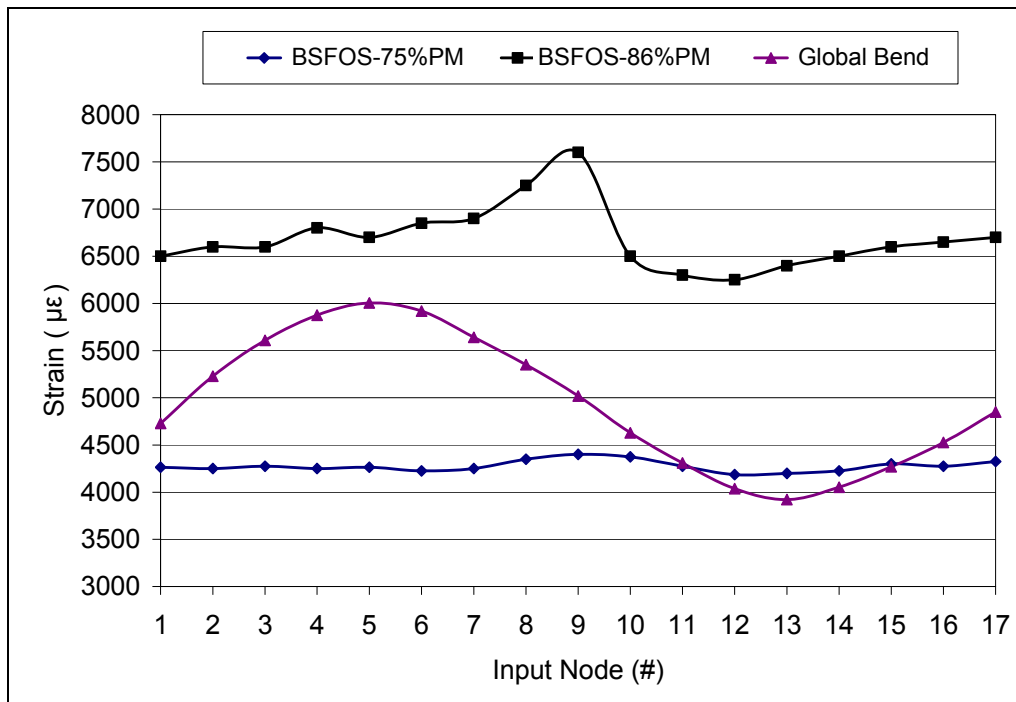
Figure 7.10 Validating Strain Distribution Patterns in ANN Protocol1
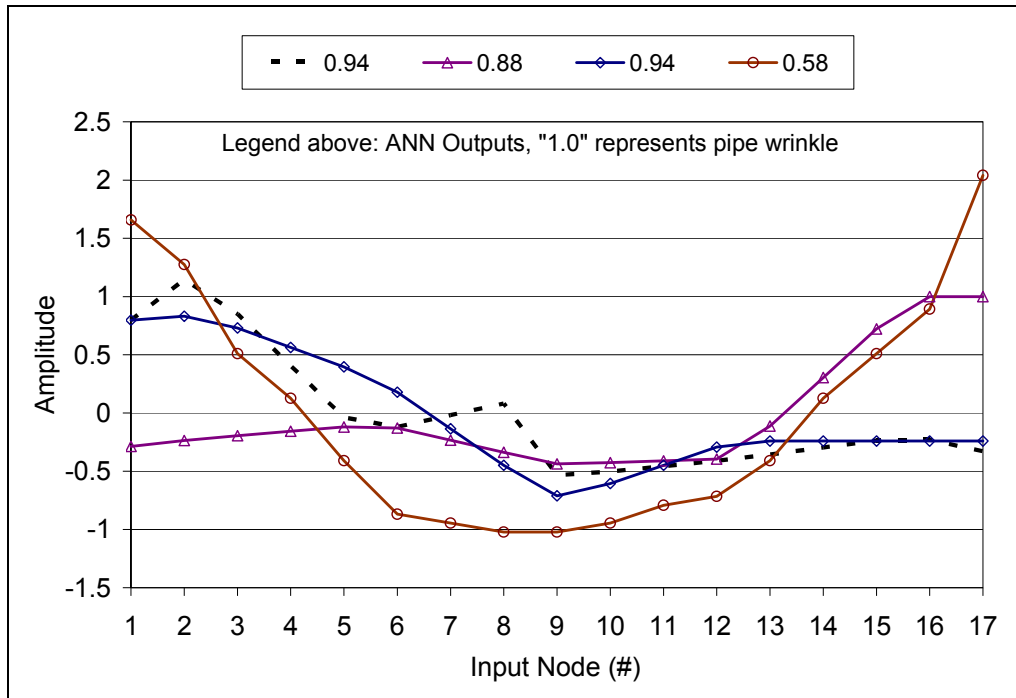
Figure 7.11 Misclassified Strain Distribution Patterns in ANN Protocol 2
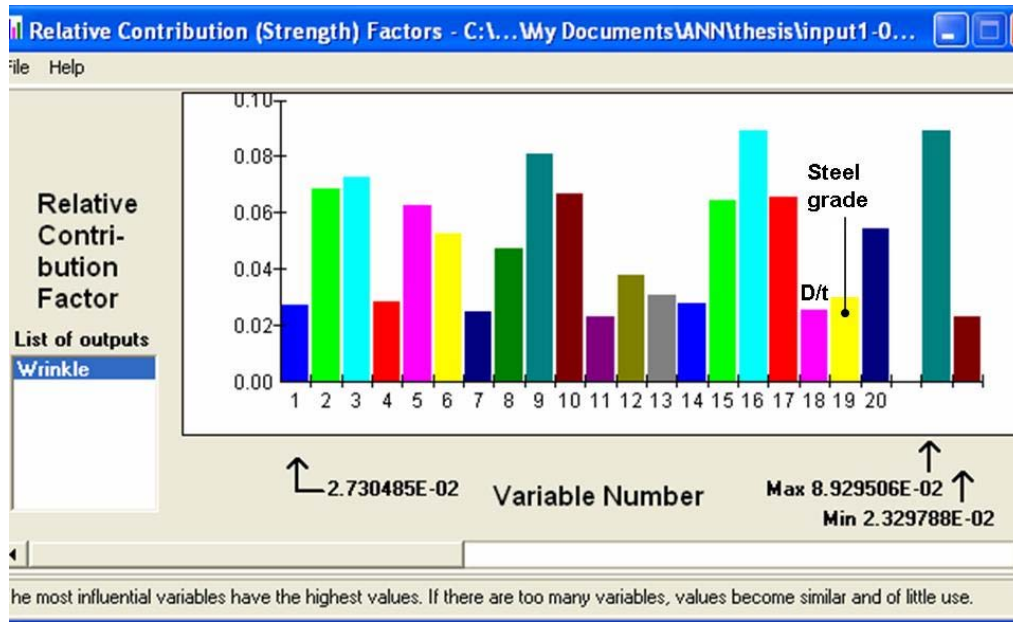
Figure 7.12 Histograms of the Parametric Contributions for 20 Input Parameters

255

Parameters: Inputs: 17 neurons Hidden: 17 neurons Outputs: 1 neurons **Conditions**

Distributed strain array, (Li,Ai), totally 17 pairs

1/ 0

1: Safe Condition

0: either Warning Condition or Wrinkling Condition

(a) ANN(1)

Parameters: Inputs: 18 neurons Hidden: 18 neurons Outputs: 1 neurons **Conditions**

A total of 17 distributed strains

Internal pressure

1/ 0

1: Wrinkling Condition

0: Warning Condition

(b) ANN(2)

Figure 7.13 Architectures of the ANN(1) and ANN(2)
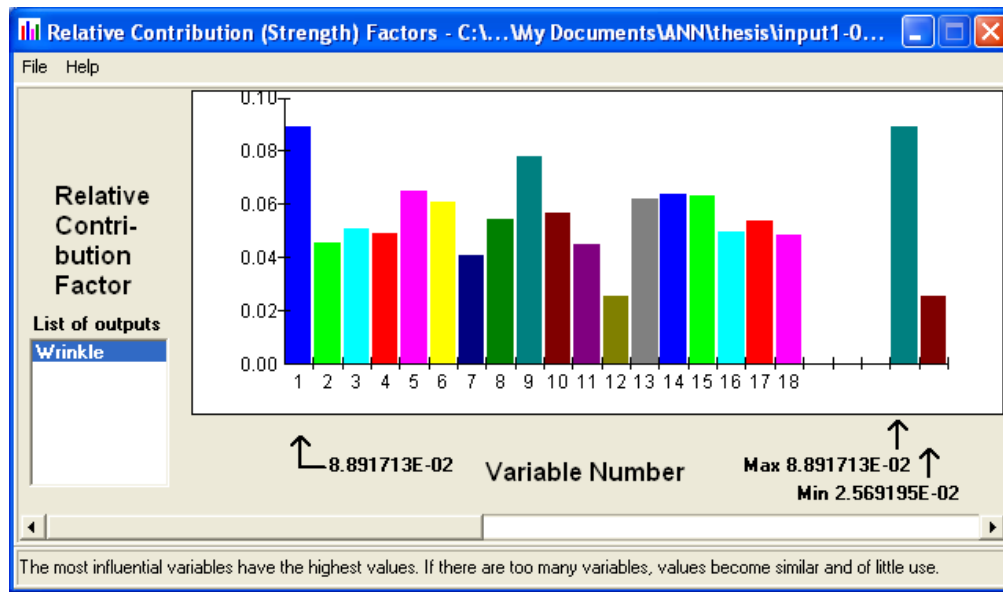
Figure 7.14 Input Parameters' Contribution to the Output of ANN(2)
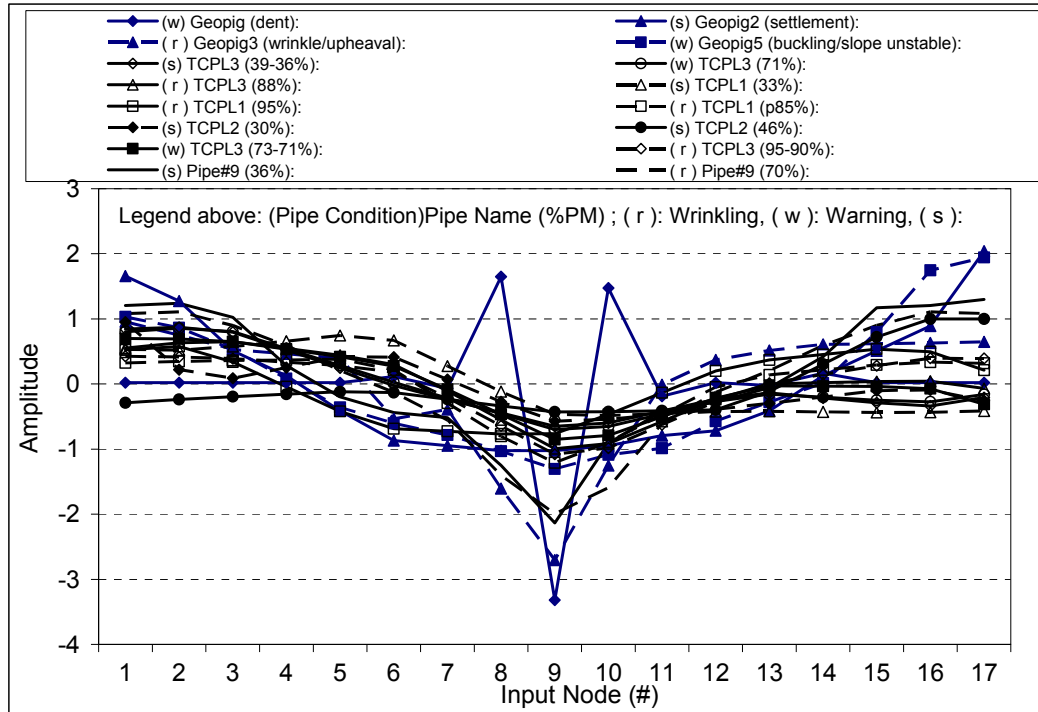
Figure 7.15 Validating Strain Distribution Patterns for Plain Pipes
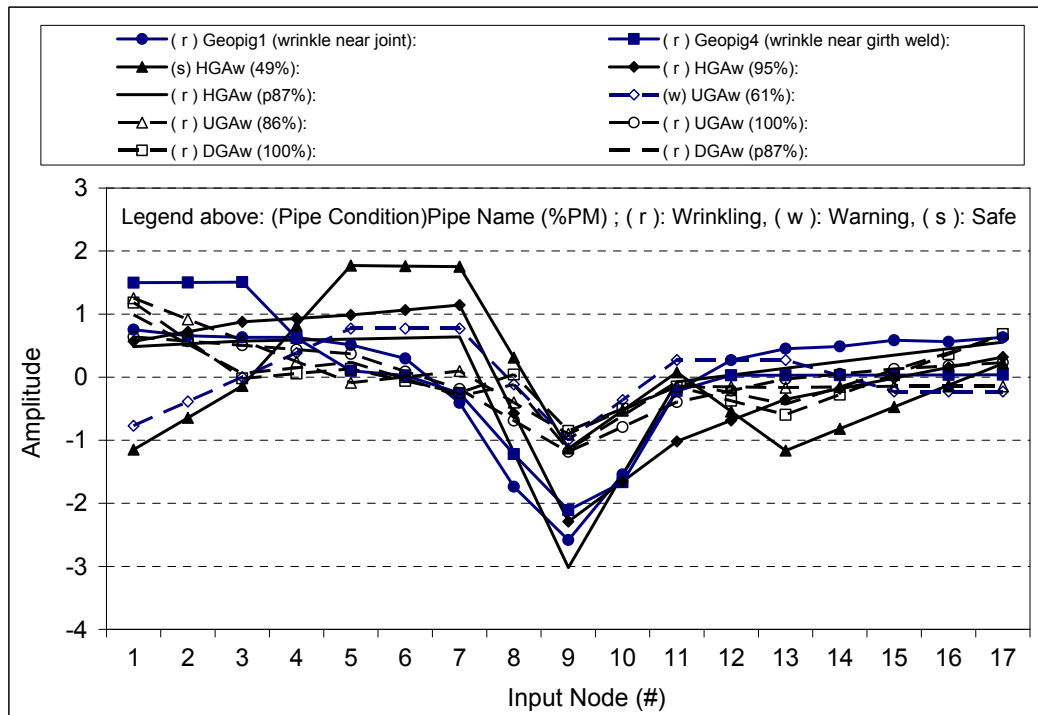
Figure 7.16 Validating Strain Distribution Patterns for Girth Weld Pipes

258
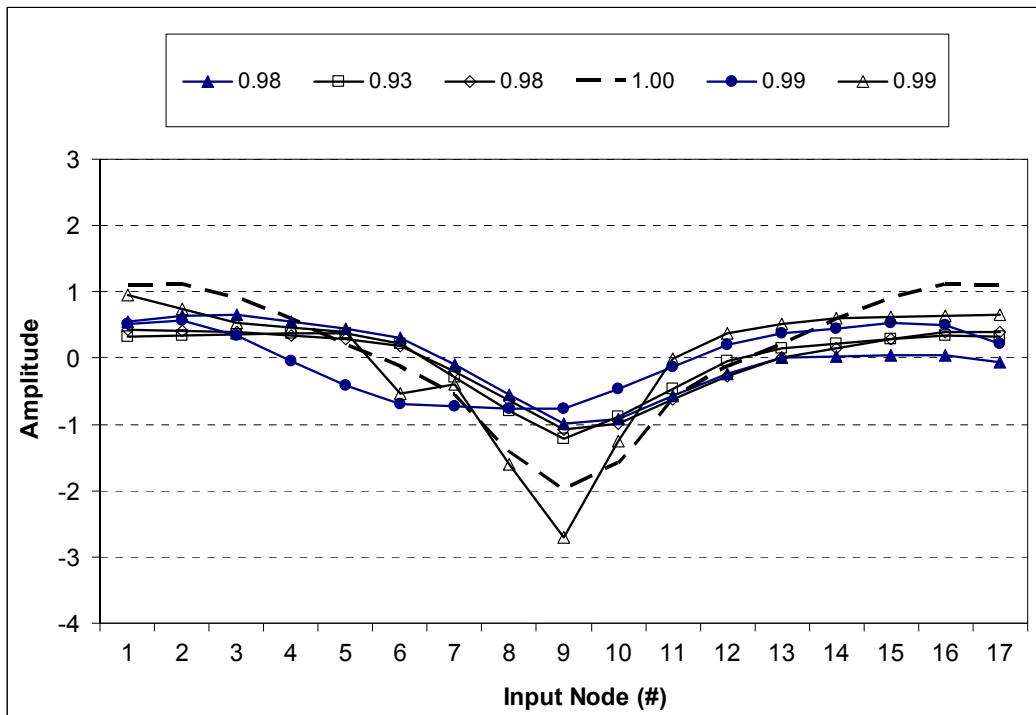
Figure 7.17 High-score Patterns in ANN(2)
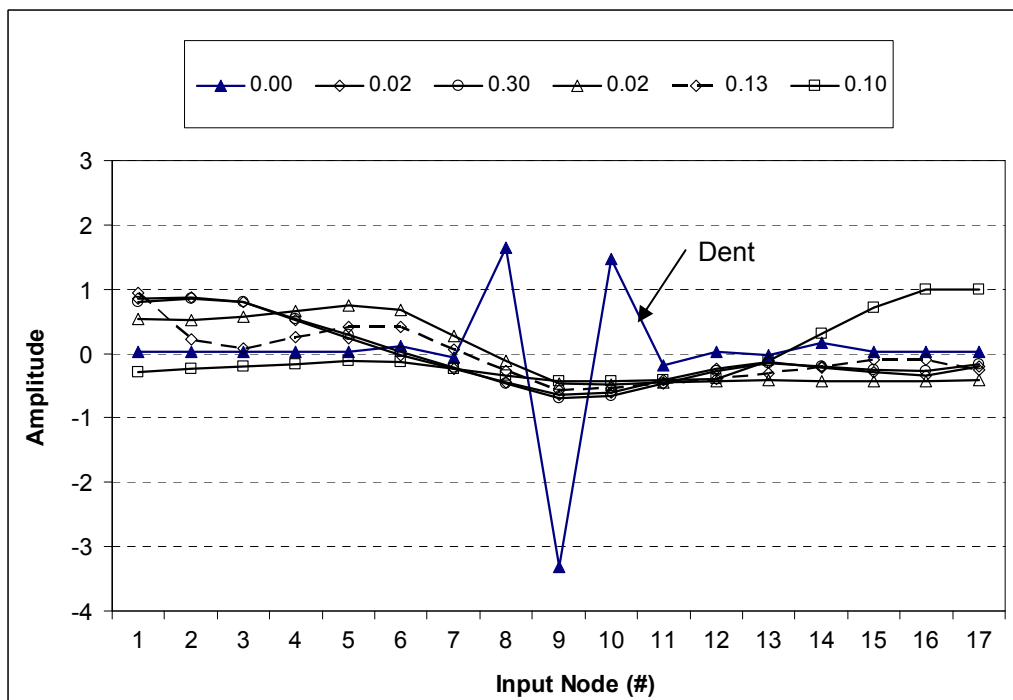
Figure 7.18 Low-score Patterns in ANN(2)
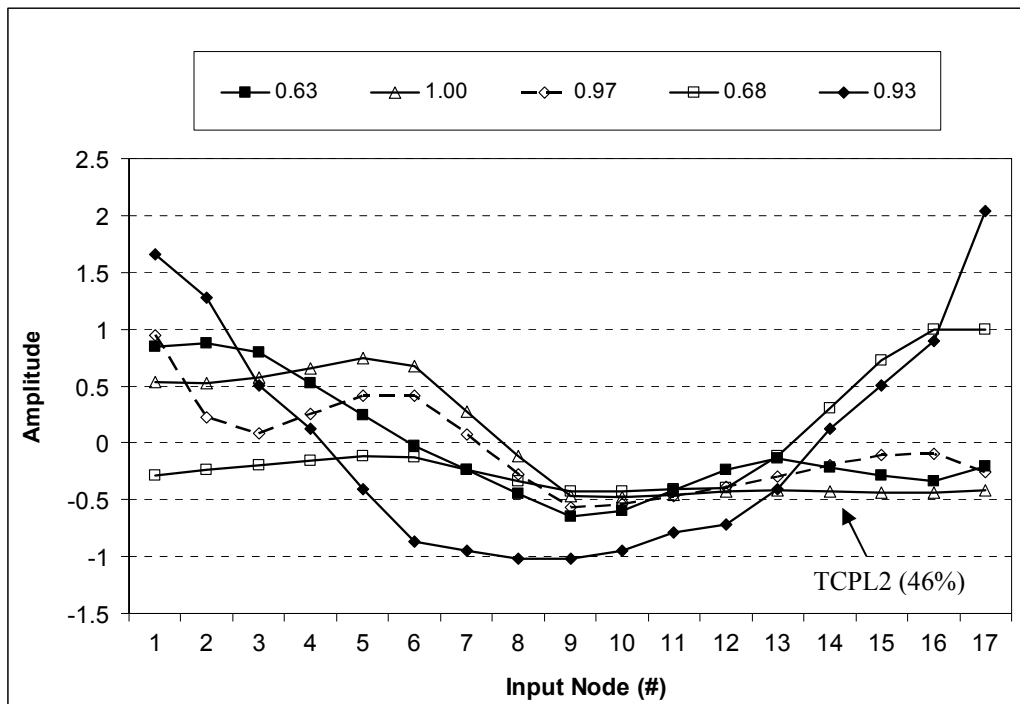
Figure 7.19 High-score patterns in ANN(1)
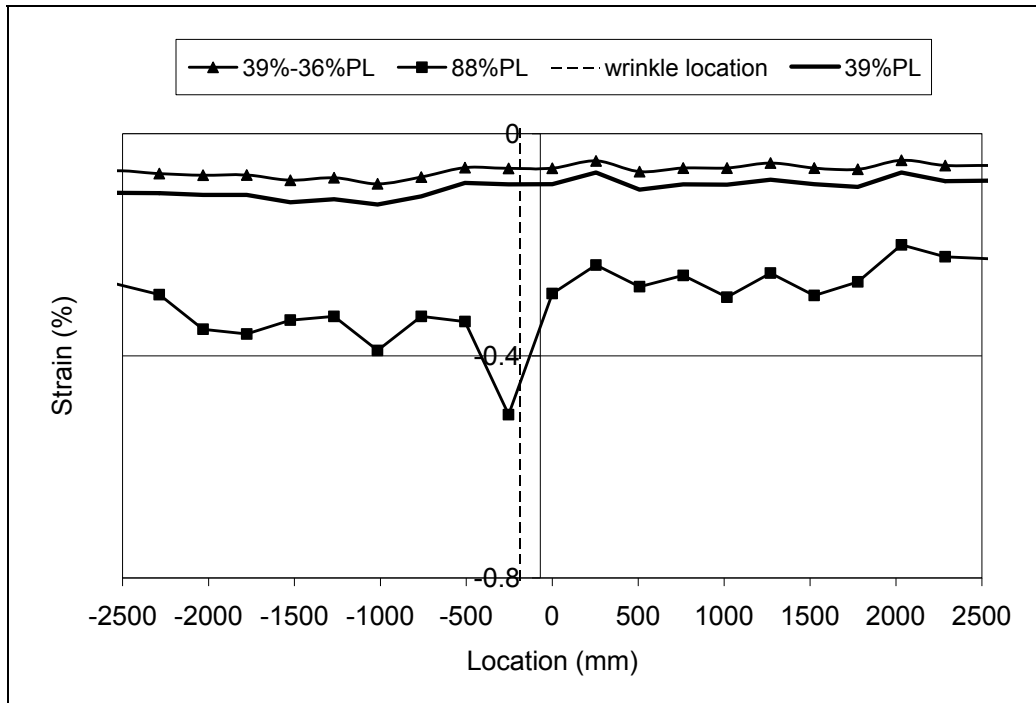
Figure 7.20 Strain Distribution Patterns of TCPL3 Pipe Before Normalization
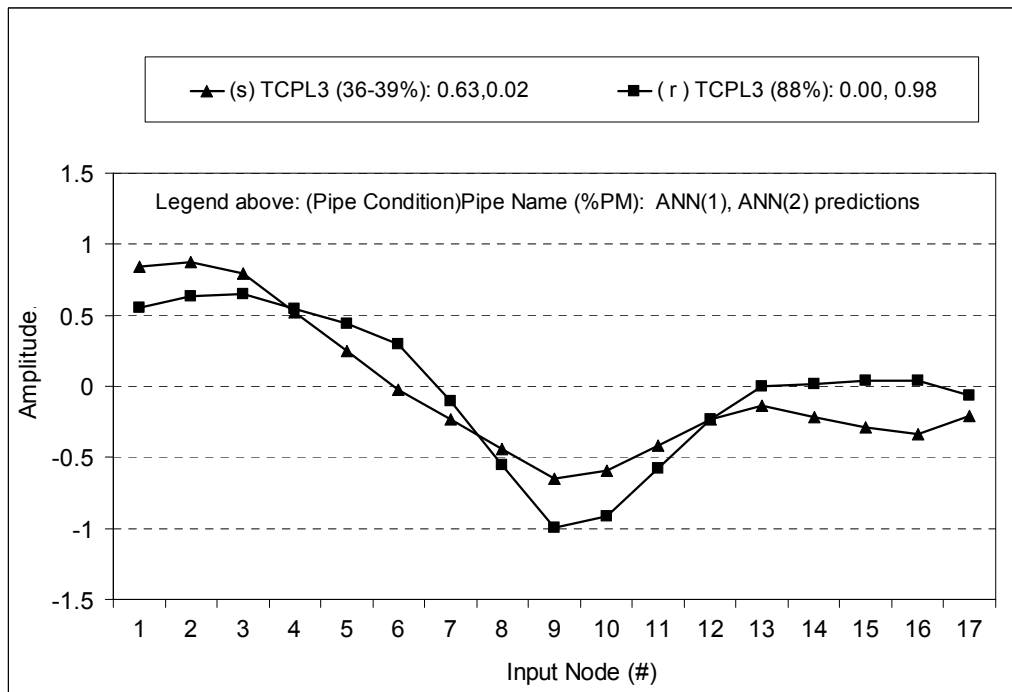
Figure 7.21 Strain Distribution Patterns of TCPL3 Pipe After Normalization

8. SUMMARY, CONCLUSIONS, AND RECOMMENDATIONS

8.1 Summary

The development of SHM system in this thesis integrates a distributed strain sensing system (such as the BSFOS system), the finite element analysis (FEA), and a damage detection model using the artificial neural network (ANN). The proposed system will provide engineers with continuously real-time data to calibrate their previous operating model and to reliably diagnose pipe buckling condition without interrupting the normal operation of buried pipelines.

Comparison of the available monitoring technologies used in buried pipelines revealed that the distributed sensory systems, such as Geopig and the recently developed Brillouin scattering fiber-optic sensing (BSFOS) system, were probably the most appropriate systems for carrying out distributed measurements in buried pipeline buckling.

Further investigation on six sets of field pipelines and 15 sets of experimental line-pipes, all of which failed in local buckling, has shown that the behavioural signatures of the buckled pipes could be identified during the development of the strain distributions. The strain distributions changed from a relatively consistent distribution to a multiple-waves distribution with increase of the applied load or the pipe deformation. As the applied loading approached the attainment of the limit point, localized strains occurred on the strain distribution and concentrated at the wrinkle location.

The feasibility of using distributed strain sensors to detect the inception of pipe wrinkling was further validated by conducting two full-scale pipe buckling tests at laboratory and an excavation experiment on a 914.4 mm diameter buried pipeline of 27,573 mm in length. The tests have shown the potential and robustness of using the distributed strain sensory system on buried pipes in detecting pipe wrinkling.

In addition to the experimental studies, the patterns (or signatures) of the strain distributions of pipe buckling under combined loading were systematically studied by using about 900 strain distributions developed from FEA. The FE models developed in this research were validated by the experimental data from ten full-scale high strength pipe tests. Good agreements between the FEA and experimental results were obtained. The average prediction-to-test ratio was 1.05 with a standard deviation of 0.178 for the critical strain; and the average prediction-to-test ratio was 1.02 with a standard deviation of 0.029 for the peak moment. Similar prediction-to-test ratios were also obtained for the local compressive strains near the wrinkle location before the pipe reached the critical strain, around 70% to 90% of the peak moment. A statistical index, the Pearson product-moment correlation coefficient was used to compare the compressive strain distribution patterns over the wrinkle locations. The correlation analysis showed that there is more than a 0.83 correlation between the FEA and test results.

The behavioural characteristics of the strain distribution patterns during pipe wrinkling were identified from the FEA. The compression strain distribution at say 35% of the peak moment remain relatively constant; but when the moment reaches around 75% of the peak moment, the strain distribution shows a wave-shaped distribution and dominating strain localization appears. This wave pattern can be used as a warning sign for pipe wrinkling. Finally, with increase of load or deformation, the dominating strain localization becomes apparent, normally around 85% to 90% of the peak moment. It can be treated as pipe wrinkled. The wrinkle development along the compression side of the pipe can also cause longitudinal strain localization at the neighbouring positions, even at the tension side of the pipe. In addition to the above behavioural signatures, the signature index, the correlation index of tension-side strain distributions, and the strain ratio index on the compression side, derived from the distributed strains, were investigated for the feasibility of using these indices as the deterioration criteria of the pipeline buckling.

The relationships of strains at different locations, axially and circumferentially, were also studied so that the location and spacing of the distributed strain sensors could be installed effectively and practically on the buried pipelines. A total of 16 different pipe conditions were studied to identify those relationships.

Based on the behavioural signature and signature indices of pipe buckling, an integrated methodology to monitor the health of buried pipe buckling using distributed strain sensory systems was proposed. It includes the procedures of data processing, damage detection, pipe-wrinkling warning, and data storing. The development of the damage detection model (DDM) was the focus of the proposed methodology. Four Artificial Neural Network (ANN) protocols, ANN(1), ANN(2), ANN(3), and ANN(4), were the core of the DDM.

The threshold patterns corresponding to the three pipe conditions, i.e. the safe, warning, and wrinkling conditions, were determined first by the observation of the strain distributions and the load versus the deformation curves. Since the observation alone cannot determine the thresholds for the warning and wrinkling conditions, the statistical methods were applied to determine the threshold patterns representing these two conditions. In addition, in order to increase the ability of the DDM in identifying the pipe buckling conditions, the Pearson product-moment correlation analysis was used to exanimate the similarity of the strain distributions of these two conditions. Through correlation analysis, the threshold patterns for the warning and the wrinkling conditions were determined.

After the threshold patterns had been determined, the framework of the DDM with the proposed ANN protocols for detecting buried pipe wrinkling was developed. After comparing 78 ANN protocols, it was determined that the optimal model for monitoring the health of pipeline buckling by identifying distributed strain patterns was an integrated model developed by combining ANN(1) to ANN(4) using 3-layer neurons. Different pipe types, plain pipes and girth weld pipes, were diagnosed by two sets of the ANN protocols, ANN(1) and ANN(2), and ANN(3) and ANN(4), respectively.

In the damage detection model, to identify plain pipes' conditions, ANN(1) used 17, 17, and 1 neurons respectively in the input, hidden, and output layers to examine if a monitored pipe segment is under the safe condition. ANN(2) used 18, 18, and 1 neurons respectively in input, hidden, output layers to distinguish pipe wrinkle events from the abnormal condition. In addition, ANN(1) used logistic functions (sigmoidal functions) for all layers; the ANN(2) used logistic functions in input scaling, and Gaussian function as the activation function in both the hidden and the output neurons.

For girth weld pipes, ANN(3) used 17, 17, and 1 neurons respectively in input, hidden, and output layers to identify a segment as being in safe or abnormal condition. ANN(4) used 18, 20, and 1 neurons respectively in the input, hidden, and output layers to distinguish pipe wrinkle events from the abnormal condition. Both ANN(3) and ANN(4) used logistic functions for all layers.

The logic discriminating thresholds of 0.65, 0.70, 0.85, and 0.60 were used to filter the outputs of the ANN protocols, ANN(1), ANN(2), ANN(3), and ANN(4), respectively, so that the onset of pipe wrinkling can be reliably predicted.

The DDM was validated by a total of 26 data collected from both the experimental pipe tests and the buried pipes in the field. The pipes have different material properties, geometric properties, loading conditions, moment gradients, soil conditions, manufacturing procedures, and operating conditions. The rate of correct recognition of the integrated damage detection model approached to 90%. The generation capacity and limits of the proposed ANN protocols were also studied.

8.2 Conclusions

The conclusions based on the results of this research program can be drawn as follows:

1. The BSFOS system could reveal wrinkle locations at a much earlier loading stage than any other systems, such as Geopig. The test showed that the BSFOS system was able to detect pipe buckling at 75% of the peak moment, which corresponds to about 32% of the critical buckling strain. Furthermore, the BSFOS system survived buried condition, severe winter weather, and the excavation processes.

2. While the BSFOS system and digital camera system are appropriate for measuring the distributed strains along a pipe, the laser profile system used in the experiment can only be used for monitoring the deflection profile of the pipe specimen. For the BSFOS system and camera system, the strain error can be smaller than 100 micro-strains, and the equivalent gauge length can be less than 100 mm.

3. The FE models appropriately simulated the longitudinal strain distributions of a line-pipe during buckling. An initial imperfection with amplitude equals to 18% and 20% of the wall thickness of the pipe respectively for the girth-welded pipes and the plain pipes was used in the FE models. For the plain pipes, the blister shape imperfection was used in the models, while the offset imperfection was created at the girth weld location for the girth-welded pipes.

4. The overall behaviour, including the strain distribution patterns, of the high strength pipes is similar to that of the conventional strength pipes.

5. The FE models provided better simulation of the distributed strains for the pipes whose wrinkle occurred in the middle of the pipes than the ones whose wrinkle occurred close to the end of the pipes. Furthermore, better simulation occurred on the compression-side strains than on the tension-side strains.

6. The Pearson product-moment correlation coefficient is a reliable index for evaluating the similarity of the strain distribution patterns for the pipe buckling, but is probably too sensitive to bias data to be a promising index for monitoring buried pipelines in the field.

7. Monitoring the development of the longitudinal strain distributions on the compression side can reliably detect the onset of pipe wrinkling. The signature index, correlation index of tension-side strain distributions, and the strain ratio index on the compression side can be used as a secondary signature to track pipe wrinkle growth. The behavioural signatures of the pipe wrinkle revealed on these indices usually close to the peak moment or after the limit point.

8. If a distributed strain monitoring system are installed along a line pipe at 8 different positions with a 45° circumferentially interval spacing, at least a 90% correlation with the true maximum strain distribution could be obtained.

9. At the onset of the pipe wrinkling, no apparent ovalization was observed on the buckled pipes, especially for pressurized pipes.

10. Although the D/t ratio, material property, internal pressure, externally loading conditions, and manufacturing process are important parameters to the critical compressive strain of a pipe, only internal pressure and manufacturing process, such as girth weld and cold bend, are found to have significant influences on the strain distribution patterns along a pipe. In addition, the strain distribution shapes and wrinkle shapes were disturbed by the D/t ratio for the girth-welded pipes.

11. The strain distribution pattern at about 40% of the peak moment (or peak load) can be considered as the threshold pattern for the safe condition. The maximum strain over the pipe at this load stage was less than 20% of the critical strain. The strain distribution shape of the safe pattern was relatively flat along the pipe.

12. The strain distribution pattern at 70% of the peak moment was chosen as the threshold pattern of the warning condition. The corresponding

maximum strain at this load stage is less than 40% of the critical strain. The strain distribution shape of the warning pattern included short waves and, probably, a localized strain at the wrinkle location.

13. The strain distribution pattern at 90% of the peak moment was chosen as the threshold pattern for the wrinkling condition. The corresponding maximum strain is between 45% and 65% of the critical strain. The strain distribution shape of the wrinkling pattern was a wave distribution with a dominating strain localized at the wrinkle location.

14. Based on the behavioural signatures of pipe buckling, an integrated damage detection model (DDM) with four ANN protocols was proposed to monitor the health of buried pipe buckling using distributed strain sensory systems. Overall accuracy of the proposed damage detection model approached to 90% for the identification of the pipe conditions.

15. Due to the distinctly different strain distribution patterns, two sets of ANN protocols were used in the DDM to identify the pipe conditions in plain pipes and girth-welded pipes, respectively.

8.3 Recommendations

Recommendations for the Finite Element Models

1. The finite element (FE) models developed herein used an isotropic strain hardening material model. However, significant anisotropic material properties are generally observed in high strength steel pipes. It is postulated that the strain distribution patterns will not be affected by the material anisotropy in this research. The validity of this assumption needs to be further studied.

2. The pipe length used in the FE models was 3.5D or longer in order to prevent a pipe wrinkle from occurring near the end of the pipe. This is reasonable since the strain distributions fed into the DDM were extracted from the processed data in a 1.5D range. However, if the extracted range

becomes larger, say 3D, the length of pipe models should be longer than 3.5D. The effect of pipe length used in the FE models needs to be further investigated.

Recommendations for the Damage Detection Model

3. Normalization is normally used for the proposed warning system, but the trade-off of the normalization probably results in false warning for pipes under the safe condition. The effect of the normalization was mitigated by applying the logic discriminant "IF…Then" in the current damage detection model. However, a data processing technique should be studied to solve the shortcoming of the normalization.

4. Because of the lack of field data, most of the training and testing data used in the ANN were obtained from the simulations of the FE models. In general, ANN makes much better predictions for interpolated data than for extrapolated data. Hence, a broader range of strain distribution patterns and more experimental and field data are needed to enhance the accuracy and capability of the proposed DDM.

5. Even though the inputs of the ANN use a total of only 17 measurements evenly over a 1.5-m interval, these measurements were enough to identify the behavioural signature of the strain distribution patterns. However, some of the 17 input parameters had shown no apparent contribution to the ANN model (see Figure 7.14), especially for the strains between the spike shape and the inflection points of the strain distribution curve, because of the effect of normalization (see Figures 7.7). These trivial strains could be removed from the input neurons. However, the effect of these trivial strains on the capacity of the ANN prediction should be further investigated.

6. Use of the logic discriminating thresholds to filter the outputs of the ANN protocols can improve the accuracy of the damage detection model in the identification of the pipe conditions. It is recommended that other methods

269

to determine the logic discriminating thresholds should be further investigated, such as Fuzzy logic method.

7.   Additional field or experimental data are needed for the longitudinal strain distributions at the different positions in the circumferential direction of a pipe. The data will be extremely valuable for using the proposed damage detection model to track the wrinkle growth by monitoring distributed strain patterns at different positions.

8.   Because ANN recognises strain distribution patterns based on the distinction among the patterns, but not a specific magnitude of loads or strains, the ANN cannot report the exact loading stage or strain ratio. Therefore, the capability of the damage detection model will be influenced by the uncertainties of the BSFOS strain measurements, the criteria to determine threshold patterns, and the procedure to find the optimal ANN protocols. These uncertainties need to be further clarified and taken into account in the overall damage detection model.

Recommendations for Instrumentation

9.   It is recommended that a distributed sensory system installs along the line pipe at 8 different positions with a 45° circumferentially interval spacing (see Figure 4.46). In addition, to allow the system to reliably detect onset of the pipe wrinkling, the strain sensors should be spaced in less than 0.16 diameters (0.16D).

10. Monitoring strain distributions on the multiple positions not only makes tracking wrinkle growth possible, but also provides alternatives when the critical strain measurement is unavailable. Although the algorism of the multiple-route strain monitoring has been proposed in this research, further improvement and refinement are needed.

11. For the digital camera application in the line-pipe experiments, it is recommended that the distributed strains should be extracted in 20 mm spacing from the camera system to reduce the noise effect. In addition, the

digital camera system can replace conventional demec measurement in future line-pipe experiments.

12. The digital camera, used in this project, is calibrated at 1% strain range, but strains measured in the post-buckling stage are sometimes much larger than 1%. In addition, the digital camera was not used to monitor the diamond mode buckling in this project. This deformation of diamond mode buckling probably forms a shadow that may decrease the precision of the digital camera measurements. Therefore, the digital camera should be calibrated in a larger strain range and the diamond mode buckling.

REFERENCES

Adeli, H., 2001. "Neural Networks in Civil Engineering: 1989–2000", Computer-Aided Civil and Infrastructure Engineering, vol. 16, No. 2, pp. 126–142.

Amali, R., Noroozi, S., Vinney, J., Sewell, P, and Andrews S., 2006. "Predicting Interfacial Loads Between the Prosthetic Socket and the Residual Limb for Below-Knee Amputees – A Case Study", Strain, vol. 42, pp. 3-10.

Asuero, A.G., Sayago, A. and Gonz´alez, A.G., 2006. "The Correlation Coefficient: An Overview", Critical Reviews in Analytical Chemistry, Taylor and Francis Group, LLC, vol. 36, pp. 41-48

Bao, X., Webb D.J., and Jackson D.A., 1993. "32-km Distributed Temperature Sensor based on Brillouin Loss in an Optical Fiber", Optics Letters, vol. 18, pp. 1561-1563.

Bastianini, F.,Cargneluttib, M., Tommasoa, A. D., and Toffaninc M., 2003. "Distributed Brillouin Fiber Optic Strain Monitoring Applications in Advanced Composite Materials", Proceedings of SPIE, vol. 5057, pp. 478-485.

Beale, R. and Jackson, T., 1990. "Neural Computing: An Introduction", CRC Press.

Bezerra, E.M., Ancelotti, A.C., Pardini, L.C., Rocco, J.A.F.F., Iha, K., Ribeiro, C.H.C., 2007. "Artificial Neural Networks Applied to Epoxy Composites Reinforced with Carbon and E-glass Fibers: Analysis of the Shear Mechanical Properties", Material Science and Engineering: A, vol. 464, pp. 177-185.

Bouwkamp, J. G. and Stephen, R. M., 1973. "Large Diameter Pipe under Combined Loading", Journal of Transportation Engineering, ASCE, vol. 99, pp. 521-536

Card, L., 2004. "Unsupervised Neural Computation for Event Identification in Structural Health Monitoring", Master Thesis, University of Manitoba, Winnipeg, Manitoba.

Chae, M. J., and Abraham, D. M. 2001. "Neuro-Fuzzy Approaches for Sanitary Sewer Pipeline Condition Assessment", Journal of Computer in Civil Engineering, January, pp. 4-14

Cheng, J.J.R., 2004. "Potential and Challenges of Using SHM in the Canadian Energy Industry", Proceedings of Structural Health Monitoring Workshop, pp. 47-60.

Codd, E.F., 1970. "A Relational Model of Data for Large Shared Data Banks", Communications ACM, vol. 13, No. 6, pp.377- 387

Covas, D., Ramos, H., and Betâmio de Almeida, A., 2005. "Standing Wave Difference Method for Leak Detection in Pipeline Systems", Journal of Hydraulic Engineering, ASCE, December, pp. 1106-1116.

Cohen, J., Cohen P., West, S.G., and Aiken, L.S., 2003. "Applied Multiple Regression/Correlation Analysis for the Behavioral Sciences", 3rd Edition, Lawrence Erlbaum Associates, Hillsdale, New Jersey.

Czyz, J.A. and Wainselboin, S.E., 2003. "Monitoring Pipeline Movement and Its Effect on Pipe Integrity Using Inertial/Caliper In-Line Inspection", Proceedings of Rio Pipeline Conference, IBP575_03.

Czyz , J.A. and Adams, J.R., 1994. "Computation of Pipeline-Bending Strains Based on Geopig Measurements", Pipeline Pigging and Integrity Monitoring Conference, Houston, Texas, February.

Das, S., Cheng, J.J.R. and Murray, D.W., 2002. "Fracture in Wrinkled Pipeline under Monotonic Loading", Proceedings of the 4th International pipeline conference, Calgary, Alberta, IPC 2002-27097.

Datta, T.K., 1999. "Seismic Response of Buried Pipelines: a State-of-the-Art Review", Nuclear Engineering and Design, vol. 192, pp. 271–284.

Dorey, A.B., 2001. "Critical Buckling Strains on Energy Pipeline", Ph.D. dissertation, Department of Civil and Eenvironmental Engineering, University of Alberta, Edmonton, Alberta.

He, M., 2007. "Study of the Excavation Effects on Buried Pipelines", M.Sc. dissertation, Department of Civil and Eenvironmental Engineering, University of Alberta, Edmonton, Alberta.

Hegazy, T., Tully, S., and Marzouk, H., 1998. "A Neural Network Approach for Predicting the Structural Behavior of Concrete Slabs", Journal of Civil Engineering, vol. 25, pp. 668-677.

Hibbit, Karlsson, Sorensen Inc., 2002 and 2003. "ABAQUS/Standard ABAQUS Theory Manual", Hibbit, Karlsson, Sorensen Inc., Pawtucket, Rhode Island.

Horiguchi, T., Kurashima, T., and Tateda, M., 1989. "Tensile Strain Dependence of Brillouin Frequency Shift in Silica Optical Fibers", IEEE Photonics Technology Letters, vol. 1, pp. 107-108.

Housner, G.W., Bergman, L.A., Caughey, T.K., Chassiakos, A.G., Claus, R.O., Masri, S.F., Skelton, R.E., Soong, T.T, Spencer, B.F., and Yao, J.T.P., 1997. "Structural Control: Past, Present, and Future", Journal of Engineering Mechanics, ASCE, September, pp. 897-971.

Inaudi, D., and Clisic, B., 2006. "Long-range Pipeline Monitoring by Distributed Fiber Optic Sensing", Proceedings of the 6th International pipeline conference, Calgary, Alberta, IPC2006-10287.

Ishikawa, N., Endo, S., and Kondo, J., 2006. "High Performance UOE Linepipes", JFE Technical Report, January, No. 7.

ISIS., 2001. "Design Manual No. 1 and No. 2", ISIS Canada.

Kesavan, A., John, S. and Herszberg, I., 2008. "Structural Health Monitoring of Composite Structures using Artificial Intelligence Protocols", Journal of Intelligent Material Systems and Structures, vol. 19, pp. 63-72.

Kesavan, A., John, S. and Deivasigamani, M., 2006. "Structural Health Monitoring of Composite T-joints for Assessing the Integrity of Damage Zones", Proceedings of SPIE, vol. 6167, pp. 1-12.

Kurashima, T., Horiguchi, T., and Tateda, M., 1990. "Thermal Effects on Brillouin Frequency Shift in Jacketed Optical Silica Fibers", IEEE Photonics Applied Optics, vol. 29, pp. 2219-2222.

Lara, P.F., 1987, "Revisiting the Failure Criteria of Buried Pipelines", Petroleum Division, ASME, vol. 6, pp. 143-154.

Lee, B., 2003. "Review of the Present Status of Optical Fiber Sensors", Optical Fiber Technology, vol. 9, pp. 57–79.

Legendre, S., Massicotte, D., Goyette, J., and Bose, T. K., 2000. "Wavelet-Transform-Based Method of Analysis for Lamb-Wave Ultrasonic NDE Signals", IEEE Transactions on Instrumentation and Measurement, vol. 49, pp. 860-865.

Lewicki, M.S., 1998. "A Review of Methods for Spike Sorting: the Detection and Classification of Neural Action Potentials", Network: Computation in Neural Systems, vol. 9, pp. R53-R78.

Ling, H.I., Mohri, Y., Kawabata, T., Liu, H., Burke, C., and Sun, L., 2003. "Centrifugal Modeling of Seismic Behavior of Large-Diameter Pipe in Liquefiable Soil", Journal of Geotechnical and Geoenvironmental Engineering, ASCE, December, pp. 1092-1101.

Los Alamos National Laboratory, 2003. "A Review of Structural Health Monitoring Literature: 1996-2001", Los Alamos National Laboratory Report, LA-13976-MS, Los Alamos National Laboratory, California.

Lukasiewicz, S.A., Czyz, J.A., Sun, C., and Adeeb, S., 2006. "Calculation of Strains in Dents Based on High Resolution In-Line Caliper Survey", Proceedings of the 6th International Pipeline Conference, Calgary, Alberta, IPC2006-10101.

McCulloch, W. S., Pitts, W., 1943. "A Logical Calculus of Ideas Immanent in Nervous Activity", Bulletin of Mathematical Biophysics, vol. 5, pp.115-133.

Minsky, M. L. and Papert, S. A, 1969. "Perceptrons", MIT Press, Cambridge.

Mohareb, M., Alexander, S. D. B., Kulak, G. L. and Murray, D. W., 1993. "Laboratory Testing of Line Pipe to Determine Deformational Behavior", Proceedings of 12th International Conference on OMAE, ASME, vol. V-Pipeline Technology, pp. 109-114.

Mohareb, M.E., 1995. "Deformational Behaviour of Line Pipe", Ph.D. dissertation, Department of Civil and Environmental Engineering, University of Alberta, Edmonton, Alberta.

Mehrotra, K., Mohan, C.K., Ranka, S., 2000. "Elements of Artificial Neural Networks", MIT Press, Cambridge, Mass. pp. 4-7, 70-78, and 86-88.

Montgomery, D. C., Runger, G. C., and Hubele, N. F., 2006. "Engineering Statistics", 4th Edition, John Wiley and Sons, Inc, pp. 42-47.

Moser, A. P., 2001. "Buried Pipe Design: External Loads", 2nd Edition, McGraw-Hill professional Engineering, Chapter 2, pp. 9-58.

Mufti, A., Tennyson, R.C., and Cheng, J.J.R., 2003. "Integrated Sensing of Civil and Innovative FRP Structures", Progress in Structural Engineering and Materials, John Wiley and Sons, Inc.

Murray, D. W., 1997. "Local Buckling, Strain Localization, Wrinkling and Postbuckling, Response of Line Pipe", Engineering Structures, vol. 19, pp. 361-371.

Naoki, F., Hiroshi, Y., Shinobu, K., Takahito, W., and Tomoki, M., 2003. "Experimental and Analytical Study of Cold Bending Process for Pipelines", Journal of Offshore Mechanics and Arctic Engineering, ASME, vol. 125, pp. 153-157.

National Instruments., 2003. "IMAQ Vision Concepts Manual: Pattern Matching", National Instruments Corporation, Texas, Part Number 322916B-01, Chapter 12.

National Instruments., 2002. "Signal Processing Toolset User Manual: the Fundamentals of Wavelet Analysis", Texas, Chapter 9.

Nobahar, A., Kenny, S., and Phillips, R., 2007. "Buried Pipelines Subject to Subgouge Deformations", International Journal of Geomechanics, ASCE, May/June, pp. 206-216.

O'Rourke, M. and Liu, X., 1999. "Response of Buried Pipelines Subject to Earthquake Effects", MCEER, Buffalo NY.

O'Rourke, M. and Ayala G., 1993. "Pipeline Damage due to Wave Propagation", Journal of Geotechnical Engineering, vol. 119, September, pp. 1490-1498.

Palmer, A.C. and Williams, P.J., 2003. "Frost Heave and Pipeline Upheaval Buckling", Canadian Geotechnical Journal, vol. 40, pp. 1033–1038.

Pau, L.F. 1981. "Failure Diagnosis and Performance Monitoring". Marcel Dekker Inc., New York, N.Y.

Pichler, B., Hellmich, C., Mang, H.A., and Eberhardsteiner, J., 2006. "Loading of a Gravel-Buried Steel Pipe Subjected to Rockfall", Journal of Geotechnical and Geoenvironmental Engineering, November, pp. 1465-1473.

Pretorius, J.v.R., Shoor, M.C.V., Muller, G. J., and Jessiman, A.W., 2005. "Piezoelectric Structural Acoustic Leak Detection for Pressurized Ppipelines", Smart Structures and Materials, Industrial and Commercial Applications of Smart Structures Technologies, Proceedings of SPIE, vol. 5762, pp. 212-223.

Ravet, F., Zou, L., Bao, X., and Chen, L., 2004. "Demonstration of the Detection of Buckling Effects in Steel Pipelines and Beams by the Distributed Brillouin Sensor", Proceedings of SPIE, vol. 5579, pp. 58-65.

Ravet, F., Zou, L., Bao, X., Chen, L., Huang R.F., and Khoo, H.A., 2006. "Detection of Buckling in Steel Pipelines and Column by the Distributed Brillouin Sensor", Journal of Optical Fiber Technology, vol.12, pp. 305-311.

Reed, C., Alastair, J., and Smart, D., 2004. "Techniques for Monitoring Structural Behavior of Pipeline Systems", AWWA Research Foundation.

Rosenblant, F., 1958. "The Perceptron, a Probabilistic Model for Information Storage and Organization in the Brain", Psychics Review, vol. 62, pp. 386-408.

Rummelhart, D. E., Hinton, G. E., McClelland, J. L., 1986. "A General Framework for Parallel Distributed Processing", Parallel Distributed Processing: Explorations in the Macrostructure of Cognition, 1.

Rumelhart, D.E., 1987. "Parallel Distributed Processing - Vol. I", MIT Press, Cambridge, Mass, pp. 31-40.

Sadek S., Iskander, M.G., and Liu, J., 2003. "Accuracy of Digital Image Correlation for Measuring Deformations in Transparent Media", Journal of Computing in Civil Engineering, ASCE, vol. 17, pp.88-96.

Sen, M., 2006. "Behaviour of Cold Bend Pipes under Combined Loads", Ph.D. dissertation, Department of Civil and Eenvironmental Engineering, University of Alberta, Edmonton, Alberta.

Shinozuka, M., Ballantyne, D., Borcherdt, R., Buckle, I., O'Rourke, T., and Schiff, A., 1995. ''The Hanshin–Awaji Earthquake of January 17, 1995. Performance of lifelines'', Technical Report, NCEER, Buffalo, N.Y.

Song, B., 2007. "Effectiveness of the Stress Relief Procedures and Their Effects on Local Buckling Behaviour of Buried Pipes", Ph.D. dissertation, Department of Civil and Environmental Engineering, University of Alberta, Edmonton, Alberta.

Sola, J. and Sevilla, J., 1997. "Important of Input Data Normalization for the Application of Neural Networks to Complex Industrial Problems", IEEE Transactions on Nuclear Science, vol. 44, June, pp. 1464-1468.

Spainhour, L. K. and Rasdorf, W.J., 1996. "Entity-Relationship Modeling of Composite Materials Data", Journal of Computing in Civil Engineering, July pp.226-235

Stephens, M.J. and Kulak, G.L., 1982. "Local Buckling of Thin-Walled Tubular Steel Members", Structural engineering report No. 103, Department of Civil and Environmental Engineering, University of Alberta, Edmonton, Alberta.

Sutherland, J. and Paz, H., 2000. "Advances in In-Line Inspection Technology for Pipeline Integrity", Processings of Annual International Pipeline Congress. Morelia, Mexico.

Suzuki, N., Kondo, J., Endo, S., Ishikawa, N., Okatsu, M., and Shimamura, J., 2006. "Effects of Geometric Imperfection on Bending Capacity of X80 Linepipe", Proceedings of the 6th International Pipeline Conference, ASME, Calgary, Alberta, IPC06-10070.

Teh, C.I., Wong, K.S., Goh, T.C., and Jaritngam, S., 1997. "Prediction of Pile Capacity Using Neural Networks", Journal of Computing in Civil Engineering, April, pp. 129-138.

Teng, J.G, Roger, J.M. 2004. "Buckling of Thin Metal Shell". Spong Press, Taylor & Francis Group. pp. 42-87, and pp. 286-343.

Tennyson, R.C, Banthia, N., Rivera, E., Huffman, S., and Sturrock, I., 2007. "Monitoring Structures Using Long Gauge Length Fibre Optic Sensors", Canadian Journal of Civil Engineering, vol. 34, pp. 422-429.

Tutuncu, I. and O'Rourke, T.D., 2006. "Compression Behavior of Nonslender Cylindrical Steel Members with Small and Large-Scale Geometric Imperfections", Journal of Structural Engineering, ASCE, August, pp. 1234-1241.

Udd, E., 1991. "Fiber Optic Sensors: An Introduction for Engineers and Scientists", John Wiley and Sons, Inc.

Udd, E., 2007. "Review of Multi-parameter Fiber Grating Sensors", Fiber Optic Sensors and Applications V, Proceedings of SPIE, vol. 6770, pp. 02.

Widrow, B. and Hoff, M., 1960. "Adaptive Switching Circuits", Western Electronic Show and Convention, Convention record, Institute of Radio Engineers (now IEEE). vol. 4, pp. 96-104.

Worden, K., Pierce, S.G., Manson, G., Philp, W.R., Staszewski, W.J., and Culshaw, B., 2000. "Detection of Defects in Composite Plates Using Lamb Waves and Novelty Detection" , International Journal of Systems Science, vol. 31, pp. 1397–1409.

Xu, H.Z., Zhang, D., 2006. "Wavlet-based Data Processing for Distributed Fiber Optic Sensors", Proceedings of the 5th International Conference on Machine Learning and Cybernetics, Dalian, p.p.13-16.

Yoosef-Ghodsi, N., Cheng, J.J.R., Murray D., Doblanko R., and Wilkie, S., 2000. "Analytical Simulation and Field Measurements for A Wrinkle on The Norman Wells Pipeline", Proceedings of the 2000 International pipeline Conference, Calgary, Alberta, pp. 931-938.

Yoosef-Ghodsi, N., 1994. "Behavior of Girth-welded Line Pipe", Structural engineering report No. 203, Department of Civil and Environmental Engineering, University of Alberta, Edmonton, Alberta.

Yu, L., Wang, S., and Lai, K.K., 2006. "An Integrated Data Preparation Scheme for Neural Network Data Analysis", IEEE Transactions on Knowledge and Data Engineering, vol. 18, pp. 217-230.

Zhou, Z. and Murray, D.W., 1993. " Numerical Structural Analysis of Buried Pipelines", Structural Engineering Report No. 181, Department of Civil Engineering, University of Alberta, Edmonton, Alberta.

Zimmerman, T., Timms, C., Xie, J., and Asante, J., 2004. "Buckling Resistance of Large Diameter Spiral Welded Linepipe", Proceedings of the 4th International Pipeline Conference, ASME, Calgary, Alberta, IPC04-0364.

Zou, L., Ferrier, G.A., Shahraam, A.V., Yu Q., Chen, L., and Bao, X., 2004. "Distributed Brillouin Scattering Sensor for Discrimination of Wall-thinning Defects in Steel Pipe under Internal Pressure", Applied Optics, vol. 43, pp. 1583-1588.

Appendix A

A HSS Column Test Using Digital Camera System

A digital camera system would be used to measure the pipe deformation profile as well as distributed strains during pipe buckling in the high-strength pipe buckling experiment. Because this camera system was the first time to be used in pipe experiments at the U of A, before the full-scale pipe experiment, a test of a hollow structural section (HSS) column under an eccentric compressive load was processed by using 1000 kN Material Test System (MTS) at the U of A. This test's purpose was to understand the feasibility of applying the digital camera system to pipe buckling experiments. The test's set-up and gauge layout are shown in Figures A.1 and A.2. Strain gauges and demec gauges were used in this test to validate the camera system. Due to the limit of the clamps of the MTS, test stopped as the global curvature was up to 0.005 rad/m and the maximum compression-side strain was 0.85%. When the test completed, the camera system had taken images at 15 loading stages. To acquire reasonable strains on the HSS column from the camera system, the following three methods were used to compute the strains measured by the camera system, and these strains were respectively compared with the strains obtained from strain gauges and demec gauges.

- Camera strains: strains were measured beside the strain gauge locations and calculated directly by software Vic-3D in the digital camera system. The software analyzed strain data in every 0.1 mm interval.

- Camera averaged strains: each strain was an average of the camera strains over the 200 mm interval centered at the middle length of the respective strain gauge.

- Camera demec-strains: the HSS column's relative displacements between two demec points in 200 mm spacing (or 8 in spacing) was measured by the camera system, and then an average strain ε_{dem} was obtained by computing the ratio of the elongation (L_1-L_0) to the original length L_0 between the two demec points, i.e. an initial point and an end point. The relevant formula used to calculate strain ε_{dem} are presented in equations A.1 to A.3:

$$\varepsilon_{dem} = \frac{L_1 - L_0}{L_0} \qquad\qquad (A.1)$$

$$L_1 = \sqrt{[(Z_e + w_e) - (Z_i + w_i)]^2 + [(Y_e + v_e) - (Y_i + v_i)]^2} \quad (A.2)$$

$$L_0 = \sqrt{(Z_e - Z_i)^2 + (Y_e - Y_i)^2} \qquad\qquad (A.3)$$

Where

v_e displacement at the current loading stage at an end point along the Y-axis

v_i displacement at the current loading stage at an initial point along the Y-axis,

w_e displacement at the current loading stage at an end point along the Z-axis.

w_i displacement at the current loading stage at an initial point along the Z-axis.

Y_e position at an end point along the Y-axis (the vertical axis),

Y_i position at an initial point along the Y-axis (the vertical axis)

Z_e position at an end point along the Z-axis (out-of-plane axis),

Z_i position at an initial point along the Z-axis (out-of-plane axis),

The above positions were recorded at the referenced loading, and the displacements were set as zero at this loading stage. The comparisons of strains measured by the different instruments such as strain gauges, demec points, and digital cameras are presented in Figures A.3 and A.4. In the Figures A.3, if the measured results fall onto the discriminant line or the diagonal dummy line, it means that these strains are identical to those measured by the strain gauges. Figure A.3 shows that when strain range was larger than 0.4%, the camera strains and the demec readings were almost identical, and the camera strains were slightly larger than strain gauge readings. The average of the ratios of the camera strains to strain gauge readings was 1.04 along with the standard deviation, 0.004; the average of the ratios of the camera strains to demec readings was 0.98 along with a very low deviation, 0.001. Figure A.4 reveals that the camera demec-

strains were slightly smaller than the strains measured by both the demec points and the strain gauges in the large deformation range. The results from the camera system are reasonable; because the gauge length is larger for the camera demec-strains than the camera strains, the camera strains were more precise.
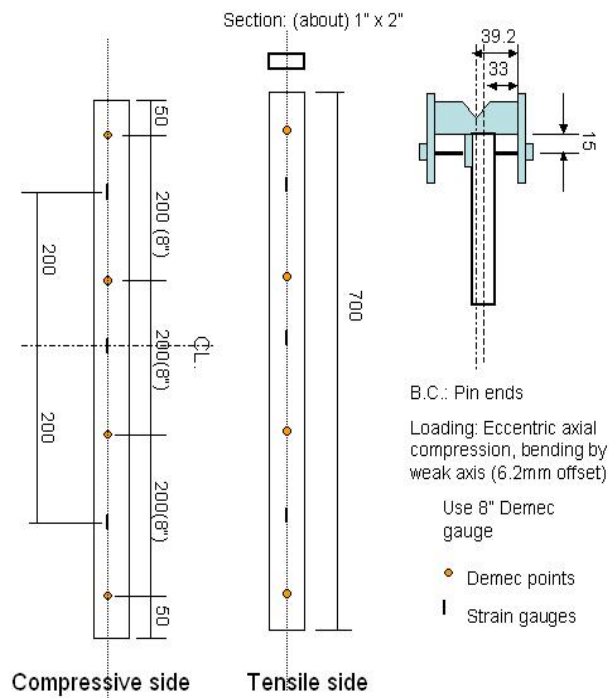
Figure A.1 Set-Up on the Pipe

Unit: mm

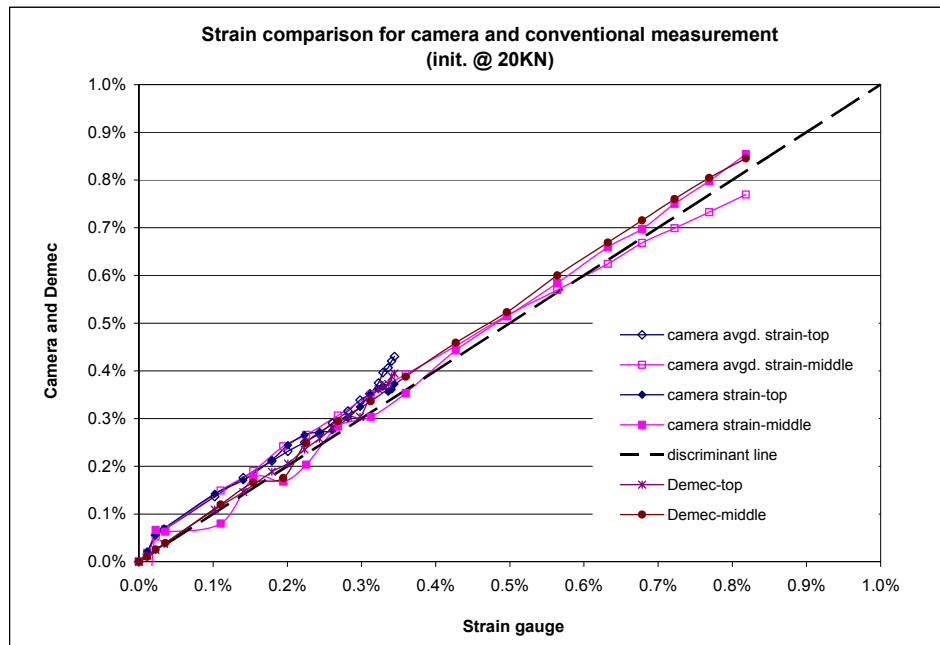Figure A.2 Instruments Layout in HSS Column Buckling Test

284
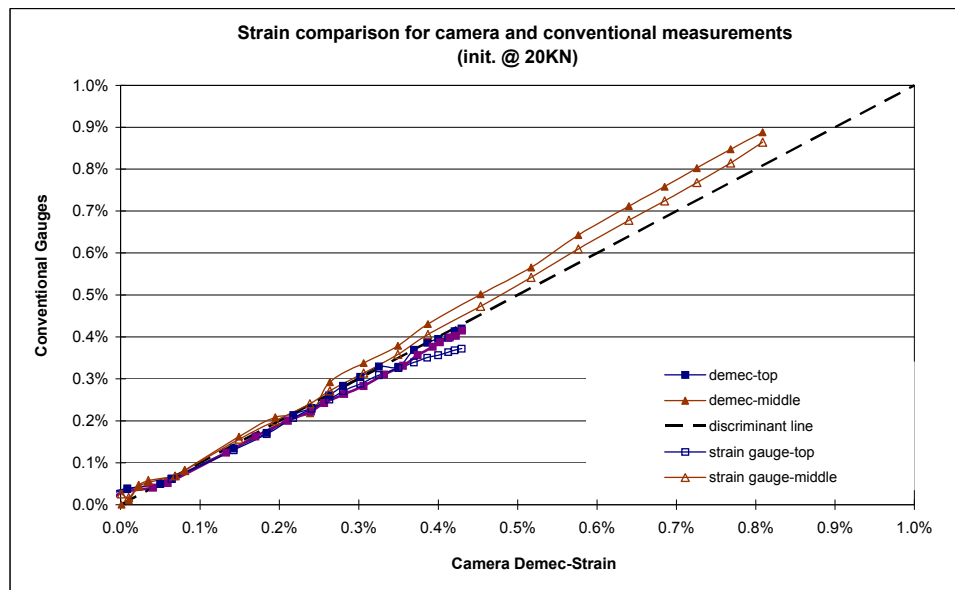
Figure A.3 Strain Comparison for Strain Gauge, Demec Reading and Camera Data

Figure A.4 Strain Comparison for Camera Demec, Strain Gauge, and Demec Reading

285

Appendix B

**The Relation of the Longitudinal Compressive Strains, Pipe Deformations
and Loading Stages**

Deformation of a pipeline under combined loadings is usually concerned by the pipeline industry because extreme deformation on the pipe not only causes pipe damage, but also leads to loss in the pipe's function. The maximum deformation on the pipeline is usually limited in order to allow that in-line inspection tools can pass the pipeline. For the above purpose, Mohareb (1995) proposed a deformation-limit-state criterion by defining longitudinal compressive strain corresponding to 95% of the peak moment in the post-buckling stage. In addition, 8 pipe specimens were investigated and their properties and conditions are show in Table B.1. The deformation profiles of these pipes are shown in Figures B.1 to B.8, and the loading stage and the strain magnitude corresponding to the each deformation profile are also presented in the legends of the figures. As can be seen, when the loading reached 95% of the peak moment in the post-buckling stage, the pipes' wrinkle deformations had been larger than 10 mm (see Figures B.1 to B.8). The 10-mm wrinkle on the pipe's surface could be identified by human eyes, and, thus, the wrinkle occurring after 95% of the peak moment in the post-buckling stage was defined as a visible wrinkle in this research program. The corresponding averaged compressive strain could be 1.5 times of the critical strain.

Table B.1 Specimen Dimensions and Test Conditions

Specimen	Grade (MPa)	Diameter (mm)	D/t	Length (mm)	Internal pressure (%SMYS)	Girth Weld	Loading patterns
Pipe#1	X80h (550)	30	59	2667	0	No	Monotonic bend
Pipe#2	X80h (550)	30	58	2667	0	Yes	Monotonic bend
Pipe#8	X80 (550)	30	57	2667	76	No	Monotonic bend
Pipe#9	X80h (550)	30	57	2667	77	No	Monotonic bend
Pipe#10	X100h (690)	24	39	2667	77	No	Monotonic bend
Pipe#12	X100h (690)	30	58	2667	77	Yes	Monotonic bend
Pipe#14	X100h (690)	30	55	2667	77	No	Monotonic bend
Pipe#15	X100h (690)	36	66	3200	0	No	Monotonic bend
h: new generation steel pipe							
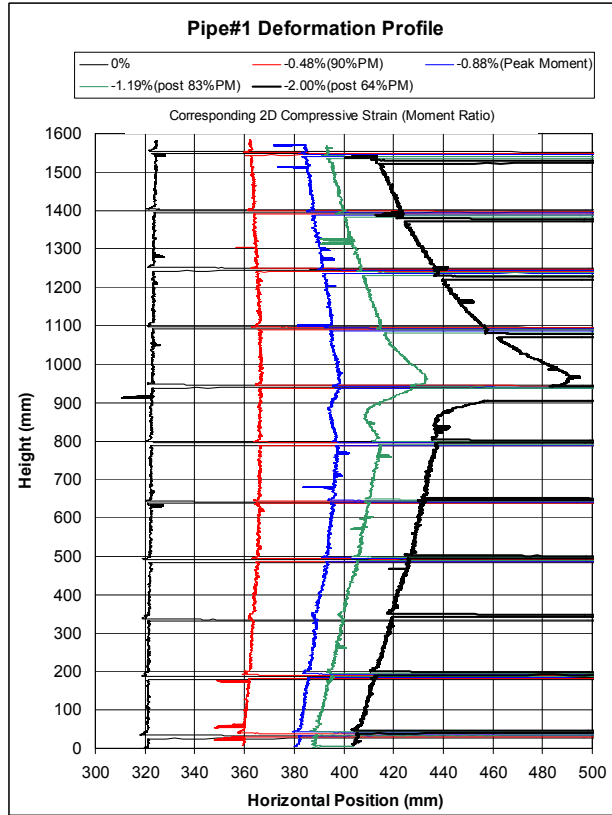
Figure B.1 Deformation Profile for Pipe#1
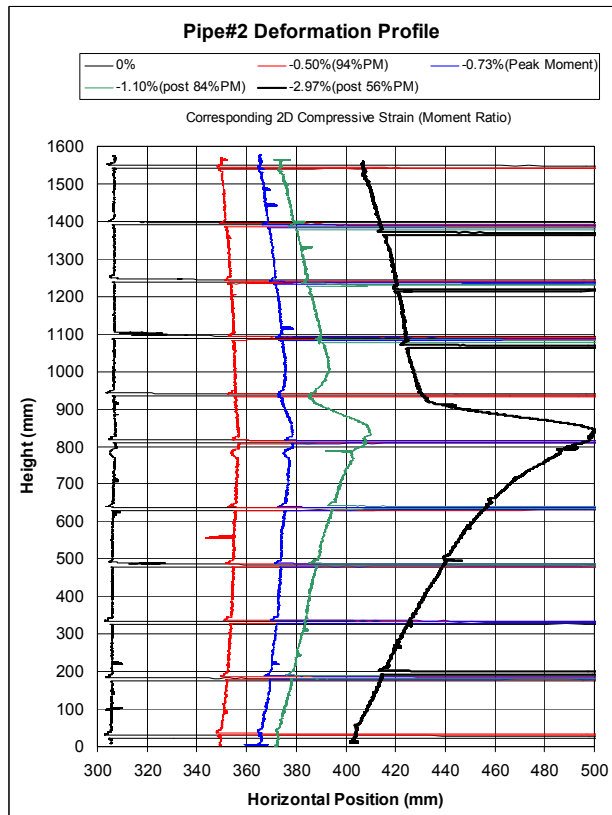
Figure B.2 Deformation Profile for Pipe#2
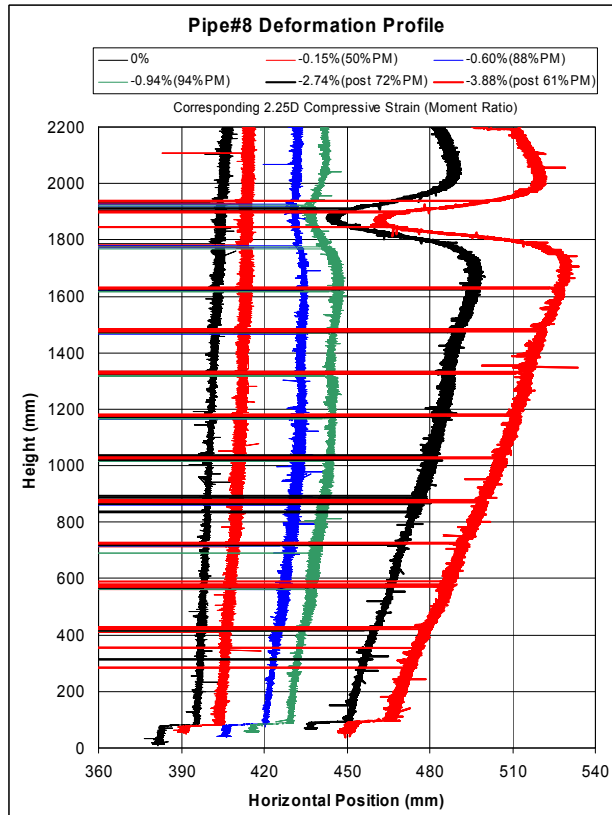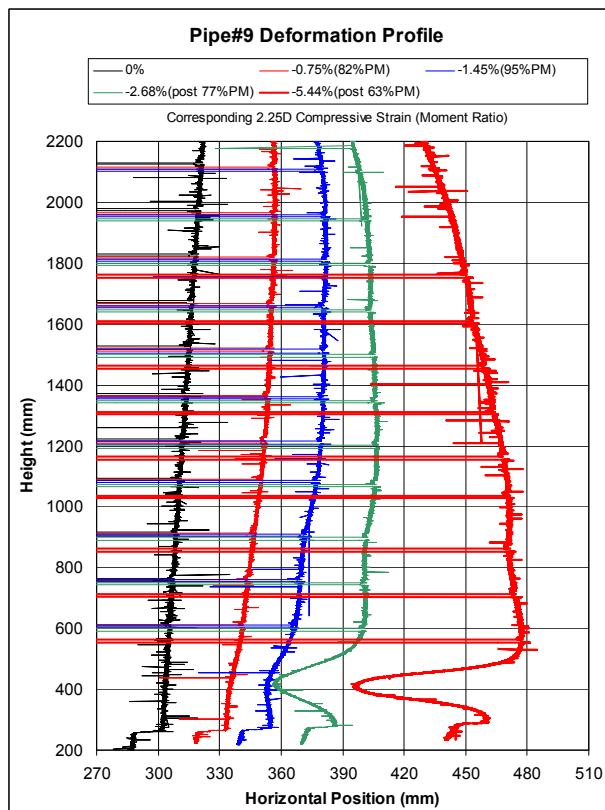
Figure B.3 Deformation Profile for Pipe#8

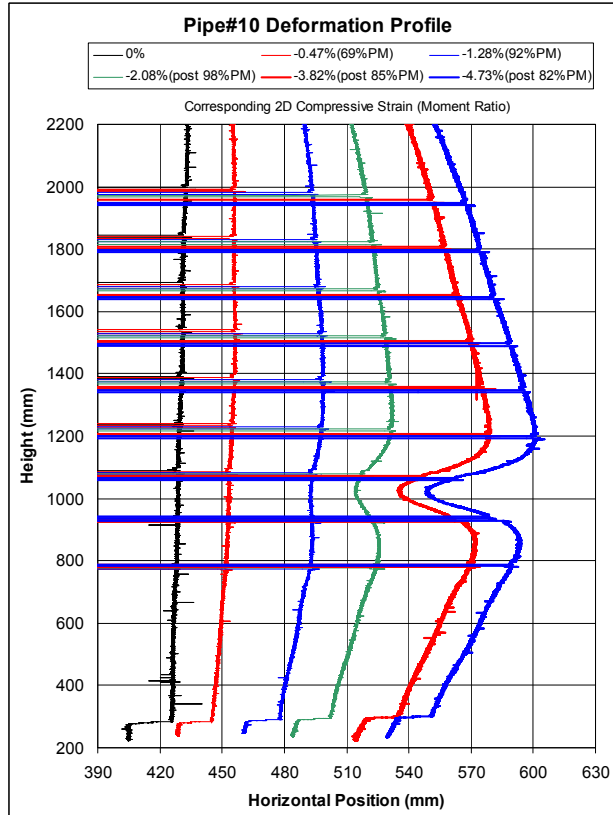Figure B.4 Deformation Profile for Pipe#9
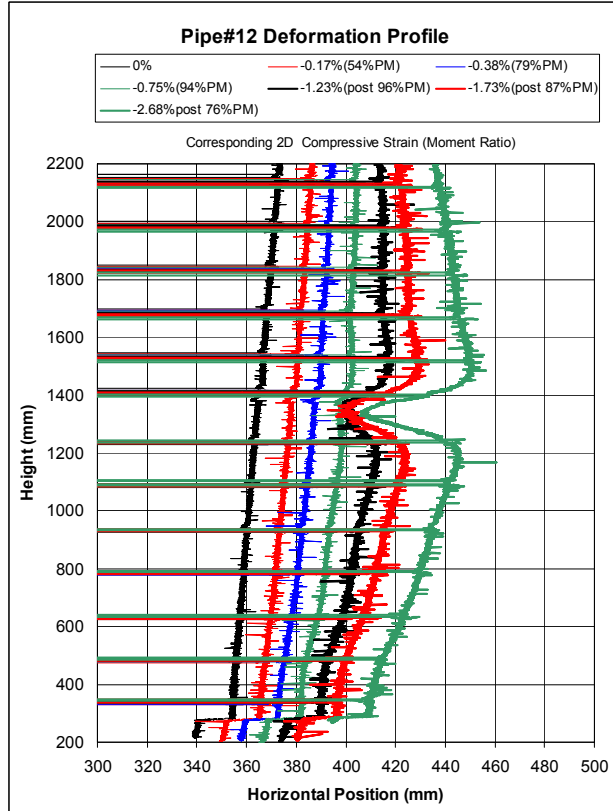
290

Figure B.5 Deformation Profile for Pipe#10

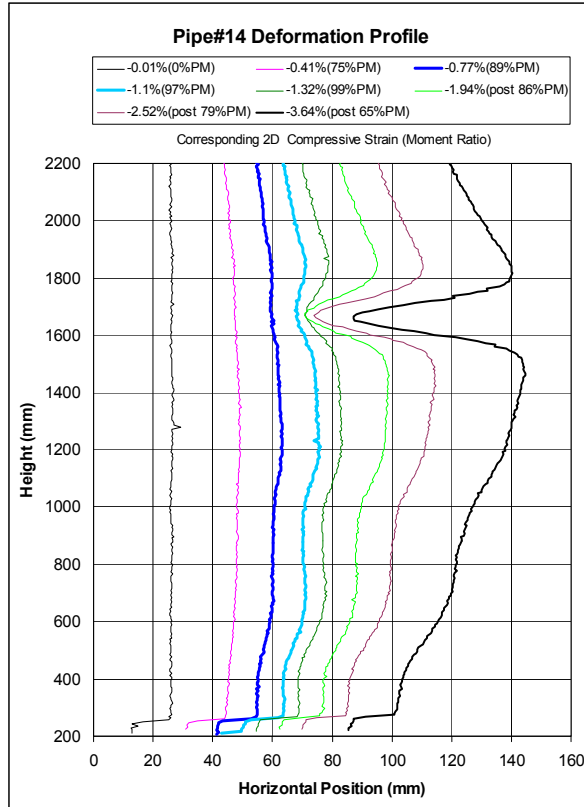Figure B.6 Deformation Profile for Pipe#12
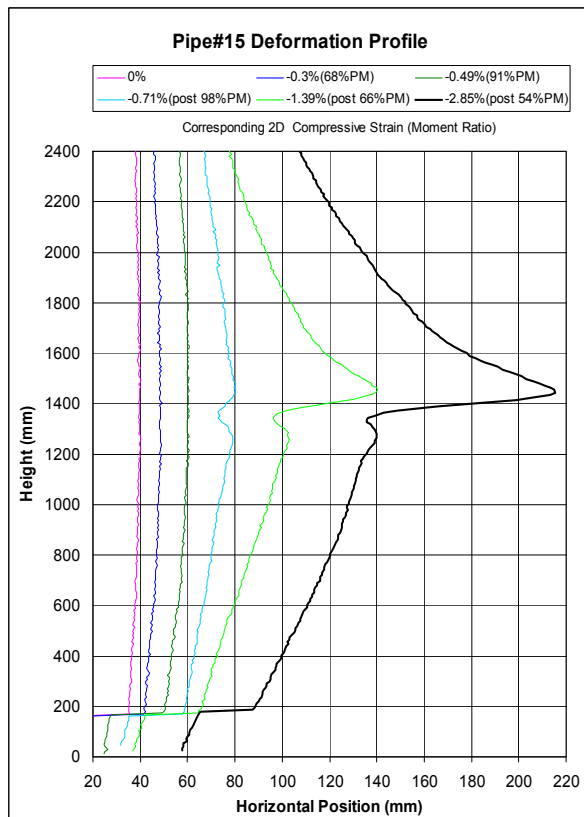
Figure B.7 Deformation Profile for Pipe#14

Figure B.8 Deformation Profile for Pipe#15

Appendix C

Longitudinal Strain Distributions along the Buckling Pipes Simulated by Finite Element Models

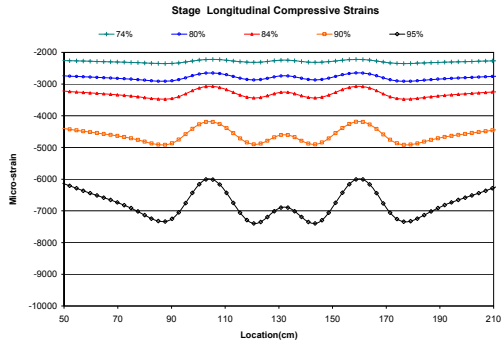# C.1 Strain Distributions along Pipes under a Bend Load
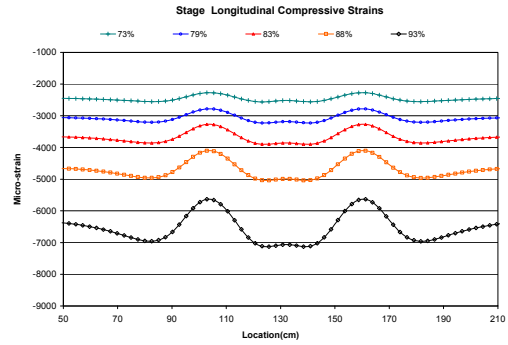

Figure C.1 Strains for Pipe
X65dt40U00

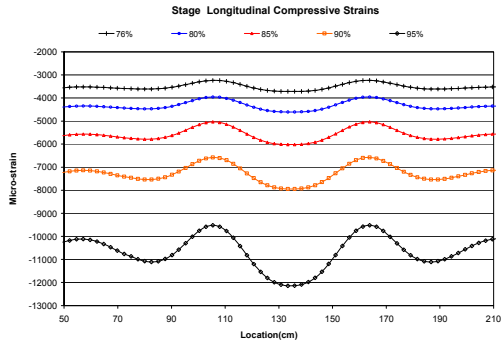Figure C.2 Strains for Pipe
X65dt40U40

Figure C.3 Strains for Pipe
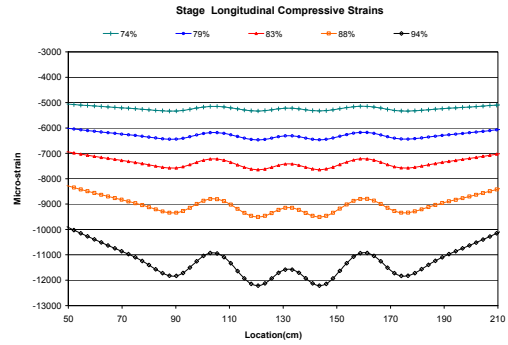X65dt40U80

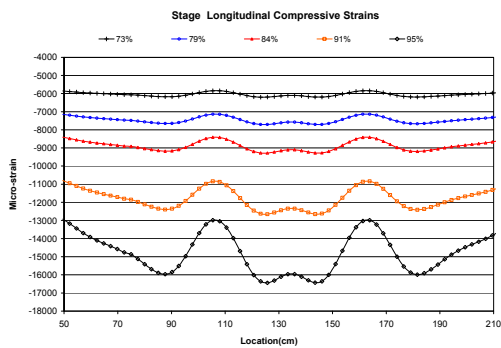Figure C.4 Strains for Pipe
X100hdt40U00

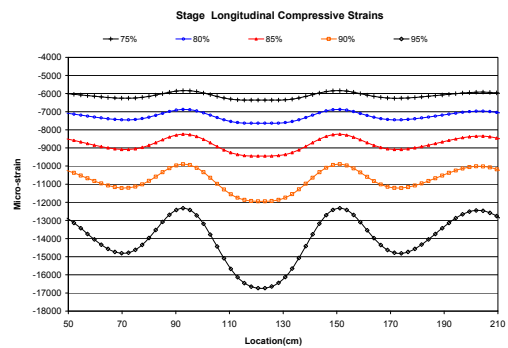Figure C.5 Strains for Pipe
X100hdt40U40

Figure C.6 Strains for Pipe
X100hdt40U80

294

Figure C.7 Strains for Pipe
X65dt60U00

Figure C.8 Strains for Pipe
X65dt60U40

Figure C.9 Strains for Pipe
X65dt60U80

Figure C.10 Strains for Pipe
X80hdt60U00

Figure C.11 Strains for Pipe
X80hdt60U40

Figure C.12 Strains for Pipe
X80hdt60U80

Figure C.13 Strains for Pipe
X65dt80U00
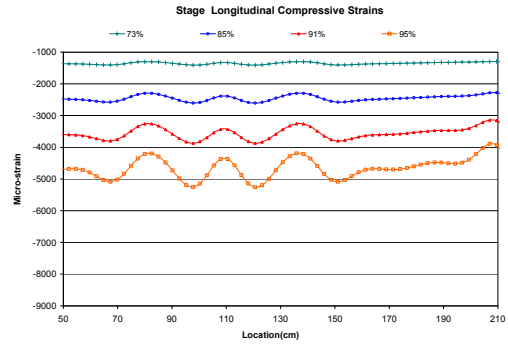
Figure C.14 Strains for Pipe
X65dt80U40
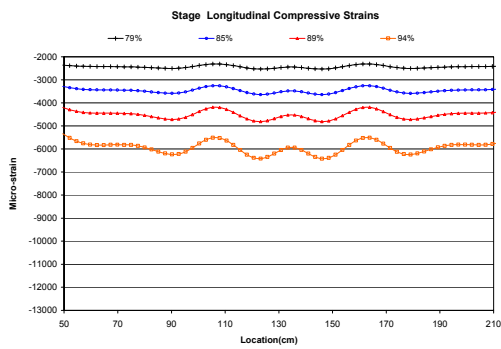
Figure C.15 Strains for Pipe
X65dt80U80
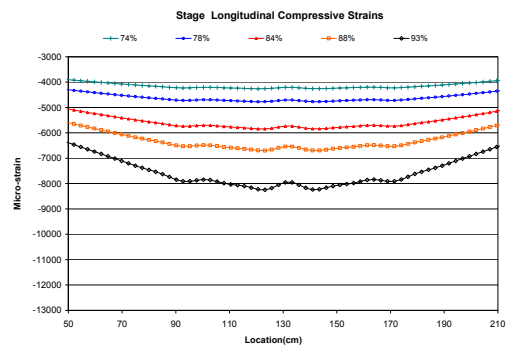
Figure C.16 Strains for Pipe
X100hdt80U00
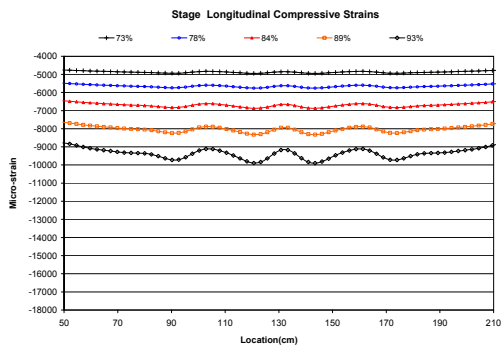
Figure C.17 Strains for Pipe
X100hdt80U40
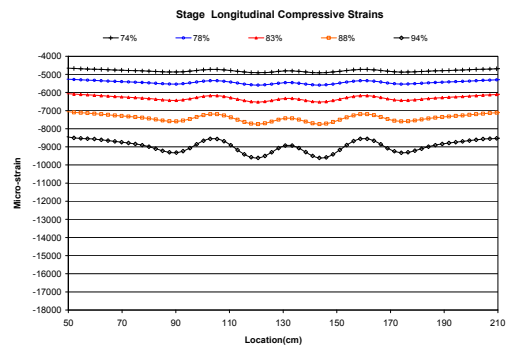
Figure C.18 Strains for Pipe
X100hdt80U80

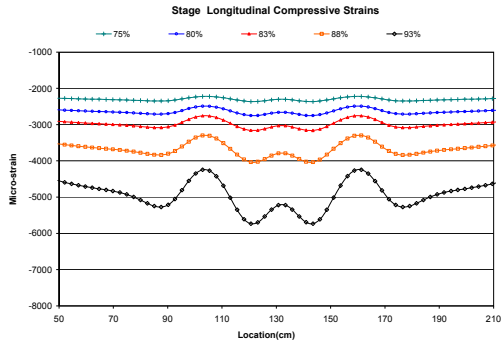# C.2 Strain Distributions along Girth-welded Pipes under a Bend Load
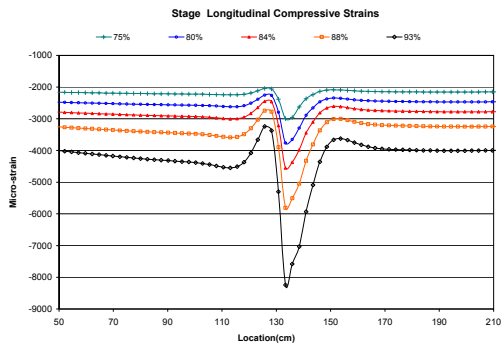
Figure C.19 Strains for Pipe X65dt40U00w
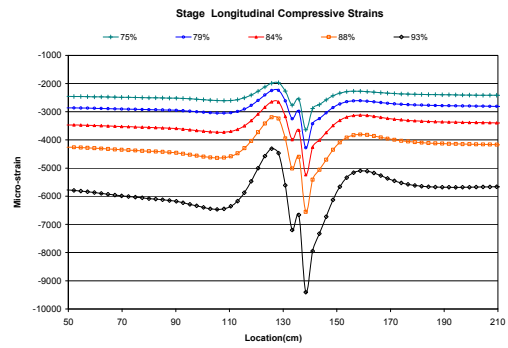
Figure C.20 Strains for Pipe X65dt40U40w
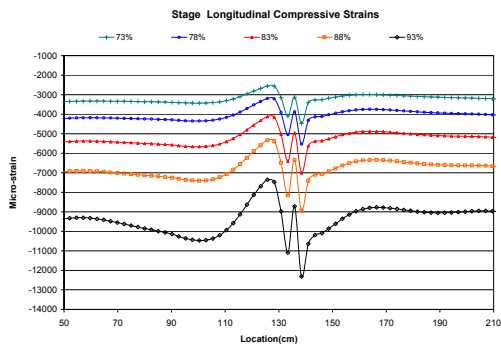
Figure C.21 Strains for Pipe X65dt40U80w
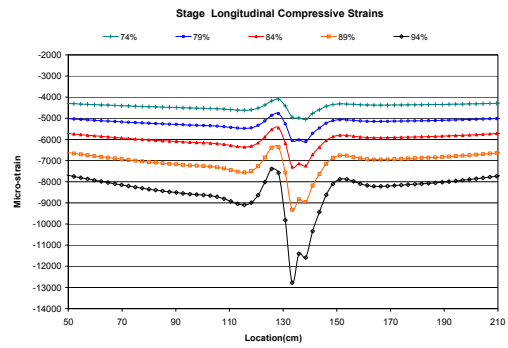
Figure C.22 Strains for Pipe X100hdt40U00w
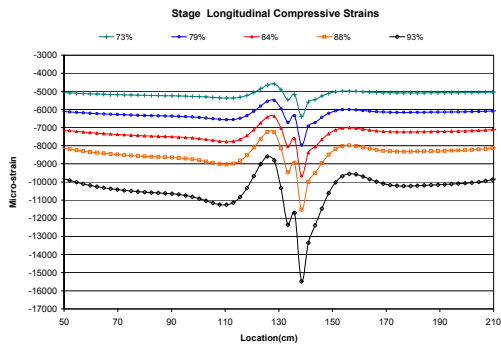
Figure C.23 Strains for Pipe X100hdt40U40w
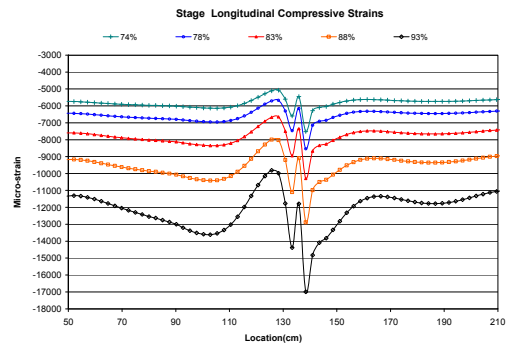
Figure C.24 Strains for Pipe X100hdt40U80w

297
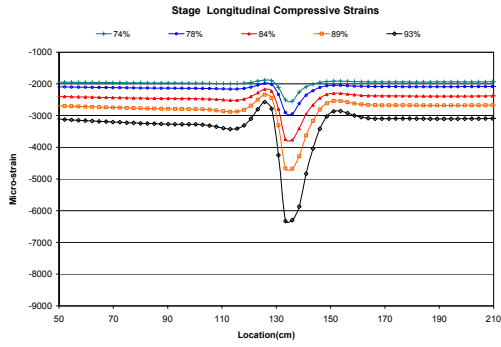
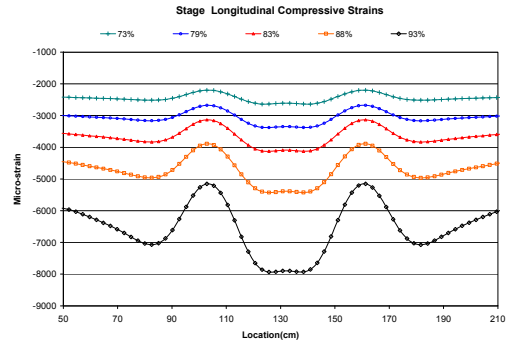Figure C.25 Strains for Pipe
X65dt60U00w
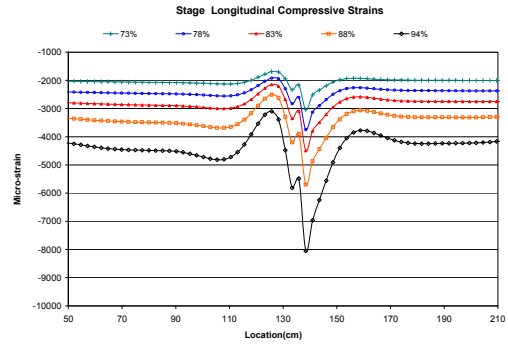
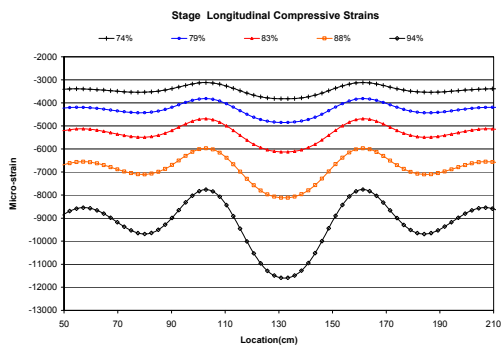Figure C.26 Strains for Pipe
X65dt60U40w
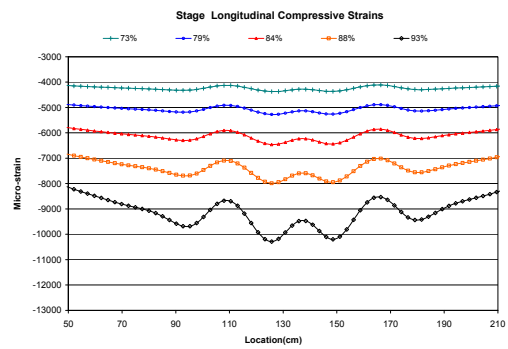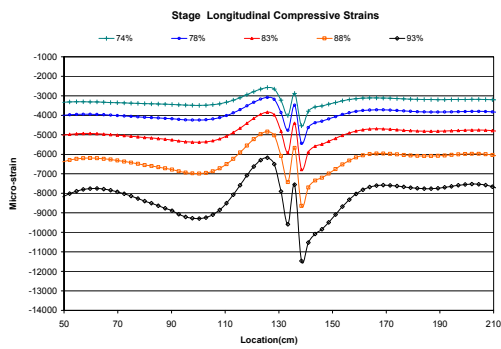

Figure C27. Strains for Pipe
X65dt60U80w
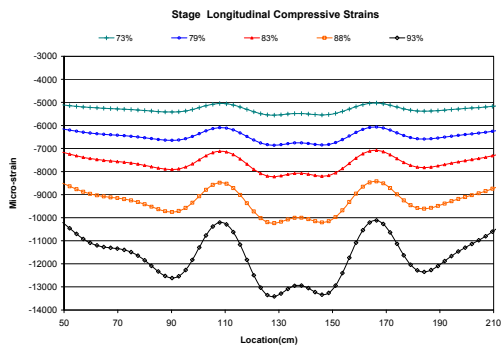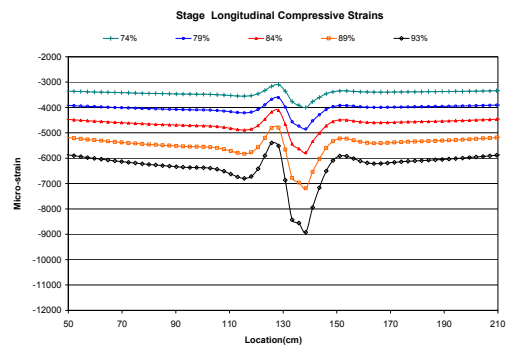

Figure C.28 Strains for Pipe
X80hdt60U00w
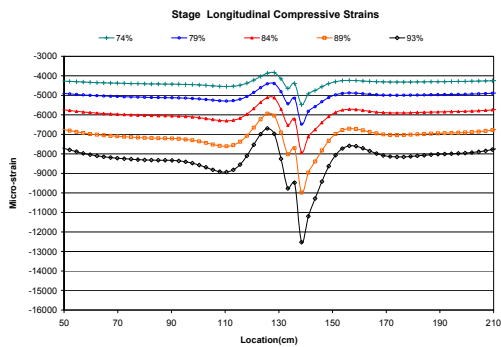
Figure C.29 Strains for Pipe
X80hdt60U40w
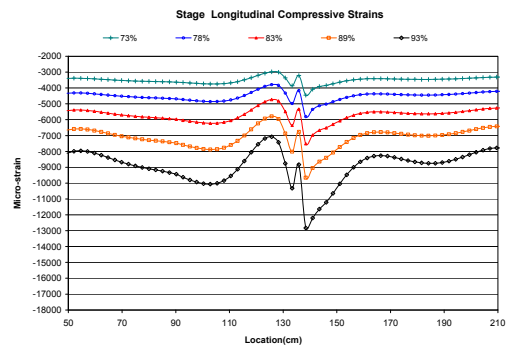
Figure C.30 Strains for Pipe
X80hdt60U80w

298
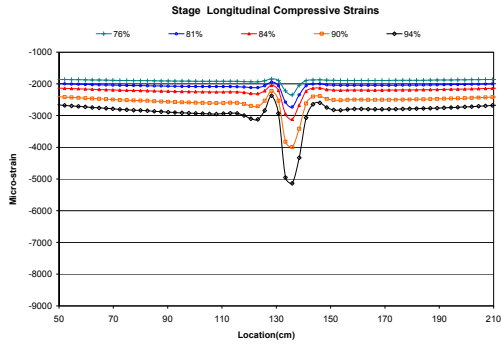
Figure C.31 Strains for Pipe
X65dt80U00w
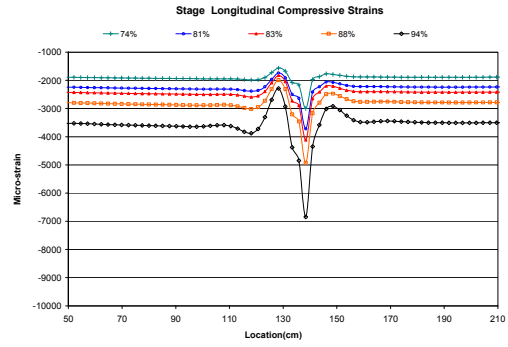
Figure C.32 Strains for Pipe
X65dt80U40w
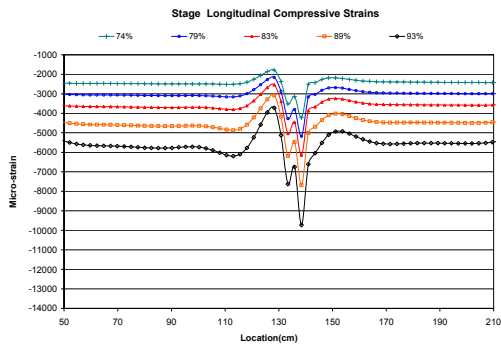
Figure C.33 Strains for Pipe
X65dt80U80w
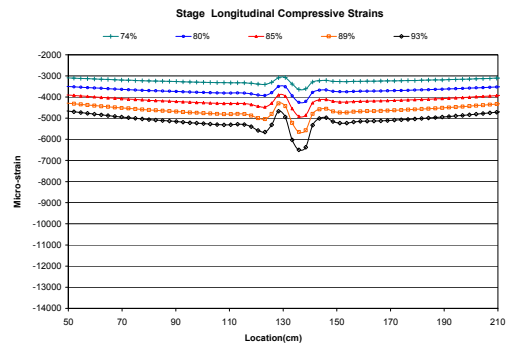
Figure C.34 Strains for Pipe
X100hdt80U00w
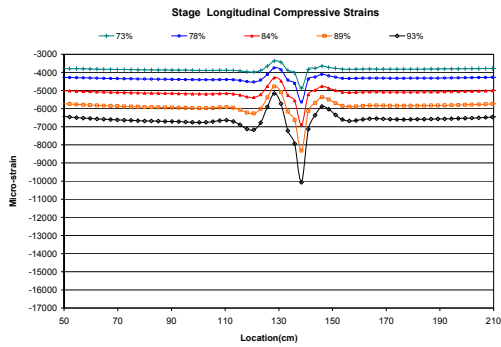
Figure C.35 Strains for Pipe
X100hdt80U40w
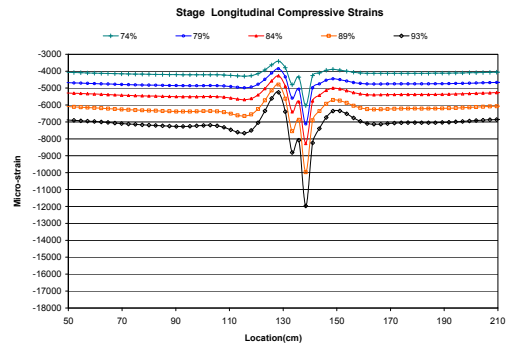
Figure C.36 Strains for Pipe
X100hdt80U80w

C.3 Strain Distributions along Pipes under an Axially Compressive Load
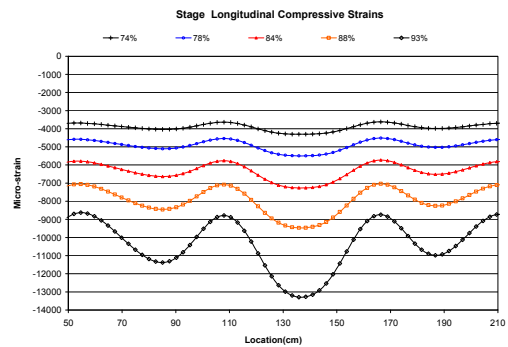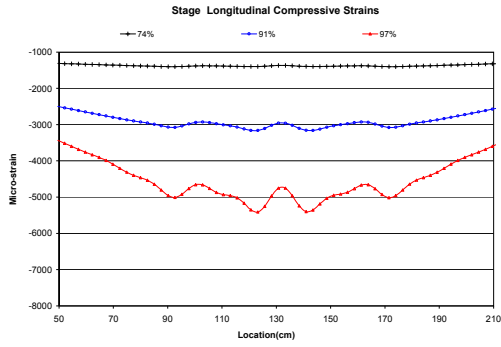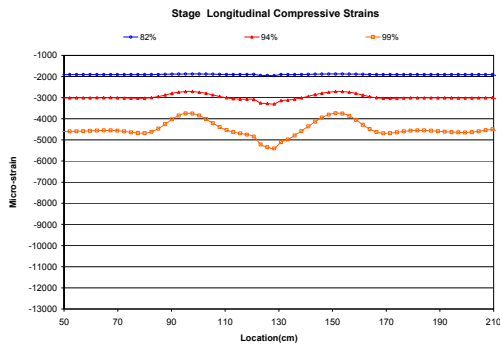

Figure C.37 Strains for Pipe
X65dt40C00
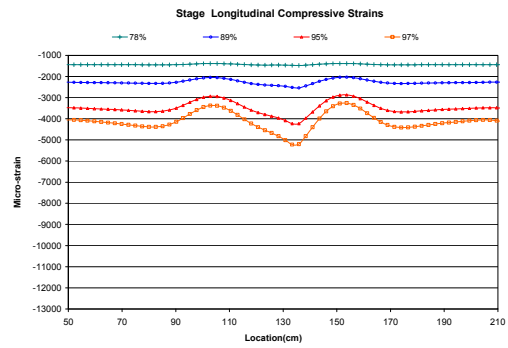
Figure C.38 Strains for Pipe
X65dt40C40
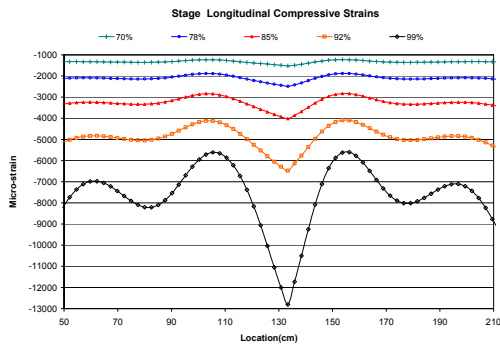
Figure C.39 Strains for Pipe
X65dt40C80
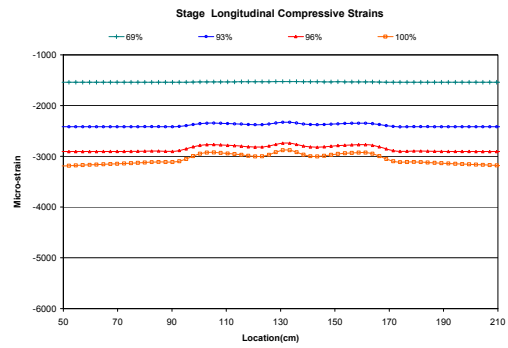
Figure C.40 Strains for Pipe
X65dt80C00
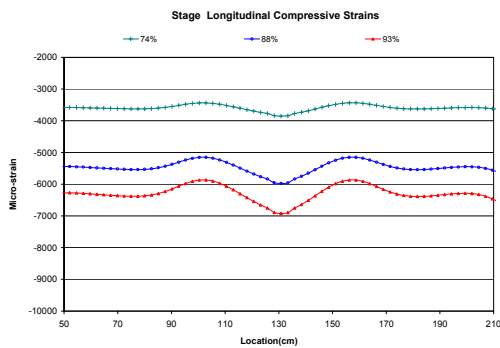
Figure C.41 Strains for Pipe
X80hdt40C80
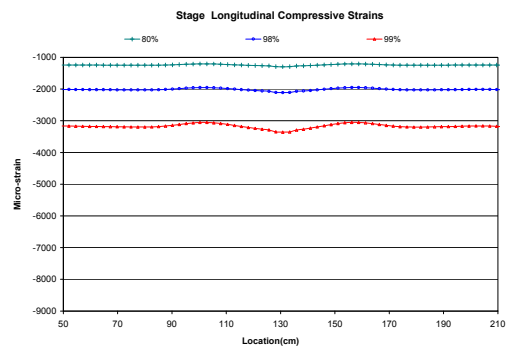
Figure C.42 Strains for Pipe
X100hdt40C80

Appendix D

**Conceptual Frameworks of Tracking Pipe Wrinkle Growth**

D.1 Identification of Tensile Strain Distribution Patterns:

As mentioned in Section 5.2.2.1, monitoring the distributed tensile strains on the buried pipeline could be as a criterion to detect pipe wrinkle, because the tensile strain distribution patterns change significantly after pipe buckling. Generally, the strain distribution pattern retains a relative flat distribution on the tension side before pipe softens; after pipe softens and pipe's dominating wrinkle forms, the strain distribution pattern gradually becomes an evident curve-distribution on the tension side. Nevertheless, moment gradient may exist on the some field pipes such as cold-bended pipes, and, consequently, a curve distribution occurs probably before pipe wrinkle initiates. Therefore, relative strains should be used to mitigate this effect on identification of signature patterns on the tension side.

ANN protocols can be built according to the similar procedure shown in the Section 7.3 to identify the relative strain distributions on the tension side for detecting pipe wrinkle. However, in the beginning of the warning system's operation, very few or even no real data are available to verify the ANN protocols, and, hence, a correlation coefficient curve probably can be instead of the ANN protocol in the warning system to detect the pipe wrinkle. The concept of using the correlation coefficient as an index of the behvioural signature of a wrinkled pipe was discussed in Section 5.2.2.1. A flow chart of using the correlation coefficient curve to detect the pipe wrinkle is presented in Figure D.1.

To generate the correlation coefficient curves, time series data are needed. Each data should be relative strains, and, thus, initial strains need to be collected. As discussed in Section 3.2.2, the tensile strain distributions of the cold-bended pipes had presented a vivid curve shape at about 70% of the peak moment. Therefore, if the proposed damage detection model (DDM) is used along with this criterion, the initial strains can be collected once DDM identifies the pipe as being in the warning condition; otherwise, the initial strains could be recorded after the operation of a pipeline. As well, the correlation coefficient was computed by comparing the strain distribution pattern with the reference pattern. Therefore, if the proposed damage detection model is used, onset of the pipe wrinkling can be

302

detected, and the relative strain distribution occurring at this specific period can be recorded as the reference pattern. After the reference pattern is obtained, the pipeline operators can track the development of the pipe wrinkle by comparing the reference pattern with a pattern recorded on the subsequent period. However, if the damage detection model cannot be used, pipe engineers should decide a specific period to record a reference pattern.

The procedure using correlation coefficient curve to find the pipe wrinkle is summarized as follows:

(1)   Acquire the processed data for the initial data, reference pattern, three sets of strain distribution patterns respectively at three sequential periods on the tension side, and their corresponding periods. The procedure of data processing shown in Section 7.1 can be used, but, herein, the maximum strain is the maximum tensile strain.

(2)   Compute relative strains for the reference pattern and the three sets of the strain distribution patterns.

(3)   Compute correlation coefficients by comparing the three sets of relative strain distributions with the reference pattern.

(4)   Normalize these three correlation coefficients. The normalization formula can use Equation 5.4 in Section 5.2.2.3.

(5)   Connect the three normalized correlation coefficients to generate a correlation-coefficients-versus-periods curve, similar to the curves shown in Figure 5.37.

(6)   Compute a slope between the neighbouring coefficients on this curve. A total of two slopes were obtained for the 3 coefficients.

(7)   Compute the change in these two slopes.

(8)   If the slope change is above the design threshold, a visible wrinkle has formed on the monitored pipe; otherwise, the strain distribution and its corresponding time at the next inspection period will replace the last data as the third set of the patterns, and the procedure will be repeated from (2).

Because the pipe wrinkle results in the change of strain distribution patterns on the tension side during the latter loading stage, e.g. during the post-buckling stage, as discussed in Chapter 5, this criterion is more apparent to be used for detecting a visible wrinkle occurring on the monitored pipe rather than the onset of the pipe wrinkling. However, it need to be careful for applying correlation coefficients in monitoring buried pipelines because the correlation coefficients are very sensitive to bias data (Asuero et al. 2006). As a non-meaningful deviation occurs in strain distributions, the correlation coefficients may be changed significantly in order to provide misleading information.

D.2 Detection of Strain Ratios Growth:

The strain ratio growth criterion is applied only in the critical position along the pipe segment, and its concept of the criterion and definition of the strain ratio were mentioned in Sections 5.2.2.2 and 6.3.1. Yoosef-Ghodsi (1994) studied the experimental results, and concluded that once wrinkling starts, the local strain over the wrinkle area increases much more rapidly than dose the overall strain. Lara (1987) studied the failure criterion of buried pipelines, and found that pipe wrinkle occurring on the pipe caused a rapid slope change in the strain ratio curve when the strain ratios were recorded in consecutive periods. Theoretically, strain ratio grows rapidly once pipe softens, and, thus, the threshold of the slop change corresponding to a wrinkle forming on the pipe should be selected in the loading stage after pipe softens; as the period of time corresponding to the increment of applied loadings or deformations is known, the threshold could be determined. However, no sufficient data are available in the current research to determine a reliable threshold and for this criterion. Therefore, only the conceptual scheme is proposed as a secondary reference index. In addition, this criterion probably cannot early detect pipe wrinkling; consequently, this criterion is more suitable to be used for preventing pipe damage from unacceptable wrinkle on the monitored pipe.

The time series data for this criterion should contain at least three sets: the first set of the data is collected just after the instruments start operation; once the damage detection model identifies pipe as being in the wrinkling condition where the corresponding strain ratio is less than 65% of the critical strain, the second set of time series data is collected. The advantages of using this data set as the second set of the time series data are explained below:

- The pipe wrinkling location has been defined, so that the pipeline operators can monitor only on the critical segment for growth of the pipe wrinkle. In the way, the time of data processing and the data collected during the inspection periods will be significantly reduced.

- For girth-welded pipes and cold-bended pipes, strain concentration sometimes occurs during an early loading stage and, consequently, causes strain ratios to grow from the early loading stage, e.g. 50% of the peak load. It is noted that this strain concentration in the cold-bended or girth-welded pipes probably does not result from the pipe wrinkle, but from the manufacturing process of the pipes. Using this specific data set as the second set of the time series data should be able to mitigate this problem.

After the second data is collected, the distributed strains are recorded in the subsequent period as the third data set.

Figure D.2 shows the procedure of using the strain ratio growth criterion to detect a pipe wrinkle. The procedure is summarized below:

(1)   Acquire the processed data for the first set, the second set, and the third set of strain distribution patterns on the critical position, and their corresponding periods. The procedure of data processing shown in Section 7.1 can be used to acquire the data above.

(2)   Compute strain ratios for these three sets of the strain distributions.

(3)   Normalize these three strain ratios. The normalization formula can use Equation 5.4 in Section 5.2.2.3.

(4) Connect the three normalized strain ratios to generate a strain-ratios-versus-periods-of-time curve, similar to the graph shown in Figure 5.38.

(5) Compute a slope between the neighbouring ratios on this curve. A total of two slopes were obtained for the 3 ratios.

(6) Compute the change in these two slopes

The difference between the two slopes is assessed. If the difference is above the designed threshold, an unacceptable wrinkle has occurred; otherwise, the third set of the data is updated by the new data acquired in the next inspection. Repeat the procedure (2) to (7) until the unacceptable wrinkle is detected.

```
         ┌─────────────────────────────────────┐
        ╱  Acquire processed data for the initial ╲
       ╱   data, reference pattern, three sets of   ╲
      ╱    strain distribution patterns at three     ╲
     ╱     sequential periods, and their              ╲
      ╲    corresponding periods.                    ╱
       ╲   (tension position)                       ╱
        └─────────────────────────────────────┘
                        │
                        ▼
    ┌──────────────────────────────────────────┐
    │ Compute relative strains for the collected patterns │◄──────────┐
    └──────────────────────────────────────────┘           │
                        │                                   │
                        ▼                          ┌────────────────┐
    ┌──────────────────────────────────────────┐  │ Acquire strain  │
    │ Compute the correlation coefficients by comparing │  │ distribution pattern│
    │ the three patterns with the reference pattern │  │ and the         │
    └──────────────────────────────────────────┘  │ corresponding period│
                        │                          │ at the next inspection│
                        ▼                          │ period, and they will│
    ┌──────────────────────────────────┐          │ replace the last set of│
    │ Normalize the three correlation  │          │ strain distribution│
    │ coefficients                     │          │ pattern and its │
    └──────────────────────────────────┘          │ corresponding period│
                        │                          └────────────────┘
                        ▼                                   ▲
    ┌──────────────────────────────────────────┐           │
    │ Connect the three normalized correlation │           │
    │ coefficients to generate a correlation-  │           │
    │ coefficients-versus-periods-of-time curve │           │
    └──────────────────────────────────────────┘           │
                        │                                   │ No
                        ▼                                   │
    ┌──────────────────────────────────┐                   │
    │ Compute slopes for the neighbouring │                 │
    │ coefficients on this curve       │                   │
    └──────────────────────────────────┘                   │
                        │                              ╱◄────┘
                        ▼                             ╱ ╲
    ┌──────────────────────────────────┐   ────────►╱ Above╲
    │ Compute the difference between   │            ╲thresh-╱
    │ the two slopes                   │             ╲ old ╱
    └──────────────────────────────────┘              ╲  ╱
                                                       │ Yes
                                                       ▼
                                              ╭──────────────────╮
                                              │  Visible wrinkle  │
                                              ╰──────────────────╯
```

Figure D.1 Flow Chart for Detection of Visible Wrinkle by Monitoring Tensile
Strain Distribution Patterns

307

Acquire the first set, the second set and the third set of the time series data in the specific periods. (critical position)

Compute strain ratios for these three sets of the strain distributions

Normalize the three strain ratios

Connect 3 sets of the normalized strain ratios to generate a strain-ratios-versus-periods-of-time curve

Compute slopes for the neighbouring ratios on this curve

Compute the difference between the two slopes

Above threshold

No

Yes

Acquire strain distribution pattern and the corresponding period at the next inspection period, and they will replace the third set of the time series data

Unacceptable wrinkle

Figure D.2 Flow Chart for Detecting the Growth of Pipe Wrinkle Using Strain Ratios Growth Criterion

Appendix E

**The Components, Learning Algorithm, Heuristic Procedure in ANN, and
Sample Commands for Integrating the ANN Models**

E.1 The Components of ANN

A typical multilayer ANN (see Figure E.1) includes six main components: neurons or processing units, scaling function, state of activation, output function, pattern of connectivity (or perceptron), and learning rule. These components are explained as follows:

E.1.1 Neurons

A neuron is a unit where information is received and transmitted. All processing in the ANN is carried out in the neurons, and, hence, the mathematical operators used to scale data, to sum weighs, and to amplify or t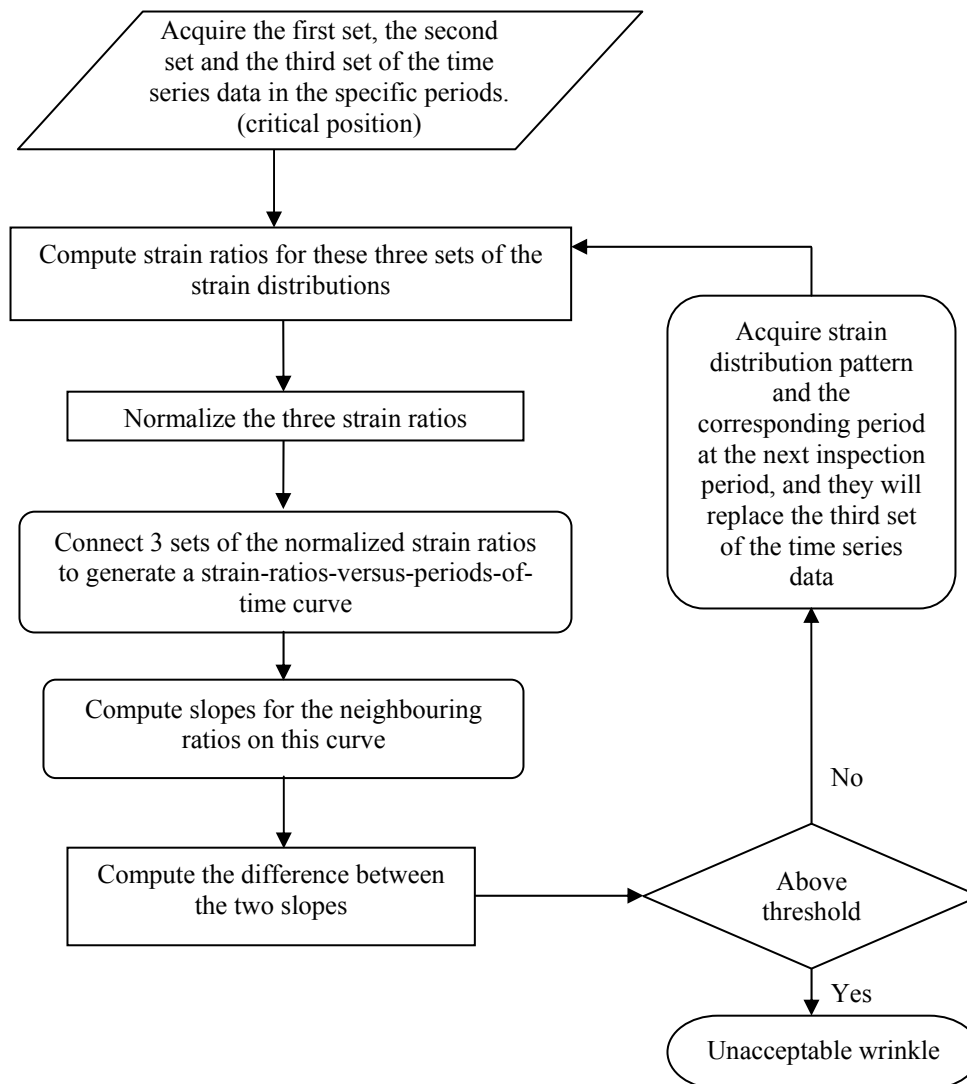o threshold data are performed in here. Neurons are organized into multiple layers containing input, output and hidden layers. A connect from a neuron to the other neuron is called a perceptron as shown in Figure E.1. The multilayer perceptrons can be as classifiers and is explained in the following paragraph:

In a multilayer perceptron (MLP), the neuron in the second layer has its threshold set so that it turns on only in the pre-set circumstance. In this way, the inputs can be classified into different groups, and each of the groups is discriminated by a linear boundary in pattern space. The outputs from the neurons in the second layer is passed to the next layer of the neurons via a perceptron with adaptable weights, and then the output in the third layer forms convex hull in pattern space. The output from the current layer is as the input of the further layer of the neurons via another perceptron with adaptable weights, and this input generates a new output which can form any arbitrary region in pattern space. Counting the number of active weight layers, or the number of active perceptron layers in the above operation of the ANN, that is a three-layer network. Beale and Jackson (1990) recommended that the number of the layers used in MLP should be no more than three.

E.1.2 Scaling function, State of activation, and Output function

Scaling function works in the input neuron. It converts the input data into a rational range that is suitable to the ANN operation. The interval of the range is usually among 1 to -1.

The activation is used in hidden layer neurons to allow the ANN to capture features and sub-features within a set of data. The most common activation function is sigmoidal function, because it is continuous s-shape function and the smooth curve makes this function easy to devise learning algorithms. The sigmoidal function's trend is roughly similar to neural fire rate of the biological neurons.

Each neuron transmits its output to the next neighbor or to the external environment through the output function, and the output is always a scalar value.

E.1.3 Weights

Weight (w) is used in the connectivity, and each represents the strength of connection between neurons. Functions of the weights in the ANN can be seen as coefficients of variables in the multiple regressions.

E.1.4 Learning Rule

Weights are revised through a computing procedure, which is a learning rule. A variety of learning algorithms have been proposed. Supervised learning and unsupervised learning are the main division that is based on whether or not the desired result is known for sample data used to train ANN. Respective to either supervised or unsupervised learning algorithm, different learning algorithms are applied in the each. For example, Some learning rules, such as backpropagation, upstart, and polynomial learning rules, are applied in the supervised learning; while the other rules, such as competitive learning and self organizing map, are usually used in the non-supervised learning (Mehrotra et al. 2000).

E.2 Backpropagation Learning Rule

The fundamental formulas of the backpropagation algorithm can be seen as a mechanism which is a generalized multiple regression analysis with the method of least mean square. The learning rule in a linear single layer network is presented in the following equations E.1 to E.4. Herein, y represents an actual output, f_{th} is a threshold function, w_i is a weigh applied in the connectivity between input node i and the output node, x_i represents an input on node i, and d represents the desired output. Because best learning is acquired usually through an iteratively computing procedure, in the following equations, t represents a specific step, and $t+1$ represents the step after the specific step.

$$y(t) = f_{th}[\sum_{i=0}^{n} w_i(t)x_i(t)] \tag{E.1}$$

Through the delta rule:

$$\Delta = d(t) - y(t) \tag{E.2}$$

If output is not desired, then

$$w_i(t+1) = w_i(t) + \eta * \Delta * x_i(t) \tag{E.3}$$

Otherwise,

$$w_i(t+1) = w_i(t) \tag{E.4}$$

Where Δ is an output error and η represents a gain term. The above learning rule is also called the Widrow-Hoff least mean squares (LMS) filter adaptive algorithm, and this kind of adaptive linear neurons is called ADALINEs. The ADALINEs converges to least squares error $E_p = (d - y)^2$ through gradient descent.

As the above concept is applied in a 2-layer perceptron as shown in Figure E.1, the calculation of the output error of neurons is modified from the equation E.2 to a form of square error, as shown in equation E.5:

$$E_p = \frac{1}{2}\sum_j (d_{pj} - y_{pj})^2 \qquad (E.5)$$

In which E_p is the error function for an input pattern p, d_{pj} represents the desired output for the pattern p on the output layer j, y_{pj} is the actual output at this layer. Because of feed-forward procedure of the multiple layer perceptrons (MLP), data is fed to the ANN from input neurons, through hidden neurons, to output neurons. A net input t_{pk} in the hidden layer k is obtained by multiplying the weights w_{ik} on the connectivity between the layers i and k by the outputs of the nodes y_{pi}, respectively, in the input layer, as shown in equation E.6:

$$t_{pk} = \sum_i w_{ik} y_{pi} \qquad (E.6)$$

Then the actual output y_{pk} from each node in the hidden layer k is by acting the threshold function f_k on the weighted sum t_{pk}, as expressed in equation E.7:

$$y_{pk} = f_j(t_{pk}) \qquad (E.7)$$

The same procedure used in equations E.6 and E.7 forwards to the next perceptron in the hidden layer k and the output layer j. Then the actual output y_{pj} from each node in the layer j is by acting the threshold function f_j on the weighted sum t_{pj}, as expressed in equation E.8:

$$y_{pj} = f_j(t_{pj}) \qquad (E.8)$$

Herein, the feed-forward procedure is finished. The delta rule in the MLP is derived by attempting to minimize the error in the output of the perceptron between the layers k and j through gradient descent. The error function E_p can

313

acquire a minimum by computing the partial derivative of the error with respect to each weight w_{kj}, as shown in the equations E.9:

$$\frac{\partial E_p}{\partial w_{kj}} = \frac{\partial E_p}{\partial t_{pj}} \frac{\partial t_{pj}}{\partial w_{kj}}$$
(E.9)

The following term δ_{pj} is defined as an error change and chain rule is applied in equation E.9 to be as equation E.10:

$$\delta_{pj} = -\frac{\partial E_p}{\partial t_{pj}} = -\frac{\partial E_p}{\partial y_{pj}} \frac{\partial y_{pj}}{\partial t_{pj}} = (d_{pj} - y_{pj})f_j^{'}(t_{pj})$$
(E.10)

Accordingly, using the error change δ_{pj} and the following equation E.11 backward revises the weighs w_{kj}, connecting the output layer and the hidden layer:

$$w_{kj}(t+1) = w_{kj}(t) + \eta \delta_{pj} y_{pk}$$
(E.11)

Continuously to revise weighs backward for the previous layer perceptron. Because of the desired outputs are unknown in the hidden nodes, through the error transmission from the output nodes and by using the chain rule, the equation E.10 is modified into the following equation E.12:

$$\delta_{pk} = f_k^{'}(t_{pk}) \sum_j \delta_{pj} w_{kj}$$
(E.12)

Then, the weighs w_{ik} connecting the hidden layer k and the input layer i is revised backward by using equation E.13:

$$w_{ik}(t+1) = w_{ik}(t) + \eta \delta_{pk} y_{pi}$$
(E.13)

In the equations E.11 and E.13, the gain term η is called learning rate. Equations E.5 to E.13 are fundamental formula used in backpropagation learning rule for a multilayer artificial neuron network.

E.3 Heuristic Procedure for the ANN Model with Backpropagation Learning Rule

Heuristic procedure is recommended to be used in building an ANN model with the backpropagation training algorithm. The heuristic procedure could have the following 10 steps:

(1)   Selection of model inputs and outputs:

- Full inputs that are possible to affect outputs are used in a preliminary protocol, and then ones with low sensitivity should be deleted in a final protocol.

- The best models usually only have a single output parameter.

(2)   Defining the model domain:

- Models need to be divided for contradictory areas of the domain.

- A single output with two models or two outputs with a model are usually useful for the above condition.

(3)   Data pre-processing:

- Data patterns that do not contribute to training should be eliminate.

- Data inspection and sampling are needed.

- Data scaling or normalization should be applied.

(4)   Selection of training/testing cases

- Training cases should be representative of the problem domain.

- Data set is randomly divided into training and testing sets.

- The number of training cases affects the accuracy of prediction.

In addition, to provide a reliable convergence in ANN with backpropagation algorithm, the number of training sets depends mainly on the number of input neurons and the similarity among training patterns.

A rule of thumb shows that the number of training sets, N_t, should be at least 5 times the number of weights, $|w|$, in network (Mehrotra et al.

2000), and this rule can be referred to the following formula (Baum et al. 1989):

$$N_t > \frac{|w|}{(1 - A\%)} \qquad \text{(E.14)}$$

Accordingly, if the number of training sets uses 5 times the number of weights, the accuracy of ANN model's prediction, A%, is 80%. However, this rule could be too conservative. By observing the relationship among the number of training sets, the number of weights, and the accuracy of ANN model's prediction in the previous research projects (Hegazy et al. 1998, Amali et al. 2006, Kesavan et al. 2008), the number of the training sets used in these projects is only one-thirds to one-hundredths of the required number calculated by Baum's formula.

(5)   Number of neurons:

The number of neurons is dependent on the number of training sets and the number of parameters. The number of neurons in a hidden layer, N_h, is usually obtained experimentally. In Neuroshell2, the number of the hidden neurons is computed based on the following formulas:

$$N_h = \frac{1}{2}(N_i + N_o) + \sqrt{N_t} \qquad \text{(E.15)}$$

Where
N_i: number of the input neurons
N_o: number of the output neurons
N_t: number of the patterns in training sets

(6)   Scaling function and Activation function

Scaling function is used in the input layer to scale data from their numeric range into a range that the neural network can deals with problems

316

efficiently, while, sometimes, it is applied in output layer to scale output data from the ranges used by the network into numeric range.

Activation function is used in the hidden neuron and output neuron. As mentioned, a weighted sum in the layer has to beyond the threshold level, so that the sum can be output and move into the next layer. The threshold level is built by activation function. A variety of activation functions, such as linear, sigmoid (logistic), hyperbolic tangent (Tanh), and Gaussian functions, were used in the thesis, and are shown in the Figures E.2 (a) to (d). As well, the main characters of these functions are briefly explained below:

Sigmoid function:

It is a smooth curve, and is most popular to be used when the outputs are as categories. Furthermore, Biomedicine researchers think this asymptotic trend of the function curve is very close to thinking model of the human.

Hyperbolic Tangent (Tanh) function:

This function is an increasing curve. It seldom used in ANN, but, however, it is useful for some specific cases, especially when linear function is applied in an output layer. A successful example used in identification of distributed strain signatures has been published by Kesavan et al. (2008).

Gaussian function:

This function is recommended by NeuroShell2 software for continuous valued outputs. This function has own a classic bell shaped curve that is far different from increasing curves of conventional activation functions, such as sigmoid function. The unique character of the bell shaped curve is

to map high values into low ones, and map mid-range values into high ones.

(7)   Initial weight values

As mentioned, the delta rule in the MLP is derived by attempting to minimize the error in the output of the perceptron between the two layers through gradient descent. The error function can acquire a minimum by computing the partial derivative of the error with respect to each weight. Consequently, the weight value needs to be randomized initially; otherwise, the gradient descent rule may never be able to leave the start point.

(8)   Learning rate and momentum

- Learning rate affects the speed and correction of convergence.
- The learning rate is selected as large as possible, but without leading to oscillation.
- Adding momentum term can improve network learning speed and dampen out oscillations

(9)   Stopping criteria for training:

The training should stop when

- The testing error is sufficiently small
- The testing error begins to increase
- Coefficient of multiple determination (R^2) for classification of the ANN approaches asymptote

(10)   Evaluation of model stability:

Changing the method of the data sorting only and remaining other parameters same ensure that model results are independent of method of data sorting

Inputs: i　　　　Hidden: k　　　Outputs: j

Initial Weight
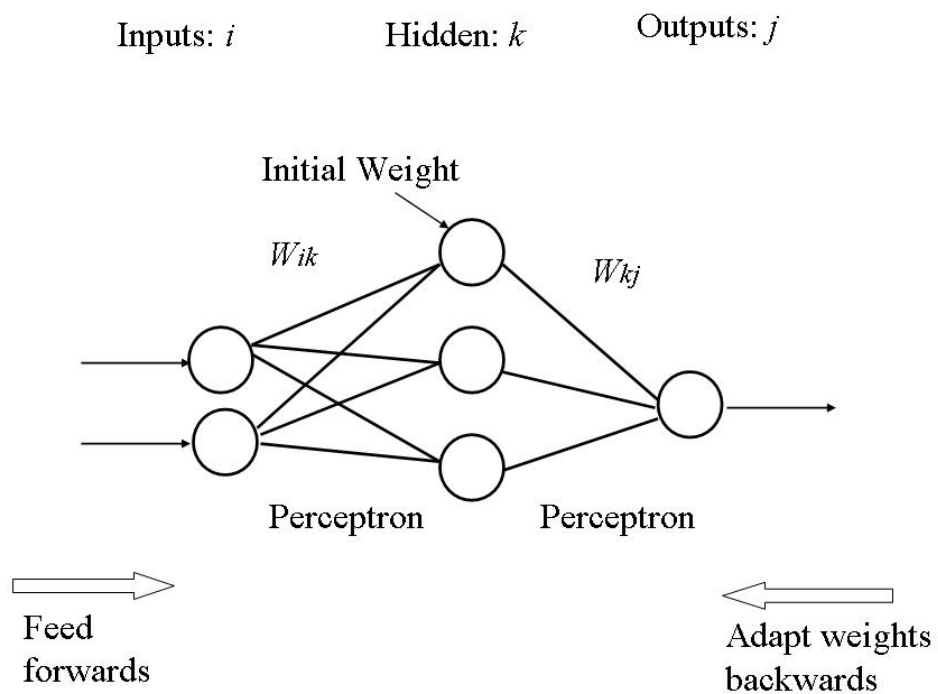
W_{ik}　　　　　W_{kj}

Perceptron　　　　Perceptron

Feed
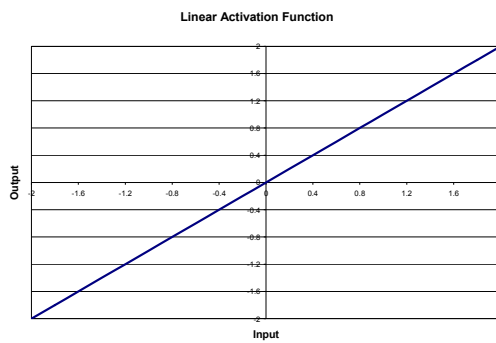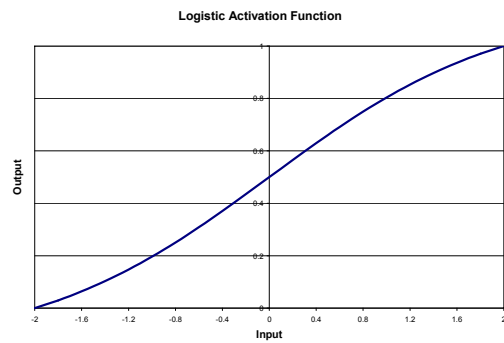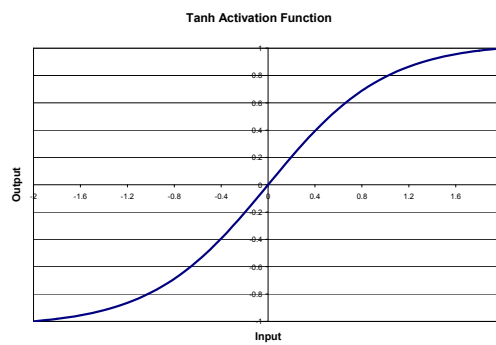forwards

Adapt weights
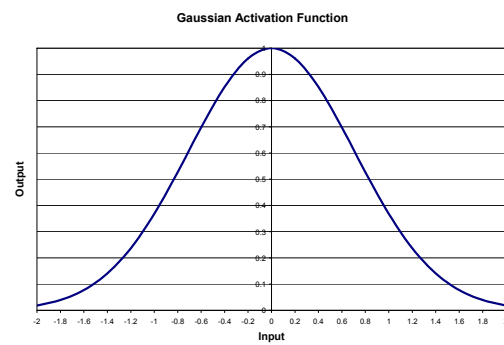backwards

Figure E.1 Multilayer ANN (Perceptron)

(a) Linear Function

(b) Logistic-sigmoidal Function

(c) Hyperbolic Tangent (Tanh) Functions

(d) Gaussian Function

Figure E.2 Activation Functions

E.4 The Application of Trained ANN Models in Windows Operation System:

After ANN model's source code is generated in Runtime facilities of NeuroShell2, the completely trained ANN models can link MS Excel with dynamic link library (DLL) by using the add-in function Predict( ) or using VBA. The following example uses Predict function to call the trained ANN(2), inputs-18-5r1, in MS Excel 2000:

=Predict(filename, input_range, output_number);

[Example] =Predict("C:\ANN\inputs-18-5r1.def",$A$1:$A$20,1)